

2016

Modeling flocculation and deflocculation processes of cohesive sediments

Xiaoteng Shen

College of William and Mary - Virginia Institute of Marine Science

Follow this and additional works at: <https://scholarworks.wm.edu/etd>



Part of the [Civil Engineering Commons](#), [Environmental Engineering Commons](#), and the [Oceanography Commons](#)

Recommended Citation

Shen, Xiaoteng, "Modeling flocculation and deflocculation processes of cohesive sediments" (2016). *Dissertations, Theses, and Masters Projects*. Paper 1539616853.
<https://dx.doi.org/doi:10.25773/v5-rz6r-q217>

This Dissertation is brought to you for free and open access by the Theses, Dissertations, & Master Projects at W&M ScholarWorks. It has been accepted for inclusion in Dissertations, Theses, and Masters Projects by an authorized administrator of W&M ScholarWorks. For more information, please contact scholarworks@wm.edu.

Modeling Flocculation and Deflocculation Processes of Cohesive Sediments

A Dissertation

Presented to

The Faculty of the School of Marine Science
The College of William and Mary in Virginia

In Partial Fulfillment
Of the Requirements for the Degree of
Doctor of Philosophy

by

Xiaoteng Shen

2016

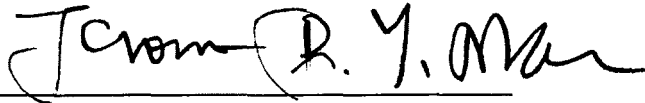
APPROVAL SHEET

This dissertation is submitted in partial fulfillment of
the requirements for the degree of
Doctor of Philosophy



Xiaoteng Shen

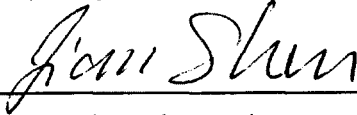
Approved, by the Committee, November 2015



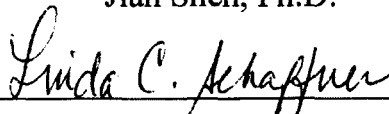
Jerome P.-Y. Maa, Ph.D.
Committee Chairman / Advisor



Carl T. Friedrichs, Ph.D.



Jian Shen, Ph.D.



Linda C. Schaffner, Ph.D.



Earl J. Hayter, Ph.D.
U.S. Army Corps of Engineers
Vicksburg, Mississippi

DEDICATION

The experience is like a song, when listened to, refreshing, suddenly finalizing, lamenting the youth no longer, but the melody is lingering, the rhythm is babbling, while the singer is new. I would like to dedicate this dissertation to my beloved family as well as to all my friends who have accompanied me with their affection, love, and encouragement through this cherished time.

TABLE OF CONTENTS

	Page
ACKNOWLEDGMENTS	vii
LIST OF TABLES	ix
LIST OF FIGURES	x
AUTHOR'S NOTE	xvi
ABSTRACT	xvii
CHAPTERS	
I. GENERAL INTRODUCTION	2
Problem statement	3
Scope and objectives	7
Outline	8
References	10
II. MODELING FLOC SIZE DISTRIBUTION OF SUSPENDED COHESIVE SEDIMENTS USING QUADRATURE METHOD OF MOMENTS	13
Abstract	14
Introduction	15
Model description and numerical methods	19
Case studies	31
Results and discussions	36
Conclusions	43
Acknowledgements	45
Appendix 2-A: Wheeler's algorithm	46
Notation	51
References	53

III. NUMERICAL SIMULATIONS OF PARTICLE SIZE DISTRIBUTIONS:
 COMPARISON WITH ANALYTICAL SOLUTIONS AND KAOLINITE
 FLOCCULATION EXPERIMENTS 71

- Abstract 72
- Introduction 73
- Review of quadrature method of moments 75
- Validations with analytical solutions 79
- Experimental validations for kaolinite suspensions 90
- Discussion 98
- Conclusions 99
- Acknowledgements 100
- List of global symbols 101
- References 104

IV. A CAMERA AND IMAGE PROCESSING SYSTEM FOR FLOC SIZE
 DISTRIBUTIONS OF SUSPENDED PARTICLES 128

- Abstract 129
- Introduction 130
- Experiment setup 135
- Image analysis procedure 142
- Application for kaolinite suspensions 155
- Conclusions 162
- Acknowledgements 164
- References 165

V. FLOC SIZE DISTRIBUTIONS OF SUSPENDED KAOLINITE IN AN ADVECTION TRANSPORT DOMINATED TANK: MEASUREMENTS AND MODELING	192
Abstract	193
Introduction	194
Experiment setup	198
Floc distribution model	209
Results and discussions	216
Conclusions	220
Acknowledgements	221
References	222
 VI. CONCLUSIONS AND PERSPECTIVES	 243
Conclusions	244
Future study	245
References	250
 APPENDICES	
A. FLOC SIZE DISTRIBUTION BOX MODEL	254
B. EXAMPLE OF INPUT FILE OF FLOC SIZE DISTRIBUTION BOX MODEL	283
C. MICRO-CONTROLLER OPERATING PROGRAM	285
D. EMPIRICAL IMAGE PROCESSING SOFTWARE	289
E. TURBULENCE CHARACTERISTICS COMPUTING SOFTWARE	295
 VITA	 302

ACKNOWLEDGMENTS

I am extremely grateful to the Virginia Institute of Marine Science (VIMS, Gloucester Point, VA) community for supporting my education, my research, and I over the past 52 months.

I would first like to extend my deepest gratitude to my major advisor, Dr. Jerome P.-Y. Maa, for his tireless commitment to and support of my dissertation project and my academic career in VIMS. He is always patient, enthusiastic, and wise. He guided me into the area of marine science, and taught and showed me how to do logical research, scientific writing, and audience-oriented presentations. I always enjoy our discussion time every week.

I am also immensely appreciative for the rest of my wonderful committee members: VIMS faculty Dr. Carl T. Friedrichs, Dr. Jian Shen, and Dr. Linda C. Schaffner, and outside member Dr. Earl J. Hayter (U.S. Army Corps of Engineers, Vicksburg, MS). Their expertise, insight, and guidance have been instrumental in the development of this dissertation. I also thank Dr. Courtney K. Harris who graciously served as the moderator for my qualifying examination and the final defense.

I would like to acknowledge Dr. Yixin Yan, Dr. Yuyang Shao, and Dr. Chaofeng Tong from Hohai University (Nanjing, Jiangsu Province, China), and Dr. Jinfeng Zhang from Tianjin University (Tianjin, China), for their instructive comments during this study. This dissertation also benefitted from those who give me assistance for several experimental apparatus or reagents, especially Dr. Jeffrey D. Shields and Dr. Grace M. Cartwright.

Thank you to all my “New Kids” classmates. I never forget the wonderful time we spent on the eastern shore, during disorientation, and on Halloween. Thank you to all my Chinese friends in Gloucester County, Williamsburg, and Newport News. You wipe out my loneliness, and I feel warm when you are around. Thank you to all my sport buddies. I will never forget playing soccer with you at Woodville Park and VIMS Fort Area, playing basketball at William & Mary Recreation Center, playing volleyball at VIMS Page House lawn area, and playing tennis at York High School. I have not gained too much weight because of you. Also thank you to all VIMS staff that provides business, information, networking, and library support, and everyone else who made my experience at VIMS so wonderful. Special thanks to Mr. Daniel Kaufman and the consultants in William & Mary Writing Resource Center who help me to polish most of my manuscripts. Special thanks to Mr. Wenlin Ding, Mr. Lei Sun, Ms. Annie Cheung, and Ms. Xue Gu. I really do not know how to express my sincere thanks to you using words.

“The world is a book and those who do not travel read only one page.” Special thanks given to those who have been with me visiting various gorgeous attractions around the United States and Western Europe, such as Williamsburg Bush Garden & Colonial Williamsburg, Virginia Eastern Shore & Chincoteague Island, Virginia Great Falls, Shenandoah National Park, North Carolina Outer Banks, West Virginia Blackwater Falls & Canaan Valley, Grand Canyon, Hoover Dam, Valley of Fire, Red Rock Canyon, Death Valley, Crater Lake, Starved Rock, as well as cities including New York, Boston, Washington D.C., Chicago, Las Vegas, Seattle, San Francisco, Los Angeles, San Diego, Brussels, Bruges, Ghent, Paris, Luxemburg, Köln, Rudesheim, and Den Haag.

Successful completion of this dissertation would not have been possible without the support of VIMS Student Research Grant, Chinese Scholarship Council (CSC) Scholarship, and a grant from Korea Institute of Ocean Science and Technology. I would also like to express my heartfelt gratitude to the Physical Sciences Nichols Travel Award Committee, who awarded me the Nichols Fellowship in 2013 and to the School of Marine Science Graduate Program Fellowships Committee, who awarded me the Olsson Family Graduate Student Fellowship in 2014. I am also highly excited to have the excellent professional development opportunity to serve as a graduate teaching assistant working with Dr. Christopher J. Hein for the course “Marine Geology” in Fall 2015 semester.

Last but certainly not least, I would like to thank my family, especially my parents, for their tolerance and understanding. Without their unconditional love and unfailing support, I would not be where I am today. To all those mentioned above and anyone I forgot to mention, I extend my thanks by dedicating the following words from “You Raise Me Up” (music by Secret Garden’s Rolf Lovland and lyrics by Brendan Graham):

You raise me up, so I can stand on mountains;
You raise me up to walk on stormy seas;
I am strong when I am on your shoulders;
You raise me up to more than I can be.

Thanks again to everyone for keeping my spirits up and giving me your continual support.

LIST OF TABLES

Page

CHAPTER II

Table 2.1	The flocculation parameter C_1 and C_2 derived through QMOM–PBM optimization by comparison with the experimental results of Furukawa and Watkins (2012) for colloidal montmorillonite	61
-----------	---	----

CHAPTER IV

Table 4.1	Summary of experimental conditions, camera measurement results and model simulation results.....	174
-----------	--	-----

LIST OF FIGURES

	Page
<u>CHAPTER I</u>	
Fig. 1.1 Sediment dynamics in natural environments (Modified from Maggi, 2005)	12
 <u>CHAPTER II</u>	
Fig. 2.1 Comparison between steady state experimental and simulated FSDs for (a) (b) calibration and (c) (d) verification results for suspended kaolinite with mass concentration 0.5 g/L and various shear rates	62
Fig. 2.2 Comparison between steady state experimental and simulated median size for suspended kaolinite with mass concentration 0.5 g/L and various shear rates	63
Fig. 2.3 Model computed time evolution of FSDs for suspended kaolinite at various shear rates with sediment mass concentration $c = 0.5$ g/L	64
Fig. 2.4 An example of the model-calculated temporal evolution of lower order moments of FSD for suspended kaolinite (Solid line – directly tracked in the model; dashed line – derived using the simulated class sizes and the corresponding weights)	65
Fig. 2.5 An example of the model-calculated temporal evolution of De Broukere mean, Sauther mean, and median size for suspended kaolinite. The solid circle is the experimentally observed median size (data from Mietta et al. (2008))	66
Fig. 2.6 An example of the model-calculated temporal evolution of death (loss) and birth (gain) of floc number and floc volume for suspended kaolinite	67
Fig. 2.7 An example of model-calculated temporal change of floc numbers (δm_0) due to aggregation and breakup for suspended kaolinite	68
Fig. 2.8 Comparison of model-calculated temporal evolution of d_{60} (hydrodynamic mean size) of colloidal montmorillonite with measured data (all symbols) from Furukawa and Watkins (2012). (a) Pure Montmorillonite with different salinity, (b) Montmorillonite with xanthan for different salinity, and (c) Montmorillonite with a fixed salinity of 7.2 ppt, but different organic matter. Lines are the results of this model study. Constants and other conditions are summarized in Table 2.1.	69

Fig. 2.9	The model-calculated FSD for pure montmorillonite mixture with salinity = 7.2 and 1.8 ppt	70
----------	---	----

CHAPTER III

Fig. 3.1	Time evolution of PSDs for the pure coagulation event with a constant coagulation kernel, $\beta_0 = 1$ (Case I)	110
Fig. 3.2	Time evolution of normalized moments for the pure coagulation event with a constant kernel (Case I). Circles are analytical solutions at selected times; solid lines are direct numerical predictions; dashed lines are indirect predictions by using Eq. 3.4.....	111
Fig. 3.3	Percentage error for the first seven moments against intensity of coagulation (I_{agg} , see Eq. 3.12 for definition) for the pure coagulation event with a constant kernel (Case I). Solid lines are for the moments that are directly simulated; dashed lines are for the moments that are indirectly calculated by using Eq. 3.4. m_3 is excellently predicted so that the error is not reported.....	112
Fig. 3.4	Time evolution of various characteristic sizes for the pure coagulation event with a constant kernel (Case I). Solid lines are for selected mean size (i.e., d_{10} , d_{32} , and d_{43}); the dashed line is the number-based median size (D_{50}); and the dotted line is for mode (or peak) size.	113
Fig. 3.5	Time evolution of PSDs for the pure coagulation event with sum coagulation kernel (Case II). Solid lines are analytical solutions; circles are numerical model predictions.....	114
Fig. 3.6	Time evolution of (a) m_0 and (b) m_6 , and (c) relative error of $f_1(m_c)$ (Eq. 3.21a) and $f_2(m_0)$ (Eq. 3.22a) for these two pure coagulation events with different Brownian kernels (Case III).....	115
Fig. 3.7	Time evolution of predicted normalized PSDs for these two pure coagulation events with different Brownian kernels (Case III).....	116
Fig. 3.8	Time evolution of normalized PSDs for the pure breakup event with a power law kernel (Case IV).	117
Fig. 3.9	Time evolution of normalized PSDs for the combined coagulation and breakup events with a constant coagulation kernel and a power law breakage kernel (Case V).....	118

Fig. 3.10	Time evolution of various characteristic sizes for the combined coagulation and breakup events with a constant coagulation kernel and a power law breakage kernel (Case V). Solid lines are for selected mean size (d_{10} , d_{32} , and d_{43}); dashed line is the median size (D_{50}); dotted line is the mode size.	119
Fig. 3.11	Simulated time evolution of PSDs for Case VI, which includes a sum coagulation kernel, a power breakup kernel, and a binary fragmentation distribution function. The steady state result from Vanni (2000) is also given for a comparison.....	120
Fig. 3.12	(a) Time evolution of mean and median sizes, and (b) comparison of experimental and predicted steady state PSDs for kaolinite flocculation in a mixing chamber with a suspended sediment concentration of 0.52 g/L and a shear rate of 45 s^{-1}	121
Fig. 3.13	Sensitivity tests for different constant and variable fractal dimensions in the flocculation model for their (a) mean sizes and (b) PSD predictions.....	122
Fig. 3.14	Sensitivity tests for different sizes of primary particles in the flocculation model for their (a) mean sizes and (b) PSD predictions. Dashed lines are for the cases in which primary particles are normal distributions with mean/median size $5 \mu\text{m}$ and various variances.....	123
Fig. 3.15	Sensitivity tests for different C_1 and C_2 (with the same ratio of C_1/C_2) in the flocculation model for their (a) mean sizes and (b) PSD predictions.....	124
Fig. 3.16	Sensitivity test for different fragmentation distribution functions in the flocculation model for their (a) mean sizes and (b) PSD predictions.....	125
Fig. 3.17	Predictions of PSDs for (a) ternary breakup and (b) uniform breakup by matching experimental mean size through changing C_2	126
Fig. 3.18	Predictions of PSDs based on 2, 3, 4, 5 and 7 quadrature nodes.....	127

CHAPTER IV

Fig. 4.1	Electric circuit for controlling camera for picture taking and LED light. D1 to D12 are the same surface mounted 1 watt white LED OVSPW1BCR4. C1 to C4 are capacitors with the number marked in unit of μF . Other electronic components are marked in the figure.....	175
----------	---	-----

Fig. 4.2	The mixing chamber. The impeller is installed 4 cm above the bottom. The maximum chamber-averaged shear rate is 217 s^{-1}	176
Fig. 4.3	Example of image analyzing procedure for silver coated hollow glass spheres with nominal size $10 \mu\text{m}$. (a) Original greyscale figure, (b) after background removing, (c) after thresholding, and (d) after removing out-of-focus particles. Note that (a) and (b) are displayed as its negative with contrast adjustment. Since abundant particles are obtained in one image in this case, only the central $1/27 \times 1/27$ are represented in this diagram, so that the particle No. 11 in (c) is not on the border of the image.....	177
Fig. 4.4	Example to show the different background intensity in an image for polystyrene particles. 16×10 subareas are selected to cover the entire 4912×3264 pixels	178
Fig. 4.5	Example of gradients for each pixel and the selection of the critical gradient for kaolinite suspensions.....	179
Fig. 4.6	Example of microscope image (magnified 400 times) of the silver coated hollow glass spheres. Even with 100 times magnification, the image is sharp enough to be used as a ground truth for validation purposes.	180
Fig. 4.7	Comparison of FSDs from images taken by using the microscope and the camera for the silver coated hollow glass spheres. Vertical line segments in the bar plot show the standard deviation of ten randomly selected images.....	181
Fig. 4.8	Example of a microscope image (magnified 100 times) of the polystyrene particles.....	182
Fig. 4.9	Comparison of FSDs from images taken by using the microscope and the camera for the polystyrene particles.....	183
Fig. 4.10	The difference in calculated FSD and mean size with respect to the number of total polystyrene particles included in images used for processing FSD. Each symbol denotes one image, and the right most symbols represent using 49 images with a number of more than 2,500 particles. The dashed line represents that required by the British Standard, i.e., 625 particles, or 11 images.....	184
Fig. 4.11	The difference in each bin of the measured FSDs to show the convergence. The result of using 50 images is assumed as the ground truth.....	185
Fig. 4.12	Model calibration and simulation for pure kaolinite flocculation results for various shear rates and suspended sediment concentrations.....	186

Fig. 4.13	Effects of salinity on equilibrium FSDs of suspended kaolinite with shear rate = 55 s^{-1} and suspended sediment concentration = 0.28 g/L	187
Fig. 4.14	Time evolution of OBS counts during flocculation tests for various guar gum dosages. Shear rate $G = 55 \text{ s}^{-1}$ and initial suspended kaolinite concentration $c = 0.52 \text{ g/L}$	188
Fig. 4.15	Experimental results to show the effect of guar gum dosage on the equilibrium FSDs of kaolinite suspension in tap water. Shear rate $G = 55 \text{ s}^{-1}$ and initial suspended sediment concentration $c = 0.52 \text{ g/L}$	189
Fig. 4.16	The change of mean and median kaolinite floc sizes caused by different guar gum dosages. Vertical line segments represent the variation of measurements at 23.0 hr, 23.5 hr, and 24.0 hr. Shear rate $G = 55 \text{ s}^{-1}$ and initial suspended kaolinite concentration $c = 0.52 \text{ g/L}$	190
Fig. 4.17	Comparison of experimental and model-simulated equilibrium FSDs for kaolinite suspension with guar gum concentration $c_{\text{guar}} = 5 \text{ mg/L}$, shear rate $G = 55 \text{ s}^{-1}$, and initial suspended kaolinite concentration $c = 0.52 \text{ g/L}$	191

CHAPTER V

Fig. 5.1	Experimental Setup. The plot of the streamtube along the dashed line is not drawn to scale. It is small near the pump and becomes large when far away. The vertical coordinate, z , starts at the tank bottom and the stream tube coordinate, s , starts at $z = 30 \text{ cm}$	229
Fig. 5.2	Example of the energy dissipation rate calculated by using the vertical velocity component of the energy spectrum.....	230
Fig. 5.3	Response of OBS counts during the experimental period.....	231
Fig. 5.4	Schematic diagram of the controlling system for acquiring images.....	232
Fig. 5.5	Example of intensity diagram for the light source of (a) a green laser module and (b) twelve LEDs.....	233
Fig. 5.6	Control volume to derive the governing equation of the conceptual 1-D FSD model along a streamtube. Filled circles represent floc with size L and the number density of this size floc is n	234

Fig. 5.7	Flow properties along the conceptual streamtube. Circles are measured results, and diamonds are estimated. Lines in (a) (b) and (c) are fitted results, while in (d) (e) and (f) are modeled results based on data shown in (b) and (c). (U_s – flow velocity along the streamtube; ε – energy dissipation rate; K – TKE; D – eddy diffusivity; G – local shear rate; λ – Kolmogorov scale).....	235
Fig. 5.8	Measured FSDs at varying elevation close to the side wall of the tank.....	236
Fig. 5.9	Time evolution of mean size along the streamtube, with symbol “x” and “o” denoting predicted and measured results at residence time $t = 33$ s.....	237
Fig. 5.10	Normalized moments $m_k(t = 33 \text{ s}) / m_k(t = 0)$ ($k = 0, 1, 2, 3, 4, 5$) at $t = 33$ s along the streamtube.....	238
Fig. 5.11	Time evolution of normalized total particle number along the streamtube. Lines are plotted every 2 s. The initial number is assumed the same along the streamtube.....	239
Fig. 5.12	Example of simulated time evolution of FSDs at 50 cm above the bottom of the tank close to the side wall ($s = 176$ cm). Measured FSD at $t = 33$ s are also plotted for comparison.....	240
Fig. 5.13	Model predictions of time evolution of mean sizes at three selected locations	241
Fig. 5.14	Model predictions of FSDs at $t = 33$ s and at the equilibrium state for three selected locations.....	242

AUTHOR'S NOTE

The chapters that comprise this dissertation were written in manuscript format for scientific publication. Thus, the formatting of each chapter (except the first and last chapter for general introduction and conclusion) follows the guidelines of the publication to which the manuscript was or will be submitted. At the time of writing, citations for individual chapters are as follows:

CHAPTER II

Shen, X., Maa, J.P.Y., 2015. Modeling floc size distribution of suspended cohesive sediments using quadrature method of moments. *Marine Geology* 359, 106–119.

CHAPTER III

Shen, X., Maa, J.P.Y. Numerical simulations of particle size distributions: Comparison with analytical solutions and kaolinite flocculation experiments. Submitted to *Marine Geology*.

CHAPTER IV

Shen, X., Maa, J.P.Y. A camera and image processing system for floc size distributions of suspended particles. Submitted to *Marine Geology*.

CHAPTER V

Shen, X., Maa, J.P.Y. Floc size distributions of suspended kaolinite in an advection transport dominated tank: Measurements and modeling. Submitted to *Ocean Dynamics*.

ABSTRACT

The transport and fate of cohesive sediments are responsible for many engineering, environmental, economic and policy issues that relate to, for example, siltation and dredging in navigation channels, water quality, water turbidity, pollutant transports, and biological ecosystem responses. Our current understanding, however, is insufficient to conduct accurate quantitative predictions of these processes. This is because the cohesive particles in natural waters will flocculate, which determines the settling, and thus the deposition behaviors. The simulation of flocculation processes is a primary challenge since the time variation of Floc Size Distribution (FSD) is controlled by a partial differential equation that also contains the integration of FSD itself. Previous models either address less characteristic sizes, which produce biased FSDs, or are incapable of modeling a relative large study domain in order to better express the FSDs with more size groups. In this study, a cohesive sediment flocculation model developed based on the framework of Population Balance Model (PBM) is solved by the Quadrature Method Of Moments (QMOM). This PBM–QMOM flocculation model has reasonably compromised by both the model robustness and model efficiency. The former lies in the capability of describing the time evolution of the FSDs with a maximum of eight size classes, and the latter is reflected in its efficiency to solve PBM with transport terms and the potential to be coupled in a flow-mud estuary model. The model predictions are compared to both the analytical (or trusted class method) results for general PBMs (i.e., beyond the scope of specific research field), and the published experimental results of kaolinite suspension and colloidal montmorillonite. After that, an experimental activity has been carried out to develop a Sony NEX-5R camera system (with extension tubes and close-up) to automatically acquire floc images under various controlled environments, and to use MATLAB software to process the FSDs. This process is validated by the results of two set of sample particles. The validated camera system is first applied in a five liter mixing chamber to investigate the effects of salinity and selected organic matters on kaolinite flocculation. Then, the camera system is improved and assembled in a waterproof house for underwater use to provide data for a conceptual one-dimensional application in a relatively large turbulence tank. The flow field of the tank is measured by an acoustic Doppler velocimetry. The flocculation processes in the mixing chamber or cylindrical tank are modeled by PBM–QMOM and validated by camera statistical FSDs. While chemical and biological effects are not explicitly included in PBM–QMOM (implicitly included in fitting parameters) at this time to address the basic mechanisms of flocculation, these effects can be further extended when the process itself is better understood through other laboratory experiments or field measurements.

Key Words: cohesive sediments; floc size distribution; population balance; quadrature method of moments; image acquisition and processing system.

**MODELING FLOCCULATION AND DEFLOCCULATION
PROCESSES OF COHESIVE SEDIMENTS**

CHAPTER I
GENERAL INTRODUCTION

1. Problem statement

Natural open water systems (oceans, estuaries, lagoons, rivers, lakes, reservoirs, etc.) are inseparable from the sediments suspended in the water column or deposited in the water bed. Although people since ancient times have known that flows transport sediment influencing river diversion, food production, and channel navigation, the scientific treatment of cohesive sediment transport is only of recent origin. In the United States, much of the early work of cohesive sediments was based on studies of Ray Krone (1922 – 2000) and Emmanuel Partheniades (1926 –) at University of California, Berkeley in 1960s, working with sediment pioneer Hans Albert Einstein (1904 – 1973), the son of Albert Einstein. Later, Ashish J. Mehta, himself a student of Emmanuel Partheniades, “has given the necessary boost to this complex research area to make the science mature and independent” (Toorman, 2013). They are the founders of cohesive sediment science.

Only recently, the fragmentation of findings of cohesive sediments across many different journals and proceeding volumes were summarized systematically in the following books:

- *Introduction to the Physics of Cohesive Sediment Dynamics in the Marine Environment* by J. C. Winterwerp and W. G. M. van Kesteren in 2004 (Book review see North et al., 2005);
- *Cohesive Sediments in Open Channels: Properties, Transport, and Applications* by Emmanuel Partheniades in 2009 (Book review see Shi, 2010);
- *An Introduction to Hydraulics of Fine Sediment Transport* by Ashish J. Mehta in 2013 (Book review see Toorman, 2013 and Friedrichs, 2014).

Although one might not expect to find everything related to cohesive sediments in the above

three books (such as structural kinetics models for thixotropy and population balance models for flocculation), they provide a comprehensive introduction on latest hot topics of cohesive sediments from theoretical fundamentals to field and laboratory experiments. The bi- or triennial conference series INTERCOH (International Conference on Cohesive Sediment Transport Processes, <http://www.intercoh.org/>) initiated by Reg Parker and Ashish J. Mehta in 1981, is an international platform for scientists and engineers all around the world to meet and discuss the latest progress on cohesive sediments in natural environments, with the most recent 13th INTERCOH held in September 2015, in Katholieke Universiteit Leuven, Belgium. The active universities and institutes working on cohesive sediment properties include, but are not limited to the affiliations such as Massachusetts Institute of Technology, United States Army Corps of Engineers, Woods Hole Oceanographic Institution, Virginia Institute of Marine Science, University of California - Berkeley, Stanford University, University of Florida, University of Maryland, Texas A&M University, University of Delaware, Delft University of Technology (Netherlands), Katholieke Universiteit Leuven (Belgium), Institut français de recherche pour l'exploitation de la mer (IFREMER, France, English: French Research Institute for Exploitation of the Sea), Hydraulics Research Wallingford (UK), and East China Normal University (China).

Cohesive sediments, generally referred to as mud (Winterwerp and van Kesteren, 2004), are discrete particles which consist mostly of clay ($\leq 4 \mu\text{m}$) and silt ($\leq 62.5 \mu\text{m}$) particles with water, but often contain varying amounts of sand and/or organic materials (Tver, 1979). Particles smaller than $0.1 \mu\text{m}$ do not settle and are considered to be “dissolved”, while larger particles ($> 62.5 \mu\text{m}$) are considered “coarse”. Thus, mud defined as discrete particles

predominately in the 0.1 – 62.5 μm size range is, to a fair degree, a convenient definition unrelated to particle dynamics in water (Mehta, 2013), although the coarse/fine and particulate/dissolved boundaries are also impacted by types of particle minerals and organic matter. Cohesive sediments are a valuable resource in building materials (e.g., Winterwerp and van Kesteren, 2004) and can offset marsh and wetland losses (e.g., McAnally, 2000). Nevertheless, contaminated and/or excess fine sediments may cause various environmental and engineering, and thus, economical and policy issues. For example, organic (such as PolyChlorinated Biphenyl, or PCBs) and inorganic (such as heavy metals) pollutants attached to fine cohesive sediment particles might move into the food chain and threaten the entire eco-system. Besides, fine sediments hinder navigation facilities. In reality, the cost of maintaining these fairways and harbor basins through dredging can be very high, particularly when the sediments to be removed are contaminated. Such dredging operations have various ecological impacts such as light attenuation, nutrient loading, physiological impairment, and changes of habitat quality (Smith, 2010).

To study sediment transport, it is important to understand the relationship between two representative characteristics, the hydrodynamics of the carrier flow and the dynamics of sediments (Son, 2009). Sediment particles, either individual grain or aggregates, may originate from the water column or in the bed. As shown in Fig. 1.1, once in suspension, turbulent mixing may lead the suspended aggregates to collide, attach, and further aggregate to form large flocs. Meanwhile, when the large flocs cannot withstand the shear stress, they may break up into small particles. This process of simultaneous aggregation and breakage is called flocculation. Currents and waves cause shear and normal stresses on the bed. If the

shear stress is strong enough, light flocs might erode and re-suspend from the water/bed interface, and may take part in the flocculation processes again. Biology plays an important role in cohesive sediment behavior. For example, bioturbation (such as burrowing) of benthic organisms causes the sediment to be mixed. Also, flocculation can be modified by the presence of sticky organic matter (e.g., extracellular polymeric substances, or EPS, excreted by bacterial or algae). Particles provide a food source for marine species. These species may excrete fecal pellets, which are referred to as “bio-aggregates”.

Among various processes of cohesive sediments, flocculation is the most important feature that distinguishes cohesive sediments from non-cohesive sediments. The flocculation alters the pattern of sediment settling and transport, and subsequently complicates the dispersal of the suspended sediments. Therefore, the inclusion of flocculation in sediment transport models is a primary requirement to quantitatively predict the behaviors of cohesive sediments (Xu, 2009). However, our current understanding of sediment transport is insufficient to conduct quantitative simulations of cohesive sediment behaviors. The research carried out in this dissertation investigates the flocculation and deflocculation processes of cohesive sediments through numerical simulations and laboratory experiments. While this study is motivated to better understand the flow-mud systems in natural waters, it also serves as relevant research for general flocculation processes in the water treatment industry (Ducoste, 2002) and bioreactor industry (Han et al., 2003), as well as relevant research for general quadrature method of moments (McGraw, 1997) which is modified as the solution method of the flocculation model in this study.

2. Scope and objectives

The work in this study mainly focuses on solving the governing equations that describe the flocculation and deflocculation processes of cohesive sediments in typical estuaries. Biological flocculation of cohesive sediments is acknowledged, but is only considered in the fitting parameters of the model at this time. Short period wind waves are neglected in this study to simplify the basic mechanisms of aggregation and breakup processes, although these effects usually play an essential role on sediment transport in natural estuaries, lagoons, rivers, and lakes.

The ultimate objective of this work is to develop a reliable population balance based cohesive sediment flocculation model to simulate the evolution of FSDs. To accomplish this, specific objectives are to:

- (1) Enhance previous numerical methods to efficiently extract the FSDs during the process of solving the population balance model;
- (2) Select appropriate floc aggregation and breakage structures to represent the kinetics of cohesive sediment flocculation;
- (3) Validate the simplified cohesive sediment flocculation box model using analytical or published experimental data, by neglecting the advection, diffusion, and settling terms at first;
- (4) Make the model practical for one-dimensional (1-D) applications by designing a laboratory experiment to validate it;
- (5) Create a non-intrusive camera system, providing automatic camera and light source triggering, to acquire floc images;

(6) Develop an image processing software to find the FSDs from particle images;

(7) Assess future research needs in studying flocculation processes of cohesive sediments.

3. Outline

This dissertation is organized with six chapters and several appendices.

CHAPTER I: Introduction. This chapter describes the general background, significance, scope, objectives, and the outline of this dissertation.

CHAPTER II: Population balance box model for FSDs of kaolinite suspension and colloidal montmorillonite. Kernel structures (i.e., collision frequency, collision efficiency, breakup frequency, and fragmentation distribution function) specifically for flocculation kinetics of cohesive sediment are discussed. The model is solved using the Quadrature Method Of Moments (QMOM), based on the compromise between code robustness and efficiency. Model results are validated by using available published data.

CHAPTER III: Population balance box model for FSDs in well-studied systems for general particles and in a mixing chamber experiment for kaolinite suspensions. In this chapter the effectiveness of the QMOM approach (CHAPTER II) is further validated to demonstrate the broader applicability of this approach with a wider variety of coagulation and breakup processes. In the first part model results are compared with analytical solutions or trusted class method results for typical flocculation events, beyond the scope of specific research area. In the second part, model predictions are validated with measured FSDs of kaolinite suspension in a mixing chamber system, with sensitivity tests of model parameter selections.

CHAPTER IV: Development of the camera system and the image processing software.

The reliability of this floc image acquiring and processing system is validated by using two available sample seeding particles in a mixing chamber experiment. Thus, the effects of salinity and selected organic matter (guar gum) on flocculation of kaolinite are explored, combined with the simulation using the flocculation model described in CHAPTER I and CHAPTER II.

CHAPTER V: Extensions of the flocculation box model for 1-D application. Another laboratory experiment in an advection-dominated cylindrical tank is designed to validate the flocculation model with advection and diffusion terms. The camera system developed in CHAPTER IV is assembled in a waterproof house for underwater use to acquire images and process the FSDs to compare with model results. The flow condition in the tank is measured by a 5MHz ADV (Acoustic Doppler Velocimetry) as model input.

CHAPTER VI: Conclusion. General conclusions are addressed and future research demands are exhibited.

APPENDICES: Examples of the FORTRAN code and the input file of the flocculation model, the assembler code in the micro-controller Teensy 2.0, and the MATLAB code for image processing and turbulence properties calculating, are represented.

References

- Ducoste, J., 2002. A two-scale PBM for modeling turbulent flocculation in water treatment processes. *Chemical Engineering Science* 57, 2157–2168.
- Friedrichs, C. T., 2014. Review of *An Introduction to Hydraulics of Fine Sediment Transport* by Ashish J. Mehta. *Journal of Waterway, Port, Coastal, and Ocean Engineering* 140, 07514002.
- Han, B., Akeprathumchai, S., Wickramasinghe, S.R., Qian, X., 2003. Flocculation of biological cells: Experiment vs. theory. *AIChE Journal* 49, 1687–1701.
- Maggi, F., 2005. Flocculation dynamics of cohesive sediment. (Ph.D. Dissertation) Delft University of Technology, Netherlands.
- McAnally, W.H., 2000. Aggregation and deposition of estuarial fine sediment. (Ph.D. Dissertation) University of Florida, Gainesville.
- McGraw, R., 1997. Description of aerosol dynamics by the quadrature method of moments. *Aerosol Science and Technology* 27, 255–265.
- Mehta, A.J., 2013. An introduction to hydraulics of fine sediment transport. World Scientific Publishing Company, pp.1060.
- Partheniades, E., 2009. Cohesive sediments in open channels: Properties, transport, and applications. Butterworth-Heinemann, Elsevier, pp.358.
- Shi, J., 2010. Review of *Cohesive Sediments in Open Channels: Erosion, Transport, and Applications* by Emmanuel Partheniades. *Journal of Hydraulic Engineering* 136, 272–273.

- Smith, S.J., 2010. Fine sediment dynamics in dredge plumes. (Ph.D. Dissertation) Virginia Institute of Marine Science, College of William and Mary, Gloucester Point.
- Son, M., 2009. Flocculation and transport of cohesive sediment. (Ph.D. Dissertation) University of Florida, Gainesville.
- Toorman, E.A., 2013. Review of *An Introduction to Hydraulics of Fine Sediment Transport* by Ashish J. Mehta. Journal of Waterway, Port, Coastal, and Ocean Engineering 140, 07514001.
- Tver, D.F., 1979. Ocean and Marine Dictionary. Cornell Maritime Press, pp. 358.
- North, C.P., Milliken, K.L., van Loon, A.J., 2005.
https://www.sepm.org/jsr/book_revs/2005_revs/br_winterwerp.pdf.
- Winterwerp, J.C., van Kesteren, W.G.M., 2004. Introduction to the physics of cohesive sediment in the marine environment. Developments in Sedimentology 56, Elsevier, pp. 466.
- Xu, F., 2009. Modeling study of flocculation effects on sediment transport in estuaries. (Ph.D. Dissertation) Stony Brook University, New York.

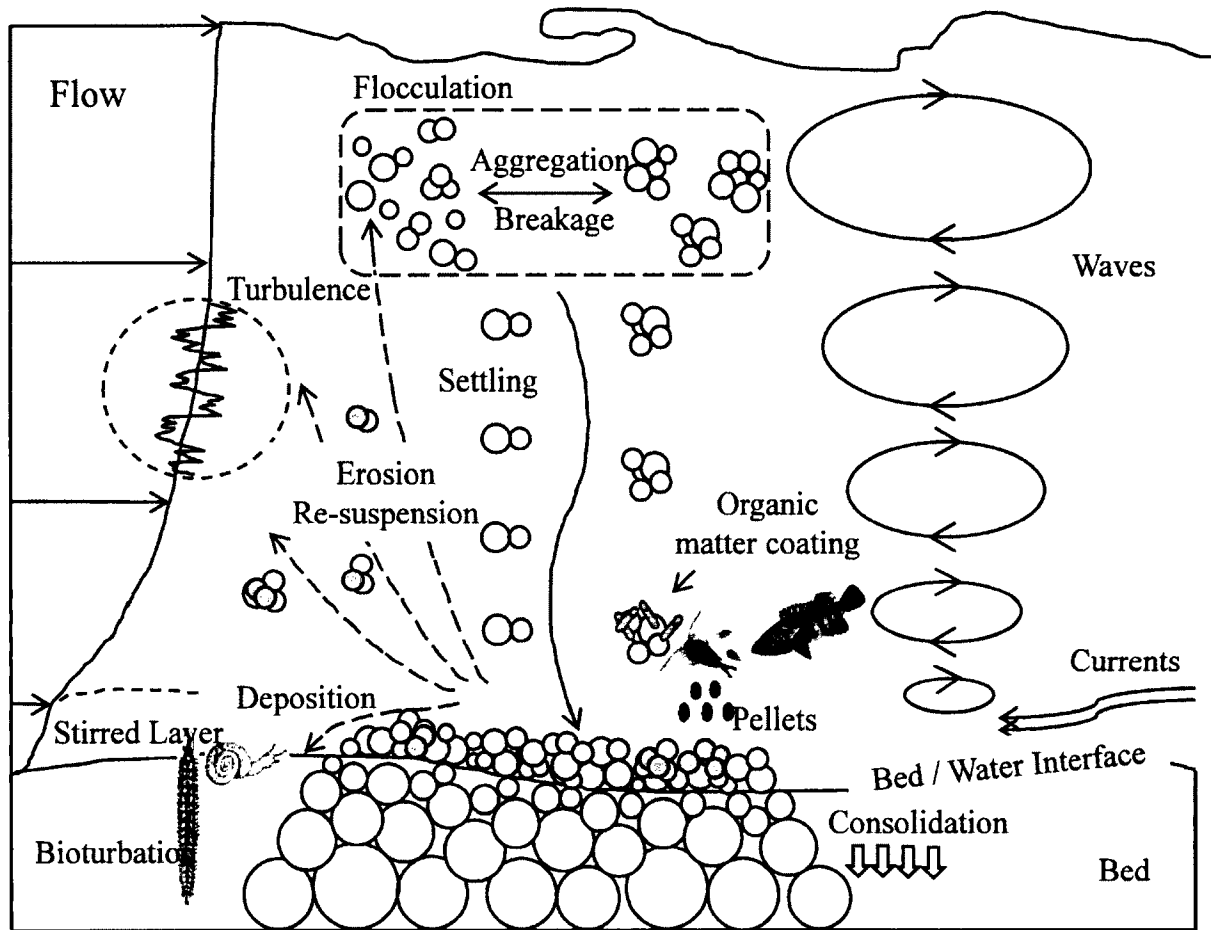


Fig. 1.1 Sediment dynamics in natural environments (Modified from Maggi, 2005).

CHAPTER II

MODELING FLOC SIZE DISTRIBUTION OF SUSPENDED COHESIVE SEDIMENTS USING QUADRATURE METHOD OF MOMENTS*

* Published as:

Shen, X., Maa, J.P.Y., 2015. Modeling floc size distribution of suspended cohesive sediments using quadrature method of moments. *Marine Geology* 359, 106–119.

Abstract

An enhanced Quadrature Method Of Moments (QMOM) is employed to solve the Population Balance Model (PBM) with a maximum of eight size classes for the purpose of describing the evolution of Floc Size Distribution (FSD) of kaolinite suspension and colloidal montmorillonite. This approach can be used to estimate many representative sizes, e.g., d_{32} (Sauter mean size), d_{43} (De Broukere mean size), d_{60} (hydrodynamic mean size), and D_{50} (median size). The following three considerations are adopted to enhance the QMOM approach: (1) An adjustable factor, which is selected based on its ability to track up to eight size classes, is implemented; (2) Moments higher than the third order are not necessarily simulated directly; (3) A restriction on the ratio between the minimum and maximum weights is used to exclude unreliable nodes. The above enhancements have been proposed by others, but are integrated for the first time in this study. Model results are verified by comparison with available experimental data. The results of this study suggest that the quadrature nodes and weights in the QMOM are the characteristic sizes and corresponding characteristic number densities to effectively predict the FSD of cohesive sediments. This study also demonstrates that the possible range of the correction factor (also sometimes referred to as “collision efficiency”) for the Euclidean collision frequency could be larger than one because of both the difference in floc structure represented by fractal dimension as well as the impacts of organic matter.

Keywords: flocculation; cohesive sediments; population balance model; quadrature method of moments; floc size distribution.

1. Introduction

The prediction of transport and fate of fine-grained suspended cohesive sediments in estuaries and adjacent coastal waters is important for many scientific and engineering applications, e.g., siltation in navigation channels and harbors, water quality, and pollutant transport. An essential process of cohesive sediment dynamics is the flocculation that determines floc size, and thus, settling velocity. Flocculation is the result of simultaneous processes of aggregation and breakage. The challenge in modeling flocculation is that many factors can influence this process, e.g., the ambient turbulence intensity, local suspended sediment concentration, static electrical forces (i.e., due to salinity and other ions), and bio-activities such as the production of Extracellular Polymeric Substance (EPS), and thus, no accurate modeling experiment has been conducted yet.

Besides the chemical and biological factors, the most relevant mechanisms responsible for flocculation are Brownian motion (e.g., Eisma, 1986), differential settling (e.g., Lick et al., 1993; Zhang and Zhang, 2011), and fluid shear (e.g., Winterwerp, 1998; Mietta et al., 2008). It is well accepted that Brownian motion (also known as “perikinetic flocculation”), the random thermal moving of particles suspended in a fluid, only affects suspended particles less than 1–2 μm , so that it is negligible in natural estuarial waters where suspended sediment size is large and ambient turbulence is strong (Van Leussen, 1994; Thomas et al., 1999; Winterwerp, 1998; McAnally, 2000). Differential settling is a process that describes faster-falling particles overtaking slower ones. Fluid shear allows one particle to capture others more efficiently because of strong, random motions among particles. The relative importance of differential settling and fluid shear, however, depends on the applications. For

example, Winterwerp (1998) and Maggi et al. (2007) showed fluid shear to be the dominant effect as the likelihood of a large (i.e., rapidly settling) particle colliding with a small (i.e., slowly falling) particle is small. This is because the trajectory of the small particle is deflected by strong hydrodynamic interactions with the larger particle. Here the hydrodynamic interaction describes the momentum transfer from a suspended particle to fluid molecules, and then from the fluid molecules to another particle (Ladd and Verberg, 2001). On the other hand, Lick et al. (1993) stated that differential settling may become the primary factor in open waters away from shore where turbulence is low. Zhang and Zhang (2011) also emphasized the effect of differential settling in their work.

In general, there are three kinds of flocculation models. The first kind of model is the simplified Lagrangian flocculation model (e.g., Winterwerp, 1998, 1999, 2002; Winterwerp and van Kesteren, 2004; Maggi, 2008, 2009; Son, 2009; Son and Hsu, 2008; 2011a; 2011b). Winterwerp (1998) first developed this kind of model for a constant fractal dimension to describe the floc shape. Later, Son and Hsu (2008) extended this model for a variable fractal dimension. An advantage of this kind of model is that it can track the evolution of a characteristic size (usually the median size) with reasonable computing efficiency, and it is easy to couple with hydrodynamic models, turbulence models, and sediment transport models (Winterwerp, 2002). A weakness is that only one characteristic size (i.e., the median floc size) is addressed. Other properties, notably the floc size distribution (FSD) and detailed evolution processes of particle number and volume, cannot be resolved by this kind of model.

The second kind of model is the extended Lattice Boltzmann Model (LBM) (e.g., Zhang and Zhang, 2011; Zhang et al., 2013). The traditional LBM is a mesoscopic hydrodynamic

model (not a flocculation model) that is mapped onto the incompressible Navier-Stokes equations (Ladd and Verberg, 2001). Ladd (1994a, 1994b) extended the LBM by adding the motion of solid particles in suspension. They treated the solid particles as imposing moving boundary conditions on the fluid. This method was further extended to explore the flocculation of cohesive sediments due to differential settling (Zhang and Zhang, 2011) and turbulent shear (Zhang et al., 2013). This latest approach provides more information, including FSD and floc settling velocities, than the first kind of model, and allows collision behaviors to be studied directly through statistical analyses of model results. However, prohibitive computational costs and memory requirements for simulating a larger study domain limit the use of this approach to only studying the process itself, e.g., determining the collision efficiency (also called correction factor in this study).

The third kind of model is the Population Balance Model (PBM) (e.g., Maggi, 2005; Prat and Docuste 2006, 2007; Maggi et al., 2007; Xu et al., 2008; Mietta et al., 2008, 2011; Lee et al., 2011; Verney et al., 2011; Furukawa and Watkins, 2012), which is the model type used in this study. PBM is essentially a transport equation that tracks number density of flocs of certain size at any location and at any time in a system. A thorough review of the origins and derivation of PBM can be found in Sporleder et al. (2012), and a summary of various methods for solving a PBM is presented in Su et al. (2009).

Among all the available methods for solving PBM, the Quadrature Method Of Moments (QMOM) is the most efficient one (Marchisio et al., 2003c; Prat and Duscoste, 2006; 2007). QMOM transfers PBM to a set of moment transport equations (McGraw, 1997), so that the lower-order moments of FSD are tracked with high accuracy with a low computational cost

(see “Section 4” for more details). In addition, their mean sizes (e.g., arithmetic mean size, Sauter mean diameter, and De Broukere mean diameter) are recorded with high accuracy. However, conventional QMOM usually fails when tracking more than four size classes, and thus, it is difficult to construct the FSD from the conventional QMOM. Su et al. (2007) employed adjustable factors assigned to different processes to track the moments of FSD with lower computational demands than that from the standard QMOM. Since the purpose of their work did not entail tracking additional size classes to find the FSD, they only used three size classes and did not report any FSD in their results.

The objective of this study is to investigate the temporal evolution of FSD, including the aggregation and breakage behaviors of cohesive sediments. To achieve this goal, the adjustable QMOM approach that solves the PBM is modified to track changes of particle density for a maximum of eight size classes. Data from two available laboratory experiments (one with suspended kaolinite and the other with colloidal montmorillonite) are simulated. Detailed information, such as the FSD itself, its mode, mean, and median size, and the processes of birth and death of floc number and floc volume are monitored.

This paper is organized as follows. Methods are described in Section 2. Section 2.1 reviews the PBM model and standard QMOM approach. Section 2.2 presents QMOM with an adjustable factor and illustrates how to apply this approach. Section 2.3 explains the selection of appropriate aggregation and breakage functions, i.e., the collision frequency, the correction factor, the breakup frequency, and the fragmentation distribution function. Section 3 describes the setup of this flocculation model. The model is calibrated and verified by comparison with available data reported by Mietta et al. (2008) and Furukawa and Watkins

(2012) for kaolinite suspension and colloidal montmorillonite, respectively. Results and discussions are included in Section 4, and concluding remarks are delivered in Section 5.

2. Model description and numerical methods

2.1 Population balance modeling and quadrature method of moments

The length-based PBM describes the change of number density for flocs with size L . A PBM box model, which is simplified by eliminating the advection, diffusion, and settling terms (see Eq. 2.1 in Marchisio et al., 2003b), is selected as the first effort in this study. This simplification is also convenient for calibration and verification using published data from Mietta et al. (2008) and Furukawa and Watkins (2012). Inclusion of these omitted terms will be restored in a future study. The simplified PBM model can be represented as

$$\begin{aligned} \frac{\partial n(L;t)}{\partial t} = & \frac{L^2}{2} \int_0^L \left[\frac{\beta((L^3 - \lambda^3)^{1/3}, \lambda) \cdot \alpha((L^3 - \lambda^3)^{1/3}, \lambda)}{(L^3 - \lambda^3)^{2/3}} \cdot n((L^3 - \lambda^3)^{1/3}; t) \cdot n(\lambda; t) \right] d\lambda \\ & - n(L;t) \int_0^\infty \beta(L, \lambda) \alpha(L, \lambda) n(\lambda; t) d\lambda + \int_L^\infty a(\lambda) \cdot b(L|\lambda) \cdot n(\lambda; t) d\lambda - a(L) \cdot n(L; t) \quad (2.1) \end{aligned}$$

where λ is the integral variable with the same dimension of floc size L , $n(L; t)$ is the number density function defined by floc size L at time t , $\beta(L, \lambda)$ is the Euclidean collision frequency function that describes the frequency of two spheres with size L and λ colliding to form a particle with size $(L^3 + \lambda^3)^{1/3}$, $\alpha(L, \lambda)$ is the correction factor (also called collision efficiency) that includes effects of particle geometry, contact efficiency, and sticking probability, $a(L)$ is a breakup frequency function that denotes the frequency of disruption for particles with size L , and $b(L|\lambda)$ is a fragmentation distribution function that represents particles with size L produced by the breakup of a particle with size λ . The first term on the right hand side of Eq.

2.1 is the birth of flocs with size L due to aggregation of smaller particles with size $(L^3 - \lambda^3)^{1/3}$ and λ . The second term on the right hand side is the death of flocs with size L due to aggregation with other particles. The third term is the birth of flocs with size L due to fragmentation of bigger particles λ , and the last term is the death of flocs with size L due to breakup into smaller particles.

The moment transfer (Hulburt and Katz, 1964; McGraw and Saunders, 1984) is applied to Eq. 2.1 using the following definition:

$$m_k = \int_0^\infty L^k n(L; t) dL \quad (2.2)$$

in which m_k is the k th order moment. Notice that the size class L varies from zero to infinity in the transformation.

After applying the transformation to Eq.1 with $k = 0, 1, \dots, K$, the PBM becomes a set of moment equations (Eq. 2.3) that are essentially a system of nonlinear integro-differential equations (Kariwala et al., 2012)

$$\begin{aligned} \frac{\partial m_k}{\partial t} = & \frac{1}{2} \int_0^\infty n(\lambda; t) \int_0^\infty \beta(L, \lambda) \cdot \alpha(L, \lambda) \cdot (L^3 + \lambda^3)^{k/3} \cdot n(L; t) dL d\lambda \\ & - \int_0^\infty L^k n(L; t) \int_0^\infty \beta(L, \lambda) \alpha(L, \lambda) n(\lambda; t) d\lambda dL \\ & + \int_0^\infty L^k \int_0^\infty a(\lambda) \cdot b(L | \lambda) \cdot n(\lambda; t) d\lambda dL - \int_0^\infty L^k a(L) \cdot n(L; t) dL \end{aligned} \quad (2.3)$$

Eq. 2.3, however, cannot be solved, either numerically or analytically, because the integrations terms have not been expressed in term of the moments yet. Fan et al. (2004) described this as the typical ‘‘closure problem’’ first identified by Hulburt and Katz (1964). To address this issue, McGraw (1997) proposed using Gaussian quadrature approximation to replace the integration terms

$$m_k = \int_0^\infty L^k n(L; t) dL \approx \sum_{i=1}^N \omega_i L_i^k = \Omega \times (\Gamma^k)^T \quad (2.4)$$

where $\Gamma = [L_1, L_2, \dots, L_N]$ is a vector with each component representing a node in the Gaussian quadrature approximation (Press et al., 1992), $\Omega = [\omega_1, \omega_2, \dots, \omega_N]$ is also a vector in which each component is the weight (also the characteristic number density) corresponding to L_i , the superscript T stands for the transpose of a vector, N is the number of size classes, and $k = 0, 1, 2, \dots, K$ is the order of moment selected. The physical meanings of the few low order moments are as follows: m_0 is the total number of flocs, and m_1 , m_2 , and m_3 are proportional to the total length, total area, and total volume of flocs, respectively. Although Eq. 2.4 is a definition equation to estimate initial m_k , it also serves as an Eigen-equation to find the Gaussian quadrature nodes Γ and the corresponding Ω , after the update of m_k .

Note that mathematically, if $K \leq 2N-1$, the ‘‘approximately equal’’ sign in Eq. 2.4 becomes exactly equal when L_i are selected as the Gaussian quadrature points (John and Thein, 2012). This makes it possible to use the QMOM approach to track evolution of moments with high accuracy. Using Eq. 2.4 to replace the integral by summation and choosing the nodes as Gaussian points, Marchisio et al. (2003a, 2003b, and 2003c) showed that Eq. 2.3 can be rewritten as

$$\begin{aligned} \frac{\partial m_k}{\partial t} = & \frac{1}{2} \sum_{i=1}^N \omega_i \sum_{j=1}^N \alpha(L_i, L_j) \cdot \beta(L_i, L_j) \cdot \omega_j \cdot (L_i^3 + L_j^3)^{\frac{k}{3}} \\ & - \sum_{i=1}^N L_i^k \omega_i \sum_{j=1}^N \alpha(L_i, L_j) \cdot \beta(L_i, L_j) \cdot \omega_j + \sum_{i=1}^N a_i \bar{b}_i^{(k)} \omega_i - \sum_{i=1}^N L_i^k a_i \omega_i \end{aligned} \quad (2.5)$$

$$\text{where } \bar{b}_i^{(k)} = \int_0^\infty L^k b(L | \lambda) dL \quad (2.6)$$

is the integral of the fragmentation distribution function $b(L|\lambda)$. In addition, the number

density function, which is actually the number-based FSD, can be estimated by using the following relationship (McGraw, 1997)

$$n(L;t) \approx \sum_{i=1}^N \omega_i(t) \delta[L - L_i(t)] \quad (2.7)$$

where δ is the Dirac delta function which means at any time t , δ is zero except at $L = L_i(t)$.

With this approximation, all the right hand terms in Eq. 2.5 can be calculated if $\alpha(L_i, L_j)$, $\beta(L_i, L_j)$, a_i , b_i , L_i , and ω_i are specified. Thus, the new moments after each time step can be estimated from Eq. 2.5.

With the new moments found after each time step, it is time to update L_i and ω_i according to Eq. 2.4 using Wheeler's algorithm (Wheeler, 1974). Some variants of this algorithm are also called "long quotient-modified difference algorithm" (Sack and Donovan, 1972) or "Chebyshev algorithm" (Upadhyay, 2012). These variants introduced different intermediate quantities to slightly modify the original algorithm (John and Thein, 2012). Eq. 2.4 mathematically illustrates the problem of finding the Gaussian quadrature points (i.e., Γ) when the moments of the unknown FSD function are known. This problem can be transferred to finding the roots of an orthogonal polynomial given by "three recurrence relation", and further transferred to finding the eigenvalues of the Jacobi matrix (Press et al., 1992). Notice that the components in the Jacobi matrix are only related to the given moments. After Γ is solved, Eq. 2.4 becomes a linear system that can be solved for Ω . This solution method is also suggested by Prat and Ducoste (2006, 2007). More details of Wheeler's algorithm are given in Appendix 2-A. After Γ and Ω are updated, Eq. 2.5 will be used to find moments for the next time step. This process will then be repeated to proceed forward in time.

For an N -node (i.e., N class sizes) QMOM approach, there are $2N$ unknowns (N nodes

and N weights) and thus, Eq. 2.5 is a set of $2N$ equations. In the Gaussian quadrature method, only a selected set of nodes and weights are needed to find the integration, and the locations of the nodes at which the FSD curve is to be evaluated are not equally spaced, i.e., the distance between any two consecutive nodes are not fixed. This implies that the weight, Ω , actually includes bin size information.

2.2 Improved adjustable QMOM

Although three or four size classes in the QMOM approach have been shown sufficient to track the lower order moments of FSD (Marchisio et al., 2003c; Prat and Ducoste, 2006), the FSD curve cannot be reasonably presented using only three or four size classes. Limitations of previous studies resulted from numerical problems associated with tracking a larger number of size groups (Upadhyay, 2012) due to the ill-condition of Eq. 2.4. This ill-conditioned behavior was inherited as a consequence of using moments with large K and a large difference between L_1 and L_N , i.e., $(L_1)^1 \ll (L_N)^K$ (Gautshi, 1968), and it may lead to negative weights and/or size that do not have physical meaning. Before this study the maximum number of size classes was limited to four, which made it difficult to reconstruct the FSD accurately using conventional QMOM.

Reducing the difference between $(L_1)^1$ and $(L_N)^K$ is the key to relaxing the severity of the ill-condition. With this understanding, Su et al. (2007) added an adjustable factor, p , in QMOM and re-defined the adjustable moments as

$$m_{k/p} = \int_0^{\infty} L^{k/p} n(L;t) dL \quad (2.8)$$

in which p is the adjustable factor, and $p = 1$ denotes the standard QMOM. With floc size in

units of μm , $k/p = 3$ (for monitoring volume conservation directly) and $p \geq 1$ (to reduce the magnitude of moments) are required to model flocculation processes of cohesive sediments.

Applying Gaussian quadrature approximation,

$$m_{k/p} = \int_0^\infty L^{k/p} n(L;t) dL = \sum_{i=1}^N \omega_i L_i^{k/p} \quad (k = 0, 1, \dots, 2N - 1) \quad (2.9)$$

Eq. 2.5 can be modified as

$$\begin{aligned} \frac{\partial m_{k/p}}{\partial t} = & \frac{1}{2} \sum_{i=1}^N \omega_i \sum_{j=1}^N \alpha(L_i, L_j) \cdot \beta(L_i, L_j) \cdot \omega_j \cdot (L_i^3 + L_j^3)^{\frac{k}{p}} \\ & - \sum_{i=1}^N L_i^{k/p} \omega_i \sum_{j=1}^N \alpha(L_i, L_j) \cdot \beta(L_i, L_j) \cdot \omega_j + \sum_{i=1}^N a_i \bar{b}_i^{(k/p)} \omega_i - \sum_{i=1}^N L_i^{k/p} a_i \omega_i \end{aligned} \quad (2.10)$$

in which the integrated fragmentation distribution function should be rewritten as

$$\bar{b}_i^{(k/p)} = \int_0^\infty L^{k/p} b(L | \lambda) dL \quad (2.11)$$

By defining $l_i = L_i^{1/p}$ (Su et al., 2007) as the “virtual size” in Eqs. 2.9–2.11, this adjustable QMOM governing equation is transferred back to the standard QMOM governing equation (Eq. 2.5) but with a less ill-conditioned Eq. 2.4 when compared with the original QMOM. This makes the numerical algorithm more stable when solving for Γ and Ω .

The essence of this improvement is to track fraction moments instead of integer moments. The advantage of this approach is that it lowers the order of moments while solving the same number of equations. Using a three-node QMOM as an example, the standard QMOM approach tracks $m_0, m_1, m_2, m_3, m_4,$ and m_5 ; with $p = 4/3$, for instance, the adjusted QMOM approach tracks $m_0, m_{3/4}, m_{3/2}, m_{9/4}, m_3,$ and $m_{15/4}$. For an eight-node QMOM with adjustable factor $p = 5$, the moments $m_0, m_{1/5}, m_{2/5}, \dots, m_3$ are tracked. The severity of the ill-condition is partially relaxed because $(L_N)^{k/p} < (L_N)^k$, and thus, the stability of solving Eq. 2.4 is improved.

To apply this method to finding FSD of cohesive sediments, the determination of the adjustable factor in Eqs. 2.9-2.11 is based on the ability to track seven or eight size classes. This is different from the method given by Su et al. (2007), which focuses on improving the accuracy and efficiency of the tracked moments. Other important issues are as follows:

(1) The third order moment is necessarily tracked directly to check volume conservation. For example, for $N = 8$, the maximum adjustable factor $p_{\max} = 5$ is suggested so that m_0 , m_1 , m_2 , and m_3 can be tracked and checked directly. Similarly, for $N = 7$, the suggested maximum adjustable factor p will be four so that m_0 , m_1 , m_2 and m_3 can still be tracked and checked directly.

(2) It is necessary to check the ratio between the minimum and maximum weights (Yuan and Fox, 2011). The selection of this ratio depends on specific applications. In this study, if $\min(\omega_i)/\max(\omega_i) < 10^{-16}$, the minimum of ω_i will be changed to zero and the corresponding node will be excluded from the model, i.e., the number of nodes will be decreased by one. The selection of this minimum ratio is based on the requirements of maximum number of nodes $N_{\max} = 7$ or 8, but maintains a reasonable stability.

The adjusted QMOM can be solved successfully by following the above-mentioned rules. The selection of initial number of nodes, however, depends only on the requirement to fit the initial FSD. Even if the initial number of nodes selected is less than N_{\max} , in the process of solving for Ω and Γ the computation will still always start with N_{\max} nodes. If the resulting ratio, i.e., $\min(\omega_i)/\max(\omega_i)$ for $i = 1$ to N_{\max} , is less than 10^{-16} , the corresponding node will be eliminated. But in the next time step, the computation again starts with N_{\max} nodes. With time, the number of nodes will increase and reach N_{\max} .

The main limitation for finding the solution is controlled by the precision of computation, rather than the computing power of CPUs. As such, at least double precision is needed, which is the level of precision supported by the PGI Fortran Compiler. With a quad-precision compiler, more nodes (i.e., size classes) would be possible. However, with the current code that supports double precision, eight nodes are possible.

2.3 Flocculation dynamics

Before a quantitative modeling of Eq. 2.10 is feasible, four parameters (i.e., Euclidean collision frequency function β , correction factor α , breakup frequency function a , and fragmentation distribution function b) should be determined. In order to provide a complete description, the following paragraphs present a summary of these parameters from previous studies.

Euclidean collision frequency β

The Euclidean formulation of collision frequency for Brownian motion, differential settling and fluid shear for two-body collision can be written as (Smoluchowski, 1917; Camp and Stein, 1943; Han and Lawler, 1992; Thomas et al., 1999; Winterwerp, 1998; Maggi, 2005; etc.):

$$\text{Brownian motion} \quad \beta^{BM}(L_i, L_j) = \frac{2 K_B T (L_i + L_j)^2}{3 \mu L_i L_j} \quad (2.12)$$

$$\text{Differential settling} \quad \beta^{DS}(L_i, L_j) = \frac{\pi}{4} (L_i + L_j)^2 |w_{s,i} - w_{s,j}| \quad (2.13)$$

Fluid shear
$$\beta^{FS}(L_i, L_j) = \frac{G}{6}(L_i + L_j)^3 \quad (2.14)$$

where K_B is the Boltzmann constant, T is the absolute temperature, μ is the dynamic viscosity of the fluid, w_s is the settling velocity, and G is the shear rate. Although Brownian motion is generally accepted as not important for simulating flocculation in estuarine flows, it is included because of the need to simulate a case study for model verification. Notice that the particle collision due to differential settling is sensitive to different formulations of settling velocity, up to two orders of magnitudes. Since differential settling is not dominant in either test case in this study, this effect is excluded in the model. The formulation of this effect can be further improved if better information regarding settling velocity becomes available.

Correction factor α for Euclidean collision frequency

Particle aggregation is a process involving approach, contact and sticking. Failure in any part of this process will lead to failure in aggregation. The Euclidean collision frequency, β , (i.e., Eqs. 2.12–2.14) only represents part of this process. For example, the shear-induced Euclidean collision frequency (Eq. 2.14) of two spherical particles L_i and L_j is defined as the possibility that the center of one particle (either L_i or L_j) will go through a control volume (with diameter $L_i + L_j$) due to the effect of ambient shear, when no other force is acting on these two particles to change their trajectory. The correction factor α specified in this study includes all of the remaining processes: geometry correction of collision frequency β_0 , contact efficiency E_0 and sticking probability α_0 , i.e.,

$$\alpha = \beta_0 \cdot E_0 \cdot \alpha_0 \quad (2.15)$$

In this study, β_0 accounts for geometry corrections for the spherical particle assumption

specified for Euclidean collision frequency function β (i.e., Eqs. 2.12–2.14). The term “geometry correction” refers here to shape or fractal corrections that account for the non-spherical aspect of natural flocs. Non-spherical properties such as surface asperities affect particle aggregation, as pointed out by Tang et al. (2014), who modeled particles as spheropolygons. From a pure geometric point of view, even particle trajectories that are predicted to cause collisions may be changed due to deviations from pure straight-line motion. Even for a perfect spherical particle, the Karman vortex in the wake is not symmetric, and this causes an oscillatory lift force that leads to oscillatory lateral motion of a falling particle, although this lateral motion is small and usually neglected for spherical particles. For irregular-shape flocs, however, this lateral motion can be severe and lead to trajectories that deviate much more from a straight line than the trajectories of a spherical particle. Since an originally thin trajectory will become a much thicker trajectory because of this oscillatory motion, the chance of collision might increase. This process should be included in the parameter β_0 that accounts for the change of trajectory of approaching particles and lead to the change of collision frequency. The parameter E_0 accounts for unsuccessful contact because of short-range forces (i.e., Van der Waals force and electrostatic repulsion force) and the lubrication force. Note that the “lubrication force”, which is a name given by Kim and Karrila (1991), is a drag force caused by the squeezing-out of fluid when two particles are close. This name, however, might be misleading because it is caused by the displacement of fluid from a fast approaching solid particle. For this reason, we would like to replace this name with “displacement force”. The parameter α_0 is a coefficient to account for the probability of successful sticking (after successful contact) including complex bio-adhesion such as caused by EPS.

Previous studies (e.g., Mietta et al., 2008, 2011; Verney et al., 2011) often referred to α as a “collision efficiency” that includes part of the effects of β_0 , E_0 , and/or α_0 , and claimed other effects in a constant. Due to a lack of consistency in the definition of this factor, biased results may occur when comparing different α values. To check this PBM model without scrutinizing the exact values of β_0 , E_0 , and α_0 at this time, $\alpha(L_i, L_j)$ is treated as a fitting constant, i.e., $\alpha(L_i, L_j) = C_1$.

Note that from their physical meaning, α should be a number limited to a maximum of one if the β_0 term is excluded (i.e., $\alpha_0 \leq 1$, $E_0 \leq 1$, and $\alpha_0 \cdot E_0 \leq 1$). β_0 could be larger than one because of different fractal properties of flocs (Lee et al., 2000), since collision frequency can be severely underestimated when using spheres to represent fractal flocs. Considering two pairs of floc with different fractal dimensions under the same fluid shear, β_0 in one pair could be much larger than that of the other pair. For example, the collision frequency for two flocs with fractal dimension 1.5 could be 774 times higher than that for two Euclidean flocs (with fractal dimension = 3.0) (Jiang and Logan, 1991). It is understood that α_0 and E_0 should also be influenced by the fractal structure of flocs. Nevertheless, the relationships between α_0 and E_0 and fractal dimension are not clear at this time. Thus, even assuming α_0 and E_0 are reduced because of the fractal structure of flocs, α might not be necessarily smaller than one because the term β_0 is included.

Breakup frequency

The breakup frequency (also known as “breakup/disaggregation kernel”) accounts for the effect of eddies present in the system with sufficient kinetic energy to break flocs (Marchisio

et al., 2003c). Fluid shear and collision between particles are the two primary reasons for floc breakage. The relative importance of these two causes is debatable. Since a floc is free to rotate according to surface forces, shear breakup has been suggested to be a minor process compared to inter-particle collision (Lick and Lick, 1988). Others (e.g., Winterwerp, 1998; Winterwerp and van Kesteren, 2004; Son, 2009), however, have argued that the effect of turbulent shear is more important for breaking flocs, since the effect of inter-particle collision would be small for flocs with a small excess density. McAnally (2000) pointed out that breakup due to flow shear may be small at a location far from the bottom boundary for open channel flows, while in the near-bed zone shear breaking may be the dominant process because of significantly greater velocity gradients.

Winterwerp's breakup frequency function (Eq. 2.16) is employed in this study (Winterwerp, 1998, 1999, 2002; Mietta et al., 2008, 2011; Maggi, 2007; Maggi et al., 2007; Xu et al., 2008; Son and Hsu, 2008, 2011a, 2011b; Son, 2009; Lee et al., 2011)

$$a(L_i) = C_2 \cdot \left(\frac{\mu}{F_y} \right)^{1/2} \cdot G^{3/2} \cdot L_i \cdot \left(\frac{L_i}{l_p} - 1 \right)^{3-\eta f} \quad (2.16)$$

Where C_2 is a breakup fitting parameter, l_p is the size of primary particle, ηf is the fractal dimension of the flocs, μ is the dynamic viscosity of fluid, and F_y is the yield strength of aggregates as determined empirically. A constant $F_y = 1.0 \times 10^{-10}$ N was used by Winterwerp (2002), Maggi et al. (2007), and Verney et al. (2011). Nevertheless, F_y may not be a constant, e.g., a range from 1.1×10^{-9} N to 4.4×10^{-8} N is possible (Kranenburg, 1999). Son (2009) derived a conceptual expression of variable floc yield strength that depends on floc size and fractal dimension. However, undetermined constants are still included in his formulation. In this study, $F_y = 1.0 \times 10^{-10}$ N is employed for simplification.

Fragmentation distribution function

The fragment distribution function (also known as “breakage/daughter distribution function”) describes the size distribution of daughter flocs after breakup. Knowledge of this function is incomplete and mainly based on conceptual assumptions (Maggi, 2005). The most commonly used functional forms are either discrete format (e.g., binary breakup with mass ratio 1:1 or 1:4, or ternary breakup with mass ratio 1:1:2) or continuous format (e.g., binomial distribution, Gaussian distribution, or log-normal distribution) (e.g., Marchisio et al., 2003b; Maggi, 2005; Prat and Ducoste, 2006; Mietta et al., 2008). In this study, the simplest assumption, i.e., binary breakup with mass ratio 1:1, is adopted.

$$b(L | \lambda) = \begin{cases} 2 & \text{if } L = \lambda/2^{1/3} \\ 0 & \text{otherwise} \end{cases} \quad (2.17)$$

and the integrated adjustable daughter distribution function can be written as (Su et al., 2007)

$$\bar{b}_i^{(k/p)} = 2^{(3-k/p)/3} L_i^{k/p} \quad (2.18)$$

3. Case studies

The FSD can be presented based on number, volume, or mass. The number-based FSD shows a high peak towards the smaller flocs while mass- and volume-based FSDs show peaks towards the larger flocs (Mietta, 2010). This is because many particles are needed to represent even a small mass for the small flocs, while a few large flocs may hold most of the mass. The accuracy of transferring a number-based FSD to a mass or volume-based FSD is based on the accuracy of floc density, which is a function of solid and fluid density, floc size, primary particle size, and fractal dimension. Although the fractal dimension can be treated

either as a constant using an average value (e.g., Winterwerp, 1998; Mietta et al., 2011) or estimated as a function of floc size (e.g., Khelifa and Hill, 2006; Maggi, 2005, 2007, 2008), it is sensitive to the transferring between number-based FSDs and volume-based FSDs.

In this study, the FSD mentioned is the number-based FSD, which is estimated from Γ and Ω . Since at least seven or eight size classes are tracked (i.e., $N_{\max} = 7$ or 8), their median size D_{50} (defined as the size where half of the population resides above this value) can be reasonably estimated, as well as many other representative sizes defined as follows:

$$d_{ij} = \left[\frac{\int_0^{\infty} L^i n(L;t) dL}{\int_0^{\infty} L^j n(L;t) dL} \right]^{1/(i-j)} \quad (2.19)$$

in which i and j are positive integers. Mugele and Evans (1951) and Sowa (1992) provided a thorough explanation of these mean diameters. Here, only a few commonly used sizes (i.e., diameters) are explained:

d_{10} : arithmetic or number mean diameter, which is most important where the number of particles is of interest, e.g., in particle counting applications.

d_{32} : Sauter mean diameter (i.e., area-weighted diameter), which is critical for applications that focus on surface area, e.g., pollutant transport and fuel combustion. The LISST-25 (Laser In-Situ Scattering and Transmissometry) instrument developed by Sequoia Scientific Inc., measures this diameter (Agrawal and Mikkelsen, 2009; Filippa et al., 2011, 2012).

d_{43} : De Broukere mean diameter (i.e., volume-weighted diameter), which is the primary value calculated by laser diffraction (Rawle, 2003). Another optical instrument from Sequoia Scientific Inc., LISST-100X, provides this diameter (Y.C. Agrawal, personal communication, May 23, 2014).

d_{60} : hydrodynamic mean diameter, defined as “the size of a hypothetical hard sphere that diffuses in the same fashion as that of the particle being measured.” This definition is given by the manufacturer of the “Dynamic Light Scattering Spectroscopy (DLS)” instrument used in the study reported by Furukawa and Watkins (2012). In short, it is the diameter of a sphere that has the same translational diffusion coefficient as the measured flocs.

The model results are compared with two published data sets in the following case studies. One study provides steady state FSD and D_{50} , and the other provides d_{60} .

3.1. Case 1: Mietta et al. (2008) carried out a numerical study to simulate the flocculation due to turbulence shear in a laboratory settling column with suspended kaolinite. Details of the laboratory experiment can be found in Maggi et al. (2002). Mietta et al. (2008) focused on the sensitivity of using different fragmentation distribution functions in their model study. The settling column in the experiment was about 5 m high with inside diameter of 0.28 m. Kaolinite with density $\rho_s \approx 2650 \text{ kg/m}^3$ and primary particle median size $l_p \approx 6 \text{ }\mu\text{m}$ was the selected sediment. Flocs were allowed to settle down the column with a sufficiently long residence time. Four homogeneous turbulence fields were generated in the entire column to examine the effect of shear rate by using an oscillating grid system that operated at four different frequencies. The suspended sediment concentration was maintained constant in the buffer tank mounted on top of the settling column. Sediments (flocs) were released into the column that connected to the buffer tank on top. Floc size was observed by a camera system with laser light source, image resolution was $6.42 \text{ }\mu\text{m/pixel}$, and the observation window was $6 \text{ mm} \times 6 \text{ mm}$. The floc size was computed based on 2D projection. Since the falling

sediment experienced a constant shear rate for a sufficiently long time during the falling course (4 m), it was assumed that steady state flocculation was reached when the sediment reached the observation location (about 0.5 m above the bottom of the column). Assuming equilibrium state (i.e., the downward flux of sediment above and below the observation section are the same), the observed floc size information may be simulated by using the developed box model that has no net flux of sediment in any direction.

To set up the flocculation model, shear-induced collision frequency (Eq. 2.14), constant correction factor, Winterwerp's breakup frequency formulation (Eq. 2.16), and binary fragmentation with mass ratio 1:1 (Eq. 2.17) are adopted. The fractal dimension is assumed to follow the power law of floc size as:

$$nf(L) = nf_p \cdot \left(\frac{L}{l_p}\right)^{d_L} \quad (2.20)$$

where nf_p is the fractal dimension of the primary particles, and d_L represents the distance from monofractal growth dynamics (Mietta et al., 2008). Here $nf_p = 3.0$ and $d_L = -0.1$ are used as suggested by Maggi (2005, 2007, 2008). The experiment is carried out with one suspended sediment concentration, $c = 0.5$ g/L and four shear rates, $G = 5, 10, 20, 40$ s⁻¹. It is assumed that all particles initially have the same size equal to the median primary particle size, l_p . The initial particle number N_0 can be estimated as

$$N_0 \approx \frac{c}{\rho_s \cdot l_p^{nf_p}} \quad (2.21)$$

The two-dimensional Downhill Simplex Method (Press et al., 1992; Maggi, 2005; Maggi et al., 2007) is used to minimize the difference between model predicted and experimental FSDs

for $G = 10$ and 40 s^{-1} with the objective to find the best fitted C_1 and C_2 as a calibration process. The time step Δt is taken as $1/G$. Calibration results are $C_1 = 0.906$ and $C_2 = 1.479 \times 10^{-4}$, which are comparable with those used by Mietta et al. (2008): $C_1 = 0.85$ and $C_2 = 2.4 \times 10^{-4}$. The other two shear rates, $G = 5$ and 20 s^{-1} , were used to verify the model results.

3.2. Case 2: Furukawa and Watkins (2012) carried out a laboratory experiment to explore the effects of organic matter (OM) on the flocculation of colloidal montmorillonite. Test cases included using pure montmorillonite and montmorillonite with three types of OM, i.e., humic acid, chitin, and xanthan gum, for different salinities $s = 1.8, 3.6, 7.2$ ppt, respectively. Humic acid is abundant in many rivers, coastal, and estuary waters. Chitin is a type of EPS that can be found in Crustacean shells, and xanthan gum is an anionic polysaccharide used as a proxy for microbial EPS. The montmorillonite was soaked in distilled water, stirred and settled for 7.5 h in a typical 1000 mL cylinder. Mixtures from the top 2.5 cm were collected repeatedly as pure montmorillonite. These selected OMs were dissolved in pure water separately to yield a stock suspension and stored cold. The test suspensions were obtained by combining the pure montmorillonite mixture, an OM suspension, and artificial seawater to yield typical values that represent selected natural environments. Floc size in a small container (20 mL) agitated by a magnetic stirrer was analyzed by using a DLS that measured the hydrodynamic mean diameter d_{60} . Furukawa and Watkins (2012) reported that $G = 40 \text{ s}^{-1}$ was the typical shear rate produced by small magnetic stir bars in the container. The flocculation mechanisms included a linear superposition of Brownian motion and fluid shear (i.e., Eq. 2.12 + Eq. 2.14) for Euclidean collision frequency, constant correction factor, Winterwerp's breakup frequency

formulation (Eq. 2.16), and binary fragmentation distribution function (Eq. 2.17). Furukawa and Watkins (2012) assumed an empirically constant fractal dimension $nf = 2.05$, a primary particle size of $0.2 \mu\text{m}$, and an equivalent particle number of $9 \times 10^{14} (/m^3)$ as the initial conditions. These values are also used in this simulation.

4. Results and discussions

4.1. Case 1: Comparison with Mietta et al. (2008)'s simulation results

Using eight-node QMOM with adjustable factor $p = 5$ for $G = 5 \text{ s}^{-1}$, and seven-node QMOM with $p = 4$ for $G = 10, 20, 40 \text{ s}^{-1}$, the predictions of FSDs match quite well with experimental results of $G = 5$ and 20 s^{-1} at steady states (Fig.2.1). Note that the cases of the other two shear rates $G = 10, 40 \text{ s}^{-1}$ are used for calibration purposes, and their FSDs are also given in Fig. 2.1 to demonstrate the level of detail this study can provide. Since the predicted FSD represents solutions of Γ and Ω , the values for each size class (i.e., L_i) are not necessarily the same as those given in Mietta et al. (2008). The model results are linearly interpolated according to the experimental size groups and normalized to satisfy the requirement that summation of the number frequency at experimental size groups equal unity.

The predicted FSDs appear to slightly underestimate the fraction of large particles (Fig. 2.1). A possible reason is that the number of large flocs is dramatically low and appeared only occasionally compared to the number of small flocs or primary particles, so that a slight bias away from large particles is present in the number-based distribution. Another possible reason is that the constant correction factor α assumption and/or Winterwerp's breakup frequency and/or binary breakup assumption are not sufficient to present the essential properties of

kaolinite flocculation. Improvements might be made by changing these parameters in the model and tracking more characteristic size groups to find a better fitting curve. Nevertheless, it is not recommended to do so at this time until a clearer understanding of these processes is achieved.

The predicted median size (D_{50}) is slightly larger than that from the published data for small shear rates, but the predicted D_{50} is smaller than the experimental results for $G = 40 \text{ s}^{-1}$ (Fig. 2.2). This trend may be a result of using calibration constants obtained from $G = 10 \text{ s}^{-1}$ and 40 s^{-1} . Also, this trend might suggest that the modeled aggregation process is stronger than it should be at small shear rate. Note that the experimental median size is calculated using the experimental FSD because Mietta et al. (2008) did not include this parameter.

In contrast to other PBM–QMOM models, the time variation of FSDs can be given in this simulation (Fig.2.3) for various shear rates. Note that the FSDs are normalized to ensure that the summation of the number frequency (i.e., the normalized number density) for all the tracking nodes is unity. Although all particles are initially assumed as primary particle with a median size l_p , size groups smaller than l_p can be expected during flocculation. Physically this is possible because there can be a few particles smaller than the median primary particle size. Mathematically, the integral domain is from 0 to infinity, so that any positive value is possible. In other words, unless the integral domain is specified between l_p and infinity rather than between 0 and infinity, the inclusion of floc with size smaller than l_p cannot be excluded. The alteration of integral domain will change the standard Gaussian quadrature approximation to “Gauss–Radau quadrature approximation” (Press et al., 1992). This change, however, may lead to a worse ill-conditioned Eq. 2.4, and thus, is not used in this study. The

duration to approach steady state flocculation decreases as shear rate increases (Fig. 2.3). A bimodal FSD may appear during the process before reaching steady state. For example, these can be seen at $t = 6$ h for $G = 5 \text{ s}^{-1}$, $t = 3$ h for $G = 10 \text{ s}^{-1}$, $t = 80$ min for $G = 20 \text{ s}^{-1}$, and $t = 30$ min for $G = 40 \text{ s}^{-1}$. Further verification of this phenomenon, however, is pending on additional experiments.

Several features produced from this study, with suspended sediment kaolinite concentration of 0.5 g/L and shear rate $G = 10 \text{ s}^{-1}$ are presented as examples. Moments of FSD are key parameters tracked in this study, as well as other standard QMOM approaches. Since the number of nodes is seven ($N = 7$) with an adjustable factor $p = 4$, only m_0 , m_1 , m_2 , and m_3 (among the 14 moments) are used directly (see solid lines in Fig. 2.4), while moments higher than the third order are evaluated using Eq. 2.4 (see dashed lines in Fig. 2.4). The total sediment mass should be conserved so that the third moment m_3 is always the same. On the other hand, the number of particles (i.e., m_0), the length of all flocs (i.e., m_1), and the area of all flocs (i.e., m_2) are all decreasing with time because of flocculation. They reach equilibrium (i.e., when aggregation and breakage intensity are the same) after a few hours. In contrast, the higher order moments (e.g., m_4 to m_6) are all increasing with time, though these too reach steady state after a few hours.

The model simulated time variation of the characteristic size (Fig. 2.5) shows that all of the mean sizes increase dramatically in the first 2–3 hr during which the aggregation process is dominant. With floc size increasing, breakage becomes gradually more competitive and finally reaches steady state after 5–6 hr. The volume-weighted characteristic mean size d_{43} shows a larger value than the area-weighted characteristic mean size d_{32} . This study also

predicts the median size D_{50} , which shows a much slower rate of increase over the first two hours because most of the particles are still primary particles with size l_p or small flocs. After there are a sufficient number of large flocs, the pace starts to increase quickly and finally reaches steady state. Because the peak of the FSD changes somewhat frequently (not shown) for this case, the calculated D_{50} shows small ripples near the end. Further study is necessary to find the reason for the frequent change of the peak node.

Both the number of death particles (the first and the third term on the right hand side of Eq. 2.5) and birth particles (the second and last term on the right hand side of Eq. 2.5) diminish over time with a decreasing rate, and finally reach an equilibrium status (Fig. 2.6a). At the beginning, the death particle number is twice that of the birth particle number, but these numbers gradually converge. The higher amount of death particles during the first few hours may be due to more small particles aggregating into large particles (because there are more small particles during that period of time). Nevertheless, the volume of death particles should equal the volume of birth particles at any time to maintain the same total sediment volume (Fig. 2.6b). It is interesting to notice that the peak response rate occurs around 1.2 hr, which is the most dramatic time for particle volume exchange.

With a decreasing rate, the aggregation effect (the first two terms on the right hand side of Eq. 2.5) shows that the process to form large flocs is dominant but the net rate decreases with time and approaches a steady state after about 5 hr. The breakage effect (the last two terms on the right hand side of Eq. 2.5) shows that within a short period of time (~ 0.2 hr) the birth of flocs caused by breakage is significant. Mathematically this is possible because there is no restriction to prevent the given primary particles to further break into small particles,

and there are plenty of primary particles during that period. After 0.2 hr, however, the number of primary particles is reduced and the breakage of large flocs (produced by the aggregation process) may produce flocs that are not necessarily small. Thus, the change of floc numbers decreases again, and also finally reaches a steady state (Fig. 2.7). This demonstrates that the aggregation effect is dominant at the beginning because of a shortage of large flocs, and over time breakage becomes competitive when a sufficient number of large and fragile flocs exist in the system.

A time step of $\Delta t = 1/G$ and 288,000 time steps were used along with $G = 5, 10, 20,$ and 40 s^{-1} and process times of 16, 8, 4, and 2 hr, respectively, to let the modeled FSD reach steady state. The computing CPU times were around 31 s, 27 s, 27 s, and 27 s, respectively, based on a Lenovo T530 laptop with Intel i7 CPU, 2.90GHz, and 4GB memory. The computation time was mainly dependent on the number of total time steps, and only changed slightly when the maximum number of quadrature nodes was different. Notice that although the selection of Δt followed the suggestion of Mietta et al. (2008), the steady state FSD solution in this study was not sensitive to the time step Δt . This is in contrast to the results of Mietta et al. (2008). For example, when $\Delta t = 0.1 \text{ s}, 0.2\text{s}, 1\text{s},$ and 10 s were used for $G = 10 \text{ s}^{-1}$ in this study, the FSD results were practically the same. Steady state median sizes were $19.50 \mu\text{m}, 19.52 \mu\text{m}, 19.44 \mu\text{m},$ and $19.46 \mu\text{m},$ respectively, compared to the experimental result of $18.20 \mu\text{m}.$

4.2 Comparison with Furukawa and Watkins (2012)'s experiments for colloidal montmorillonite

In this study, the evolutions of the hydrodynamic mean size, d_{60} , for pure montmorillonite mixture, and montmorillonite with humic acid, chitin, and xanthan gum, for salinities 7.2, 3.6, and 1.8 ppt, are simulated with an average shear rate $G = 40 \text{ s}^{-1}$. Aggregation and breakage fitting parameters C_1 and C_2 are given in Table 2.1. Other constants are specified as described in Sec. 3.2. The simulated results are obtained with eight-node QMOM and adjustable factor $p = 1$. This case is unique because the primary particle size is less than $1 \text{ }\mu\text{m}$, so that the difference between $(L_1)^1$ and $(L_N)^K$ is not very large. For this reason, the standard QMOM (i.e., $p = 1$) is applicable to this case. C_1 and C_2 for different conditions are given by minimizing the difference between modeled d_{60} and measured d_{60} . Experimental results of Furukawa and Watkins (2012) show that the effect of OM on flocculation of montmorillonite varies with different types of OM. For instance, xanthan gum prompts aggregation while humic acid and chitin reduce flocculation of colloidal montmorillonite (Fig. 2.8c). In addition, for the same suspension, higher salinity yields stronger aggregation and larger mean size (Fig. 2.8a and Fig. 2.8b).

In the breakup frequency function used by Furukawa and Watkins (2012), the term $(\mu/F_y)^{1/2}$ (see Eq. 2.16) was merged in C_2 . In this study, however, yield strength $F_y = 1.0 \times 10^{-10} \text{ N}$ and dynamic viscosity $\mu = 1.0 \times 10^{-3} \text{ kg/(m}\cdot\text{s)}$ are assumed to be constants, and therefore $(\mu/F_y)^{1/2}$ term was excluded in the breakage coefficient C_2 . By using this approach, the breakage coefficients C_2 in this study and $C_2/(\mu/F_y)^{1/2}$ in Furukawa and Watkin's study are on the same order of magnitude. The range of C_1 used in this study (0.92 to 13.5) is very different than that employed by Furukawa and Watkins (0.306 to 1). The primary reason for this discrepancy is that there is no restriction of α in this study, but Furukawa and Watkins

(2012) limited α to a maximum of one. It is understood that the correction factor α can be larger than one depending on fractal dimension, since α not only reflects unsuccessful contact and unsuccessful sticking, but also accounts for a correction of floc geometry for the Euclidean collision frequency as well as impacts of organic matters. Following this argument, the selected C_1 and C_2 values with this model show a better agreement than the modeling results of Furukawa and Watkins (2012), especially for the case of montmorillonite with xanthan gum.

Since this modeling effort predicts the time evolution of FSDs, the time required to approach an equilibrium state can be identified by the change of d_{60} (Fig. 2.8) as well as from the change of FSDs (Fig. 2.9). It appears that pure montmorillonite with salinity 1.8 ppt approaches equilibrium in 2 hr, but this is not the case for pure montmorillonite with salinity 7.2 ppt. In addition, for this case study the evolution of the median size as well as the peak size show a smooth curve without any ripples, unlike the results for kaolinite (Fig. 2.5).

With time step $\Delta t = 1$ s and simulating 2 hr in real process time (i.e., a total of 7,200 time steps) for all conditions, the computing CPU time was around 3 s based on the same Lenovo T530 laptop. This was expected since the only difference among cases was the selection of different constants C_1 and C_2 .

The C_2 value is usually on the order of 10^{-4} (e.g., Maggi et al., 2007; Lee et al., 2011) if Eq. 2.16 is selected as the breakup frequency function, while C_1 can vary in a wide range according to different environmental conditions such as salinity, ζ -potential, organic matters, and sediment compositions. An increase of C_1 and C_2 will result in an increase and decrease of floc size, respectively. Generally, the ratio of C_1/C_2 is positively correlated with salinity

and negatively correlated with the absolute values of ζ -potential (Mietta et al., 2011). However, these effects might not be pronounced for different sediment compositions and with different organic matters (Furukawa and Watkin, 2012).

5. Conclusions

This study presents a numerical model that effectively simulates the time variation of Floc Size Distribution (FSD) of cohesive sediments using the box formulation of the Population Balance Equation (PBE). A modified Quadrature Method Of Moment (QMOM) is employed to track the FSD using seven or eight floc sizes and their number density. The following are the specific conclusions:

1. This is the first time the flocculation processes of cohesive sediments were simulated using QMOM to solve the PBE and to find the FSDs directly instead of only monitoring their moments.
2. Benefits of this modified method include low computational demands, similar to standard QMOM, and alleviation of the ill-condition, which allows this approach to use up to eight quadrature nodes for finding the FSD directly.
3. While using this model to mimic the experimental results carried out by Maggi et al. (2002) for kaolinite suspension, the selected constants ($C_1 = 0.906$ and $C_2 = 1.479 \times 10^{-4}$) in aggregation and breakage processes were similar to those given by Mietta et al. (2008). This ability of the model to reproduce the results of Mietta et al. (2008) increases our confidence in the accuracy of the model.

4. While simulating the experimental results given by Furukawa and Watkins (2012) for colloidal montmorillonite, the first constant, C_1 , required a relative large range (from 0.92 to 9.0) in order to match the observations well. The possibility of a large C_1 indicates that effects of organic matter and floc geometry on aggregation may be important.
5. A selection of $N_{\max} = 7$ or 8 for Gaussian Quadrature nodes is possibly the maximum, and this coincides with the following conditions to select the adjustable factor p : $k/p = 3$ for checking volume conservation directly and $p \geq 1$ to relax the ill-condition caused by $(L_1)^1 \ll (L_N)^K$ in Eq. 2.4.
6. The computation efficiency is excellent for this kind of model. For example, only approximately 30 s is required to simulate a process that occurred over 16 hr, with time step $\Delta t = 0.2$ s, total time steps = 288,000, eight quadrature nodes, and adjustable factor $p = 5$. The computing cost is mainly dependent on the total number of time steps.
7. Further extension of this model into one-, two-, and three dimensions and linking this with a hydrodynamic model are follow-up research objectives. Meanwhile, more studies on the determination of flocculation parameters, especially the corrector factor α , the breakup frequency function a , and the fragmentation distribution function b , are required to include various other chemical and biological effects.

Acknowledgments

This research has been partially supported by the Virginia Institute of Marine Science (VIMS) Student Research Grant, a research grant (Contract number: 774080) from Korea Institute of Ocean Science and Technology (KIOST), China Scholarship Council (CSC) scholarship, and the innovation project of science and technology for college graduates of Jiangsu Province, China (No. CXZZ11_0446). This paper is Contribution No. 3423 of the Virginia Institute of Marine Science, College of William & Mary.

Appendix 2-A: Wheeler's Algorithm

This algorithm is for solving the quadrature nodes Γ , i.e., L_i ($i = 1, 2, \dots, N$) and their weights Ω , i.e., ω_i ($i = 1, 2, \dots, N$) from the $2N$ moments m_k ($k = 0, 1, \dots, 2N-1$) using Eq. 2.4.

The essence of this algorithm is to find the unknown Gaussian quadrature nodes and the corresponding unknown weights. Press et al. (1992) showed that there exists a set of unique orthogonal polynomials $P_j(L)$ that satisfy the recurrence relation

$$P_{-1}(L) = 0, \quad P_0(L) = 1,$$

$$P_j(L) = (L - A_j)P_{j-1}(L) - B_jP_{j-2}(L) \quad (j = 1, 2, \dots, N) \quad (\text{A2.1})$$

with coefficients

$$A_j = \frac{\langle L \cdot P_{j-1}, P_{j-1} \rangle}{\langle P_{j-1}, P_{j-1} \rangle} \quad (j = 1, 2, \dots, N) \quad (\text{A2.2})$$

$$B_j = \frac{\langle P_{j-1}, P_{j-1} \rangle}{\langle P_{j-2}, P_{j-2} \rangle} \quad (j = 2, 3, \dots, N) \quad (\text{A2.3})$$

where the roots of the polynomial $P_N(L)$ are equivalent to the nodes of the N -node Gaussian quadrature (Gautschi, 2004; Thein, 2011). Here, the symbol $\langle \rangle$ denotes the scalar inner product of two functions $f(L)$ and $g(L)$ over an unknown weight function $n(L)$:

$$\langle f, g \rangle = \int_0^{\infty} f(L) \cdot g(L) \cdot n(L) dL \quad (\text{A2.4})$$

In this application, the unknown weight function, $n(L)$, will be the FSD (Thein, 2011).

Re-organize Eq. A2.1 as that shown in Press et al. (1992)

$$L \cdot P_{j-1}(L) = A_j \cdot P_{j-1}(L) + B_j P_{j-2}(L) + P_j(L) \quad (j = 1, 2, \dots, N) \quad (\text{A2.5})$$

and rewrite it in a matrix form, Eq. A2.5 becomes

$$L \cdot \begin{bmatrix} P_0(L) \\ P_1(L) \\ P_2(L) \\ \vdots \\ P_{N-2}(L) \\ P_{N-1}(L) \end{bmatrix} = \begin{bmatrix} A_1 & 1 & & & & & \\ B_2 & A_2 & 1 & & & & \\ & B_3 & A_3 & 1 & & & \\ & & \ddots & \ddots & \ddots & & \\ & & & B_{N-1} & A_{N-1} & 1 & \\ & & & & B_N & A_N & \end{bmatrix} \cdot \begin{bmatrix} P_0(L) \\ P_1(L) \\ P_2(L) \\ \vdots \\ P_{N-2}(L) \\ P_{N-1}(L) \end{bmatrix} + P_N(L) \begin{bmatrix} 0 \\ 0 \\ 0 \\ \vdots \\ 0 \\ 1 \end{bmatrix} \quad (\text{A2.6})$$

Let

$$T = \begin{bmatrix} A_1 & 1 & & & & & \\ B_2 & A_2 & 1 & & & & \\ & B_3 & A_3 & 1 & & & \\ & & \ddots & \ddots & \ddots & & \\ & & & B_{N-1} & A_{N-1} & 1 & \\ & & & & B_N & A_N & \end{bmatrix}$$

$$P(L) = [P_0(L) \ P_1(L) \ P_2(L) \ \cdots \ P_{N-1}(L)]^T$$

$$e_{N-1} = [0 \ 0 \ 0 \ \cdots \ 0 \ 1]^T$$

then Eq. A2.6 can be rewritten as

$$L \cdot P(L) = T \cdot P(L) + P_N(L) \cdot e_{N-1} \quad (\text{A2.7})$$

When L_j (with $j = 1$ to N) are the roots of $P_N(L)$, it leads to $P_N(L_j) = 0$, and thus, Eq. A2.7

becomes an Eigen-equation, i.e.,

$$(L_j I - T) \cdot P(L_j) = 0 \quad (\text{A2.8})$$

where I is a unit (or identity) matrix, $(L_j I - T)$ must be a singular matrix to have non-trivial solutions, and L_j is the eigenvalue of matrix T . For greater efficiency in finding L_j , it is better to apply a diagonal similarity transformation to matrix T and change it to a symmetrical matrix J that has the same eigenvalues of matrix T , as suggested by Press et al. (1992) and John and Thein (2012).

Left multiplied by matrix D , Eq. A2.8 becomes $L_j D P = D T P = (D T D^{-1})(D P)$. By further

writing $J = DTD^{-1}$ and $Q = DP$, Eq. A2.8 is transferred to Eq. A2.9 which shows L_j are the eigenvalues of both matrices T and J :

$$(L_j I - J) \cdot Q = 0 \quad (A2.9)$$

where

$$D = \begin{bmatrix} 1 & & & & \\ & 1/\sqrt{B_2} & & & \\ & & 1/\sqrt{B_2 \cdot B_3} & & \\ & & & \ddots & \\ & & & & 1/\sqrt{B_2 \cdot B_3 \cdots B_N} \end{bmatrix}$$

and the real, symmetric, tri-diagonal Jacobi matrix J of order N is represented as

$$J = \begin{bmatrix} A_1 & \sqrt{B_2} & & & & \\ \sqrt{B_2} & A_2 & \sqrt{B_3} & & & \\ & \sqrt{B_3} & A_3 & \sqrt{B_4} & & \\ & & \ddots & \ddots & \ddots & \\ & & & \sqrt{B_{N-1}} & A_{N-1} & \sqrt{B_N} \\ & & & & \sqrt{B_N} & A_N \end{bmatrix} \quad (A2.10)$$

The elements in this Jacobi matrix are given by Eqs. A2 and A3. Therefore, finding the Gaussian quadrature nodes is transferred to solving an eigenvalue problem of Eq. A2.9 in which all the coefficients A_j ($j = 1, 2, \dots, N$) and B_j ($j = 2, 3, \dots, N$) are only related to the various moments of FSD (McGraw, 1997) and can be estimated sequentially. In this study, all the eigenvalues of matrix J were solved using the implicit QL method, a subroutine available in EISPACK (<http://www.netlib.org/eispack/>).

However, using Eqs. A2.2 and A2.3 directly to find A_j and B_j is tedious and impractical for high orders (i.e., large N). For this reason, a much simpler and straight-forward approach, Wheeler's algorithm, is recommended by John and Thein (2012) for using the computed moments to construct the Jacobi matrix. A detailed proof of Wheeler's algorithm can be

found in Thein (2011). Here, only the procedures that are used to build the Jacobi matrix are summarized (John and Thein, 2012):

First the intermediate quantities $S_{i,j}$ are initialized by

$$S_{-1,j} = 0, \quad S_{0,j} = m_j / m_0 \quad \text{where } j = 0, 1, \dots, 2N-1 \quad (\text{A2.11})$$

Then the following relationships

$$\sigma_i = S_{i,i+1} - S_{i-1,i} \quad (\text{A2.12})$$

$$\rho_i = -\sigma_i \cdot S_{i,i+1} + S_{i,i+2} - S_{i-1,i+1} \quad (\text{A2.13})$$

$$S_{i+1,j} = \rho_i^{-1} (-\sigma_i S_{i,j} + S_{i,j+1} - S_{i-1,j}) \quad (\text{A2.14})$$

are used recursively to find σ_i (with $i = 0$ to $N-1$), ρ_i (with $i = 0$ to $N-2$) and $S_{i+1,j}$ (with $i = 0$ to $N-2$ and $j = i+2$ to $2N-2-i$). Finally, these intermediate terms are used to construct the Jacobi matrix.

$$A_{i+1} = \sigma_i \quad (i = 0, 1, \dots, N-1) \quad (\text{A2.15})$$

$$B_{i+1} = \sqrt{\rho_i} \quad (i = 1, \dots, N-1) \quad (\text{A2.16})$$

For example, if $N = 2$, following Eqs. A11–A16, the elements in the Jacobi matrix can be written as

$$A_1 = m_1 / m_0 \quad (\text{A2.17})$$

$$A_2 = \frac{m_3 m_0^2 - 2m_0 m_1 m_2 + m_1^3}{m_2 m_0^2 - m_0 m_1^2} \quad (\text{A2.18})$$

$$B_2 = \frac{m_2 m_0^2 - m_1^2}{m_0^2} \quad (\text{A2.19})$$

Once the Jacobi matrix is obtained, the determination of Γ and Ω is accomplished by finding its eigenvalues and eigenvectors: Γ are the eigenvalues of J , and Ω can be found as (Press et al., 1992; McGraw, 1997; Marchisio et al., 2003a, 2003b, 2003c)

$$\omega_i = m_0 \cdot v_{i1}^2 \quad (i = 1, 2, \dots, N) \quad (\text{A2.20})$$

where v_{i1} is the first component of the i th normalized eigenvector of J . Note that $v_i = (v_{i1}, v_{i2}, \dots, v_{iN})$ is the eigenvector corresponding to the eigenvalue L_i and normalized to $v \cdot v = 1$.

Notation

- a breakup frequency function
- b fragmentation distribution function
- $\bar{b}^{(k)}$ k th moment of fragmentation distribution function
- c sediment mass concentration
- C_1 aggregation fitting parameter
- C_2 breakage fitting parameter
- d_{10} arithmetic mean size
- d_{32} Sauter mean size
- d_{43} De Broukere mean size
- d_{60} hydrodynamic mean size
- D_{50} median size
- E_0 contacting efficiency
- F_y yield strength
- G shear rate
- J Jacobi matrix
- K_B Boltzmann constant
- l_p median size of primary particle
- L particle size
- L_i characteristic size class; Gaussian quadrature points
- m_k k th order moment of the FSD
- n number density function

nf fractal dimension of flocs
 nf_p fractal dimension of primary particle
 N number of characteristic size groups
 N_0 initial particle number
 N_{\max} maximum number of nodes
 p adjustable factor
 s salinity
 t time
 T absolute temperature
 w_s settling velocity

Greek letters

α correction factor for Euclidean collision frequency function, $\alpha = \beta_0 \alpha_0 E_0$
 α_0 sticking probability
 β Euclidean collision frequency function
 β_0 shape or porosity corrections for Euclidean collision frequency
 Γ nodes of Gaussian quadrature approximation, $\Gamma = [L_1, L_2, \dots, L_N]$
 δ Dirac delta function
 μ dynamic viscosity of the fluid
 ρ_s bulk density of clay mineral
 ω_i characteristic number density; weights corresponding to L_i
 Ω weights of Gaussian quadrature approximation, $\Omega = [\omega_1, \omega_2, \dots, \omega_N]$

References

- Agrawal, Y.C., Mikkelsen, O.A., 2009. Shaped focal plane detectors for particle concentration and mean size observations. *Optics Express* 17, 23066–23077 (Optical Society of America).
- Camp, T.R., Stein, P.C., 1943. Velocity gradients and internal work in fluid motion. *Journal of the Boston Society of Civil Engineers* 30, 219–237.
- Eisma, D., 1986. Flocculation and de-flocculation of suspended matter in estuaries. *Netherlands Journal of Sea Research* 20, 183–199.
- Fan, R., Marchisio, D.L., Fox, R.O., 2004. Application of the direct quadrature method of moments to polydisperse gas-solid fluidized beds. *Powder Technology* 139, 7–20.
- Filippa, L., Freyre, L., Trento, A., Alvarez, A.M., Gallo, M., Vinzon, S., 2011. Laboratory evaluation of two LISST-25X using river sediments. *Sediment Geology* 238, 268–276.
- Filippa, L., Trento, A., Alvarez, A.M., 2012. Sauter mean diameter determination for the fine fraction of suspended sediments using a LISST-25X diffractometer. *Measurement* 45, 364–368.
- Furukawa, Y., Watkins, J.L., 2012. Effect of organic matter on the flocculation of colloidal montmorillonite: A modeling approach. *Journal of Coastal Research* 28, 726–737.
- Gautschi, W., 1968. Construction of Gauss–Christoffel quadrature formulas. *Mathematics of Computation* 22, 251–270.
- Gautschi, W., 2004. Orthogonal polynomials: computation and approximation. Numerical Mathematics and Scientific Computation. Oxford University Press, New York.

- Han, M., Lawler, D.F., 1992. The (relative) insignificance of G in flocculation. *Journal – American Water Works Association* 84, 79–91.
- Hulburt, H.M., Katz, S., 1964. Some problems in particle technology: A statistical mechanical formulation. *Chemical Engineering Science* 19, 555–574.
- Jiang, Q., Logan, B.E., 1991. Fractal dimensions of aggregates determined from steady-state size distributions. *Environment Science & Technology* 25, 2031–2038.
- John, V., Thein, F., 2012. On the efficiency and robustness of the core routine of the quadrature method of moments (QMOM). *Chemical Engineering Science* 75, 327–333.
- Kariwala, V., Cao, Y., Nagy, Z.K., 2012. Automatic differentiation-based quadrature method of moments for solving population balance equations. *AIChE Journal* 58, 842–854.
- Khelifa, A., Hill, P.S., 2006. Models for effective density and settling velocity of flocs. *Journal of Hydraulic Research* 44, 390–401.
- Kim, S., Karrila, S.J., 1991. *Microhydrodynamics: Principles and selected applications*. Butterworth-Heinemann, Boston.
- Kranenburg, C., 1999. Effects of floc strength on viscosity and deposition of cohesive sediment suspensions. *Continental Shelf Research* 19, 1665–1680.
- Ladd, A.J.C., 1994a. Numerical simulations of particulate suspensions via a discretized Boltzmann equation. Part I. Theoretical foundation. *Journal of Fluid Mechanics* 271, 285–309.
- Ladd, A.J.C., 1994b. Numerical simulations of particulate suspensions via a discretized Boltzmann equation. Part II. Numerical results. *Journal of Fluid Mechanics* 271, 311–339.

- Ladd, A.J.C., Verberg, R., 2001. Lattice–Boltzmann simulations of particles–fluid suspensions. *Journal of Statistical Physics* 104, 1191–1251.
- Lee, B.J., Toorman, E., Molz, F.J., Wang, J., 2011. A two-class population balance equation yielding bimodal flocculation of marine or estuarine sediments. *Water Research* 45, 2131–2145.
- Lee, D.G., Bonner, J.S., Garton, L.S., Ernest, A.N.S., Autenrieth, B.L., 2000. Modeling coagulation kinetics incorporating fractal theories: A fractal rectilinear approach. *Water Research* 34, 1987–2000.
- Lick, W., Huang, H.N., Jepsen, R., 1993. Flocculation of fine-grained sediments due to differential settling. *Journal of Geophysical Research* 98, 10279–10288.
- Lick, W., Lick, J., 1988. Aggregation and disaggregation of fine-grained lake sediments. *Journal of Great Lakes Research* 14, 514–523.
- Maggi, F., 2005. Flocculation dynamics of cohesive sediment. Ph.D. Dissertation, Netherlands: Delft University of Technology.
- Maggi, F., 2007. Variable fractal dimension: A major control for floc structure and flocculation kinematics of suspended cohesive sediment. *Journal of Geophysical Research* 112, C07012.
- Maggi, F., 2008. Stochastic flocculation of cohesive sediment: Analysis of floc mobility within the floc size spectrum. *Water Resources Research* 44, W01433.
- Maggi, F., 2009. Biological flocculation of suspended particles in nutrient-rich aqueous ecosystems. *Journal of Hydrology* 376, 116–125.

- Maggi, F., Mietta, F., Winterwerp, J.C., 2007. Effect of variable fractal dimension on the floc size distribution of suspended cohesive sediment. *Journal of Hydrology* 343, 43–55.
- Maggi, F., Winterwerp, J.C., Fontijn, H.L., van Kesteren, W.G.M., Cornelisse, J.M., 2002. A settling column for turbulence-induced flocculation of cohesive sediments. in: Wahl, T.L., Pugh, C.A., Oberg, K.A., Vermeyen, T.B., (Eds.), Proceedings of HMEM2002 Conference, Estes Park, Colorado.
- Marchisio, D.L., Pikturna, J.T., Fox, R.O., Vigil, R.D., Barresi, A.A., 2003a. Quadrature method of moments for population-balance equations. *AIChE Journal* 49, 1266–1276.
- Marchisio, D.L., Vigil, R.D., Fox, R.O., 2003b. Quadrature method of moments for aggregation-breakage processes. *Journal of Colloid and Interface Science* 258, 322–334.
- Marchisio, D.L., Vigil, R.D., Fox, R.O., 2003c. Implementation of the quadrature method of moments in CFD codes for aggregation-breakage problems. *Chemical Engineering Science* 58, 3337–3351.
- McAnally, W.H., 2000. Aggregation and deposition of estuarial fine sediment. Ph.D. Dissertation, Gainesville: University of Florida.
- McGraw, R., 1997. Description of Aerosol Dynamics by the Quadrature Method of Moments. *Aerosol Science and Technology* 27, 255–265.
- McGraw, R., Saunders, J.H., 1984. A condensation feedback mechanism for oscillatory nucleation and growth. *Aerosol Science and Technology* 3, 367–380.
- Mietta, F., 2010. Evolution of the floc size distribution of cohesive sediments. Ph.D. Dissertation, Netherlands: Delft University of Technology.

- Mietta, F., Chassagne, C., Verney, R., Winterwerp, J.C., 2011. On the behavior of mud floc size distribution: model calibration and model behavior. *Ocean Dynamics* 61, 257–271.
- Mietta, F., Maggi, F., Winterwerp, J.C., 2008. Chapter 19: Sensitivity to breakup functions of a population balance equation for cohesive sediments. *Sediment and Ecohydraulics 9* (INTERCOH 2005), 275–286.
- Mugele, R.A., Evans, H.D., 1951. Droplet size distribution in sprays. *Industrial and Engineering Chemistry* 43, 1317–1324.
- Prat, O.P., Ducoste, J.J., 2006. Modeling spatial distribution of floc size in turbulent processes using the quadrature method of moment and computational fluid dynamics. *Chemical Engineering Science* 61, 75–86.
- Prat, O.P., Ducoste, J.J., 2007. Simulation of flocculation in stirred vessels – Lagrangian versus Eulerian. *Chemical Engineering Research and Design* 85, 207–219.
- Press, W.H., Teukolsky, S.A., Vetterling, W.T., Flannery, B.P., 1992. Numerical Recipes in Fortran: The art of scientific computing, second ed. Cambridge University Press, Cambridge, United Kingdom.
- Rawle, A., 2003. Basic principles of particle-size analysis. *Surface Coatings International Part A: Coatings Journal* 86, 58–65.
- Sack, R.A., Donovan, A.F., 1972. An algorithm for Gaussian quadrature given modified moments. *Numerische Mathematik* 18, 465–478.
- Smoluchowski, M., 1917. Versuch einer Mathematischen Theorie der Koagulationskinetik Kolloider Lösungen. *Zeitschrift für Physikalische Chemie* 92,129–168. (in German)

- Son, M., 2009. Flocculation and transport of cohesive sediment. Ph.D. Dissertation, Gainesville: University of Florida.
- Son, M., Hsu, T.J., 2008. Flocculation model of cohesive sediment using variable fractal dimension. *Environmental Fluid Mechanics* 8, 55–71.
- Son, M., Hsu, T.J., 2011a. The effects of flocculation and bed erodibility on modeling cohesive sediment resuspension. *Journal of Geophysical Research: Oceans* 116, C03021.
- Son, M., Hsu, T.J., 2011b. Idealized study on cohesive sediment flux by tidal asymmetry. *Environmental Fluid Mechanics* 11, 183–202.
- Sowa, W.A., 1992. Interpreting mean drop diameters using distribution moments. *Atomization and Sprays* 2, 1–15.
- Sporleder, F., Borka, Z., Solsvik, J., Jakobsen., H.A., 2012. On the population balance equation. *Reviews in Chemical Engineering* 28, 149–169.
- Su, J.W., Gu, Z.L., Li, Y., Feng, S.Y., Xu, X.Y., 2007. Solution of population balance equation using quadrature method of moments with an adjustable factor. *Chemical Engineering Science* 62, 5897–5911.
- Su, J.W., Gu, Z.L., Xu, X.Y., 2009. Advances in numerical methods for the solution of population balance equations for disperse phase systems. *Science in China Series B: Chemistry* 52, 1063–1079.
- Tang, F.H.M., Alonso-Marroquin, F., Maggi, F., 2014. Stochastic collision and aggregation analysis of kaolinite in water through experiments and the spheropolygon theory, *Water Research* 53, 180–190.

- Thein, F., 2011. On the efficiency and condition of the core routine of the quadrature method of moments (QMOM). Diploma thesis, Germany: Otto-von-Guericke-Universität Magdeburg.
- Thomas, D.G., Judd, S.J., Frawcett, N., 1999. Flocculation modeling: a review. *Water Resources* 33, 1579–1592.
- Upadhyay, R.R., 2012. Evaluation of the use of the Chebyshev algorithm with the quadrature method of moments for simulating aerosol dynamics. *Journal of Aerosol Science* 44, 11–23.
- van Leussen, W., 1994. Estuarine macroflocs and their role in fine-grained sediment transport. Ph.D. Dissertation, Netherlands: University of Utrecht.
- Verney, R., Lafite, R., Brun-Cottan, J.C., Le Hir, P., 2011. Behaviour of a floc population during a tidal cycle: Laboratory experiments and numerical modelling. *Continental Shelf Research* 31, S64–S83.
- Wheeler, J.C., 1974. Modified moments and Gaussian quadratures. *Journal of Mathematics* 4, 287–296.
- Winterwerp, J.C., 1998. A simple model for turbulence induced flocculation of cohesive sediment. *Journal of Hydraulic Research* 36, 309–326.
- Winterwerp, J.C., 1999. On the dynamics of high-concentrated mud suspensions. Ph.D. Dissertation, Netherlands: Delft University of Technology.
- Winterwerp, J.C., 2002. On the flocculation and settling velocity of estuarine mud. *Continental Shelf Research* 22, 1339–1360.

- Winterwerp, J.C., van Kesteren, W.G.M., 2004. Introduction to the physics of cohesive sediment in the marine environment, in: van Loon, T. (Ed.), WL/ Delft Hydraulics & Delft University of Technology, Delft, Netherlands.
- Xu, F.H., Wang, D.P., Riemer, N., 2008. Modeling flocculation processes of fine-grained particles using a size-resolved method: Comparison with published laboratory experiments. *Continental Shelf Research* 28, 2668–2677.
- Yuan, C., Fox, R.O., 2011. Conditional quadrature method of moments for kinetic equations. *Journal of Computational Physics* 230, 8216–8246.
- Zhang, J.F., Zhang, Q.H., 2011. Lattice Boltzmann simulation of the flocculation process of cohesive sediment due to differential settling. *Continental Shelf Research* 31, S94–S105.
- Zhang, J.F., Zhang, Q.H., Maa, J.P.Y., Qiao, G.Q., 2013. Lattice Boltzmann simulation of turbulence-induced flocculation of cohesive sediment. *Ocean Dynamics* 63, 1123–1135.

Table 2.1 The flocculation parameter C_1 and C_2 derived through QMOM–PBM optimization by comparison with the experimental results of Furukawa and Watkins (2012) for colloidal montmorillonite.

Cases	C_1		C_2	
	This Study	Furukawa	This Study	Furukawa
Montmorillonite only, $s = 7.2$ ppt	4.0	1.0	2.346 E-4	3.668 E-4
Montmorillonite only, $s = 3.6$ ppt	3.5	1.0	2.682 E-4	4.238 E-4
Montmorillonite only, $s = 1.8$ ppt	1.5	0.484	9.050 E-4	8.190 E-4
With Humic Acid, $s = 7.2$ ppt	0.92	0.306	1.341 E-4	2.672 E-4
With Chitin, $s = 7.2$ ppt	0.95	0.401	3.352 E-4	8.949 E-4
With Xanthan gum, $s = 7.2$ ppt	13.5	1.0	2.514 E-4	1.099 E-4
With Xanthan gum, $s = 3.6$ ppt	9.0	1.0	3.352 E-4	2.182 E-4
With Xanthan gum, $s = 1.8$ ppt	2.5	0.856	6.704 E-4	6.593 E-4

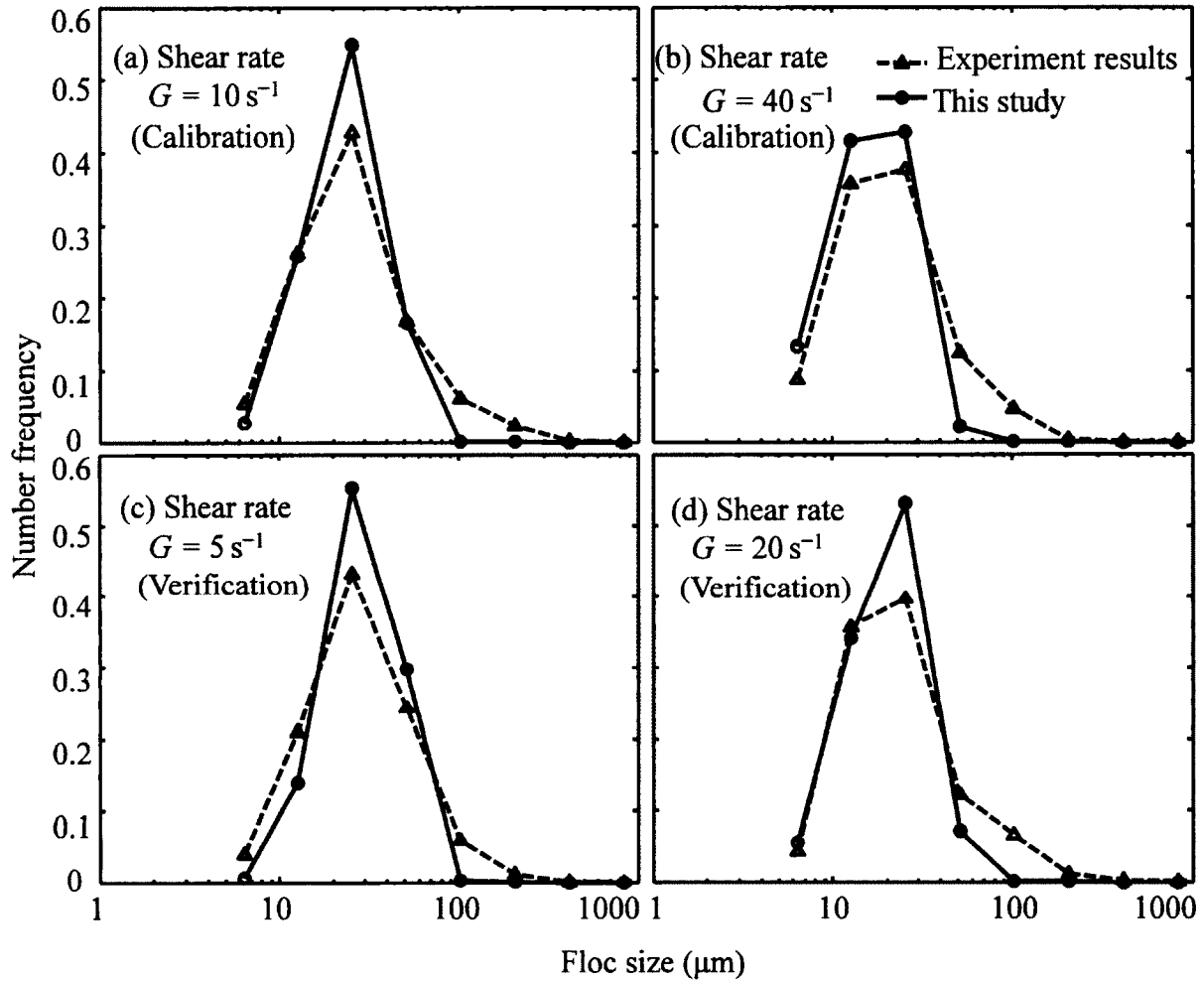


Fig. 2.1 Comparison between steady state experimental and simulated FSDs for (a) (b) calibration and (c) (d) verification results for suspended kaolinite with mass concentration 0.5 g/L and various shear rates.

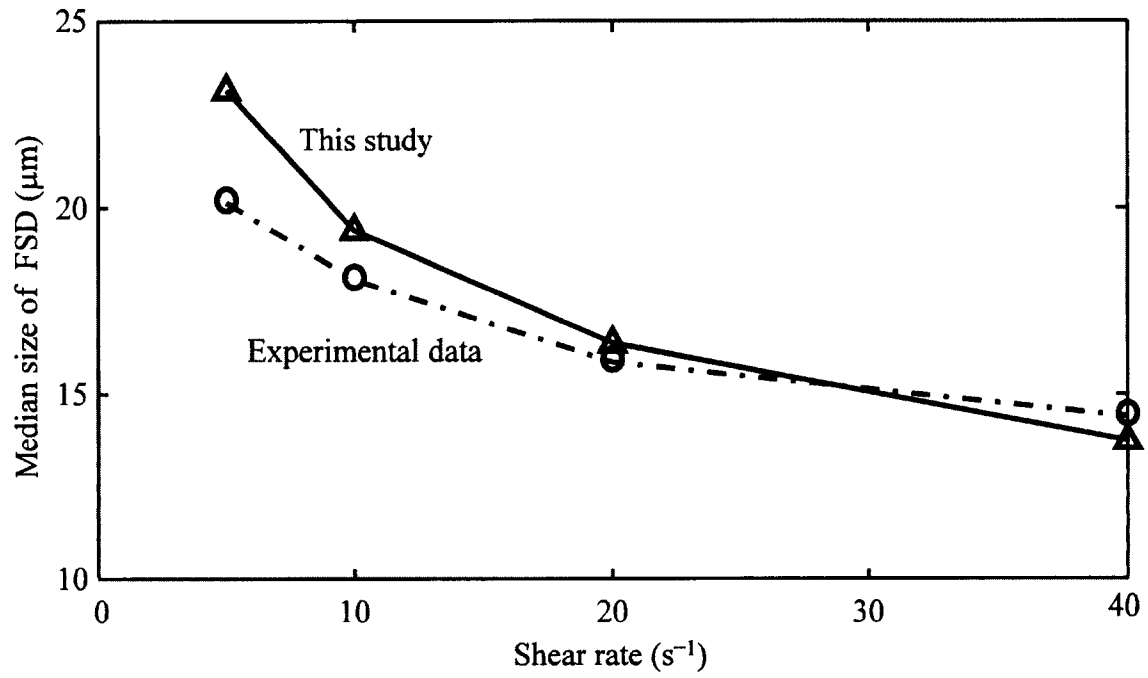


Fig. 2.2 Comparison between steady state experimental and simulated median size for suspended kaolinite with mass concentration 0.5 g/L and various shear rates.

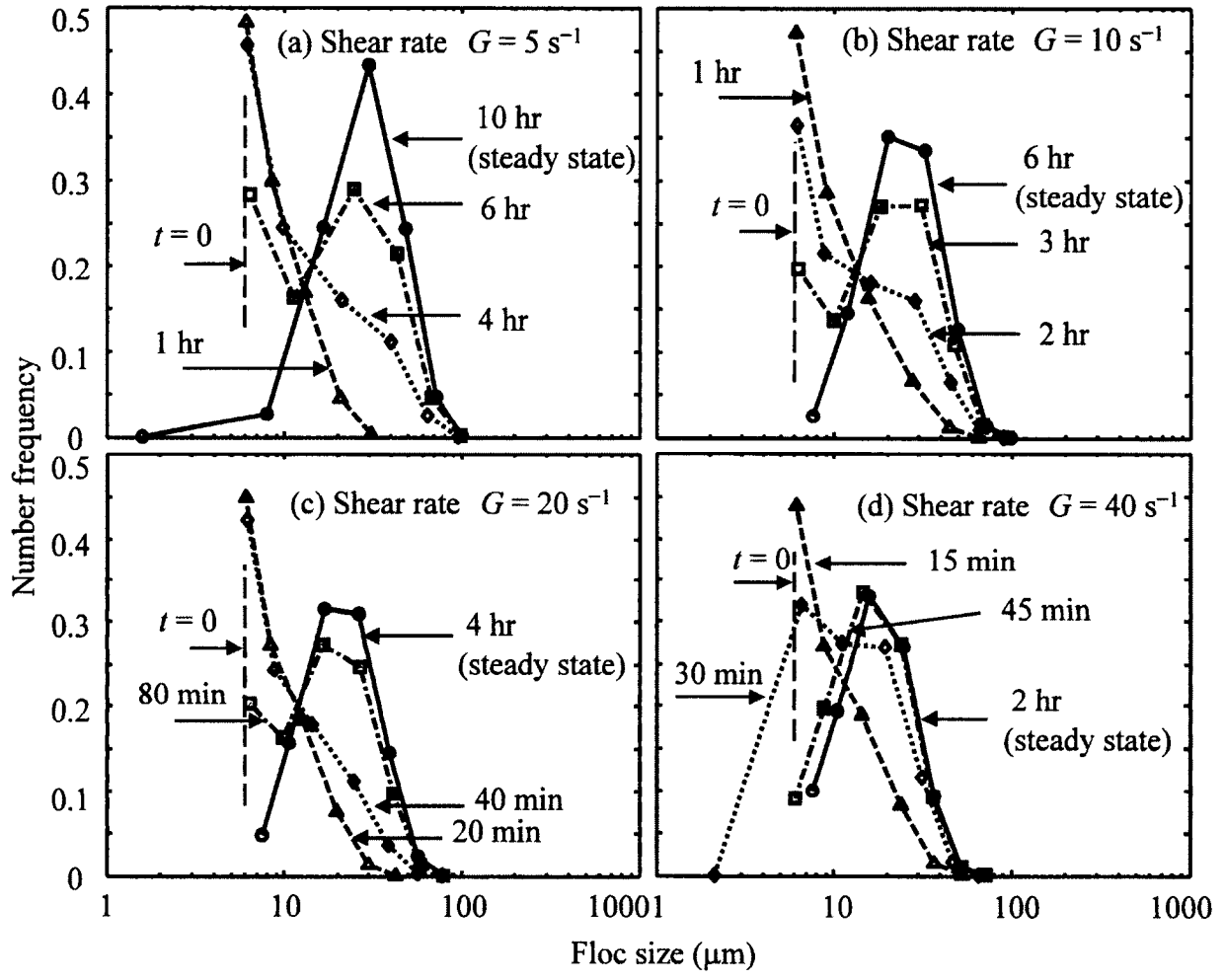


Fig. 2.3 Model computed time evolution of FSDs for suspended kaolinite at various shear rates with sediment mass concentration $c = 0.5 \text{ g/L}$.

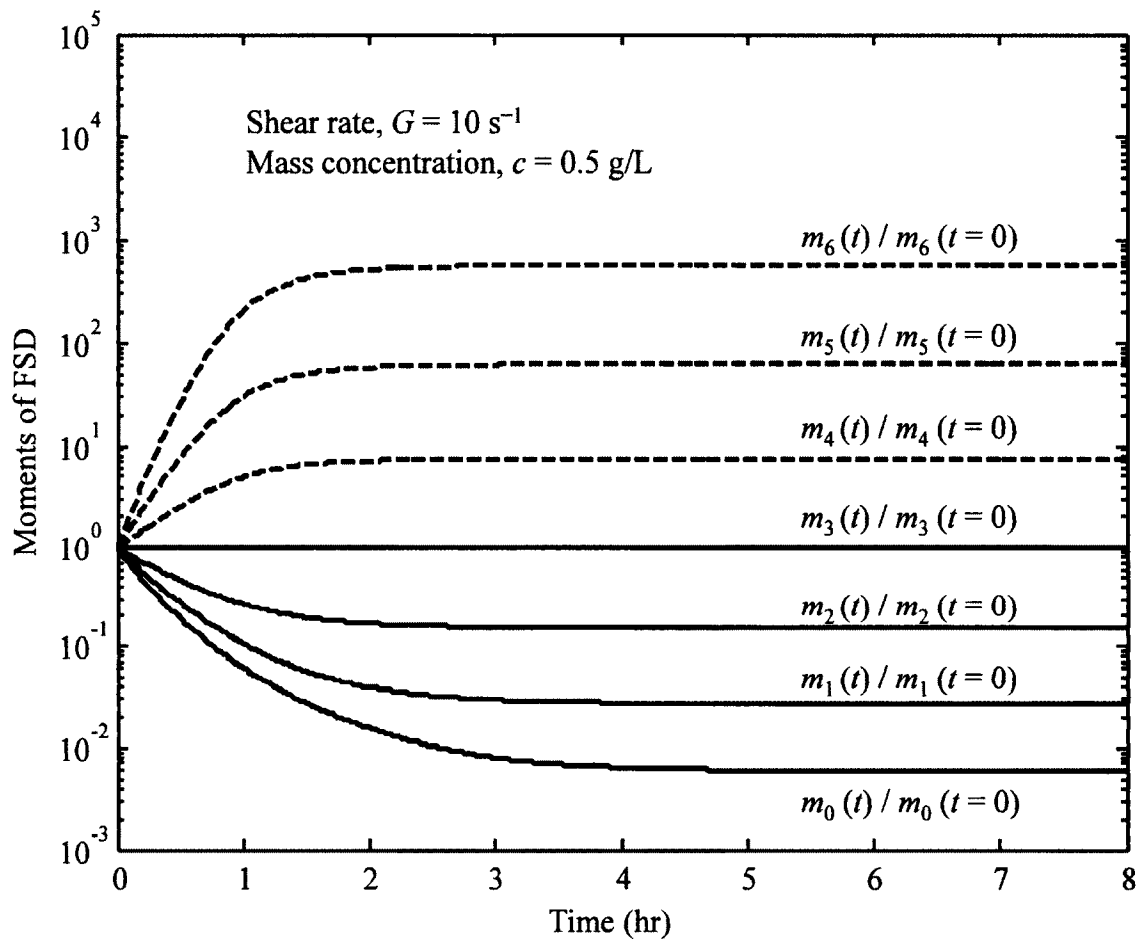


Fig. 2.4 An example of the model-calculated temporal evolution of lower order moments of FSD for suspended kaolinite (Solid line – directly tracked in the model; dashed line – derived using the simulated class sizes and the corresponding weights.)

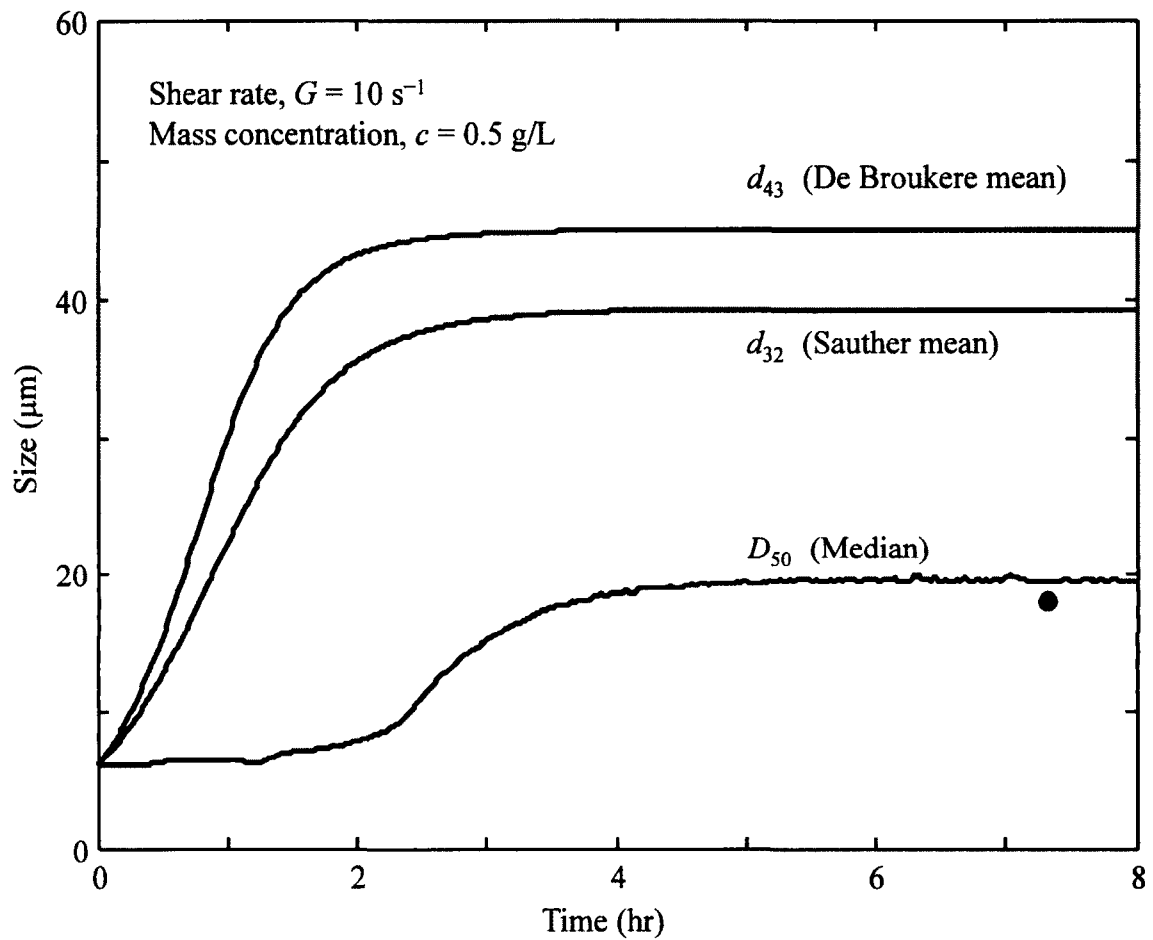


Fig. 2.5 An example of the model-calculated temporal evolution of De Broukere mean, Sauther mean, and median size for suspended kaolinite. The solid circle is the experimentally observed median size (data from Mietta et al. (2008)).

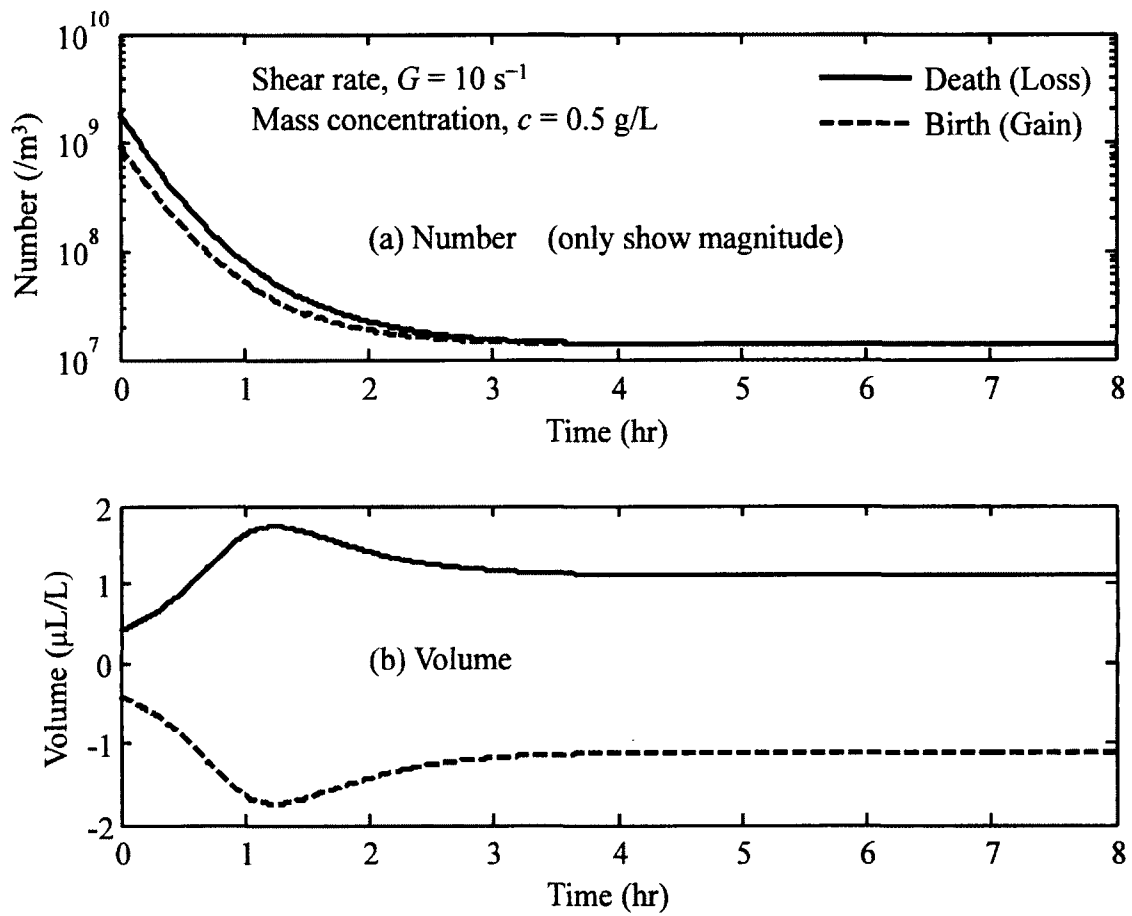


Fig. 2.6 An example of the model-calculated temporal evolution of death (loss) and birth (gain) of floc number and floc volume for suspended kaolinite.

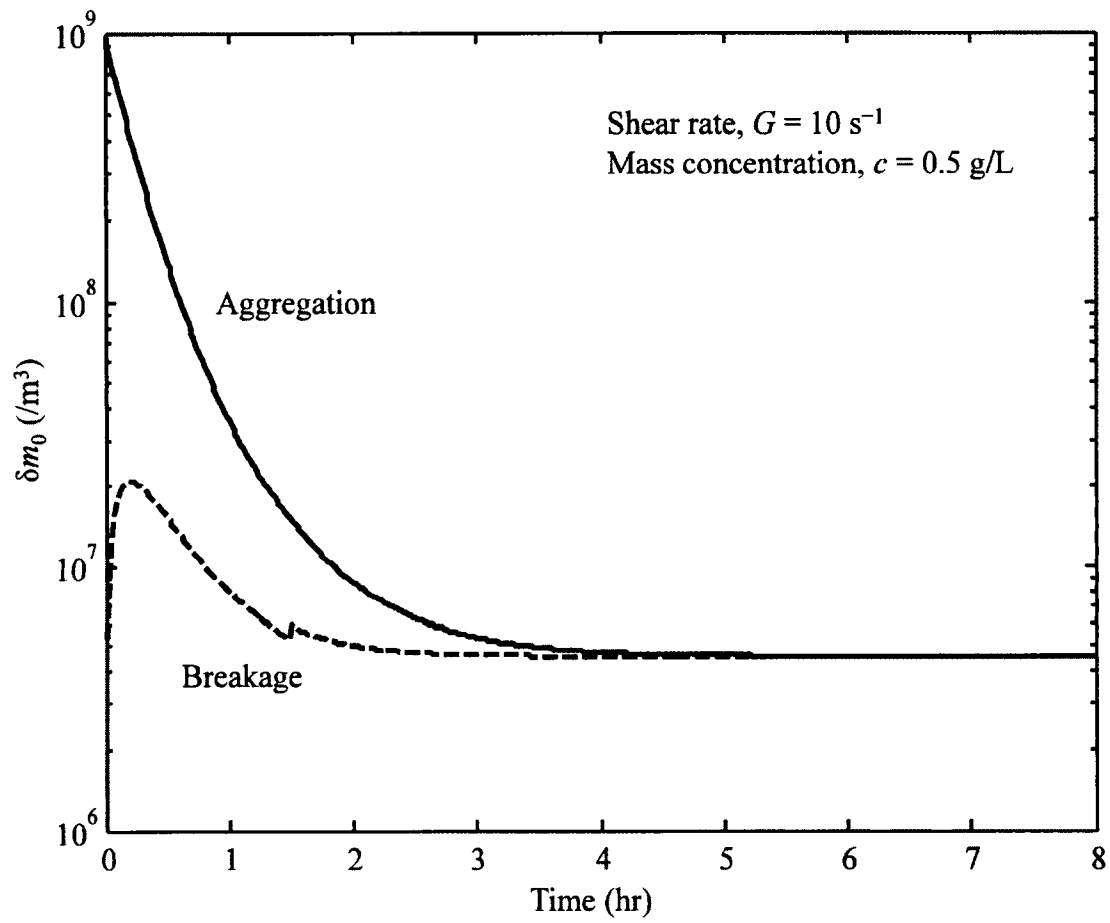


Fig. 2.7 An example of model-calculated temporal change of floc numbers (δm_0) due to aggregation and breakup for suspended kaolinite.

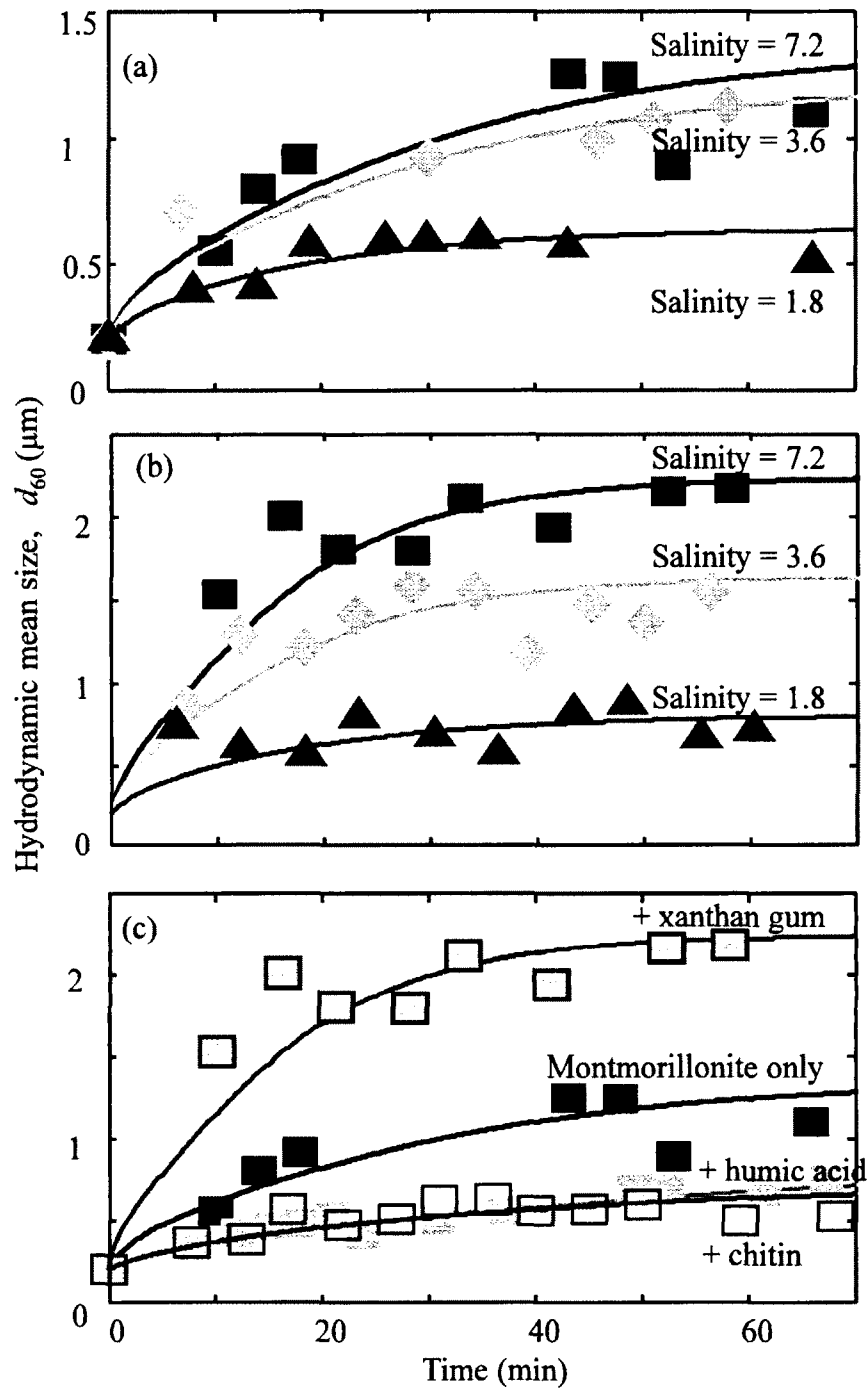


Fig. 2.8 Comparison of model-calculated temporal evolution of d_{60} (hydrodynamic mean size) of colloidal montmorillonite with measured data (all symbols) from Furukawa and Watkins (2012). (a) Pure Montmorillonite with different salinity, (b) Montmorillonite with xanthan for different salinity, and (c) Montmorillonite with a fixed salinity of 7.2 ppt, but different organic matter. Lines are the results of this model study. Constants and other conditions are summarized in Table 2.1.

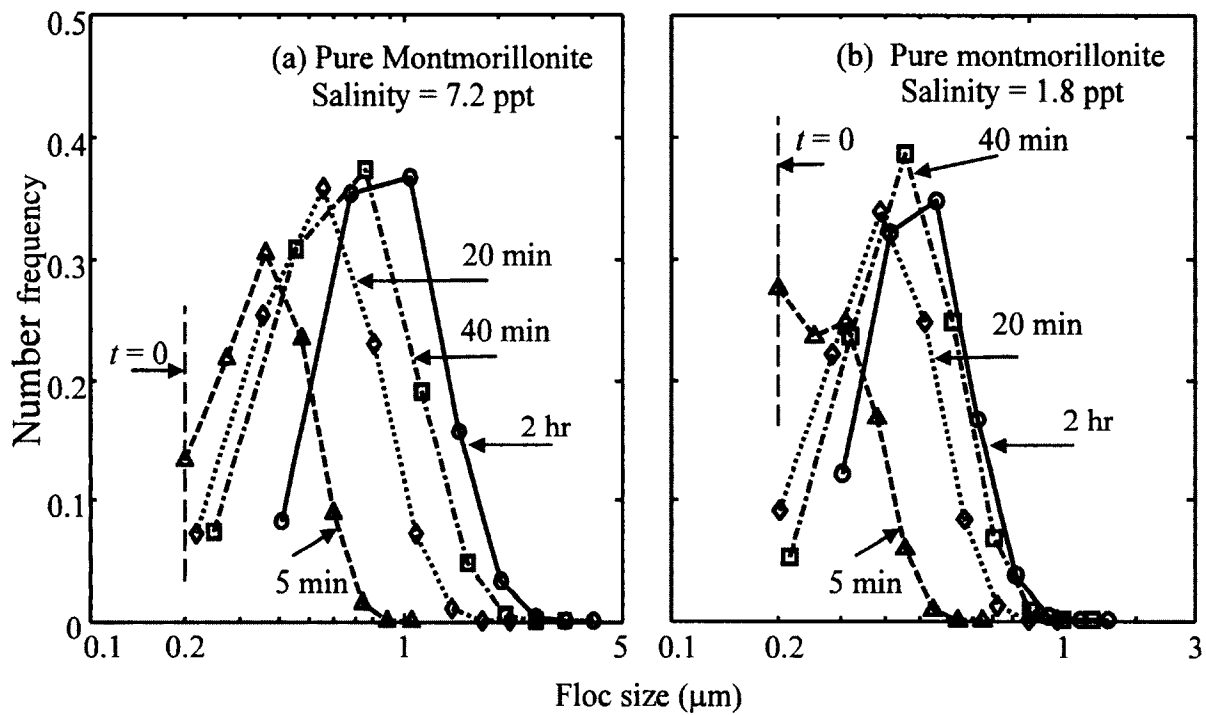


Fig. 2.9 The model-calculated FSD for pure montmorillonite mixture with salinity = 7.2 and 1.8 ppt.

CHAPTER III

NUMERICAL SIMULATIONS OF PARTICLE SIZE DISTRIBUTIONS: COMPARISON WITH ANALYTICAL SOLUTIONS AND KAOLINITE FLOCCULATION EXPERIMENTS

Abstract

The population balance equation has been used for several decades to describe the evolution of particle populations caused by aggregation and breakup processes. Only recently has it been used to efficiently and directly predict the temporal variation of Particle Size Distribution (PSD) for cohesive sediments by using the Quadrature Method Of Moments (QMOM). In this study, an extension of that effort carries out additional validations that compare with analytical solutions for pure coagulation systems, pure breakup systems, and combined coagulation and breakup systems. Besides, a laboratory experiment is conducted in a five liter mixing chamber to provide steady state PSD of suspended kaolinite with a chamber-averaged kaolinite concentration 0.52 g/L and shear rate 45 s^{-1} . The model results match reasonably well with both those from analytical solutions and kaolinite flocculation experiment results. Sensitivities regarding the selecting of different model input parameters (such as fractal dimensions, primary particle sizes, aggregation and breakage fitting parameters, and fragmentation distribution functions) are also checked. The results further confirm the capability of QMOM to predict PSD using its quadrature nodes and the corresponding weights.

Keywords: kaolinite; population balance; quadrature method of moments; particle size distribution; mixing chamber experiments; sensitivity tests

1. Introduction

The time evolution of Particle Size Distribution (PSD) has been a concern in estuarine particulate dynamics for many decades. Simplified floc growth models only track “averaged” particle size, assuming that all particles are uniformly distributed (with their median size) and self-similar (same size with same structure and same number of primary particles) (e.g., Winterwerp, 1998). Although one of the major assumptions of using a constant fractal dimension in such floc growth models has been later improved by others (Khelifa and Hill, 2006; Maggi et al., 2007; Son and Hsu, 2008) for variable fractal dimensions, the entire PSD is still either neglected or has to be re-constructed based on other assumptions (e.g., assuming log-normal distribution with a single peak, see Shin et al., 2015). In natural environments, however, it is not uncommon to observe bimodal or multi-modal distributions (e.g., Yuan et al., 2009) especially when organic matters are abundant, thus median size only is not sufficient and may deviate significantly sometimes. For these reasons, the Population Balance Equation (PBE) that can describe the PSD is more desirable for simulating the complicated phenomena in cohesive sediment transport.

PBE is a nonlinear integro-partial differential equation with source and sink terms to account for the gains and losses of particles with any particular size per unit volume. The history of applying PBE in mud flocculation is much shorter than the applications in other fields, such as granulation, precipitation, milling, spraying, droplet, bubble, crystallization, emulsion polymerization, leaching, and aerosol. In fact, only recently has PBE been applied to simulate time evolution of PSD for suspended sediment flocculation (e.g., Maggi et al., 2007; Mietta et al., 2008; Lee et al., 2011; Shen and Maa, 2015). A review of the origins,

frameworks, current applications, and future prospects of the PBE can be found in Sporleder et al. (2012) and Ramkrishna and Singh (2014).

In a general population balance framework, different external and internal properties might be included. Here external properties refer to the location of particles in physical space and time, and internal properties may include one or several distinguishable traits of particles such as density, size, volume, shape, and contents (e.g., concentration of different components). These properties are represented in a particle state space (ξ, \mathbf{x}, t) where ξ is the internal space, \mathbf{x} is the external space, and t is time. In population balance, one assumes that a particle number density function $n(\xi, \mathbf{x}, t)$ can describe the distribution of particles at every point in the particle state space (ξ, \mathbf{x}, t) , and the total number of particles in any region in the state space can be described by integrating the number density over the desired internal and external region (Ramkrishna, 2000).

In estuaries and coastal regions, the reliability of a sediment transport model depends significantly on the estimation of settling velocity, which is a function of particle size and particle density. By selecting fractal dimension (n_f) as a fitting parameter, particle density is described as a function of particle size rather than an additional internal property. Therefore, at current stage, particle size L might be the only internal property, i.e., $\xi = L$, so that the number density function $n(L, \mathbf{x}, t)$ becomes the number-based PSD.

Recently, Shen and Maa (2015) adopted an enhanced QMOM to simulate the PSD of cohesive sediments during coagulation and breakup processes. In their work, the time evolution of PSDs are reasonably simulated using at least seven (in some cases eight) quadrature points. Nevertheless, the effectiveness of the QMOM approach should be further

validated with data from well-studied systems to demonstrate the broader applicability of this approach with a wider variety of coagulation and breakup processes. To accomplish this objective, two approaches are selected: (1) Selected validation cases that include pure coagulation systems, pure breakup systems, and combined coagulation and breakup systems for which either analytical solutions or trusted simulation results are available for validations. (2) A laboratory experiment is conducted with suspended kaolinite to check the effectiveness of the model. Furthermore, the sensitivities on selected input parameters are studied in order to observe the model behavior. The details of each approach are presented after a brief description of the solution technique.

2. Review of quadrature method of moments

In this study, only the box PBE formulation (i.e., neglecting the diffusion, advection and/or settling terms) is considered to focus on the coagulation and breakup processes rather than the transport processes, and thus, the external symbol x is omitted in the number density function. Note that aggregation is a process where two or more particles collide and stick together to form a larger particle and breakup is a process that particles break into two or more fragments (Kumar, 2006). In a closed system, the number of particles may change due to coagulation and breakup, but the total volume of particles will not be affected.

Although many internal properties can be involved, only the particle size, L , is used in this study, and with the above simplifications, the particle state vector (ξ, x, t) is simplified to (L, t) . Thus, the size-based dynamic PBE in continuous form in a closed homogeneous system for coagulation and breakup events can be written as (Marchisio et al., 2003b;

Gimbun et al., 2009; Kariwala et al., 2012; Shen and Maa, 2015):

$$\begin{aligned} \frac{\partial n(L,t)}{\partial t} = & \frac{L^2}{2} \int_0^L \left[\frac{\beta((L^3 - \lambda^3)^{1/3}, \lambda)}{(L^3 - \lambda^3)^{2/3}} \cdot n((L^3 - \lambda^3)^{1/3}, t) \cdot n(\lambda, t) \right] d\lambda - n(L,t) \int_0^\infty \beta(L, \lambda) n(\lambda, t) d\lambda \\ & + \int_L^\infty a(\lambda) \cdot b(L|\lambda) \cdot n(\lambda, t) d\lambda - a(L) \cdot n(L, t) \end{aligned} \quad (3.1)$$

where $n(L, t)$ is the number density function for a particular particle size L at time t , with units of $m^{-1}m^{-3}$ where m^{-1} represents a range of particle size which coincides with the term “density,” and m^{-3} represents “per unit volume” which is sometimes omitted in the term “number density.” $\beta(L, \lambda)$ is the coagulation kernel, in units of m^3/s , representing particles with size L and size λ colliding to form a particle of size $(L^3 + \lambda^3)^{1/3}$, $a(L)$ is the breakup frequency function (also known as “breakup kernel”), in units of s^{-1} , that describes the frequency of disruption of particles with size L , $b(L|\lambda)$ is the fragmentation distribution function, in units of m^{-1} , and symbol “ $|$ ” describes the breakup of a particle with size λ (which is larger than size L) into daughter fragments and one or some of these daughter fragments have size L . The coagulation and breakup source and sink terms include: (1) gain of particles with size L due to coagulation of smaller particles (first term in the right hand side of Eq. 3.1), (2) loss of particles with size L due to their coagulation with other particles (second term in the right hand side of Eq. 3.1), (3) gain of particles with size L due to fragmentation of bigger particles (third term in the right hand side of Eq. 3.1), and (4) loss of particles with size L due to their own fragmentation into smaller particles (fourth term in the right hand side of Eq. 3.1).

Using method of moments, the moments of PSD, rather than the PSD itself are tracked directly. The k th moment of PSD is given by (Hulburt and Katz, 1964)

$$m_k = \int_0^{\infty} L^k n(L,t) dL \quad (3.2)$$

where k is an integer, and the lower order moments are related to the physical meanings of PSD. For example, m_0 is the total number of particles per unit volume; m_1 , m_2 , m_3 are proportional to the total length, total surface area, and total volume of the particles per unit volume, respectively. In addition, when settling properties of particles are addressed, m_4 is proportional to the total surface area of sphere particle settling per unit time, and m_5 is proportional to the settling flux of the suspended spheres (Mehta, 2013). One advantage of moment-based method is that various moment-defined diameters can be easily calculated as (Mugele and Evans, 1951; Sowa, 1992)

$$d_{ij} = \left[\frac{\int_0^{\infty} L^i n(L,t) dL}{\int_0^{\infty} L^j n(L,t) dL} \right]^{1/(i-j)} = \left(\frac{m_i}{m_j} \right)^{1/(i-j)} \quad (3.3)$$

where i and j are integers. For example, d_{10} is referred to as arithmetic mean size (mean of number-based PSD), d_{32} is Sauter mean size (i.e., mean of surface area-based PSD), d_{43} is De Broukere mean size (i.e., mean of volume-based PSD), and d_{20} is the surface-area ‘number’ mean diameter of spheres in a system, and for most of the time, the word ‘number’ is omitted. d_{20}^2 denotes the second origin moment of number-based PSD. When multiplying $\pi d_{20}^2/4$ by the total number of spheres in the system, one will get the total area of particles. Various characteristic size d_{ij} also determine the variance, skewness, and kurtosis of the PSDs (Sowa, 1992).

The QMOM employs the Gaussian approximation for the integrals in Eq. 3.2 (McGraw, 1997)

$$m_k = \int_0^{\infty} L^k n(L,t) dL \approx \sum_{i=1}^N \omega_i L_i^k \quad (3.4)$$

in which L_i are the Gaussian abscissas (also known as “nodes”, “pivots”, “mesh points”, or “quadrature points”), ω_i are the corresponding weights (i.e., the characteristic number density for size class L_i) that include information of bin size, and N is the number of quadrature nodes. Note that for k less than or equal to $(2N - 1)$, the “approximately equal” sign in Eq. 3.4 becomes exactly equal since L_i are auto-selected as Gaussian quadrature points (Thein, 2011; John and Thein, 2012).

For the purpose of saving computing cost and improving accuracy of moments predictions, Su et al. (2007) suggest an adjustable factor, q , to track the fractional moments (i.e., $m_0, m_{1/q}, m_{2/q}, \dots, m_{k/q}$)

$$m_{k/q} = \int_0^\infty L^{k/q} n(L, t) dL \approx \sum_{i=1}^N \omega_i L_i^{k/q} \quad (3.5)$$

This adjustable factor can also be used to reduce the severity of the ill-condition, making it possible to have more nodes (i.e., 7 or 8 nodes and weights) in order to directly construct PSDs (Shen and Maa, 2015).

After using the moment transformation, Gaussian approximation for the first $2N$ moments, and an adjustable factor q , Eq. 3.1 can be written as follows:

$$\begin{aligned} \frac{\partial m_{k/q}}{\partial t} = & \frac{1}{2} \sum_{i=1}^N \omega_i \sum_{j=1}^N \beta(L_i, L_j) \cdot \omega_j \cdot (L_i^3 + L_j^3)^{\frac{k}{\beta q}} - \sum_{i=1}^N L_i^{k/q} \omega_i \sum_{j=1}^N \beta(L_i, L_j) \cdot \omega_j \\ & + \sum_{i=1}^N a_i \bar{b}_i^{-(k/q)} \omega_i - \sum_{i=1}^N L_i^{k/q} a_i \omega_i \quad (k = 0, 1, \dots, 2N - 1) \end{aligned} \quad (3.6)$$

in which the fragmentation distribution function $b(L | \lambda)$ in Eq. 3.1 should be rewritten as (Su et al., 2007)

$$\bar{b}_i^{-(k/q)} = \int_0^\infty L^{k/q} b(L | \lambda) dL \quad (3.7)$$

Detailed processes of using N -node QMOM to solve PBE can be found elsewhere (e.g.,

Shen and Maa, 2015), and the computer codes in FORTRAN are also available in Shen (2016).

3. Validations with analytical solutions

Six cases are selected: (1) three cases for pure coagulation, (2) one for pure breakup, and (3) two for combined coagulation and breakup. All simulations were carried out on a Lenovo T530 laptop with Intel i7 CPU, 2.90GHz, and 4GB memory.

3.1 Pure coagulation process

Three types of coagulation kernels with either analytical solutions or asymptotic solutions for the PSDs and/or the moments are available for validation.

Case I: Constant coagulation kernel

$$\beta(L_i, L_j) = \beta_0 \quad (3.8)$$

For instances in which the physical process is unknown, Kapur and Fuerstenau (1969) introduce the constant kernel (also known as “size-independent kernel”) in granulation research. This is usually the first choice based on an assumption that it describes particles colliding completely at random and coalescing independent of their size (Marshall, 2012). With this simple kernel, Scott (1968) contributed to the analytical solutions of the moments and the PSD. The initial particle distribution was selected as

$$n(L) = \frac{3N_0}{v_0} L^2 \exp\left(-\frac{L^3}{v_0}\right) \quad (3.9)$$

where $N_0 = m_0(t = 0)$ is the total number of particles per unit volume at the beginning (in units of m^{-3}), v_0 is the initial mean volume of the particles (in units of m^3). Eq. 3.9 satisfies

the following

$$\int_0^{\infty} n(L)dL / N_0 = 1 .$$

Since this is a general, analytical formulation, the units of L , N_0 , and v_0 are not important and simply require consistency. The proper units of L , N_0 , and v_0 need to be specified only when using this equation to check if an experiment has a constant coagulation or not. Because of this reason, the units of the above parameters as well as the units of β_0 are omitted in the modeling and only follow the discussion for cases that have an analytical solution for comparison. In order to compare the model results with those given in earlier studies, all of the constants are selected to match those of the comparison studies. For example, Marchisio et al. (2003a) used $N_0 = 1$, $v_0 = 1$, and $\beta_0 = 1$, and thus, the same values are also selected in this study. Although $N_0 = 1$ (i.e., total number of particles per unit volume equal to 1) is not typical, it is fine to use this condition if $n(L)$ is not limited to be an integer number.

Scott (1968) gave the analytical solution for the moments as

$$m_k(t) = m_k(t=0) \cdot \left(\frac{2}{2 + N_0 \beta_0 t} \right)^{1-k/3} \quad (3.10)$$

and the analytical solution of PSD for this pure coagulation process as

$$n(L,t) = \frac{12 N_0 L^2}{v_0 (T_a + 2)^2} \exp\left(\frac{-2L^3}{v_0 (T_a + 2)} \right) \quad (3.11)$$

where $T_a = N_0 \beta_0 t$ is dimensionless time.

Using the current model with adjustable factor $q = 4$, the PSD is simulated using seven quadrature points ($N = 7$). The initial moments are estimated by integrating the initial PSD (i.e., Eq. 3.9) using the MATLAB “integral” function.

The predicted and analytical PSDs compare well at $t = 0, 10, 50, 100, 200$ s (Fig. 3.1).

The Y-axis is the normalized PSD so that the summation of weights (number frequency) for the seven automatically tracked quadrature points is one.

The simulated moments also match well with those given by Eq. 3.10; both are normalized by the initial moments (Fig. 3.2). It should be noted that since seven nodes with adjustable factor $q = 4$ are selected in this case, the moments up to $m_{13/4}$ are tracked directly. In other words, m_0 , m_1 , m_2 , and m_3 are given directly from the model, while the order of moments higher than 13/4 (e.g., m_4 , m_5 , and m_6) are estimated using the output abscissas and the corresponding weights with Eq. 3.5. The third moment m_3 remains constant during the entire computation duration which indicates that the total particle volume is conserved. This is the first step to confirm that the model is performed correctly. For a coagulation dominant process, the moments of order lower than three (e.g., m_0 , m_1 , and m_2) should decrease with time. The decreasing rate is highest at the beginning because of the high number of particles. With time, the number of particles decreases, and so does the rate of decreasing for lower moments. Eq. 3.10 indicates that $m_0(t)$ will linearly decrease with time when $N_0\beta_0t \gg 2$ and that is shown in Fig. 3.2 when $t > 150$ s. The moments higher than third order (e.g., m_4 , m_5 , and m_6) increase with time for the opposite reason.

In order to evaluate the progress of aggregation and identify the percentage of completed aggregations, Marchisio et al. (2003a) suggested using the intensity of coagulation, given as

$$I_{\text{agg}} = 1 - \frac{m_0(t)}{m_0(0)} \quad (3.12)$$

as an index, instead of time. This selection will clearly show how much of the aggregation has been completed. Here $I_{\text{agg}} = 0$ denotes no aggregation, and $I_{\text{agg}} \sim 1$ represents total

aggregation into one particle. The errors for the simulated moments relative to the analytical result at any stage of I_{agg} (Fig. 3.3) are less than 10^{-4} , even for the moments that are indirectly predicted, i.e., m_4 , m_5 , and m_6 .

The time variation of the mean sizes (e.g., arithmetic mean size d_{10} , Sauter mean size d_{32} , and De Broukere mean size d_{43}) all show excellent agreement between the predicted and analytical results due to the high accuracy of moments tracking (Fig. 3.4). In the previous study (i.e., Marchisio et al., 2003a; 2003b; 2003c) that uses QMOM methods with three or four abscissas, it is difficult to reasonably find the peak and median size of PSD even though these two parameters are the focuses for many engineering and scientific applications. In this study, the median size is simulated with seven-nodes, and the peak can also be reasonably predicted (Fig. 3.4). The small disturbances of the peak size are due to occasional fluctuations in the location of the maximum abscissas.

Case II: Sum coagulation kernel

Gelbard and Seinfeld (1978) used the following kernel to describe coagulation processes proportional to the volumes of interacting particles.

$$\beta(L_i, L_j) = \beta_0(L_i^3 + L_j^3) \quad (3.13)$$

where β_0 is a constant, and L_i and L_j are two nodes. This size dependent sum kernel is related to branched polymerization processes and aerosol coagulation in all flow conditions (Vigil and Ziff, 1989). For an exponential initial distribution (Eq. 3.9) with constant N_0 and v_0 , Scott (1968) gave the analytical PSD as follows.

$$n(L, t) = \frac{3N_0(1-T_a)}{LT_a^{1/2}} \exp\left(\frac{-L^3(1+T_a)}{v_0}\right) I_1\left(\frac{2L^3}{v_0} T_a^{1/2}\right) \quad (3.14)$$

where $T_a = 1 - \exp(-\beta_0 N_0 v_0 t)$ and $I_1(x)$ is the modified Bessel function of the first kind of order one. Note that the limit of function $I_1(x) / x$ is $1/2$ when $x \rightarrow 0$, thus, Eq. 3.14 becomes Eq. 3.9 when $t = 0$. Scott (1968) gave the analytical solution for the zero-ith order moment as

$$m_0(t) = m_0(t=0) \exp(-\beta_0 N_0 v_0 t) \quad (3.15)$$

Using an adjustable factor $q = 4$ and following those constants used by Su et al. (2008) (i.e., $\beta_0 = 0.01$, $N_0 = 1$, and $v_0 = 1$), the model simulated m_0 has a maximum error lower than 10^{-6} , when compared with Eq. 3.15 during the entire simulating time domain (i.e., 50 s, the same as in Su et al., 2008). The PSD results compare well with the analytical solution (Fig.3.5) at four selected times. Although the weights for larger particles, e.g., $L = 2$ in this case (dashed line in Fig. 3.5), apparently increase with time, the number fractions are still small compared to small particles. The mean of the PSD (i.e., d_{10}) also increases slowly through the simulating time period, while d_{32} and d_{43} increase much faster with time. This confirms that the sum kernel favors the coagulation of larger particles (Tobin et al., 1990; Marshall, 2012). The difference between the analytical solution and the results of this simulation may be due to a lack of sufficient Gaussian nodes to precisely represent the weight of large particles. Improvement is possible with more nodes, but that has not been verified yet because it would require using high precision (i.e., quad precision or more) for real numbers in a FORTRAN compiler to solve the ill-condition matrix described in the QMOM. Unfortunately, that precision is not available in the currently used PGI FORTRAN compiler. Nevertheless, reasonable agreements are still found between the predicted and analytical PSDs for all times.

Case III: Brownian coagulation kernels for two different regimes.

Depending on the size of particles and the mean free path length of the ambient gas, two different kernels can be assigned for each regime. In the first, the free-molecule regime, (i.e., particles are smaller than the mean free path length of the gas), particles behave like molecules. Based on the kinetic theory of gases, Friedlander (2000) showed the Brownian kernel in this first regime to be

$$\beta(L_i, L_j) = \beta_1 (L_i + L_j)^2 (L_i^{-3} + L_j^{-3})^{1/2} \quad (3.16)$$

In the second, the continuum regime, particles are larger than the mean free path length of the gas. Smoluchowski (1917) used the continuum diffusion theory and derived the Brownian kernel as

$$\beta(L_i, L_j) = \beta_2 (L_i^{-1} + L_j^{-1})(L_i + L_j) \quad (3.17)$$

where β_1 and β_2 are constants.

A complete analytical solution for the moments and PSDs are not available. However, Xie and Wang (2013) reported the following asymptotic solutions (i.e., $t \gg 1$) of m_0 and m_6 for these two Brownian kernels, regardless of the initial PSD. In the free-molecule regime:

$$m_0(t) \rightarrow 0.313309932 \cdot \beta_1^{-6/5} \cdot m_3^{-1/5} \cdot t^{-6/5} \quad (3.18a)$$

$$m_6(t) \rightarrow 7.022205880 \cdot \beta_1^{6/5} \cdot m_3^{11/5} \cdot t^{6/5} \quad (3.18b)$$

and in the continuum regime:

$$m_0(t) \rightarrow (81/169) \cdot \beta_2^{-1} \cdot t^{-1} \quad (3.19a)$$

$$m_6(t) \rightarrow (338/81) \cdot \beta_2 \cdot m_3^2 \cdot t \quad (3.19b)$$

Since m_3 is the total volume of all particles, it is invariant at all times, and thus, if the initial condition is given, then Eqs. 3.18 and 3.19 can be used to find the asymptotic value.

Besides, Xie and He (2013) indicated that the exact moment solution for the two Brownian kernels should satisfy the following two equations, respectively

$$f_1(m_c) = C_1 + C_2 \cdot t \quad (\text{in the free-molecule regime, } m_c = m_0 \cdot m_6 / m_3^2) \quad (3.20a)$$

$$f_2(m_0) = \frac{13^4}{3^4} \frac{\beta_2}{C_3} t + C_4 \quad (\text{in the continuum regime}) \quad (3.20b)$$

where

$$f_1(m_c) = \frac{a_2 \cdot (m_c - k_3)^{2-5H_3/6}}{2-5H_3/6} + \frac{a_1 \cdot (m_c - k_3)^{1-5H_3/6}}{1-5H_3/6} + \frac{a_0 \cdot (m_c - k_3)^{-5H_3/6}}{-5H_3/6} \quad (3.21a)$$

$$C_1 = \frac{a_2 \cdot (m_{c0} - k_3)^{2-5H_3/6}}{2-5H_3/6} + \frac{a_1 \cdot (m_{c0} - k_3)^{1-5H_3/6}}{1-5H_3/6} + \frac{a_0 \cdot (m_{c0} - k_3)^{-5H_3/6}}{-5H_3/6} \quad (3.21b)$$

$$C_2 = \frac{65\sqrt{2} \cdot \beta_1 \cdot m_3^{1/6} \cdot m_{00}^{5/6}}{5184 \cdot (m_{c0} - k_1)^{5/6H_1} \cdot (m_{c0} - k_2)^{5/6H_2} \cdot (m_{c0} - k_3)^{5/6H_3}} \quad (3.21c)$$

$$f_2(m_0) = 5 \ln m_0 + \frac{169}{C_3 m_0} - \frac{5}{2} \ln |169 + 5C_3 m_0 - 2C_3^2 m_0^2| - \frac{701}{9\sqrt{17}} \operatorname{arctanh} \frac{|4C_3 m_0 - 5|}{9\sqrt{17}} \quad (3.22a)$$

$$C_3 = m_{60} - 2m_3^2 / m_{00} \quad (3.22b)$$

$$C_4 = 5 \ln m_{00} + \frac{169}{C_3 m_{00}} - \frac{5}{2} \ln |169 + 5C_3 m_{00} - 2C_3^2 m_{00}^2| - \frac{701}{9\sqrt{17}} \operatorname{arctanh} \frac{|4C_3 m_{00} - 5|}{9\sqrt{17}} \quad (3.22c)$$

and $m_{00} = m_0 (t = 0)$, $m_{60} = m_6 (t = 0)$, $m_{c0} = m_c (t = 0) = m_{00} \cdot m_{60} / m_3^2$. Other constants in Eq. 3.21 and Eq. 3.22 are $\beta_1 = 1$, $\beta_2 = 1$, $a_0 = -0.00100408812658764$, $a_1 = 9.71923307384476 \times 10^{-5}$, $a_2 = -1.97514697514215 \times 10^{-5}$, $k_1 = 40.3611441357169$, $k_2 = -2.37665559790164$, $k_3 = 2.20012684680016$, $H_1 = 0.45115172265601$, $H_2 = -0.47035122605002$, and $H_3 = 1.01919950339400$.

For a standard log-normal initial PSD (Eq. 3.23),

$$n(L) = \frac{3N_0}{\sqrt{2\pi} \cdot w_g L} \exp\left(-\frac{(\ln(L^3 / \nu_0))^2}{2w_g^2}\right) \quad (3.23)$$

Barrett and Webb (1998) reported the variation of moments at selected times using 70-point finite element method with $N_0 = 1$, $\nu_0 = \sqrt{3/2}$, and $w_g = \sqrt{\ln(4/3)}$. Their results are assumed as an accurate solution and are used to validate the results of this study. In order to maintain accurate prediction of m_6 for comparison, the adjustable factor is selected as $q = 2$ to directly track m_6 .

The excellent agreement between predicted time evolution of m_0 and m_6 (grey solid line) and the asymptotic solutions (dark dashed line) of two Brownian kernels is evident (Figs. 3.6a and 3.6b). These also match very well with the 70-point finite element method results of Barrett and Webb (1998; solid dots in Figs 3.6a) at $t = 1, 5, 10$ s. In addition, the relative difference in $f_1(m_c)$ and $f_2(m_0)$ between this study and Eqs. 3.21 and 3.22 for the two Brownian kernels, respectively, are reported in Fig. 3.6c, with a maximum difference around 3%. Since the “exact” solution of Xie and He (2013) is derived using Taylor series expansion truncated after the third terms, their solution may also have some error included, and thus, the maximum 3% difference may be considered as an “excellent” match. These comparisons highlight the credibility of the model-predicted PSDs (Fig. 3.7). Notice that the continuous region of the Brownian coagulation kernel shows a slower coagulation rate when compared with that for the free-molecule regime (Fig. 3.7b versus Fig. 3.7a).

3.2 Pure breakup process

There are two parameters that affect the particle breakup process: the breakup kernel $a(L)$ and the fragmentation distribution function $b(L|\lambda)$. There is one analytical solution available with a specifically defined $a(L)$ and $b(L|\lambda)$. Details of this solution are given next.

Case IV: Peng and Williams (1994) presented a widely applicable breakup kernel as $a(L) = a_0 \cdot L^y$ where a_0 and y are empirically determined constants, and usually $y = 3$ is adopted to indicate that the breakage of particles is proportional to the particle volume (Kumar, 2006; Su et al., 2008). Thus, this breakup kernel is

$$a(L) = a_0 L^3 \quad (3.24)$$

where a_0 is a constant in units of $m^{-3}s^{-1}$ in order to satisfy the units of a (i.e., s^{-1}). In general, however, the units of a_0 can be any that are consistent with respect to those of L . In this case, the selection of $a_0 = 1$ follows Su et al. (2007, 2008).

There are several choices of the fragmentation distribution function (more will be discussed later). The uniform distribution function given by Marchisio et al. (2003b) is used in this case:

$$b(L|\lambda) = 6L^2 / \lambda^3 \quad (0 < L < \lambda) \quad (3.25)$$

Applying adjustable moment transformation (Eq. 3.5), Eq. 3.25 becomes (Su et al., 2007)

$$\bar{b}_i^{(k/p)}(L) = \frac{6q}{k+3q} L^{k/q} \quad (3.26)$$

With the exponential initial distribution (Eq. 3.9), Ziff and McGrady (1985) gave the analytical solution of PSD for this pure breakup process as follows

$$n(L,t) = 3L^2 \frac{N_0}{\nu_0} (1 + a_0 \nu_0 t)^2 \exp\left(\frac{-L^3}{\nu_0} (1 + a_0 \nu_0 t)\right) \quad (3.27)$$

Using an adjustable factor $q = 4$, with $N_0 = 1$, and $\nu_0 = 1$, the time variation of PSD can be simulated. The modeled and analytical PSD show excellent agreement for all selected times (Fig. 3.8). The peak size of the PSD reduces quickly in the first ten seconds, but the rate of decrease diminishes with time. The simulated moments (computed by using the MATLAB “int” function to integrate Eq. 3.27) also match the theoretical moments (not shown).

3.3 Combined coagulation and breakup processes

There are two cases simulated within this category, and the differences between these cases are in the selection of coagulation kernel, breakup kernel, fragmentation distribution function, and the initial PSD.

Case V: McCoy and Madras (2003) studied a process that combined a constant kernel for coagulation (Eq. 3.8 with a constant β_0), a power kernel for breakup (Eq. 3.24 with a constant a_0), a uniform fragmentation distribution function (Eq. 3.26), and an exponential initial distribution (Eq. 3.9). They worked out the analytical solution for PSD as follows:

$$n(L,t) = 3L^2 \frac{N_0^2}{\nu_0} [\phi(T_a)]^2 \exp\left(-\frac{N_0}{\nu_0} L^3 \phi(T_a)\right) \quad (3.28)$$

In Eq. 3.28, the dimensionless time $T_a = \beta_0 N_0 t$, and the total number fraction at dimensionless time T_a follows

$$\phi(T_a) = \frac{\phi(\infty) \cdot [1 + \phi(\infty) \cdot \tanh(\phi(\infty) \cdot T_a / 2)]}{\phi(\infty) + \tanh(\phi(\infty) \cdot T_a / 2)}$$

where $\phi(\infty) = (2a_0 \nu_0 N_0 / \beta_0)^{1/2} / N_0$.

By selecting those constants as $\beta_0 = 100$ in Eq. 3.8, $\alpha_0 = 1 \times 10^{-6}$ in Eq. 3.24, and $N_0 = 1$, $v_0 = 100$ in Eq. 3.9, the processes could approach a steady state around 50 s. The adjustable factor $q = 4$ is used. The initial moments are obtained using the MATLAB integral function “integral.” The results shows excellent agreement with the analytical PSD at all times (Fig. 3.9). The time evolution of all the characteristic sizes shows that the coagulation and breakup processes reach equilibrium in approximately 50 s (Fig. 3.10). For the first 20 s, the coagulation process is dominant, and thus, all of these characteristic sizes are quickly increasing. With time, the effect of breakup becomes competitive with coagulation, and thus, reduces the growing rate of these characteristic sizes, and finally reaches the steady state around $t = 50$ s.

Case VI: Vanni (2000) used a class method with 2,000 size classes to study a case that includes a sum coagulation kernel, power breakup kernel, binary fragmentation distribution function, and initial distribution with a single particle size. Detailed kernel functions Vanni used are expressed as follows:

$$\beta(L_i, L_j) = L_i^3 + L_j^3 \quad (3.29a)$$

$$a(L) = \begin{cases} 0 & L \leq L_1 \\ 0.02L^3 & L > L_1 \end{cases} \quad (3.29b)$$

The fragmentation distribution function is

$$b(L | \lambda) = \begin{cases} 2 & L = \lambda / 2^{1/3} \\ 0 & \text{otherwise} \end{cases} \quad (3.29c)$$

When applying adjustable moment transformation (Eq. 3.5), Eq. 3.29c becomes (Su et al., 2007)

$$\bar{b}_i^{(k/p)}(L) = 2^{(3-k/q)/3} L^{k/q} \quad (3.29d)$$

The initial moments are given as

$$m_{k/q}(t=0) = L_1^{k/q} \quad \text{for } k=0, 1, \dots, 2N-1 \quad (3.30)$$

where L_1 is the initial particle size, and Vanni (2000) selected $L_1 = 1$. Because initially it is a uniform size, only one class size (L_1) is used. To simulate this case using the QMOM approach, adjustable factor $q = 3$ is selected to track the PSD until the process reaches the steady state. The steady state m_0 and d_{43} predicted by this study very closely match those reported in Vanni (2000), Marchisio et al. (2003b), and Su et al. (2007). The steady state PSD given by Vanni (2000) is treated as an “exact” solution for comparison. Reasonable agreement between the “exact” solution and this study can be concluded (Fig. 3.11), despite a slight overestimation of larger particles. All of the above comparisons indicate that these modeling results are reasonable and credible. Therefore, the model-predicted PSDs at $t = 0, 0.5, 2, \text{ and } 5$ s are also reported in Fig. 3.11. Note that it is possible that the simulated PSD includes sizes smaller than the initial particle size (L_1) (i.e., a narrow initial distribution with median size L_1). For example, the breakage of a particle with size L_2 ($L_2 > L_1$ but $L_2^3 < 2 \cdot L_1^3$) may result in daughter fragments with sizes smaller than L_1 .

4. Experimental validations for kaolinite suspensions

The mixing chamber is one of the three laboratory devices (the other two are oscillating grid and Couette flow device, see Serra et al., 2008) to investigate PSD responding to aggregation and breakage of cohesive soils. In this study, a five liter cubic mixing chamber is used to measure the steady state PSD of kaolinite with suspended sediment concentration

0.52 g/L. A LIGHTNIN A310 impeller with 132 mm diameter is rotating at 4 cm above the bottom to generate turbulence. Kaolinite suspensions are first stirred with the impeller's maximum speed (i.e., chamber-averaged shear rate about 217 s^{-1} , see Shen and Maa, *Submitted*) for half an hour to break the flocs, and then set to an average shear rate of 45 s^{-1} to allow flocs to aggregate. This shear rate is neither too high to break all flocs, nor too low to allow significant settling, and thus is appropriate for use in this study. After mixing for one day, the floc images are acquired by using a camera system developed by Shen and Maa (*Submitted*) that can identify flocs with a minimum size of $5 \mu\text{m}$. Images are obtained through the transparent wall of the mixing chamber. PSDs are processed using the MATLAB Image Toolbox, and the average PSDs at elapsed time = 23, 23.5, and 24 hrs (50 images at each time) are used to represent steady state PSD.

To mimic the mixing chamber results, the aggregation kernel given by Smoluchowski (1917) is used

$$\beta(L_i, L_j) = C_1 \cdot \frac{G}{6} (L_i + L_j)^3 \quad (3.31)$$

in which G is the chamber averaged shear rate (45 s^{-1}), and C_1 is the aggregation parameter; this is also referred to as the “collision efficiency”, which describes successful attachments of approaching particles after a successful collision. The breakup kernel given by Winterwerp (1998) is used

$$a(L_i) = C_2 \cdot \left(\frac{\mu}{F_y} \right)^{1/2} \cdot G^{3/2} \cdot L_i \cdot \left(\frac{L_i}{l_p} - 1 \right)^{3-n_f} \quad (3.32)$$

in which C_2 is the breakup fitting parameter, l_p is the size of primary particles, n_f is the fractal dimension of the flocs, μ is the dynamic viscosity of the fluid, and F_y is the yield strength of

flocs. The fragmentation distribution function is assumed as binary breakup (Eq. 3.29d). The selection of $C_1 = 0.85$, $C_2 = 3.2 \times 10^{-5}$, as well as other parameters, $\mu = 10^{-3}$ Pa·s, $l_p = 5 \mu\text{m}$, and $F_y = 10^{-10}$ N follows those given by Shen and Maa (*Submitted*) from the calibration results for sediment mass concentration 0.28 g/L and average shear rate 45 s^{-1} in the same system. Maximum number of nodes $N = 8$ and adjustable factor $q = 5$ are selected following Shen and Maa (2015). Fractal dimension n_f is following that given by Khelifa and Hill (2006) and Maggi et al. (2007):

$$n_f = 3 \cdot \left(\frac{L_f}{l_p} \right)^{d_L} \quad (3.33)$$

in which $d_L = -0.1$ for kaolinite suspensions (Maggi et al., 2007). It is assumed that all particles are spherical primary particles initially.

It is understood that fluid viscosity is a function of temperature, floc strength depends on floc size and fractal dimension (Son, 2009), primary particles should not be limited to one representative size, and fractal dimension is difficult to precisely assign. However, these parameters are used for simplifying the simulation, thus providing items for improvements in the future.

At steady state, the predicted mean and median sizes match excellently and the predicted PSD match reasonably well with experimental results (Fig. 3.12). Model prediction shows it takes around two hours to arrive at steady state. However, this duration required for flocculation process to reach steady state may be biased. This is because the mixing chamber does not have a constant shear rate for the entire chamber. A floc is traveling periodically through different shear zones instead of a constant shear zone (Prat and Ducoste, 2006). This

may cost more time to reach steady state. For example, Keyvani and Strom (2014) reported steady state was reached after about 34 hrs in their tank, which is bigger than the chamber used in this study, and thus, a longer duration. In fact, all the calculated moments after 2 hrs (Fig. 3.12a) can be used to predict the steady state PSD, and they do show similar predictions (Fig. 3.12b). It is also important to notice that in a Couette flow device, flocs aggregating are driven by a constant laminar shear, and it may only require 5–10 minutes to reach a steady state (Frappier et al., 2010).

Although the model performance appears excellent with these selected input parameters in both of the early studies (Shen and Maa, 2015; *Submitted*) and this study, the effect of changing to different input values has not been checked. For this reason, a sensitivity analysis of fractal dimension, primary particle size, C_1 & C_2 , number of nodes, and the fragmentation distribution function was carried out. For comparing the effect of these input parameters, a ground truth that can be described perfectly by the governing equation has to be available, but this may not exist yet, and thus, the experimental results presented in Fig. 3.12b are selected as the reference.

Fractal dimension (n_f): It has been used to estimate the shape of a particle/floc. A good understanding of n_f and floc size, can determine floc density, floc strength, floc settling velocity, etc. However, it is difficult to observe n_f directly and usually an indirect approach is selected. By carrying out an experiment (e.g., in a small settling column) to measure the size L and the settling velocity w_s of a floc, its n_f can be estimated from a modified Stokes

equation, e.g., $w_s = \frac{1}{18} \frac{(\rho_s - \rho_w)g}{\mu} L_p^{3-n_f} L^{n_f-1}$ (where ρ_s is the density of clay mineral, ρ_w is

the density of fluid, g is gravitational acceleration, and μ is dynamic viscosity of the fluid, see Winterwerp, 1998). However, it is worth to mention that even for flocs with the same size, the reversely estimated n_f may be different because of different settling velocities, since flocs might not be self-similar at all. This means the modeling of n_f itself is a difficulty. Most recent studies usually assume n_f as a constant based on empirical understanding (Winterwerp, 1998), or modeled as exponential functions (Maggi et al., 2007) based on the knowledge that larger flocs are more fragile than small flocs, and thus, large flocs have a low n_f . Steady state PSD predictions for different n_f (does not matter it is a constant or varies with size) did not show significant differences (Fig. 3.13b). For modeling mean size of PSD, however, different n_f produce different mean sizes (Fig. 3.13a), regardless of whether it is a different constant n_f or a different d_L . If a floc does have the property of self-similarity, this result implies that the aggregation parameter C_1 , as well as the breaking fitting parameter C_2 , is also a function of n_f , which is understandable since they are affected by particle structures.

Primary particle size (l_p): It is usually assumed l_p is a small constant, but how small it should be has not been checked yet. l_p itself may have a different size and has a distribution itself. Results show different primary particle sizes will lead to significantly different predictions of both PSDs and their mean sizes (Fig. 3.14). This is not surprising since particles with larger sizes but with the same aggregation kernel (i.e., collision frequency and collision efficiency) will result in larger mean sizes of PSD. It also implies that even in the same system, the calibration results of C_1 based on significantly different l_p assumptions cannot be compared directly.

One advantage for this PBE–QMOM approach is that a primary particle distribution, if available, can be easily included in the model. As shown in Fig. 3.14, a normal distribution of primary particles with a mean size of 5 μm (median and mode sizes are also 5 μm , and the size range is 0.1–10 μm) will lead to a larger mean size at steady state when compared with a single primary particle with a size of 5 μm . It is also shown that different variances, e.g., $\sigma^2 = 0.25, 1, \text{ and } 4$, will yield close predictions on both the mean sizes and the PSDs at steady state, with a larger variance corresponding to a slightly slower convergence speed. In the current model setting, particles with sizes larger than either a single l_p or the mean size of the primary particle distribution, are allowed to break up.

Absolute values of C_1 & C_2 : If a different C_1 and C_2 are selected, but keeping the same ratio of C_1/C_2 , the pace that it converges to steady state will be different. Results (Fig. 3.15) show that a large C_1 will reach steady state faster than if a small C_1 is used. This result is similar to that given by Keyvani and Strom (2014). They used almost identical primary particle sizes, and a similar C_1/C_2 ratio, but different C_1 and C_2 , to simulate mud flocculation with different histories (e.g., in their study, cycles “ps1” and “ps6”). This is probably one of the reasons why a large C_1 (close to 1) is selected in some literature when only the measured steady state PSD is available for comparison (Maggi et al., 2007; Mietta et al., 2008; Shen and Maa, 2015). For instances when calibrations are based on minimizing the differences of simulated and experimental steady state PSDs using a two-parameter (i.e., C_1 & C_2) fitting, the converged absolute values of C_1 and C_2 might not be the true values because the rate of convergence is excluded. Without knowing the convergence rate, only a correct C_1/C_2 can be

found. This is not to say, however, that a large C_1 is not possible. For a rapid aggregation, a large C_1 , sometimes, larger than one is possible from a physical point of view (Furukawa and Watkins, 2012; Shen and Maa, 2015).

Fragmentation distribution functions: It is difficult to observe the daughter size distribution after a parent floc breaks up. Therefore, the simplest assumption, binary breakup (1:1 breakup, Eq. 3.29c), is adopted in the simulation of PBE of cohesive sediment flocculation (Shen and Maa, 2015). Other possible breakup mechanisms such as uniform breakup (Eq. 3.25) and ternary breakup (Eq. 3.34, which describes a larger particle with volume λ^3 breaking up into three particles: two particles with volume $\lambda^3/4$, one particle with volume $\lambda^3/2$, and zero for others)

$$b(L|\lambda) = \begin{cases} 1 & L = \lambda \cdot (1/2)^{1/3} \\ 2 & L = \lambda \cdot (1/4)^{1/3} \\ 0 & \text{otherwise} \end{cases} \quad (3.34)$$

are available and tested. After substituting those distributions into Eq. 3.5, the integrated daughter fragmentation distribution functions for binary breakup, uniform breakup, and ternary breakup are expressed in Eq. 3.29d, Eq. 3.26, and Eq. 3.35, respectively.

$$\bar{b}_i^{(k/q)}(L) = L^{k/q} \left(2^{-\frac{k}{3q}} + 2^{1-\frac{2k}{3q}} \right) \quad (3.35)$$

Results show that model predictions are sensitive to the selection of $\bar{b}_i^{(k/q)}$ (Fig. 3.16). Using binary breakup, the model results show the largest prediction of mean size and high peak of PSD. Using the ternary breakup, the model result shows the smallest predicted mean size and a smaller peak of PSD. Results from using the uniform breakup show that the mean size and peak of PSD are between those given by using binary and ternary assumptions, and a

wider distribution span than the other two functions.

To match the referenced mean size (36.7 μm) for a different $\bar{b}_i^{(k/q)}$, the ratio of C_1/C_2 has to be changed. If fixing $C_1 = 0.85$ and decreasing the breakup parameter C_2 , the simulated mean size can be increased. The best fitting result is $C_2 = 2.2 \times 10^{-5}$ for uniform breakup, $C_2 = 1.3 \times 10^{-5}$ for ternary breakup (Fig. 3.16). It seems that using the uniform breakup gives a much better match of a PSD (Fig. 3.16b). Even using the ternary breakup shows a better agreement on the PSD prediction than the one that uses the binary breakup (Fig. 3.16a and Fig. 3.13b). This is different from that presented in Mietta et al. (2008)'s result that shows ternary breakup gives the worst prediction of the PSD.

The simulated steady state median sizes, however, show a different story: the median size predicted by binary breakup (26.7 μm) is closest to the experimental result (27.2 μm), compared with that given by ternary breakup assumption (24.5 μm) and uniform breakup assumption (22.5 μm). It is critical to notice that $\bar{b}_i^{(k/q)}$ may vary for different hydrodynamic environments and floc structures. For this reason, determining a better selection of the fragmentation distribution function has to wait until a better understanding of floc structures under the associated hydrodynamic environments is available.

Number of nodes: PSDs are predicted using 2, 3, 4, 5, and 7 nodes respectively. Results show that two or three nodes are not sufficient to find a reasonable PSD directly, despite that their representative mean diameters are still tracked excellently. Although four nodes appear to be the minimum for this case, only when using seven nodes can the PSD provide clear evidence on the existence of large flocs (Fig. 3.18). For a complicated PSD with multi-peaks, however,

seven nodes are insufficient and using more nodes or more novel moments' inversion technology is necessary. It also confirms that these automatic selected nodes in QMOM will span wider by tracking more size classes.

5. Discussion

The original objective of solving PBE using QMOM is not for tracking the PSD directly because the PSD information (represented as its number density, volume fraction, and various characteristic mean sizes) is stored in its moments. It is important, however, to explore whether QMOM can be used to interpret changes of the PSD itself. This is because for most applications with unimodal or even multimodal distributions, a directly and uniquely constructed PSD could give more information when compared with those relying on their integral moments.

At this stage, using QMOM to study cohesive sediment dynamics should be a good choice because of the fast computing pace and reasonable accuracy to represent the simple PSD in natural environments. Connecting with any currently available hydrodynamic and sediment transport models is feasible because of the low computing power requirement. This will provide a solid base to calculate the settling velocity of flocs, and improve the reliability of simulating cohesive sediment transport.

Current understanding of the aggregation and breakage kernels for cohesive sediments is limited. The poor understanding of the use of the fractal dimension is another limitation. Measurements of the primary particle size distributions, fractal dimensions, and floc size distributions in natural environments are also rare. All these limitations make the

improvement of the accuracy of QMOM unwarranted. Only after a better understanding of these processes and a better measurement technique have been developed will it be time to consider improvements for high accuracy. A few recent studies carried out by chemical scientists on improving model accuracy are good examples, such as spline-based methods (resolving PSDs based on linear, quadratic, or cubic splines, see John et al., 2007, de Souza et al., 2010, and Mortier et al., 2014), the weighted-residual method (resolving PSDs based on the generalized moments, see Lage, 2011), the extended QMOM (resolving PSDs by a sum of non-negative weight functions, see Yuan et al., 2012), and the differential maximum entropy method (resolving PSDs based on maximizing the Shannon's entropy to recover the most possible PSD, see Attarakih and Bart, 2014). At the time when the flocculation mechanisms are clear, however, the computational ability and variable precision might be sufficient to handle the high requirement on small round off errors when using QMOM, so that more size classes might be tracked even using the classical QMOM.

6. Conclusions

The following are conclusions for this study:

(1) The Quadrature Method Of Moments (QMOM) is applied to solve the size-based population balance equation for a few well studied systems. The simulated PSD results match well with the analytical (or trusted class method) solutions. In these cases, the maximum relative error for the directly tracked moments is typically smaller than 10^{-4} .

(2) The results for simulated PSD and its mean and median size for suspended kaolinite with a concentration of 0.52 g/L and a shear rate of 45 s^{-1} in a five liter mixing chamber also show a reasonable agreement.

(3) Assumptions of fractal dimensions n_f (either constant or variable n_f), primary practice sizes l_p (either a single representative size l_p , or a size distribution with its mean/median value l_p), and fragmentation distribution functions $\bar{b}_i^{(k)}$ will significantly influence the model predictions, and should be clearly specified in every model.

(4) It is difficult to make a perfect choice for the breakup distribution function. Binary breakup, ternary breakup, or uniform breakup are all possible and each may perform better in different areas. At the current stage, the binary breakup distribution is suggested because of its simplicity; nevertheless, the selection of this parameter should be checked carefully for different applications.

(5) The prediction of the steady state PSD as well as its representative size is only determined by the ratio of aggregation and breakup parameter C_1/C_2 . A better understanding of the flocculation rate is necessary to find the absolute value of C_1 and C_2 .

(6) Four nodes in QMOM appears the minimum to represent a single peak PSD, with a limitation on a small span of floc size distribution. With seven or eight nodes, the range of the floc size distribution can be extended. To simulate PSD with bi-modal or tri-modal distribution, more nodes are necessary and that will be a target for future research.

Acknowledgments

We would like to acknowledge VIMS (Virginia Institute of Marine Science) Student Research Grant, CSC (China Scholarship Council) Scholarship, a Grant (No. 774080) from KIOST (Korea Institute of Ocean Science and Technology), the State Key Program of National Natural Science of China (Grant No. 41230640 & 51339005), and the National Natural Science Foundation of China (Grant No. 51409081). The author would also like to thank Mr. D. Kaufman for helping review the English.

List of global symbols

- a breakup kernel (aka “breakup frequency function”)
- b fragmentation distribution function (aka “daughter distribution function”)
- $\bar{b}^{(k)}$ k th moment of fragmentation distribution function
- C_1 aggregation fitting parameter
- C_2 breakage fitting parameter
- d_{10} arithmetic mean size
- d_{32} Sauter mean size
- d_{43} De Broukere mean size
- D_{50} number-based median size
- F_y floc yield strength
- G tank averaged shear rate
- l_p primary particle size
- L particle size
- L_i nodes in the Gaussian approximation; characteristic sizes in PSD
- m_k k th order moment of the PSD
- n number density function
- nf fractal dimension of flocs
- N number of nodes in the Gaussian quadrature approximation
- N_0 initial number density, i.e., $m_0 (t = 0)$
- q adjustable factor
- t time
- x location in physical space (external coordinate in the particle state vector)

Greek letters

β aggregation kernel including collision frequency and collision efficiency

μ dynamic viscosity of fluid

ξ properties of particle (internal coordinate in the particle state vector)

ω_i weights in the Gaussian approximation; characteristic number densities in PSD

References

- Attarakih, M., Bart, H.J., 2014. Solution of the population balance equation using the Differential Maximum Entropy Method (DMaxEntM): An application to liquid extraction columns. *Chemical Engineering Science* 108, 122–133.
- Barrett, J.C., Webb, N.A., 1998. A comparison of some approximate methods for solving the aerosol general dynamic equation. *Journal of Aerosol Science* 29, 31–29.
- de Souza, L.G.M., Janiga, G., John, V., Thevenin, D., 2010. Reconstruction of a distribution from a finite number of moments with an adaptive spline-based algorithm. *Chemical Engineering Science* 65, 2741–2750.
- Frappier, G., Lartiges, B.S., Skali-Lami, S., 2010. Floc cohesive force in reversible aggregation: A Couette laminar flow investigation. *Langmuir* 26, 10475–10488.
- Friedlander, S.K., 2000. Smoke, dust, and haze: Fundamentals of aerosol dynamics, second ed., Oxford University Press, New York.
- Furukawa, Y., Watkins, J.L., 2012. Effect of organic matter on the flocculation of colloidal montmorillonite: A modeling approach. *Journal of Coastal Research* 28, 726–737.
- Gelbard, F., Seinfeld, J.H., 1978. Numerical solution of the dynamic equation for particulate systems. *Journal of Computational Physics* 28, 357–375.
- Gimbun, J., Nagy, Z.K., Rielly, C.D., 2009. Simultaneous quadrature method of moments for the solution of population balance equations, Using a differential algebraic equation framework. *Industrial and Engineering Chemistry Research* 48, 7798–7812.
- Hulburt, H.M., Katz, S., 1964. Some problems in particle technology: A statistical mechanical formulation. *Chemical Engineering Science* 19, 555–574.

- John, V., Angelov, I., Oncul, A.A., Thevenin, D., 2007. Techniques for the reconstruction of a distribution from a finite number of its moments. *Chemical Engineering Science* 62, 2890–2904.
- John, V., Thein, F., 2012. On the efficiency and robustness of the core routine of the quadrature method of moments (QMOM). *Chemical Engineering Science* 75, 327–333.
- Kapur, P.C., Fuerstenau, D.W., 1969. A coalescence model for granulation. *Industrial & Engineering Chemistry Process Design and Development* 8, 56–62.
- Kariwala, V., Cao, Y., Nagy, Z.K., 2012. Automatic differentiation-based quadrature method of moments for solving population balance equations. *AIChE Journal* 58, 842–854.
- Keyvani, A., Strom, K., 2014. Influence of cycles of high and low turbulent shear on the growth rate and equilibrium size of mud flocs. *Marine Geology* 354, 1–14.
- Khelifa, A., Hill, P.S., 2006. Models for effective density and settling velocity of flocs. *Journal of Hydraulic Research* 44, 390–401.
- Kumar, J., 2006. Numerical approximation of population balance equations in particulate systems. Ph.D. dissertation, Otto von Guericke University Magdeburg, Germany.
- Lage, P.L.C., 2011. On the representation of QMOM as a weighted-residual method-The dual-quadrature method of generalized moments. *Computers and Chemical Engineering* 35, 2186–2203.
- Lee, B.J., Toorman, E., Molz, F.J., Wang, J., 2011. A two-class population balance equation yielding bimodal flocculation of marine or estuarine sediments. *Water Research* 45, 2131–2145.

- Maggi, F., Mietta, F., Winterwerp, J.C., 2007. Effect of variable fractal dimension on the floc size distribution of suspended cohesive sediment. *Journal of Hydrology* 343, 43-55.
- Marchisio, D.L., Pikturna, J.T., Fox, R.O., Vigil, R.D., Barresi, A.A., 2003a. Quadrature method of moments for population-balance equations. *AIChE Journal* 49, 1266–1276.
- Marchisio, D.L., Vigil, R.D., Fox, R.O., 2003b. Quadrature method of moments for aggregation-breakage processes. *Journal of Colloid and Interface Science* 258, 322–334.
- Marchisio, D.L., Vigil, R.D., Fox, R.O., 2003c. Implementation of the quadrature method of moments in CFD codes for aggregation-breakage problems. *Chemical Engineering Science* 58, 3337–3351.
- Marshall, C.L., 2012. Multi-component population balance modeling of wet granulation via constant-number Monte Carlo. Ph.D. dissertation, Pennsylvania State University, United States.
- McCoy, B.J., Madras, G., 2003. Analytical solution for a population balance equation with aggregation and fragmentation. *Chemical Engineering Science* 58, 3049–3051.
- McGraw, R., 1997. Description of aerosol dynamics by the quadrature method of moments. *Aerosol Science and Technology* 27, 255–265.
- Mehta, A.J., 2013. An introduction to hydraulics of fine sediment transport. World Scientific Publishing Company.
- Mietta, F., Maggi, F., Winterwerp, J.C., 2008. Chapter 19: Sensitivity to breakup functions of a population balance equation for cohesive sediments. *Sediment and Ecohydraulics 9* (INTERCOH 2005), 275–286.

- Mortier, S.T.F.C., De Beer, T., Gernaey, K., Nopen, I., 2014. Comparison of techniques for reconstruction of a distribution from moments in the context of a pharmaceutical drying process. *Computers and Chemical Engineering* 65, 1–8.
- Mugele, R.A., Evans, H.D., 1951. Droplet size distribution in sprays. *Industrial and Engineering Chemistry* 43, 1317–1324.
- Peng, S.J., Williams, R.A., 1994. Direct measurement of floc breakage in flowing suspensions. *Journal of Colloid and Interface Science* 166, 321–332.
- Prat, O.P., Ducoste, J.J., 2006. Modeling spatial distribution of floc size in turbulent processes using the quadrature method of moment and computational fluid dynamics. *Chemical Engineering Science* 61, 75–86.
- Ramkrishna, D., 2000. Population balances: Theory and applications to particulate systems in engineering. Academic Press, San Diego.
- Ramkrishna, D., Singh, M.R., 2014. Population balance modeling: Current status and future prospects. *Annual Review of Chemical and Biomolecular Engineering* 5, 123–146.
- Scott, W.T., 1968. Analytic studies of cloud droplet coalescence I. *Journal of the Atmospheric Sciences* 25, 54–65.
- Serra, T., Colomer, J., Logan, B.E., Efficiency of different shear devices on flocculation. *Water research* 42, 1113–1121.
- Shen, X., Maa, J.P.Y., 2015. Modeling floc size distribution of suspended cohesive sediments using quadrature method of moments, *Marine Geology* 359, 106–119.
- Shen, X., Maa, J.P.Y., *Submitted*. A camera and image processing system for floc size distributions of suspended particles.

- Shin, H.J., Son, M., Lee, G.H., 2015. Stochastic flocculation model for cohesive sediment suspended in water. *Water* 7, 2527–2541.
- Smoluchowski, M., 1917. Versuch einer mathematischen theorie der koagulationskinetik kolloider lösungen. *Zeitschrift für Physikalische Chemie* 92, 129-168. (in German)
- Son, M., Hsu, T.J., 2008. Flocculation model of cohesive sediment using variable fractal dimension. *Environmental Fluid Mechanics* 8, 55-71.
- Son, M., 2009. Flocculation and transport of cohesive sediment. Ph.D. Dissertation, Gainesville: University of Florida.
- Sowa, W.A., 1992. Interpreting mean drop diameters using distribution moments. *Atomization and Sprays* 2, 1–15.
- Sporleder, F., Borka, Z., Solsvik, J., Jakobsen., H.A., 2012. On the population balance equation. *Reviews in Chemical Engineering* 28, 149–169.
- Su, J.W., Gu, Z.L., Li, Y., Feng, S.Y., Xu, X.Y., 2007. Solution of population balance equation using quadrature method of moments with an adjustable factor. *Chemical Engineering Science* 62, 5897–5911.
- Su, J.W., Gu, Z.L., Li, Y., Fen, S.Y., Xu, X.Y., 2008. An adaptive direct quadrature method of moment for population balance equations. *AIChE Journal* 54, 2872–2887.
- Thein, F., 2011. On the efficiency and condition of the core routine of the quadrature method of moments (QMOM). Diploma thesis, Germany: Otto-von-Guericke-Universität Magdeburg.

- Tobin, T., Muralidhar, R., Wright, H., Ramkrishna, D., 1990. Determination of coalescence frequencies in liquid-liquid dispersions: Effect of drop size dependence. *Chemical Engineering Science* 45, 3491–3504.
- Vanni, M., 2000. Approximate population balance equations for aggregation-breakage processes. *Journal of Colloid and Interface Science* 221, 143–160.
- Vigil, R.D., Ziff, R.M., 1989. On the stability of coagulation-fragmentation population balances. *Journal of Colloid and Interface Science* 133, 257–264.
- Winterwerp, J.C., 1998. A simple model for turbulence induced flocculation of cohesive sediment. *Journal of Hydraulic Research* 36, 309–326.
- Xie, M., He, Q., 2013. Analytical solution of TEMOM model for particle population balance equation due to Brownian coagulation. *Journal of Aerosol Science* 66, 24–30.
- Xie, M.L., Wang, L.P., 2013. Asymptotic solution of population balance equation based on TEMOM model. *Chemical Engineering Science* 94, 79–83.
- Yuan, Y., Wei, H., Zhao, L., Cao, Y., 2009. Implications of intermittent turbulent bursts for sediment resuspension in a coastal bottom boundary layer: a field study in the western Yellow Sea, China. *Marine Geology* 263, 87–96.
- Yuan, C., Laurent, F., Fox, R.O., 2012. An extended quadrature method of moments for population balance equations. *Journal of Aerosol Science* 51, 1–23.
- Ziff, R.M., McGrady, E.D., 1985. A kinetics of cluster fragmentation and depolymerisation. *Journal of Physics A: Mathematical and General* 18, 3027–3037.

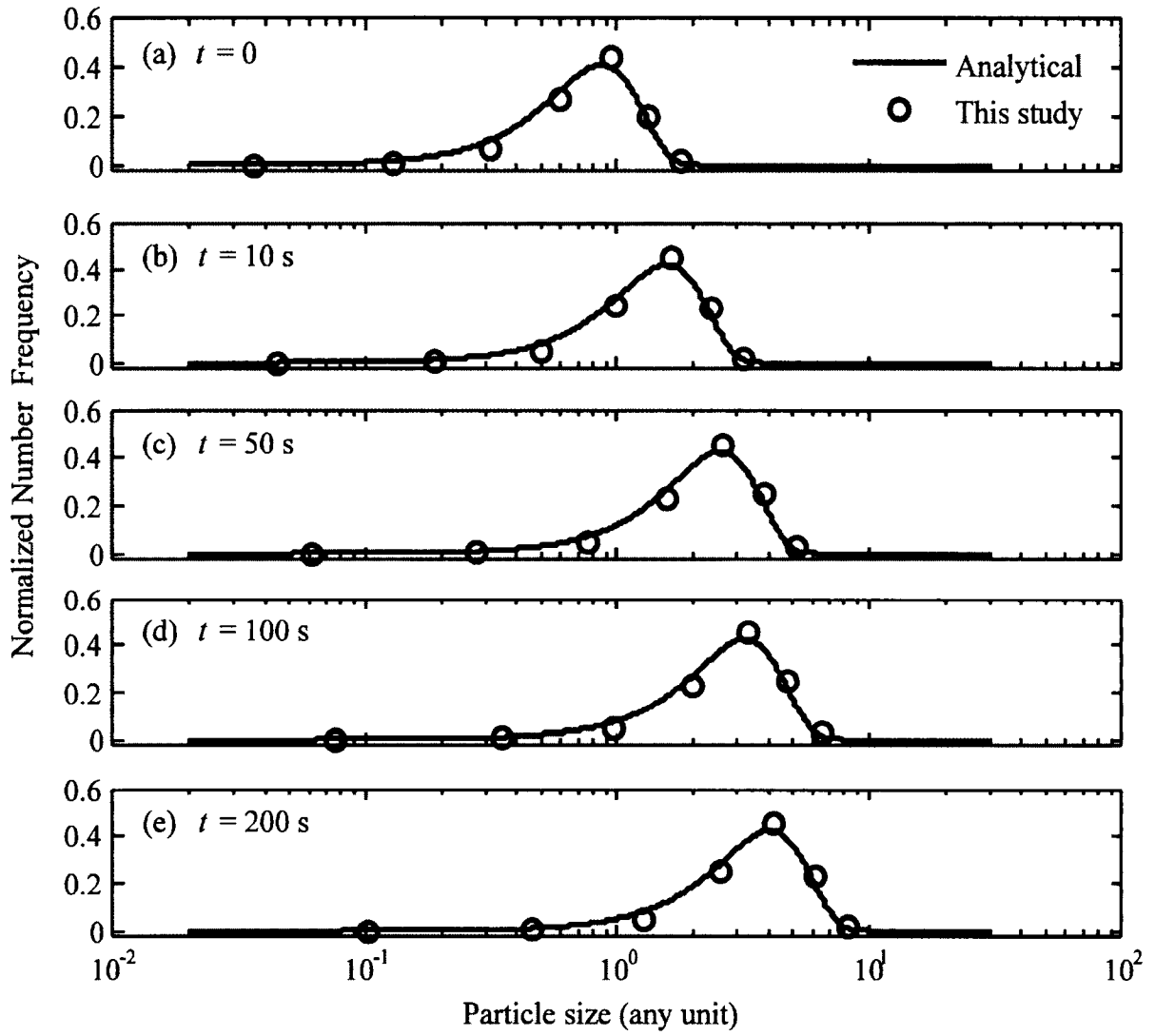


Fig. 3.1 Time evolution of PSDs for the pure coagulation event with a constant coagulation kernel, $\beta_0 = 1$ (Case I).

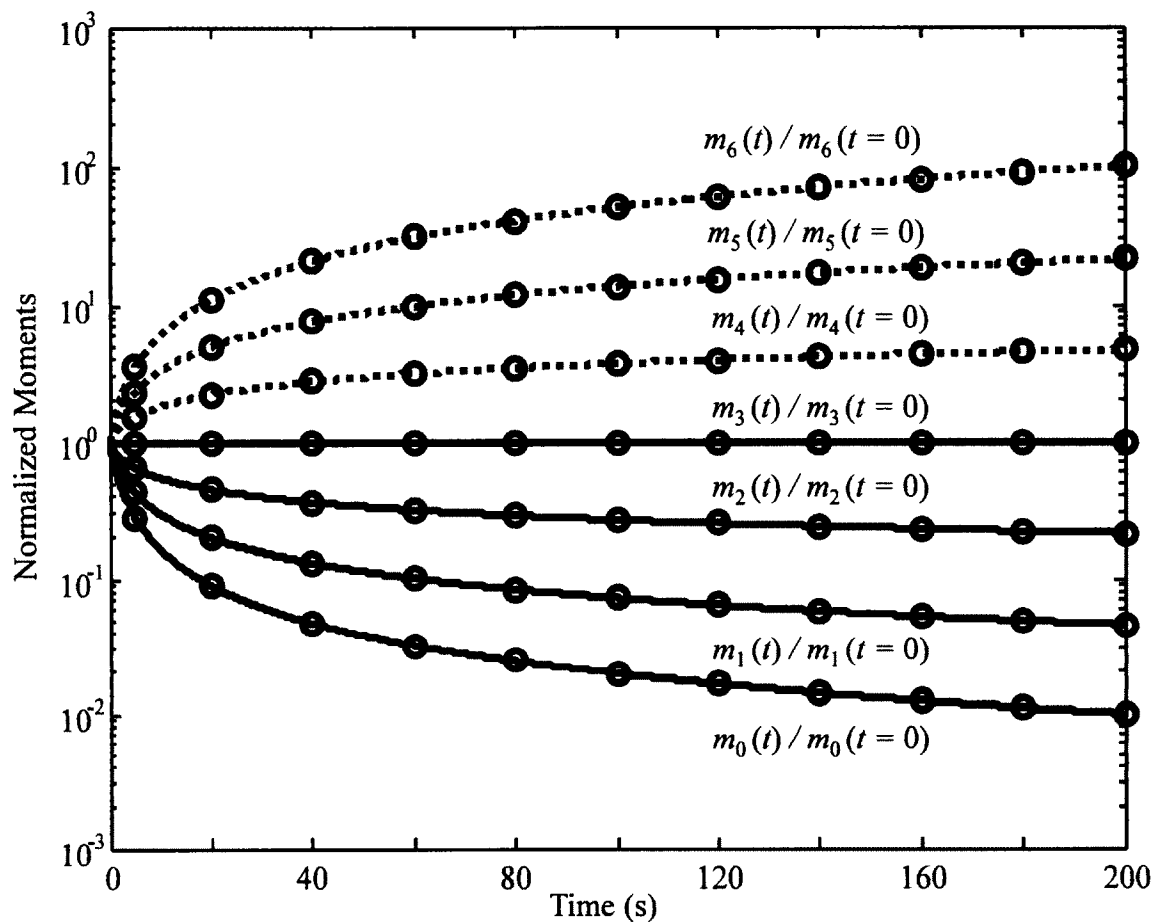


Fig. 3.2 Time evolution of normalized moments for the pure coagulation event with a constant kernel (Case I). Circles are analytical solutions at selected times; solid lines are direct numerical predictions; dashed lines are indirect predictions by using Eq. 3.4.

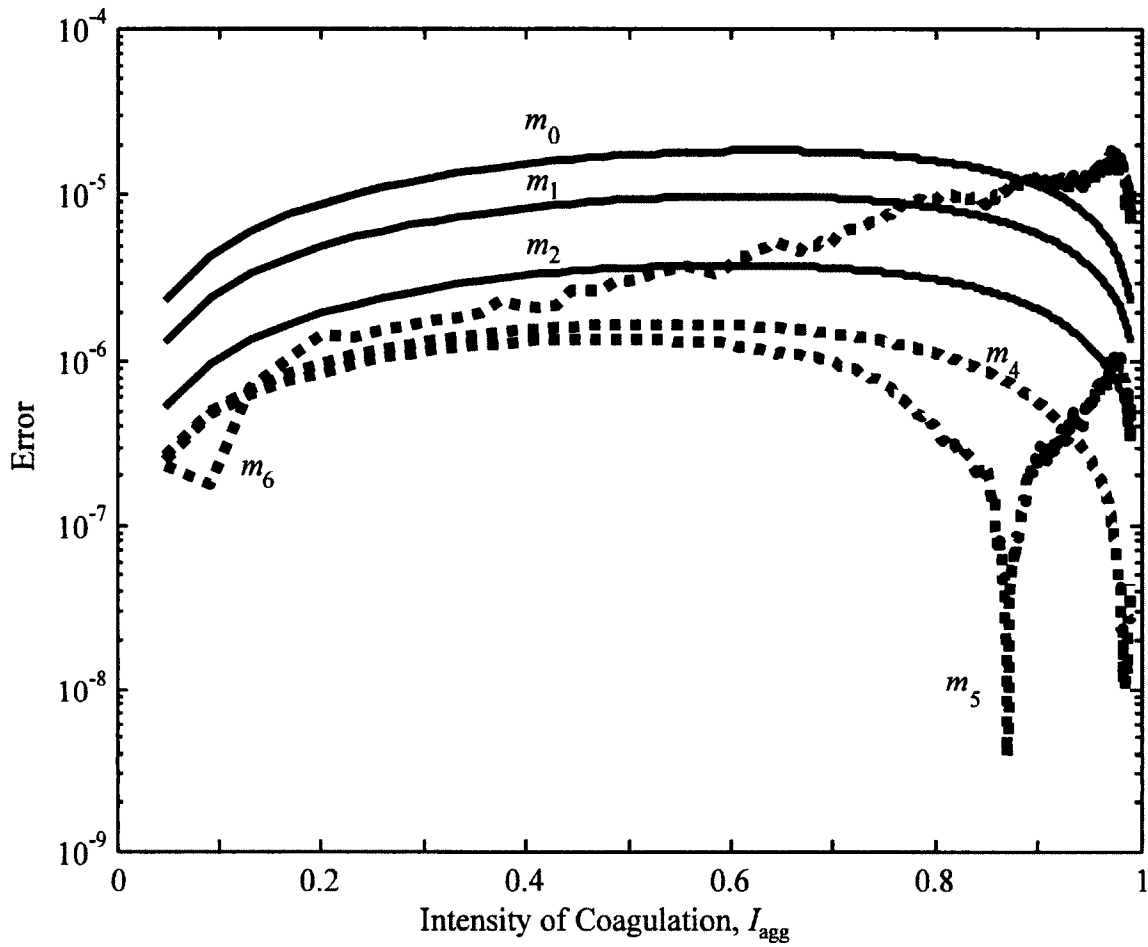


Fig. 3.3 Percentage error for the first seven moments against intensity of coagulation (I_{agg} , see Eq. 3.12 for definition) for the pure coagulation event with a constant kernel (Case I). Solid lines are for the moments that are directly simulated; dashed lines are for the moments that are indirectly calculated by using Eq. 3.4. m_3 is excellently predicted so that the error is not reported.

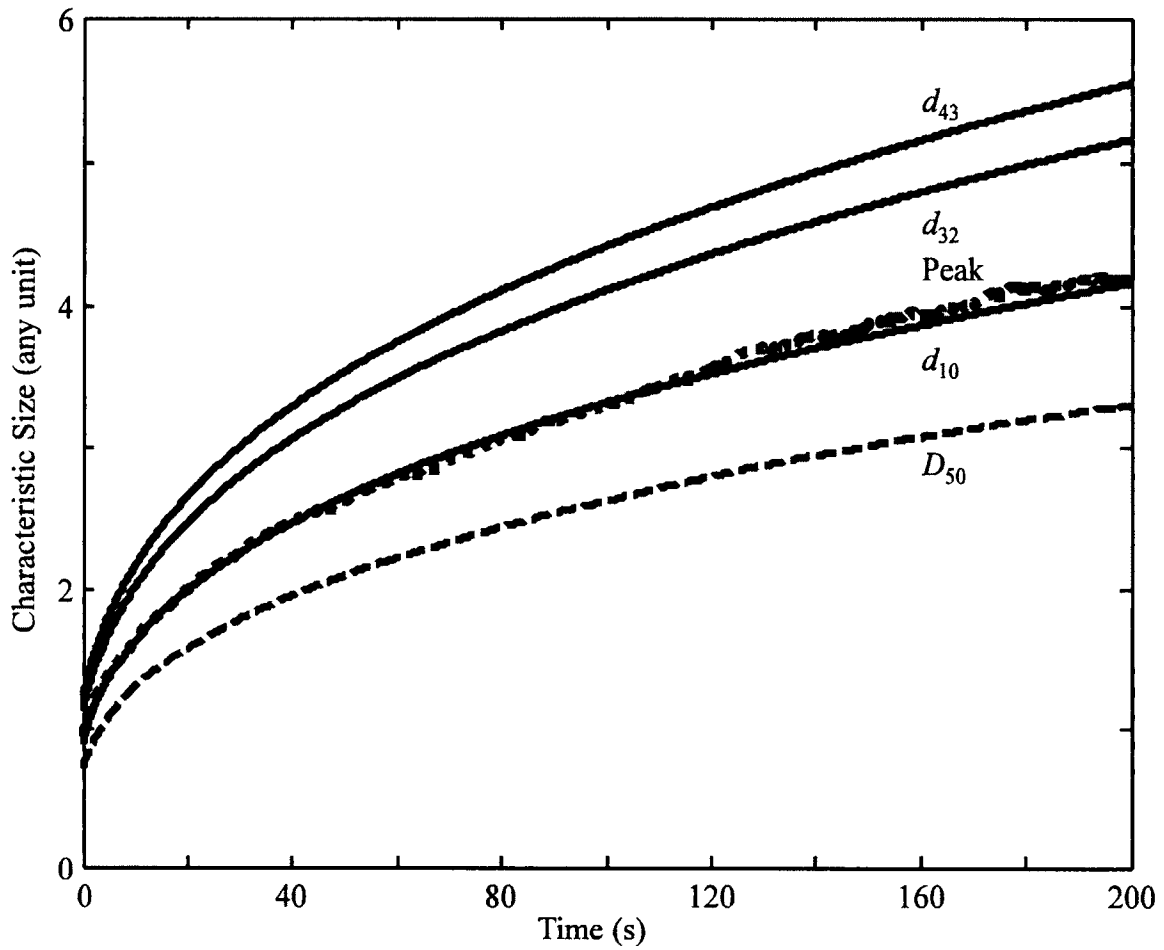


Fig. 3.4 Time evolution of various characteristic sizes for the pure coagulation event with a constant kernel (Case I). Solid lines are for selected mean size (i.e., d_{10} , d_{32} , and d_{43}); the dashed line is the number-based median size (D_{50}); and the dotted line is for mode (or peak) size.

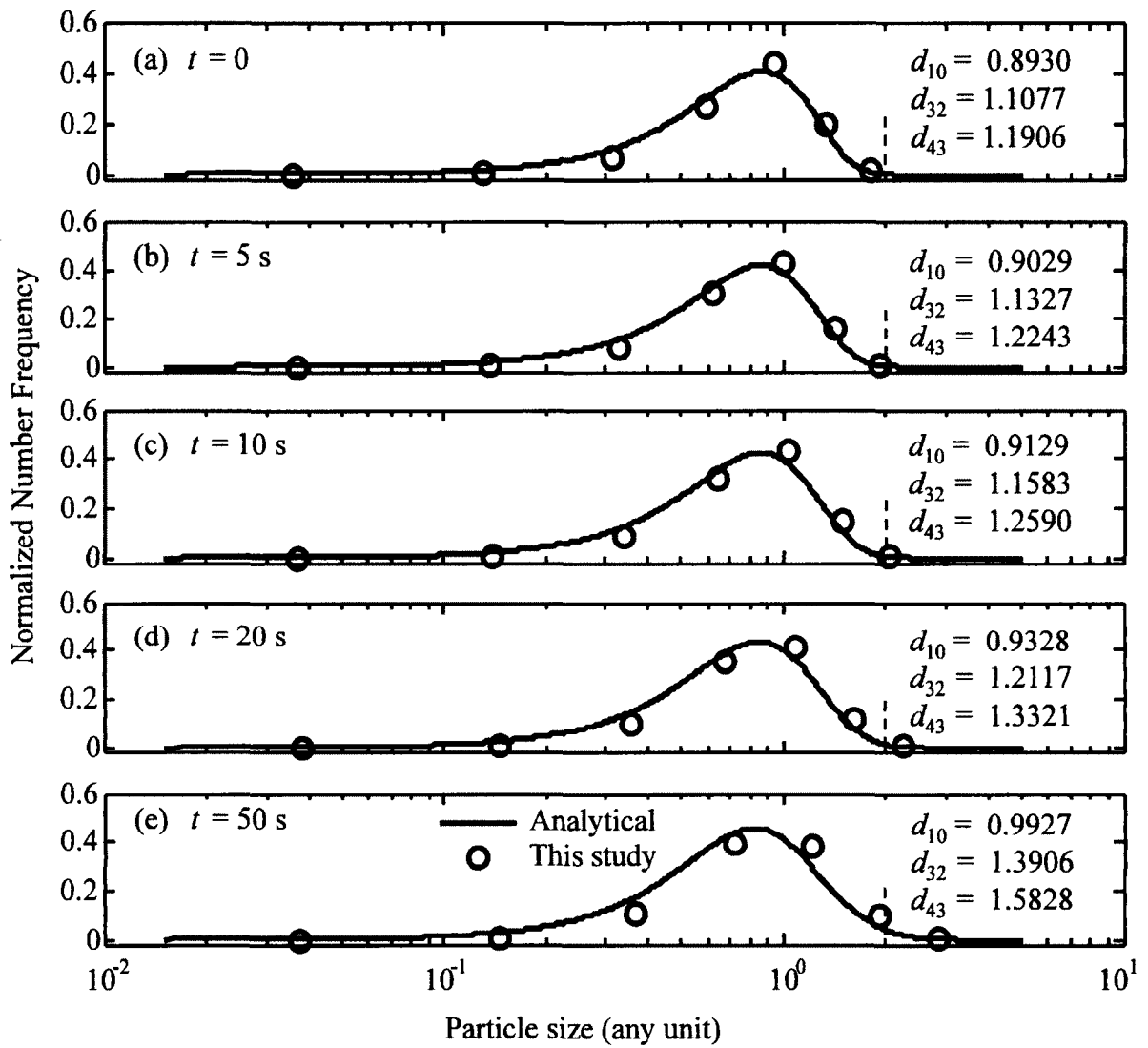


Fig. 3.5 Time evolution of PSDs for the pure coagulation event with sum coagulation kernel (Case II). Solid lines are analytical solutions; circles are numerical model predictions.

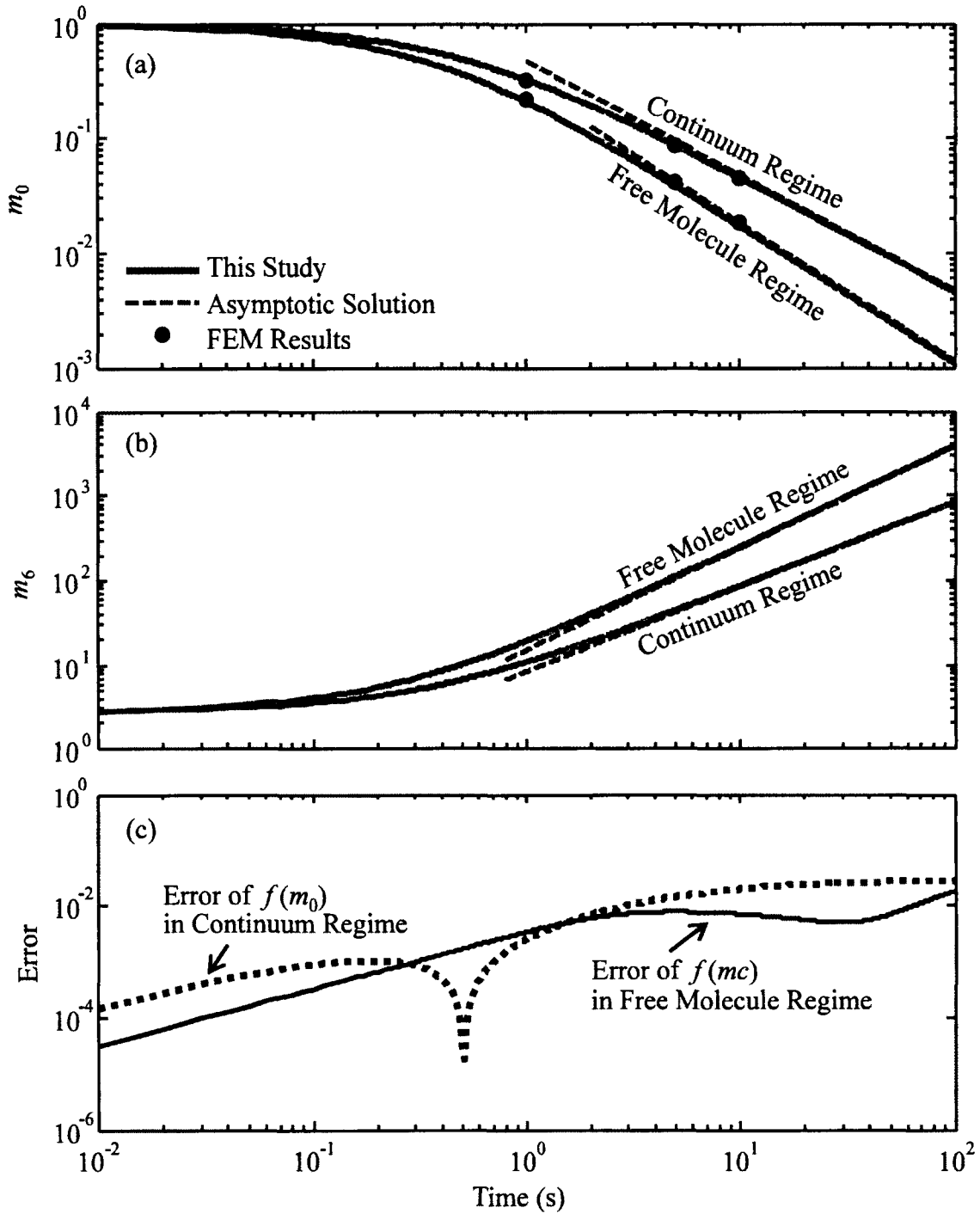


Fig. 3.6 Time evolution of (a) m_0 and (b) m_6 , and (c) relative error of $f_1(m_c)$ (Eq. 3.21a) and $f_2(m_0)$ (Eq. 3.22a) for these two pure coagulation events with different Brownian kernels (Case III).

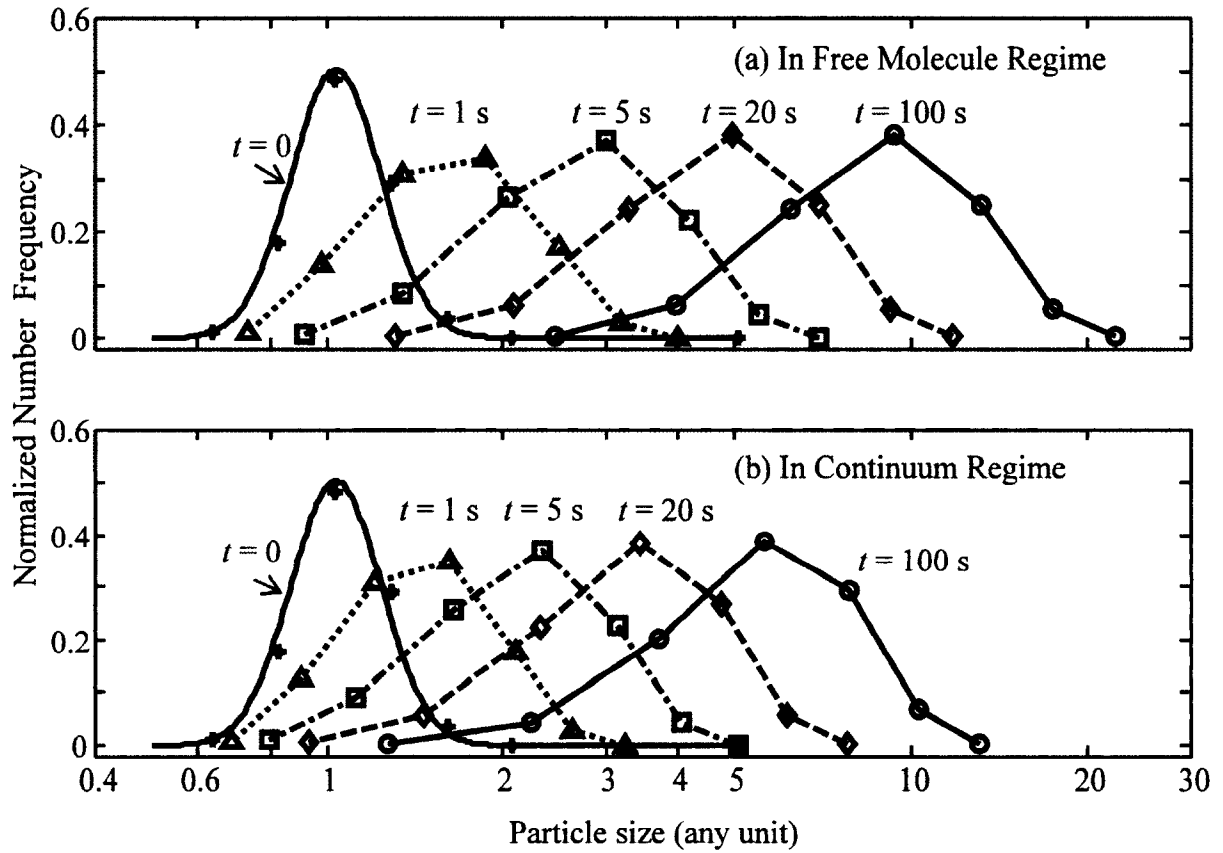


Fig. 3.7 Time evolution of predicted normalized PSDs for these two pure coagulation events with different Brownian kernels (Case III).

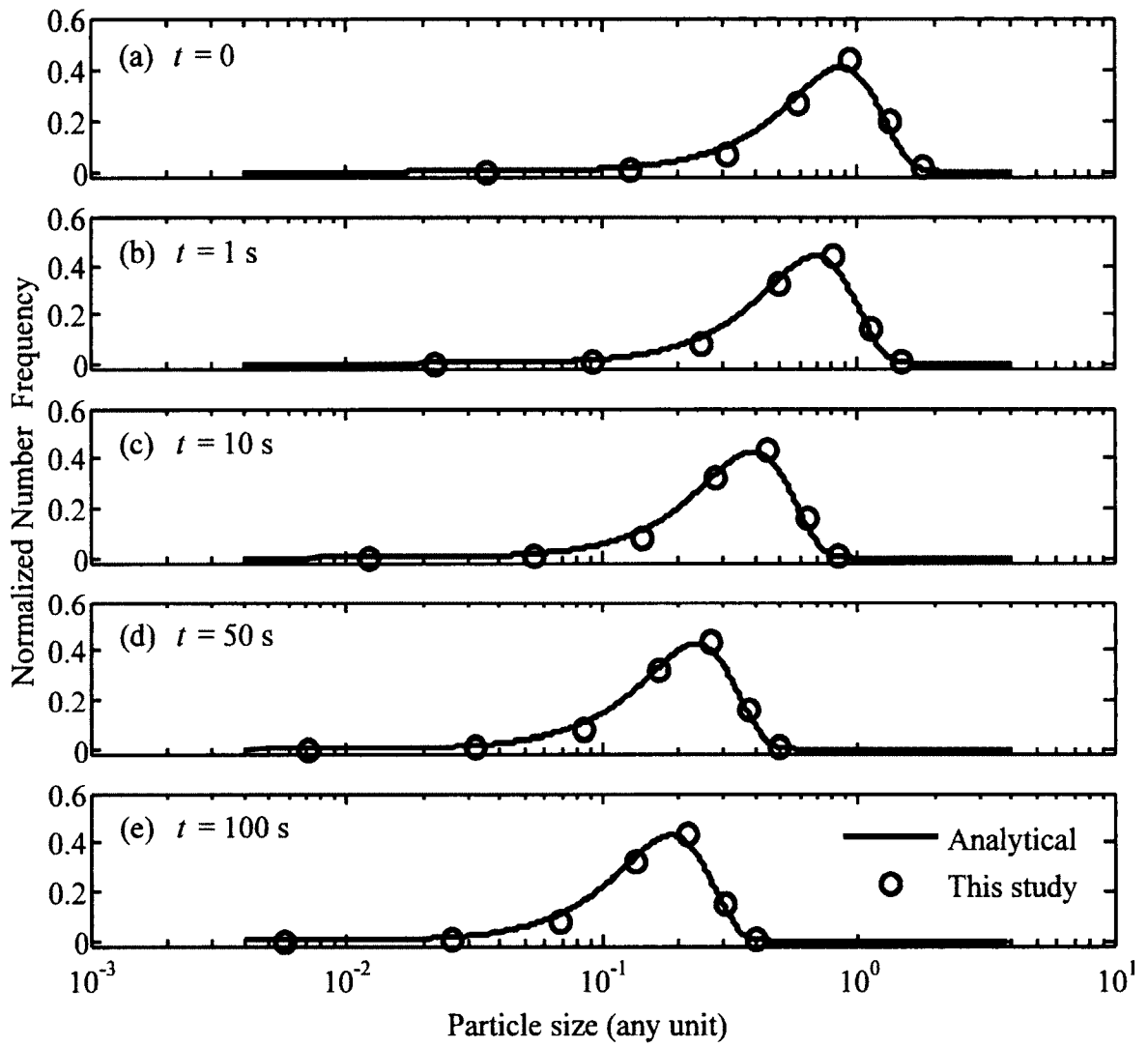


Fig. 3.8 Time evolution of normalized PSDs for the pure breakup event with a power law kernel (Case IV).

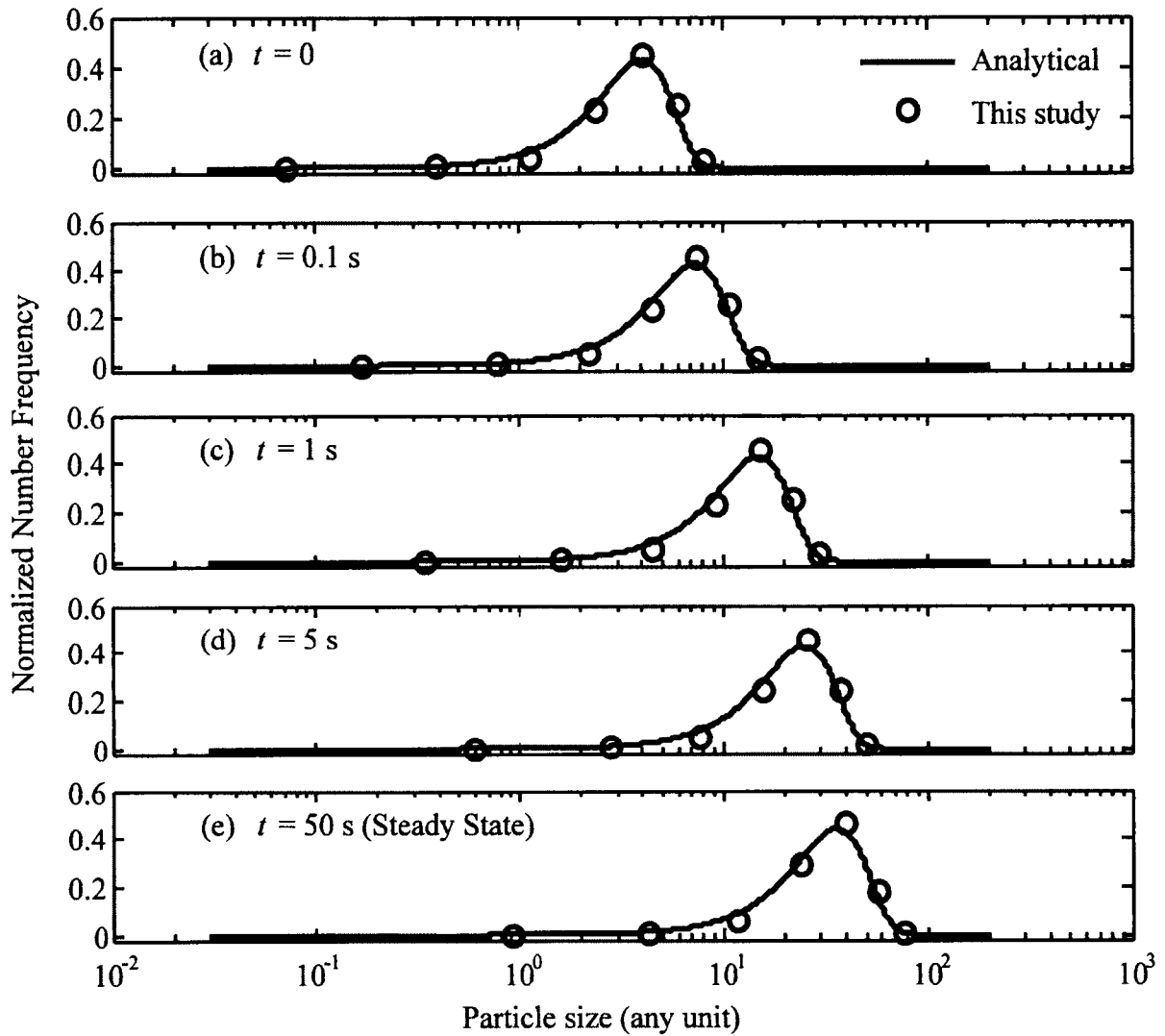


Fig. 3.9 Time evolution of normalized PSDs for the combined coagulation and breakup events with a constant coagulation kernel and a power law breakage kernel (Case V).

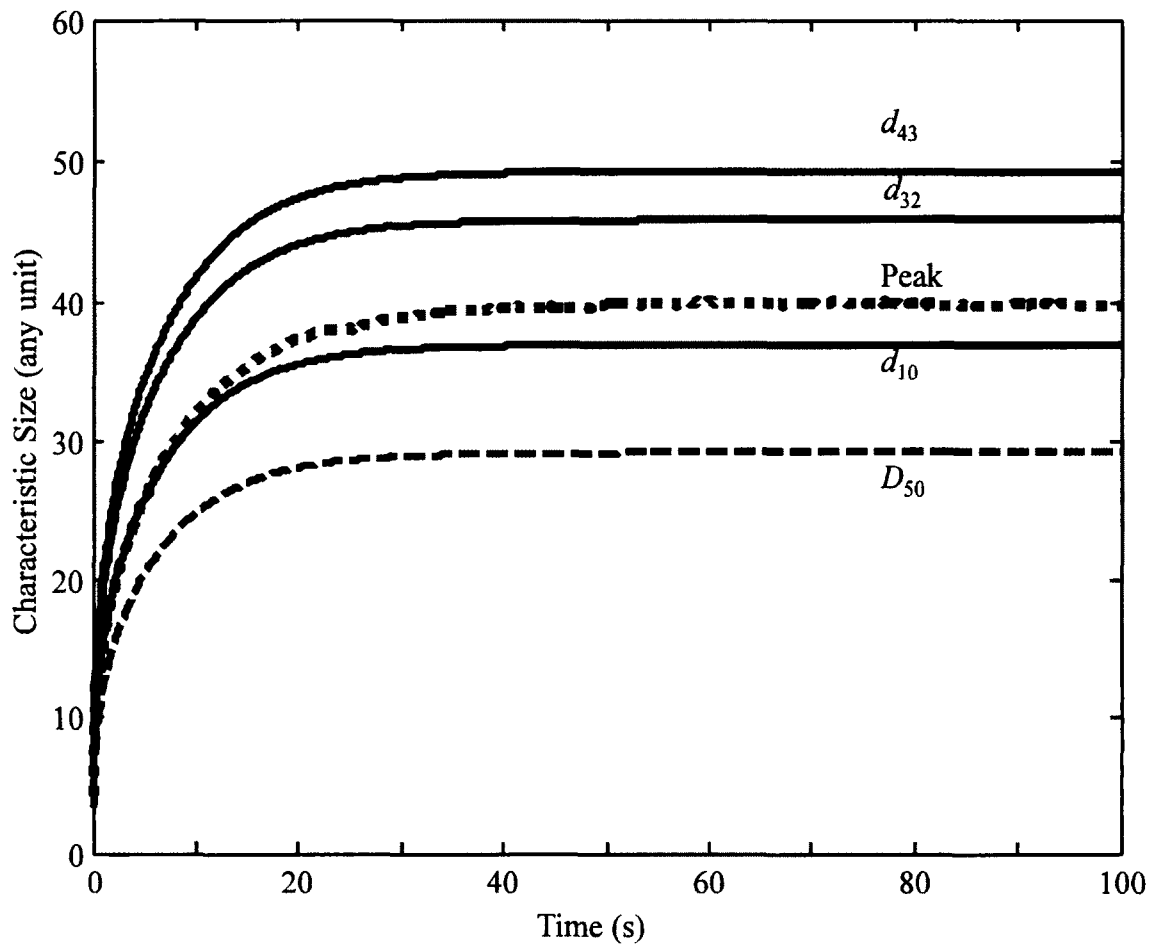


Fig. 3.10 Time evolution of various characteristic sizes for the combined coagulation and breakup events with a constant coagulation kernel and a power law breakage kernel (Case V). Solid lines are for selected mean size (d_{10} , d_{32} , and d_{43}); dashed line is the median size (D_{50}); dotted line is the mode size.

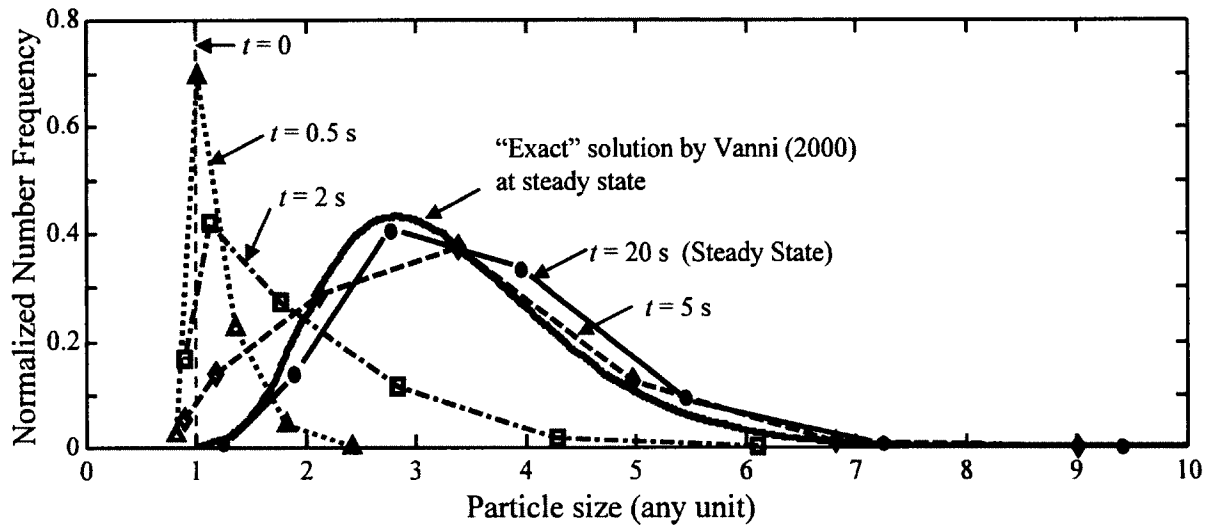


Fig. 3.11 Simulated time evolution of PSDs for Case VI, which includes a sum coagulation kernel, a power breakup kernel, and a binary fragmentation distribution function. The steady state result from Vanni (2000) is also given for a comparison.

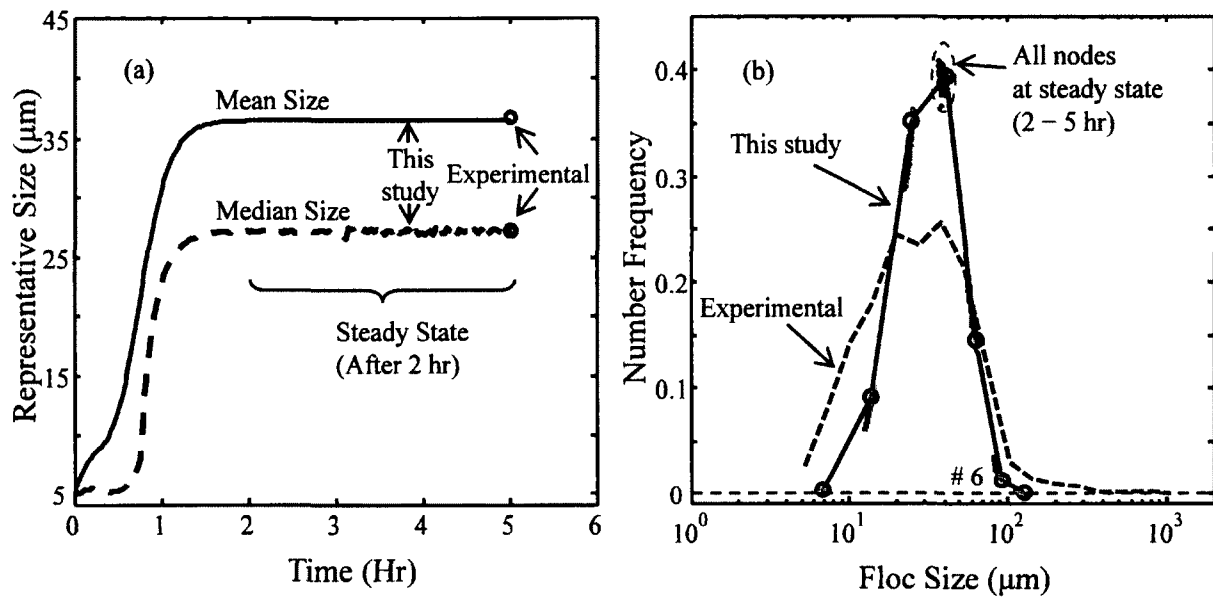


Fig. 3.12 (a) Time evolution of mean and median sizes, and (b) comparison of experimental and predicted steady state PSDs for kaolinite flocculation in a mixing chamber with a suspended sediment concentration of 0.52 g/L and a shear rate of 45 s^{-1} .

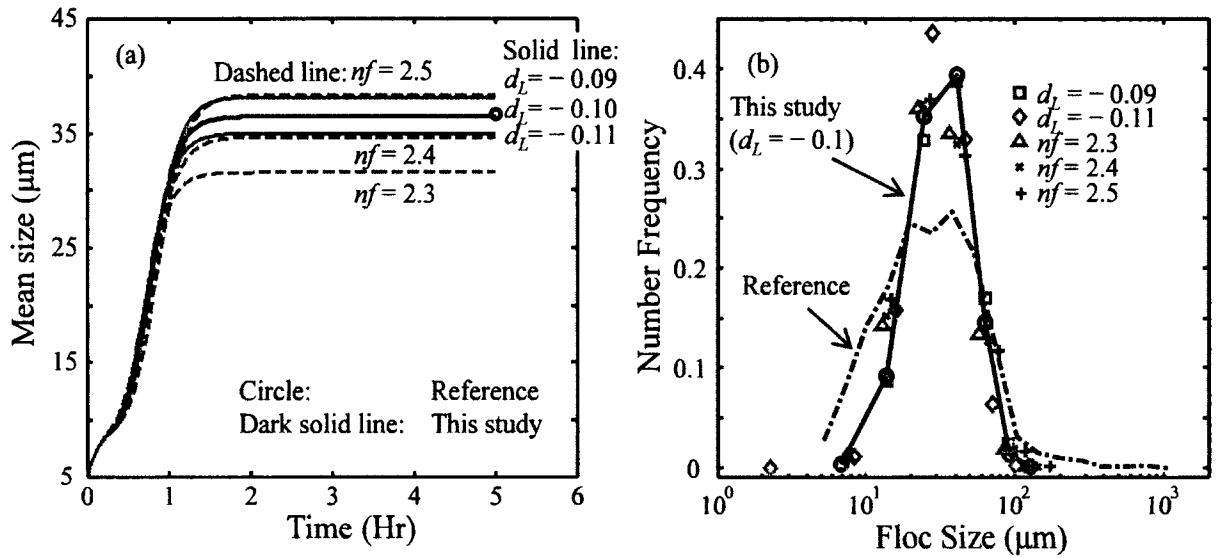


Fig. 3.13 Sensitivity tests for different constant and variable fractal dimensions in the flocculation model for their (a) mean sizes and (b) PSD predictions.

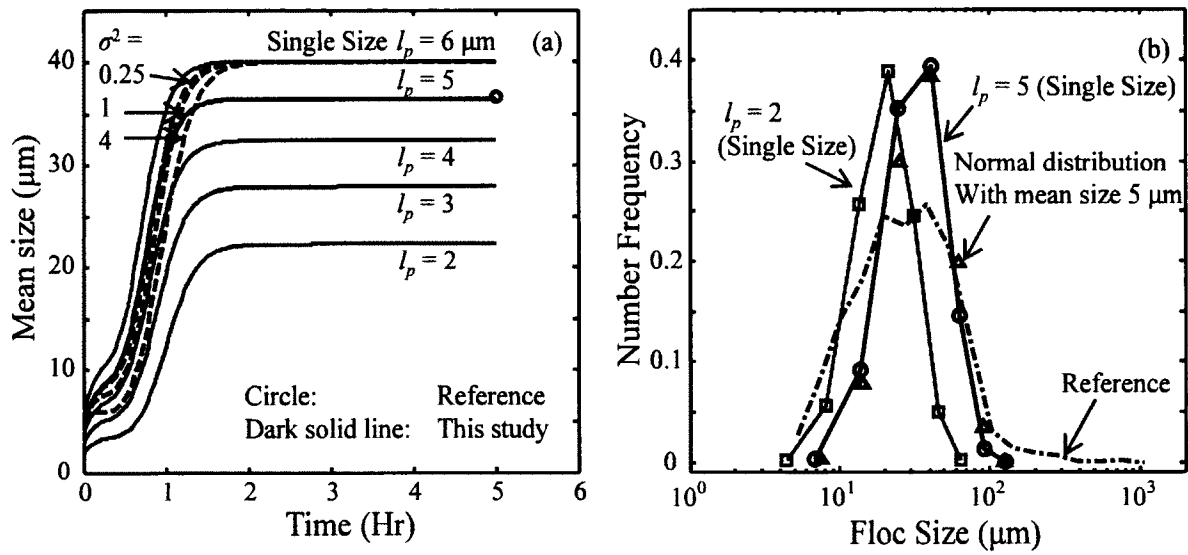


Fig. 3.14 Sensitivity tests for different sizes of primary particles in the flocculation model for their (a) mean sizes and (b) PSD predictions. Dashed lines are for the cases in which primary particles are normal distributions with mean/median size $5 \mu\text{m}$ and various variances.

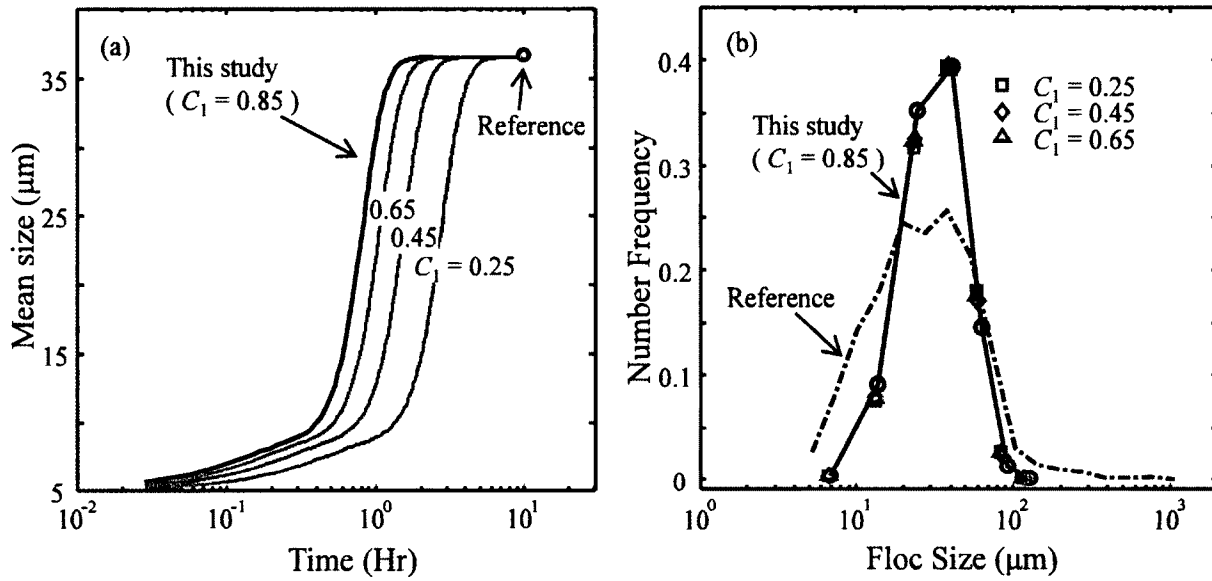


Fig. 3.15 Sensitivity tests for different C_1 and C_2 (with the same ratio of C_1/C_2) in the flocculation model for their (a) mean sizes and (b) PSD predictions.

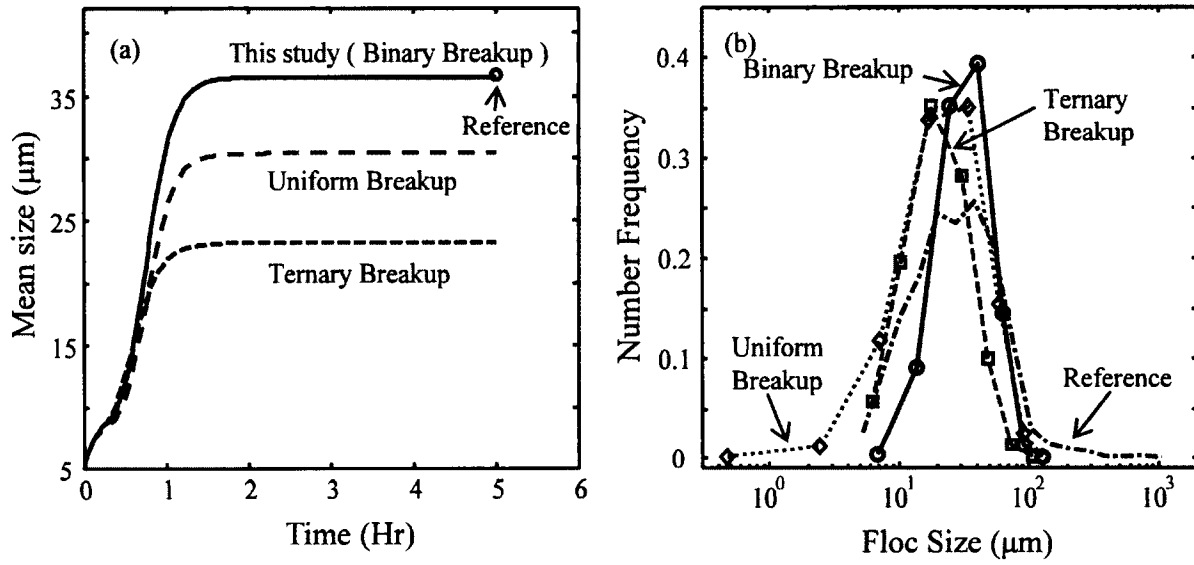


Fig. 3.16 Sensitivity test for different fragmentation distribution functions in the flocculation model for their (a) mean sizes and (b) PSD predictions.

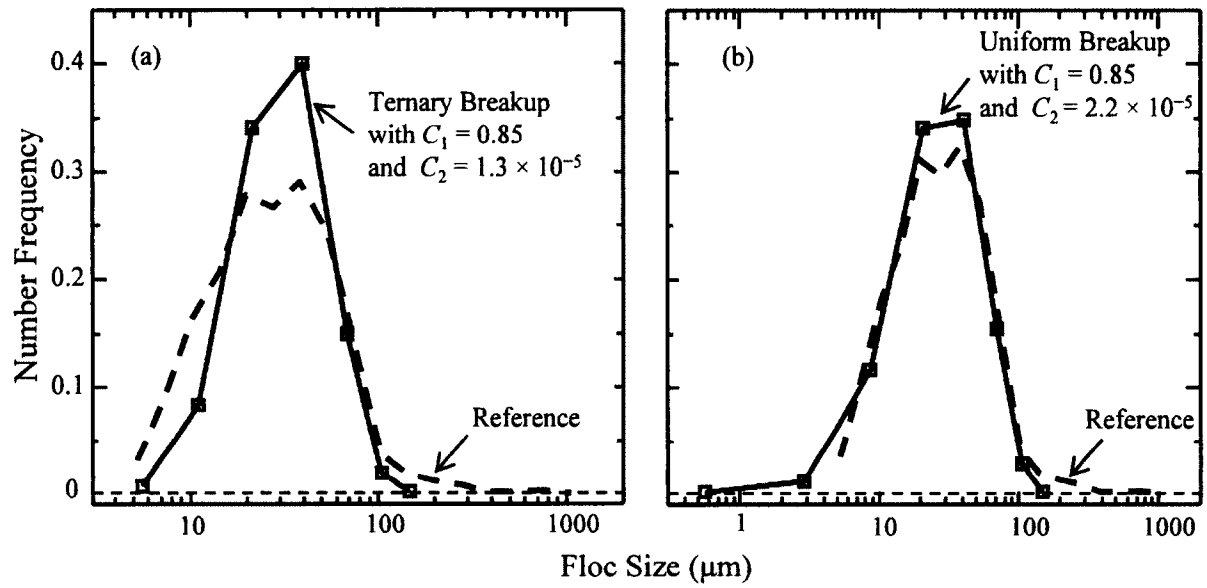


Fig. 3.17 Predictions of PSDs for (a) ternary breakup and (b) uniform breakup by matching experimental mean size through changing C_2 .

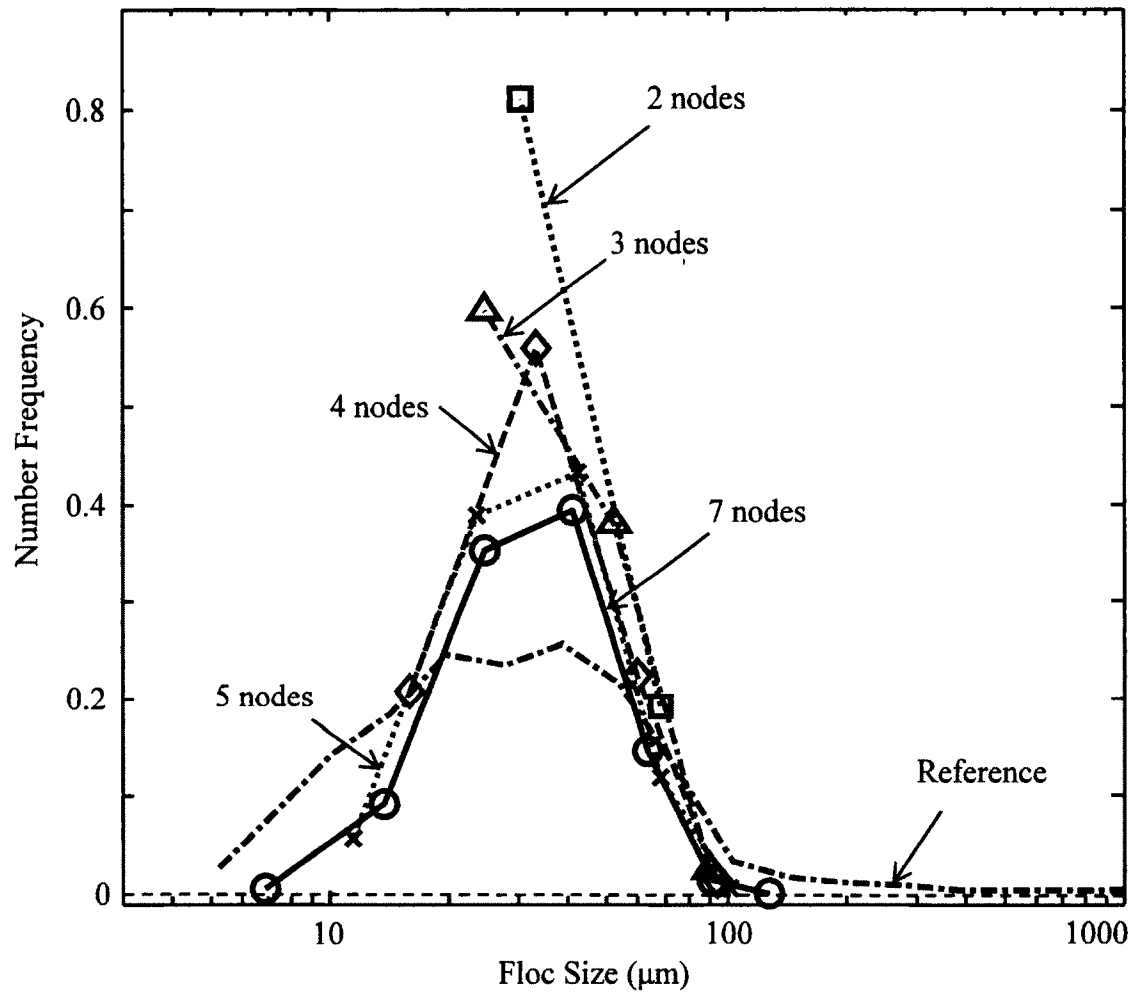


Fig. 3.18 Predictions of PSDs based on 2, 3, 4, 5 and 7 quadrature nodes.

CHAPTER IV

A CAMERA AND IMAGE PROCESSING SYSTEM FOR FLOC SIZE DISTRIBUTIONS OF SUSPENDED PARTICLES

Abstract

The observation of Floc Size Distribution (FSD) for quantitative description of its properties over a sufficient size range, from a few microns to a few millimeters, is still a challenge in most marine environments. In this study, an inexpensive image acquisition and processing system is developed for achieving this objective. Images are acquired by using a Sony Alpha NEX-5R camera body, a Sony E-mount to Nikon F-mount adaptor, extension tubes, a Nikon macro lens, and a close-up lens that can identify flocs with a minimum size of 5 μm . The light source and camera trigger are controlled by a micro-controller that was assembled for this project. These images are analyzed by using MATLAB Image Processing Toolbox. The processed floc size and their statistical distributions are confirmed with two available sample sets. The validated process is then applied to measure the steady state FSDs of kaolinite suspensions for different shear rates, suspended sediment concentrations, salinities, and a selected organic matter, guar gum. Although the presence of salt promotes flocculation of suspended kaolinite, only a small amount of salt, around 0.5 ppt, is needed to reach the saturation status. Thus for the test salinities (0.5, 1, 2, 3, 5, and 9 ppt), the measured FSDs show little difference among each other. On the other hand, guar gum affects kaolinite flocculation significantly and the maximum effect happens at a guar gum concentration around 15 mg/L when the kaolinite concentration is around 0.52 g/L. At this dosage the characteristic floc size is the largest.

Key words: nonintrusive camera system, image processing, floc size distribution, kaolinite, mixing jar experiments.

1. Introduction

In both freshwater (e.g., rivers, freshwater lakes, and reservoirs) and saltwater (e.g., estuaries, lagoons, and coastal waters) regions, abundant cohesive sediments are found in the forms of flocs. Flocs are highly porous and irregularly shaped three-dimensional aggregates that composed of smaller organic or inorganic primary particles or aggregates (Jarvis et al., 2005). Their size distribution in natural waters is a critical factor for determining the settling velocity and deposition rate of cohesive sediments, which will significantly affect various economic and ecological issues in the watershed. For example, billions of dollars are spent each year on dredging shipping channels, maintaining harbors, and managing locks along the channels. High turbidity caused by the abundance of flocs limits the penetration of sunlight into the water, which hinders the growth of water plants by inhibiting photosynthesis and affects the sight of foraging aquatic animals. Contaminants attached to these fine cohesive aggregates might move into food chains through organismal feeding activities and thereby threaten the entire ecosystem.

Flocs usually have a wide range of sizes (i.e., from a few microns to a few millimeters, and marine snow may be much larger than normal flocs) in the water column due to aggregation and breakage. Accurately determining the Floc Size Distribution (FSD) is the key to address the flocculation processes. Many techniques have been developed to find the FSDs of cohesive aggregates either in laboratories or in the field. Some instruments can only provide an averaged characteristic particle size rather than the entire FSD, such as photometric dispersion analyzer (Hopkins and Ducoste, 2003) and acoustic backscatter system (Smerdon et al., 1998). Although earlier instruments such as the Coulter Counter can

provide a full spectrum of FSD, these instruments will lead to biased FSD results. This is because flocs are disrupted under the created high shear when particles enter the orifice so that it can only be used to identify size distributions of non-breakable material, e.g., granular sediments (Gibbs, 1982; Eisma et al., 1991).

Advanced in-situ methods to measure the FSDs include laser-based approaches and image-based approaches. Two different series of laser instruments based on beam reflection and beam diffraction have been developed. Laser reflection based instruments include the Par-Tec laser backscatter instrument that is capable of detecting particles with size of 1 – 1000 μm (Phillips and Walling, 1995). The emitted laser beam is focused on a point close to the probe, and reflected by the particle surface when the beam encounters the particle. The beam spot is rotated by a rotating focusing lens, and the rotation speed of the lens, as well as the duration of the reflected laser pulse, determines the size of particle. This instrument has the merits of working at high Suspended Sediment Concentration (SSC) when compared with the instruments that rely on light transmission (Liss et al., 2005). However, basic criteria for correct measurement with a reflection laser counter, such as good homogeneity in the suspension and the uncertainty in hydrodynamic conditions, solvent, temperature, and focal point position (Monnier et al., 1996), make such instruments more suitable for process control than for studying flocculation processes in natural systems (Liss et al., 2005).

Laser diffraction instruments are now widely used to determine the FSDs. When a laser beam passes through a particulate, large particles scatter light at small angles and vice versa for small particles. The angular scattering intensity data are recorded and transferred to FSDs using Mie theory (e.g., Eshel et al., 2004), assuming a volume-equivalent sphere diameter.

One such instrument is the Malvern particle size analyzer that can identify particles with sizes of 0.01 – 3500 μm (for Mastersizer 3000, or 0.1 – 1000 μm for Mastersizer 3000E, or 0.02 – 2000 μm for Mastersizer 2000). Although this instrument can provide a large range of particle sizes and modified by Bale and Morris (1987) for field use, operational problems and a high cost of the apparatus limit the *in situ* measurement using this instrument (Phillips and Walling, 1995). Besides, if the FSDs are determined based on the samples from collection bottles, the sample procedure (e.g., collection, transport, and storage) itself will more or less disturb the flocs even when analyzing the sample immediately after a cruise. Nowadays, the commercially available LISST (Laser *In-Situ* Scattering and Transmissometry, Sequoia Scientific Inc., WA, United States) is one of the most popular instruments that is used for *in-situ* measurement of volume-based FSDs with 32 size classes (Agrawal and Pottsmith, 2000). Physical disturbances that might break up aggregates or flocs are minimized since the LISST does not pump samples. Thus, this instrument has the advantage of *in situ* use, and can estimate the settling velocity as well when combined with the OBS (Optical Backscatter Sensor) instrument (Mikkelsen and Pejrup, 2001; Fettweis, 2008; Shao et al., 2011). Nevertheless, the LISST results will usually miss either large flocs (e.g., LISST Type-C with size range 2.5 – 500 μm) or clay-sized primary particles around 2 – 4 μm (e.g., LISST Type-D with size range 7.5 – 1500 μm). Uncertainties of LISST may arise in stratified and high SSC environments. For example, Styles (2006) pointed out that salinity fluctuation leads to scattering at narrow forward angles indistinguishable from particle scattering, and Agrawal and Pottsmith (2000) indicated that multiple-scattering effects may occur when the total transmission is lower than 30% for a high SSC. Besides, LISST is usually difficult to find

FSDs in small physical environments (e.g., a relatively small tank) without sampling because of its large size (i.e., 81 cm height, 13.3 cm diameter).

Image-based approaches are another widely used method to directly observe the flocs and find the FSDs. Among these available approaches, images can be acquired either using microscopes or cameras. The microscope has the advantage of allowing individual particles to be viewed at high magnification, and give a good description on floc shape and even their internal structures. To use this approach, a small sample of suspended particles should be settled on a microscope slide for acquiring floc images (de Boer and Stone, 1999). The use of wide-mounted pipettes is a common method for floc extraction. Such extraction, however, may break up the flocs, even use large enough tube, such that the results cannot represent a true FSD. Thus, this method may only be ideal to identify the size distribution of primary particles or strong flocs.

Digital or video cameras that take images through a transparent wall, either in laboratories or at fields, can also be used to find FSD. Although they are limited by the concentration of particles in suspension and flocs are only observed as two-dimensional projections, the ability to measure FSDs with low disturbance and the wide size range (a few microns to a few millimeters) make it preferable for both field and laboratory use. Lower limit of resolution depends on the camera setup, which has been designed to detect particles down to 4 μm (Eisma et al., 1990). Examples of recent camera-based systems includes INSSEV system (IN Situ SEtTLing Velocity) developed by Fennessy et al. (1994), later improved by Manning and Dyer (2002), PICS system (Particle Imaging Camera System) designed by Smith and Friedrichs (2011), and RIPSCam system (Remote In situ Particle

Settling Camera) by Cartwright et al. (2011). The INSSEV system used a two-chamber device with an underwater video camera observing the flocs when they settle within a lower settling chamber. The PICS system combines the techniques of PIV (Particle Image Velocimetry) and PTV (Particle Tracking Velocimetry), using the former tracking small particle velocities (also as proxy for fluid velocities) and the latter tracking large particles velocities. The RIPSCam system used an electro-optical underwater Ethernet cable to connect the camera with a surface buoy that provided solar power to the batteries of the camera and transmitted data via a cell modem. Nevertheless, these instruments are either preferable for individual floc size monitoring only and sensitive to physical vibration (e.g., INSSEV), or have to combine with LISST instrument results to represent a wide range FSD due to the limitation of minimum floc size (e.g., 30 μm for PICS, and 20 μm for RIPSCam) that can be detected. In this study, the design of an automatic image acquisition camera system with a better image resolution for estimating FSD is presented. This is the first objective of this study.

Many image analysis methods, especially the use of MATLAB Image Processing Toolbox and ImageJ, are described in various literatures. ImageJ (Rasband, 1997) is an open source, freely available, Java-based program developed at U.S. National Institutes of Health that applicable to display, edit, analyze, save, and print images (e.g., Mazzoli and Moriconi, 2014; Tajima and Kato, 2011; Collins, 2007). Although ImageJ performs as well as MATLAB Image Processing Toolbox and runs much faster, it does not provide routines to distinguish out-of-focus and in-focus objects (Keyvani and Strom, 2013). For this reason, as well as to more precisely handle the processing procedure, the MATLAB functions are used in this

study to read, enhance, and analyze the acquired images. The processed results are compared with two commercially available artificial particle sets, with their images also acquired by using a microscope. This validation of the image processing is the second objective of this study.

Since kaolinite is commonly used as representative cohesive sediment in laboratories, and is one of the four abundant clay minerals (the other three are illite, montmorillonite, and chlorite) in the natural environment, this newly developed camera system and image process software is also used for pure kaolinite with different shear rates and SSCs. Additional experiments were used to check the effect of salinity and a selected organic matter on flocculation of kaolinite suspensions. That is the third objective of this study.

2. Experiment setup

2.1 Camera body and lens assembly

Floc images were collected using a Sony Alpha NEX-5R camera body and other lens. This camera body is selected because of two reasons: (1) its small size so that it can fit into a 6" pipe for field application, and (2) its large image sensor size, 23.5×15.6 mm with 4912×3264 pixels. This translates to $4.8 \mu\text{m}$ per pixel. In order to let anticipated small floc images down to $5 \mu\text{m}$ but still has a large enough number of particles within the viewing window to have meaningful statistics on FSD, there are some lens modifications necessary to have a Subject-to-Image Ratio (SIR) around 2.2 and a view window around $10.7 \text{ mm} \times 7.1 \text{ mm}$. These modifications include (1) using a Nikon Macro Nikor 55 mm lens, set at $\text{SIR} = 2 : 1$, with a NEX E mount to Nikon F mount adaptor, (2) adding three Kenko extension tubes (36

+ 20 + 12 mm) before the Macro lens, and (3) adding a +10 close-up lens on the macro lens. This lens combination was checked by taking a ruler image, i.e., the ruler subject around 10.7 mm long has an image of 23.5 mm. This means the image resolution increases to 2.2 μm per pixel. The depth of focus is around 2 mm, which was estimated by taking an image of a ruler that is attached to the hypotenuse of a triangle stand. Working distance between the subject and the lens is around 23 mm, which allow this camera system to acquire images through a transparent wall or cover with a maximum thickness around 21 mm. The aperture is set with its maximum value $f/2.8$ to allow more light passing through and blur the out-of-focus background, the shutter speed is set at least 1/1000 s to freeze the moving particles, and the ISO is set 100 to minimize image noise.

Three common issues must be addressed in a camera system: (1) the minimum number of pixels to define a floc; (2) types of light source; and (3) types of background. The first issue usually depends on the noise of the camera system and varies for different applications. For example, Maggi et al. (2007) represented FSDs with minimum size class 6.42 μm and their camera has resolution of 6.42 μm per pixel, which indicates they use as low as one pixel to represent a floc. Lintern and Sills (2006) define a floc as at least two interconnected pixels. It seems that using at least 3×3 pixels to identify a floc is the most common selection (Mikkelsen et al., 2004; Kumar et al., 2010; Smith, 2010; Smith and Friedrichs, 2011, 2015; Keyvani and Storm, 2013). In this study, the sample spherical seeding particle with size 2 – 20 μm (80A7001, Dantec Dynamics) is used to determine the minimum floc this system can identify. Details of that will be presented in section 3.7.

For the second issue, since a quick shutter speed (e.g., 1/1000 s) is required to freeze the

moving particles, extra light sources are required to illuminate particles. Light Emitting Diode (LED) illumination (e.g., Manning and Dyer, 2002; Smith and Friedrichs, 2011, 2015; Keyvani and Strom, 2014) or laser sheets (e.g., Lintern and Sills, 2006; Maggi et al., 2006) are the two most popular light sources. Laser sheets are considered to be stronger and more capable of penetrating water columns with more suspended particles when compared to LED light sources (Lintern and Sills, 2006). However, human eyes might have a chance to be injured by the strong laser beams when looking at the lens (which is assembled with laser light source) incautiously without appropriate protection. On the other hand, LED has the advantage of inexpensive, small, safe, and easy to handle. In this study, twelve LEDs are selected and mounted around the camera lens to provide light.

For the third question, both front-illumination (e.g., Van Leussen and Cornelisse, 1993; Maggi et al., 2006; Lintern and Sills, 2006) and back-illumination (e.g., Fennessy et al., 1994; Manning and Dyer, 2002; Kumar et al., 2009, 2010; Keyvani and Strom, 2013; 2014) have been used in different applications. Back-illumination displays particles as dark objects on a light background. Such a setup can reduce image smearing and make the flocs more clearly visible due to high contrast (Fennessy et al., 1994; Manning and Dyer, 2002). However, it is difficult to install a strobe light behind the subjects (i.e., make the subject between the camera and the light source) for field extensions. Front-illumination displays particles as bright on a dark background. Although such setup may cause “smearing” (because the camera gain have to work at maximum, which results in slowly decaying bright tail behind fast moving particles, as indicated by Fennessy et al., 1994) and make the image generally be represented as dark without image contrast, the light source is easy to assemble with the camera at the

same side. Besides, the error caused by “smearing” can be reduced by further judging the gradient of the light intensity between several consecutive pixels (see more in Section 3.5). For these reasons, front-illumination is applied in this study.

2.2 Camera Control

To continuously take hundreds of photo images every 2 s, releasing the shutter button and turning the LEDs on and off manually is not a practical method. For this reason, an electric control system was assembled to trigger the camera for acquiring images and control LED light source automatically (Fig. 4.1). The key electronic components in this circuit are the electronic switches, i.e., the relay TQ2SA-5V (marked as Q1) and the Field Effect Transistor (FET, marked as Q2), and the microcontroller (Teensy 2.0) which is used to control the above switches. The relay Q1 connects its Pin 3 and Pin 4 when an input 5V is applied in Pin 6, while disconnects the two pins when the voltage input is low (less than 1 V). The FET Q2 has three pins: Drain (D), Gate (G), and Source (S). The function of a FET is to open the connection between the drain and the source by applying a logical low voltage signal at the gate pin. If a logical level high voltage (i.e., more than 4 V) is applied between gate and source, the drain and source will be connected.

A DC power supply (either an adaptor that transfers 100V – 240 VAC to 15V DC, 2A, or a set of four 18650 lithium rechargeable battery that provides 15V, 2.3 AH) is needed to power Unit 1 through Pin 2 of J1. The microcontroller controls the LED flush light and the operation of photo taking. J2 connects to the camera remote control, and J3 connects to the LED module. A positive 5 V voltage regulator (V2) changes the supplied 15V to 5V to

provide power for the Teensy 2.0, and another voltage regulator V1 changes 15 V to 3 V to power the camera remote control.

The microcontroller is programmed to launch two 5 V pulses to control the two switches Q1 and Q2 through Port B1 and B2, respectively. If Port B1 (connected to Pin 6 of Q1) is high (5 V), Q1 will close its Pin 3 and Pin 4 to trigger the NEX 5's remote control for picture-taking. After about 0.1 s, the Port B1 becomes low (0 V) and Q1 will disconnect its Pin 3 and Pin 4 and wait for the next high to trigger the camera. Similarly, if Port B2 (connected to gate of Q2) is low, Q1 will be an open switch and the LEDs are turned off. When Port B2 is high, Q2 is a closed switch and the LEDs are turned on.

It is noted that the LED light is spreading up to ± 60 degrees. The strongest luminance is at 0 degree and decreasing with the angle. Since the image window is only 23.5×15.6 mm (much smaller than the cross-section of the lens), the LEDs are mounted in such a manner that they are tilted at 45 degrees from the printed circuit board, such that emitted light is projected toward the subject area in order to have a much stronger light intensity for acquiring better images. In the LED unit, D1 – D12 are divided into three pairs and each pair is connected in parallel through J3. Pin 1 of J3 is connected to Pin 2 of J1 which is maintained at 15 VDC. The reason for using this higher-than-acceptable voltage to power LEDs is to provide high intensive light as a flushing light. Since the duration of powering the LED is limited, i.e., 0.3 s for every two seconds, these LEDs will not be burned. Note that changing 15 V to 24 V is possible, but that will not significantly increase the light intensity.

The microcontroller Teensy 2.0 is programmed by using assembler language (see appendix of Shen, 2016) to use Port B1 and Port B2 to control Pin 6 of Q1 and the gate of Q2

respectively, and thus provides pulse to control the camera and the LEDs. The human-readable programmed code (with filename extension .asm) is compiled to become a machine-readable code (with filename extension .hex) by using a compiler avrasm2.exe, and import to the microcontroller by using a Teensy software. Pictures are taken around every 2 s and LEDs are flashed 0.3 s for each snapshot. Since the time to take a shot after the camera is triggered is not precisely operated (between 0.2 – 0.3 s), the camera is triggered 0.2 s before the LED is turned on. If necessary, the duration for powering the LED can be extended to 0.4 s.

2.3 Mixing chamber

Flocculation experiments were performed in a five liter cubic mixing chamber (Fig. 4.2). The top and bottom plates of the chamber are made of 1/2 inch PVC sheet, while the walls are made of plexiglass with nominal thickness 3/8 inch (actual thickness = 0.354 inch or 9.0 mm) to allow taking snapshots from the side. The mixing chamber is equipped with a commercial available impeller, LIGHTNIN A310 with diameter 5.2 inch (132.08 mm), to provide average shear rates that are reasonable uniform in the chamber. The impeller is assembled with a stainless steel shaft and driven by a DC gear motor. The difference of this chamber from that used by Prat and Ducoste (2006) is that the impeller is located close to the bottom to generate a more homogeneous flow field in the chamber. The gear motor (30VDC, 0.8A, 94 RPM) drives a 30 teeth pulley (TP20A5W6-30) and connected to a 16 teeth pulley (TP20A5W6-16) via a 3/8"-wide timing belt. Ideally, this setting will provide a 1.875 times speed increase for the A310 impeller when compared with the original motor speed. Because of the loading difference, the actual maximum rotational speed of the impeller is 162 RPM, i.e., 1.723 times speed up. The FSD measuring section is fixed at a location that is 11.5 cm

above the bottom, 8.5 cm from the side wall, and within 1 mm from the plexiglass wall.

Ducoste and Clark (1998) gave the average shear rate G_m (in unit of s^{-1}) in this mixing tank as

$$G_m = \sqrt{\frac{\rho N^3 D^5 N_p}{\mu V}} \quad (4.1)$$

where ρ is the water density (1000 kg/m^3), N is the rotational speed (in unit of Revolution Per Second, RPS), $D = 0.132 \text{ m}$, is the diameter of the impeller, $N_p = 0.3$, is an impeller-specific constant (Nagata, 1975; Spicer et al., 1996), V is the volume of the fluid in the tank (0.005 m^3), and μ is the dynamic viscosity of water, $1.0 \times 10^{-3} \text{ kg/(m}\cdot\text{s)}$.

The rotational speed of the impeller is controlled by the input voltage of the motor. Their relationship represents an excellent linear relationship with $R^2 = 0.9997$ and can be represented as

$$N = (5.786 \cdot \text{Volt} - 10.370)/60 \quad (4.2)$$

where *Volt* is the voltage applied to the motor in unit of V. This system can operate between 3 V and 30 V, which is corresponding to a rotating speed between 7 and 162 RPM of the impeller. Note that Eq. 4.1 indicates that one can control the average shear rate G_m in the chamber by controlling the rotational speed N of the impeller. This means G_m has a range from 2 to 217 s^{-1} . For example, shear rates 35, 45, and 55 s^{-1} correspond to a motor input voltage of 10.1, 11.6 and 13.0 V respectively. In this study, only the spatially averaged floc characterizations are interested, details on the hydrodynamics characteristics within the mixing chamber are not studied. Nevertheless, the mean velocity flow patterns and the local shear rate distributions are similar to those given by Ducoste et al. (1997), and Ducoste and Clark (1998, 1999).

3. Image analysis procedure

The images acquired from the camera system were analyzed by using MATLAB image processing toolbox. Several processes were applied to the raw images prior to statistical analysis, and these processes include color image to grayscale conversion, background light removing, contrast stretching, grayscale to binary conversion, small object (noise) removing, dilation and erosion, on-broader particle removing, hole-filling, and pixel gradient checking. Although the source codes for image process are listed in the appendix of Shen (2016) for further reference, the selections of number of cell for determining background light, thresholds to covert to binary image, and critical gradient to remove out-of-focus particles and noise after thresholding in the following discussions are highly empirical and should be checked for different applications.

3.1 Change color images to gray scale

Each image taken from using this system, although appearing dark in general, is a RGB image that stored in a 3D matrix with dimension $3264 \times 4912 \times 3$ in which “ 3264×4912 ” denotes the total pixel number of the image and “3” denotes the three color intensities of each pixel in red, green, and blue. This RGB image is first converted to a greyscale image by eliminating the hue and saturation information while maintaining the luminance. Here after we call this greyscale image the “original image”. The original image is stored as a 3264×4912 matrix with each component displayed as an 8-bit unsigned integer to present the intensity of a pixel ranging from 0 (black) to 255 (white). Take the coated hollow glass particles (See Section 3.7) as an example, the complement (i.e., black and white are reversed,

which means each pixel value is subtracted from the maximum value 255 and the difference is used as the pixel value in the output image) of a greyscale sample image is displayed (Fig. 4.3a). Note that since abundant small particles around 10 μm are obtained in one image in this example, only the central $1/27 \times 1/27$ region of the image are represented in Fig. 4.3a. The image histogram (the distribution of image light intensities) shows the intensity of this original image concentrated in the range of 50 to 100. For a well-exposed image, the brightness values (from 0 – 255) in the image histogram should ideally cover the entire range without clipping black or white. However, images acquired in this study usually are presented as low contrast. The narrow band histogram (50 – 100) with empty regions at the dark side (< 50) and bright side (> 100) of the histogram shows that many of the possible brightness levels are not used. Visibility of the original image can be improved by reassigning the usable limit of histogram by stretching the narrow band (50 to 100) histogram into a full band (0 to 255). This means changing the darkest pixels (with light intensity of 50) to black (light intensity to 0) and the lightest (light intensity of 100) to white (255), and in between linearly interpolated. With this stretch out, the visual contrast improves significantly (Fig. 4.3a). Notice that although a stretched image now displays the full range between black and white, it also causes a problem by filling up the gaps in the histogram with interpolated light intensity. Therefore, non-uniform illuminated background noise should be removed first.

3.2 Uneven background subtracting

Background light may be strong in some places but weaker in others. Actually, such perfect background illumination does not exist at all, since lenses or cameras may cause

vignetting in which the corners of the image are darker than the center (the light is partially absorbed by greater path length in the optics and reduced by the change in the effective aperture of the lens, as shown by Russ, 2011). A contrast or thresholding for the original image will lose the particles in bright background without removing the background *in prior*.

The background might not always be apparent from looking at the image with naked eyes. It can be detected by dividing the original image into small areas such that the minimum value of each area is considered as background. The selection of these small areas, however, depends on different applications. For example, Keyvani and Strom (2013) indicated that a circle subdomain with diameter 50 pixels gave the optimum result. Generally, this element structure cannot be either too small (probably larger than the estimated largest flocs), or too large (cannot detect high resolution background). By trial and error, a square with 300 pixels on each side was selected as the “block” in this study for all images.

The background of the original image (Fig. 4.3a) is calculated and displayed in Fig. 4.4. Since there are 4912×3264 pixels in the original image, 16×10 square blocks are used to show the minimum in each block. It clearly shows that the light is weak in the top left and top right corners while strong in the south center of the image. Thus, the background light intensity for each pixel can be re-interpreted as a continuous form by linear interpolation of the estimated background. The background is then subtracted from the original image before contrast adjustment. After background removal, the complement image (Fig. 4.3b, after contrast stretch to better examine the image in printed form) shows these particles more clearly.

3.3 Contrasting and thresholding

Now the image is a bit too dark with most of its histogram concentrated on a narrow range. An enhanced contrast is necessary before converting this greyscale image into a binary image. Contrasting rescales the image intensity by redistributing the pixel intensity values between the minimum and the maximum intensity values. However, a simple default adjustment that rescales intensity from 0 to 255 usually cannot successfully “enhance” the image because it generates noise after subtracting the background. This noise may magnify after the thresholding. Here, the image contrast (using MATLAB function “`imadjust`”) is applied with a non-linear intensity rescale using a parameter γ . If $\gamma < 1$, the mapping will be brighter; if $\gamma > 1$, the mapping will be darker; and $\gamma = 1$ denotes linearly rescaling. In order to make the darker noise (since particles should be bright) closer to the background, a nonlinear mapping is selected with $\gamma = 2$ for coated hollow glass particles and kaolinite (or $\gamma = 4.2$ for polystyrene latex) by using the trial-and-error approach. Also, input intensity value for the contrast should be clipped since most of the intensity is close to black side. Again by trial-and-error, this value is selected as 0.2 for the coated hollow glass particles, while 0.1 is used for polystyrene suspensions and kaolinite suspensions.

Then it is the time to select a threshold algorithm to convert a greyscale image into a binary image. Thresholding is a process that defines a threshold and sets all pixels with intensity higher than this threshold changing to white pixels (symbol 1), whereas the remaining are set to black (symbol 0). It is not uncommon to specify a threshold value manually (Curran et al., 2003). For an experiment with a large set of images, it is impossible to choose a single threshold for all images (Lintern and Sills, 2006) without post-processing

such as pixel gradient checking. Various automatic threshold methods are also suggested in the literature. For example, Otsu's method (Otsu, 1979) is selected as the built-in threshold function in MATLAB's tool box. This method provides a relatively low threshold such that it may include more noise in the resulting binary figure (Lintern and Sills, 2006). Maggi et al. (2006) suggest a threshold method that is based on rescaling the bi-modal histogram distribution into two Gaussian distributions to represent the background and foreground respectively, and select the intersection point of the two distributions as the threshold. However, when a clearly bi-modal histogram is unobvious, this method is hard to apply. Keyvani and Storm (2013) empirically found the "Yen method" (Yen et al., 1995; Sezgin and Sankur, 2004) works best for their applications. However, this method probably will mistake a larger out-of-focus particle for a small in-focus particle. For this reason, it is excluded in this study. The iterative method developed by Lintern and Sills (2006), and later recommended by Smith (2010), cannot display satisfied segmentation in this application. Since none of the threshold methods are generally robust, by trial-and-error, a single threshold (for kaolinite suspensions) or Otsu's method (for sample particles) is selected in this study. For example, Fig. 4.3c shows 11 particles (No. 1 – No.11) remaining after thresholding for the polystyrene particles. Notice that the noise after thresholding can be further removed by checking the gradient (Section 3.5).

3.4 Binary image processing

Before a pixel-defined floc can be clarified after comparing the results with the sample particle, it is safe to assume the minimum floc cannot be smaller than 2×2 pixels for a

front-illumination setting. Thus, small objects with area smaller than 4 pixels or minor axis length smaller than 2 pixels are firstly removed as noise. In Fig. 4.3c, particle No.9 is first removed as such noise. Secondly, dilation and erosion are applied as basic morphological correction procedures (e.g., Lintern and Sills, 2006; Shih, 2009; Smith and Friedrichs, 2011). These two processes denote adding and removing a “structure” from the outside edge of each floccule and do not have an effect on solid floccules to avoid mistaking a faint floccule for neighborhood small floccules. The selection of this “structure”, however, is user defined for different applications. Here, a 2×2 pixel square is selected since in our application the minimum particle size is generally small such that a larger “structure” might cause a biased population for small sized particles. After that, holes within a closed object are filled by assuming these holes are caused by thresholding a misty floccule. Besides, incomplete particles on the border are removed. Note that in Fig. 4.3c, particle No.11 is not on the border, since only the center $1/27 \times 1/27$ of the entire image is displayed. Finally, the first step is applied again to remove small objects before doing pixel gradient checking.

3.5 Pixel gradient checking (i.e., in focus checking and threshold noise checking)

Floccules are considered in focus if there is a steeper gradient of light intensity near the floccule edges because of sudden changes in light intensity. This sudden change of light intensity will not occur on out-of-focus floccules. Thus, estimating the gradient of the image intensity and generating a gradient matrix I_g that has the same size of the original figure I are critical to identify these in-focus particles. Such gradients can be determined by performing derivative operations using kernels as a template matching for convolution processes (Russ, 2011). As

an example of the first-order derivative, the gradient (I_g) for the horizontal change (I_{gx}) and vertical change (I_{gy}) are determined by a convolution operation (typically using the symbol “*”, defined as the integral of the product of two functions after one is shifted, i.e., $(f * g)(x) = \int_{-\infty}^{\infty} f(x-t)g(t)dt$) between a derivative kernel ($K = [K_x, K_y]$) and the original image (I), following (Gonzalez et al., 2009)

$$I_{gx} = K_x * I \quad (4.3)$$

$$I_{gy} = K_y * I \quad (4.4)$$

K_x and K_y are a $p \times p$ matrix with p usually no more than five to reduce the computation time (which is on order of p^{2p}). This selection indicates that only a limited area is considered to determine if a pixel is on the edge or not (Setayesh et al., 2013). The final gradient is estimated by using the absolute value (sometimes use square-root value) of the two components (Gonzalez et al., 2009)

$$I_g = |I_{gx}| + |I_{gy}| \quad (4.5)$$

Although the Sobel kernel, which selects K_x and K_y as two 3×3 matrixes, is one of the most widely used derivative kernels, no single edge operator kernel can guarantee its capability for different applications (Zhu, 1996). Thus to process sample images, different operators are desirable to select the best operator. The Sobel kernel, as well as other MATLAB capable default kernels in the “edge” function, however, merely introduce more noise and are impractical for this study. Thus, a two-dimensional, first-derivative Gaussian kernel was applied following that was given by Keyvani and Strom (2013):

$$K_x(x, y) = \frac{g(y-m)g'(x-m)}{\bar{K}} \quad (4.6a)$$

$$K_y = K_x^T \quad (4.6b)$$

where K_x and K_y are $p \times p$ matrixes with $p = 2m + 1$, symbol “T” denotes transpose, symbol “prime” denotes first derivative, and $g(x)$ is the one-dimensional Gaussian function with σ as the standard deviation of the distribution.

$$g(x) = \frac{1}{\sigma\sqrt{2\pi}} \exp\left(\frac{-x^2}{2\sigma^2}\right) \quad (4.7)$$

Also

$$\bar{K} = \sqrt{\sum |g(y-m) \cdot g'(x-m)|^2} \quad (4.8)$$

$$m = \sigma \left[-2 \ln(\sqrt{2\pi}\sigma\varepsilon) \right]^{0.5} \quad (4.9)$$

in which m is rounded up to the nearest integer, and σ and ε are user defined parameters. Followed those used by Keyvani and Strom (2013), $\sigma = 2$ and $\varepsilon = 0.01$ (which implies $p = 5$) were selected for this study.

The minimum rectangle that can cover a floc is defined as the Region Of Interest (ROI) of this floc. Thus, the maximum component of I_g in the ROI region is defined as the clarity value dI_i of a detected floc i (Keyvani and Strom, 2013):

$$dI_i = \max[I_g(\text{ROI}_i)] \quad (4.10)$$

A critical clarity value dI_{cr} is specified throughout, above which a floc is identified as in-focus while below which a floc is identified as out-of-focus or thresholding noise. A value of $dI_{cr} = 1.2$ was used in Keyvani and Storm (2013)’s study. However, this value relies on the light source intensity and background type. For this reason, it may vary significantly and is highly empirical for different applications. Even for the same light source, this value also depends on the reflection index of the material. Using the kaolinite image as an example (Fig. 4.5), I_{gi} smaller than 15 indicates the pixel i is in the background or interior of flocs, I_{gi} between 16 and 21 identifies weak edges of out-of-focus particles, and I_{gi} larger than 22

shows strong edges are in-focus particles. Thus, $dI_{cr} = 22$ is selected for finding the kaolinite flocs in this study. The process of removing out-of-focus particles are important, and no more than half identified flocs are remaining after this processes, compared with around 5% given by Keyvani and Strom (2014). A binary figure that shows the processed particle image for Fig. 4.3c is presented in Fig. 4.3d.

For coated hollow glass particle and polystyrene latex particles, dI_{cr} are selected as 57 and 32 respectively.

3.6 Floc characterization

Floc size is the most important floc property to describe a floc, and various representative sizes have been used to describe flocs. Among the representative sizes available, the Equivalent Circular Diameter (ECD) L is widely used (Keyvani and Strom, 2013, 2014; Smith, 2010; Lintern and Sills, 2006; Flory et al., 2004; Mikes et al., 2004). ECD can be defined as the diameter of a sphere which contains the same projection area as the floc:

$$L = \sqrt{\frac{4A}{\pi}} \quad (4.11)$$

in which A is the two-dimensional projected floc area.

The selection of ECD as the representative size is based on the assumption that floc size can be represented as a volume-equivalent diameter that a sphere with this diameter has the same volume as the true floc. Although it may over-estimate the floc size since the dimension perpendicular to the viewing plane is generally the smallest (Jarvis et al., 2005; Allen, 1997), this estimation is still useful when sufficient number of particles are detected. Verney et al. (2009) also indicated that ECD provides the closet approximation of the floc mass.

It is important to notice that floc size alone is sometimes insufficient for distinguishing a floc, since it is apparent that particle with same ECD may have different shape. Circularity (the ratio of the perimeter of a sphere that has the same area of the floc divided by the actual floc perimeter), convexity (the ratio of convex full perimeter, by imaging an elastic band placed around the particle, divided by the actual floc perimeter), and aspect ratio (the ratio of the length of the major and minor axis of an ellipse that can be used to best evaluate the region of the particle) are the most commonly used shape factors. However, no matter which shape factor one chooses, it is possible that flocs with different shapes will have the same shape factor. For example, circularity might have the same value for a long ellipse shape aggregate and a compact, spiky shape aggregate. Moreover, although adding or removing one or two pixels (which can easily happen) has minimal influence on the shape evaluation of large flocs, it does change the shape parameter value significantly for small particles consisting of only a few pixels.

In cohesive sediment dynamics, fractal dimension is a preferable shape factor to identify floc shape, since this value and the floc size directly determine the settling velocity (Winterwerp, 1998). However, no accurate method is completely reliable to extract fractal dimension from 2D images (Keyvani and Strom, 2014). In reality, one usually measures the floc size and floc settling velocity to deduce the fractal dimension, or calculates settling velocity based on measured floc size and empirically determined constant fractal dimension. Since particle shapes are not the target of this study, only the floc size is addressed.

3.7 Validations

Two sample particle sets with reported particle size distributions are used to validate the presented image analyzing procedures. The first set is Silver Coated Hollow Glass Spheres (S-HGS-10, Dantec Dynamics) with nominal size of 10 μm and size range 2 – 20 μm . Using an Olympus BX51 microscope and Nikon DXM1200 digital camera system, coated hollow glass particles suspended in tap water (Fig. 4.6, with 400 times magnification) show most of the sample particles are spherical, despite the existence of minor debris. These spherical particle images can be used to judge the image quality, thus determine the minimum number of pixels needed to determine a floc. In general particles are well dispersed except for a few clusters. For checking the accuracy of the presented algorithms for image process, a randomly selected microscope image (with 100 times magnification to allow more particles in one image; 1280 \times 1024 pixels with resolution 0.67 μm per pixel with 673 particles) was processed with thresholding using Otsu's method, grayscale to binary converting, small object removing (smaller than 2 \times 2 pixels), dilation and erosion, and on-border objects removal for getting the FSD (dashed line in Fig. 4.7). Pixel gradient checking is not necessary since the image was taken with particles sitting on a glass plate with an excellent on-focus. Thus, the contrast of particles and background under the microscope used in this study are excellent. This image follows the British Standard (BS3406 1963) that a minimum of 625 particles should be included for a meaningful FSD in a microscope image (Jarvis et al., 2005). The resulting mean and median size of the FSD are 10.1 μm and 8.5 μm , respectively, and 91.2 % of the particles are smaller than 20 μm .

To acquire images of the same set of glass spheres using the presented camera system, a

small amount (1 g) of these spheres are mixed in the five-liter mixing chamber with shear rate of 10 s^{-1} . Images are taken and processed. Because of the small magnification and the selected particle concentration, sufficient particles (much more than 625) in each image are observed. FSD from the average of twenty randomly selected images (Fig. 4.7, marked as bars) indicates a slight different distribution, i.e., more $10 \mu\text{m}$ particles are found in the images in the presented camera system. This result is more close to the nominal size, $10 \mu\text{m}$, probably because a much larger number of particles is used for FSD analysis. The standard deviation of the twenty images (the line segments on top of each bar) shows limited difference among each other suggests that 625 particles required by the British Standard should be sufficient. The average mean and median size of the FSD analyzed by the camera system is $9.9 \mu\text{m}$ and $8.8 \mu\text{m}$ respectively, with 96.6 % particles smaller than $20 \mu\text{m}$. Although the FSD from the microscope and that from the camera show slight difference, their mean and median size are consistent with the size range provided by the manufacturer. It also confirms the selection of minimum floc size for this camera system can be as low as $5 \mu\text{m}$ (i.e., using 2×2 pixels, with equivalent diameter 2.26 pixel).

Another sample particle set is non-spherical polystyrene particles with nominal size of 20 microns (Made by Hebei University of Technology, China). These particles are dispersed in diluted ethanol since it is difficult to disperse in tap water. Using the same microscope but with a 100 times magnification, the image (Fig. 4.8) shows a wide particle range and particle clusters because of charges on the surface of polystyrene particles. The FSD based on randomly selected two images with a total of 837 particles show particle size varies from $4.6 - 94.5 \mu\text{m}$, with a mean size of $22.7 \mu\text{m}$ and median size of $19.4 \mu\text{m}$ (Fig. 4.9, dashed line).

Similar to the experiment prepared for the glass spheres, a larger amount of polystyrene particles (1.5 g) are mixed in the chamber with diluted ethanol. The FSD is obtained by using the camera system with an average of 50 images (Fig. 4.9 marked as bars) showing a reasonably matched result. Because of large particle size, more clusters, and the different parameters selected in the image process, only around 50 flocs have been identified in each image. With this limitation, the FSD have to be determined by using a number of images. The exact number, however, should be selected based on the convergence of measured FSD (i.e., when increasing the number of images does not change the FSD indicates a converged FSD). Therefore, FSDs based on a sequential of 1, 2, ..., 50 images are evaluated (Fig. 4.10). This evaluation is based on the assumption that when using a total of 50 images, with the number of floc more than 2500, for analysis, the obtained FSD would be close to the true value. A relative difference in FSD (represented by the summation of all the absolute differences for all bins in the particle number frequency distribution), as well as the difference in mean size, can be estimated (Fig. 4.10). It indicates that the mean size will not significantly change when using more than 10 images, with a difference around 10%. The difference in FSD will decrease continuously as the number of images increases. FSD based on 50 images taken by this camera system (Fig. 4.9, marked as bar) results in a mean size of 20.0 μm and a median size of 15.7 μm for a total of 2675 particles. When showing the difference in each bin of each FSD (Fig. 4.11), the difference after 30 images is close to the converged FSD.

In the following application to analyze images for kaolinite suspension, FSDs based on a continuous 100 images (i.e., resulting in around 4 min for photo taking) are selected to include sufficient number of particles.

4. Application for kaolinite suspensions

4.1 Flocculation model

The flocculation box model based on population balance that includes the kinetics of aggregation and breakage of flocs with size L is given next (Shen and Maa, 2015).

$$\begin{aligned} \frac{\partial n(L,t)}{\partial t} = & \frac{L^2}{2} \int_0^L \left[\frac{\beta((L^3 - \lambda^3)^{1/3}, \lambda) \cdot \alpha((L^3 - \lambda^3)^{1/3}, \lambda)}{(L^3 - \lambda^3)^{2/3}} \cdot n((L^3 - \lambda^3)^{1/3}, t) \cdot n(\lambda, t) \right] d\lambda \\ & - n(L,t) \int_0^\infty \beta(L, \lambda) \alpha(L, \lambda) n(\lambda, t) d\lambda + \int_L^\infty \alpha(\lambda) \cdot b(L | \lambda) \cdot n(\lambda, t) d\lambda - \alpha(L) \cdot n(L, t) \end{aligned} \quad (4.12)$$

where $n(L, t)$ is the number density function defined by floc size L at time t , λ is the integrand that has the same dimension as L , β is the collision frequency function, α is collision efficiency function, α is breakup frequency function, and b is fragmentation distribution function. The first term on the right hand side of Eq. 4.12 is the birth of flocs with size L due to aggregation of smaller particles with size $(L^3 - \lambda^3)^{1/3}$ and λ . The second term on the right hand side is the death of flocs with size L due to aggregation with other particles. The third term is the birth of flocs with size L due to fragmentation of bigger particles λ , and the last term is the death of flocs with size L due to breakup into smaller particles.

For the aggregation processes, Smoluchowski (1917) suggested the shear-induced collision frequency β for two particles with size L_i and L_j under a given shear rate G_m is

$$\beta(L_i, L_j) = \frac{G_m}{6} (L_i + L_j)^3 \quad (4.13)$$

while the collision efficiency α is treated as an aggregation fitting coefficient, i.e., $\alpha(L_i, L_j) = C_1$, which includes various bio-physical influences such as salinity and organic matters. For the breakage processes, the breakup frequency function α for flocs with size L_i , suggested by Winterwerp (1998), is used in this study:

$$a(L_i) = C_2 \cdot \left(\frac{\mu}{F_y} \right)^{1/2} \cdot G^{3/2} \cdot L_i \cdot \left(\frac{L_i}{l_p} - 1 \right)^{3-nf} \quad (4.14)$$

where C_2 is the breakup fitting parameter, l_p is the size of primary particles, nf is the fractal dimension of the flocs, μ is the dynamic viscosity of the fluid, and F_y is the yield strength of aggregates as determined empirically. The fragmentation distribution function describes the size distribution of daughter flocs after breakup, and assumes a binary breakup with mass ratio 1:1 in this study (Maggi et al., 2007; Mietta et al., 2008; Furukawa and Watkins, 2012; Shen and Maa, 2015).

Eqs. 4.12–4.14 suggest that the controlling parameters for the evolution of FSDs are explicitly limited to SSCs (indicated by the number concentration of flocs) and shear rates, while other effects are simply considered in the aggregation and breakage fitting coefficients C_1 and C_2 . For this reason, finding a reasonable and logical range of C_1 and C_2 becomes important because that will prevent any unreasonable modeling.

Among all the available methods for solving Eq. 4.12, a modified QMOM approach (Shen and Maa, 2015) has been used to simulate the FSDs with a maximum of eight size classes. Using this approach, the number density term $n(L, t)$ is converted into moment terms by applying moment transformation and Gaussian quadrature approximation (McGraw, 1997) with an adjustable factor (Su et al., 2007):

$$m_{k/p} = \int_0^\infty L^{k/p} n(L; t) dL = \sum_{i=1}^N \omega_i L_i^{k/p} \quad (k = 0, 1, \dots, 2N - 1) \quad (4.15)$$

where m_k is the k th order moment of FSD, L_i and ω_i are the characteristic size classes and corresponding number densities of FSD, N is the total number of size groups, and p (can be selected between 1, 2, 3, or 4, depending on applications) is the adjustable factor.

Using Eq. 4.15, QMOM transfers the PBE (i.e., Eq. 4.12) to a set of moment transport equations which is given next:

$$\begin{aligned} \frac{\partial m_{k/p}}{\partial t} = & \frac{1}{2} \sum_{i=1}^N \omega_i \sum_{j=1}^N \alpha(L_i, L_j) \cdot \beta(L_i, L_j) \cdot \omega_j \cdot (L_i^3 + L_j^3)^{\frac{k}{3p}} \\ & - \sum_{i=1}^N L_i^{k/p} \omega_i \sum_{j=1}^N \alpha(L_i, L_j) \cdot \beta(L_i, L_j) \cdot \omega_j + \sum_{i=1}^N a_i \bar{b}_i^{-(k/p)} \omega_i - \sum_{i=1}^N L_i^{k/p} a_i \omega_i \end{aligned} \quad (4.16)$$

Based on this QMOM method, the lower-order moments of FSD are tracked with high accuracy with a low computational cost. The results given by Shen and Maa (2015) have shown that the FSDs can be efficiently and reasonably displayed by the quadrature nodes (i.e., the characteristic sizes) and corresponding weights (i.e., the characteristic number densities). In this project, this approach will be applied in the mixing chamber experiment.

4.2 Model calibration and validation

To find the two coefficients, C_1 and C_2 , pure kaolinite suspension with a SSC of 0.28 g/L was prepared in the mixing chamber. It was mixed using the highest shear rate (217 s^{-1}) for about 0.5 hr with the purposes to break it into primary particles in order to have the same initial FSD conditions, and then set to the pre-determined shear rate (45 s^{-1}) to allow the growth of flocs for two days. FSDs at time 47.0, 47.5, and 48.0 hr are collected and the average is used to represent equilibrium FSD. These three selected durations are all longer than 33.3 hrs reported by Keyvani and Strom (2014) for achieving the equilibrium state in their 13 liter mixing chamber. By selecting $C_1 = 0.85$ and $C_2 = 3.2 \times 10^{-5}$, the flocculation model can produce a FSD that is close to the measured FSD (Fig. 4.12a). The differences on mean and median size are only $0.3 \text{ }\mu\text{m}$ and $3.7 \text{ }\mu\text{m}$, respectively (Table 4.1). Then the model

was using the same C_1 and C_2 for the same concentration 0.28 g/L but a higher shear rate, 55 s^{-1} . Good comparison can be concluded (Fig. 4.12b), with the differences in mean and median sizes only 0.8 μm and 2.4 μm , respectively (Table 4.1).

The SSC is then changed to 0.52 g/L for two shear rates, 35 and 55 s^{-1} , respectively. Mietta et al. (2009) pointed out that 35 s^{-1} is probably the minimum average shear rate that can be used in this kind of mixing chamber experiment. This is because a smaller G_m will affect the prediction of FSD by reducing SSC as a result of particle deposition on the bottom of the chamber. Keynavi and Storm (2014) also selected this minimum shear rate 35 s^{-1} in their experiment. Therefore, no study for shear rate smaller than 35 s^{-1} was tested. The measured mean size for SSC = 0.52 g/L and $G = 35 s^{-1}$ is 38.4 μm , which is close to the reported mean size which is around 37 μm from a settling column experiment for pure kaolinite of SSC 0.5 g/L for the same shear rate (Maggi et al., 2007; Mietta et al., 2008). Results have shown reasonable modeled FSDs when comparing with experimental results (Fig. 4.12 c, 4.12d). The relative errors of mean and median sizes for the two cases in this study are no more than 5 % (Table 4.1).

The above experiment shows that for the same SSC, higher mean and median sizes result from a lower shear rate. For the same shear rate, higher mean and median sizes result from a higher SSC. The modeling results also match the conclusion.

4.3 Effect of salinity

In fresh waters, positive charges on the edge of a clay particle and negative charges on the face lead to a face-edge attachment that constitutes a floccard-house structure (Lintern,

2003). In saline water, the double layer is depressed and the attractive van der Waals force dominates so that the flocs are more likely to come into close contact. It is generally accepted that there is a critical salinity and above which no further flocculation is promoted (e.g., see Krone, 1962, using settling velocity as an indicator of flocculation). This threshold, however, depends on different clay mineral and sediment compositions.

In this study, the effect of salinity on pure kaolinite was explored for kaolinite SSC = 0.28 g/L and shear rate $G = 55 \text{ s}^{-1}$. Six experiments in total were conducted continuously with each one lasting for 24 hrs. Rock salt was mixed with tap water in the chamber to make an initial salinity of 0.5 ppt. The highest shear rate was first applied for 0.5 hr to break all flocs. Then the shear rate was dropped to 55 s^{-1} and run for another 23.5 hrs. FSDs were measured at 23.0, 23.5, and 24.0 hrs using the camera system. The average of these three FSDs was selected as the equilibrium FSD. After the third measurement at 24 hrs, a proper amount of rock salt was add to increase the salinity to 1 ppt, and the same procedures on applying the two shear rates and measurements of FSDs were repeated. With this, the effect of the six salinities (0.5, 1, 2, 3, 5, and 9 ppt) on FSD for kaolinite was measured. Results (Fig. 4.13) show that all the six FSDs are close, except at floc size equal to $38.4 \mu\text{m}$, where more particles are available for salinity 0.5 and 1 ppt. The similar results demonstrate that the critical salinity for affecting the flocculation process of pure kaolinite might be as low as 0.5 ppt. This is consistent with the results (0.6 ppt for kaolinite mineral) reported by Ariathurai et al. (1977), and referred to and revised by Mehta (2013). Applying $C_1 = 0.95$ and $C_2 = 1.7\text{E}-5$ (Table 4.1), all experimental FSDs with salt were simulated with one curve, and matched well. Compared with pure kaolinite for the same SSC and shear rate (Fig. 4.12b), the mean, median, and peak are shifted from 24.7, 20.9, and $27.6 \mu\text{m}$ to 37.9, 30.0, and $38.4 \mu\text{m}$ respectively.

4.4 Effect of organic matter

Suspended particle coated with organic matters are always presented in estuaries. Organic material bounded on the particles might either reinforce the flocculation (e.g., organic matter consisting fibers and mucal films secreted by bacterial activity, see Dyer, 1985), or reduce the flocculation (e.g. decomposed organic matter as a result of higher water content, see Mitchell and Soga, 2005). Organic matter content affects the inter-particle attraction or adhesion and negatively correlates with the bulk density of a cohesive soil (Avnimelech et al., 2001). In this study, guar gum (G4129 SIGMA, CAS 9000-30-0) was selected as a representative Extracellular Polymeric Substances (EPS) (Tan et al., 2012) which is the analog representative of neutral microbial exopolymers. Guar gum is a neutral (i.e., nonionic) plant polysaccharide found in the seed of *Cyamopsis tetragonoloba* (Kumar, 2000). Once dissolved, it results in a viscous and pseudoplastic aqueous solution if the concentration is high enough. The existence of hydroxyl groups and lack of carboxylic acid groups renders guar gum a neutral polarity in water.

The differences between the procedures carried out for checking salinity effect on flocculation are as follows: the effect of guar gum concentration on kaolinite flocculation was prepared independently, i.e., each kaolinite and guar gum mixture was prepared separately and discarded after the experiment. For each experiment, weighted guar gum powder was added to the kaolinite suspension and mixed for 0.5 hour with the maximum shear rate. Then the shear rate was dropped to 55 s^{-1} and run for another 23.5 hrs. Three FSDs were collected at 23.0, 23.5, and 24.0 hrs, respectively, and their average was assumed as the FSDs at the equilibrium status. The other difference is that an OBS was mounted at the corner of the

chamber, with the sensing elevation at the same level as the image window when measuring FSD, pointing toward the center of the chamber to measure the change of kaolinite SSC. It is well-known that to convert OBS readings to SSCs, in-situ calibration is required because OBS response is affected by floc size as well as by SSC. Unfortunately, the calibrated relationship, ' $ssc = 0.000443 \times (obs - 1740)$ with $R^2 = 0.9857$ ' where *obs* is the digitized OBS reading in units of counts and *ssc* is the suspended kaolinite concentration in g/L, is only conducted during the time when the maximum shear rate is applied. For this reason, it is impossible to separate the two contributions (i.e., by the decrease of kaolinite SSC or by the increase of floc size) that cause the decrease of OBS readings (Fig. 4.14). The small decrease of suspended kaolinite concentration with time is possible because there are always small areas near the bottom edges of the chamber where the bed shear stress is small and favorable for deposition. The change of floc size is also confirmed by the measurements (Figs. 4.15 and 4.16). The initial suspended kaolinite concentration is 0.54 g/L with possible variation 0.01 g/L and the final (after 24 hrs) concentration is 0.52 g/L with the same possible variation. These two concentrations are estimated using the calibration equation and ignore the contribution of the change in floc size and the possible small amount of deposition. Although the change of OBS reading is small, less than 5 %, it is marked for future study.

As the guar gum concentration increases, a secondary peak in FSD emerged around 144 μm (Fig. 4.15, see the FSD with guar gum dosage at 15 mg/L). At a higher dosage, the secondary peak diminishes while the span of size range becomes larger than that for low dosages. The change of mean and median size with guar gum concentration also shows that there is an optimal dosage to form the largest mean and median floc sizes (Fig. 4.16). This

finding consists with Furukawa et al. (2014)'s observation, although they are studying a different clay mineral (i.e., montmorillonite) so the optimal dosages are different. Different from that given by Tan et al. (2012, 2014) and Zhang et al. (2013) for guar gum and kaolinite mixture, this study does not show comparable bi-mode or tri-mode on FSD. This may be because they circulated water between their mixing jar and a small tube for measurement. In addition, the shear rate in their measuring section is very different from that in their mixing jar where flocs are developed.

Since a relatively high number of larger flocs exist because of the guar gum effect, it is generally difficult to give satisfying modeling results for both FSD and representative size at this time. This is probably a limitation of this current model because only a maximum of eight size classes is allowed. Despite this weakness, an example of FSD for guar gum concentration 5 mg/L (Fig. 4.17) matches reasonably with the difference in predicted and experimental mean and median size of 4.9 μm and 3.1 μm , respectively. There are two possible ways to improve the model: (1) relax the assumption of constant C_1 and C_2 , and (2) increase the number of nodes from 8 to 16. However, these are left for future studies.

5. Conclusions

An image acquisition and analyzing system has been developed for measuring floc size distribution (FSD) with a minimum floc size of around 5 μm , represented by 2×2 pixels. This system has been validated with sample particle sets that have given particle sizes and size ranges. Afterwards, it was applied to explore the effects of SSC, shear rate, salinity, and an organic matter (guar gum) on kaolinite flocculation. The flocculation model developed

previously for simulating FSD (Shen and Maa, 2015) was also applied to mimic the measurements with reasonable agreement. Specific conclusions include:

(1) This study shows the development of an inexpensive camera system that uses a Sony Alpha NEX-5 camera body, a Nikon micro lens, three extension tubes and a close-up lens to achieve a subject to image ratio of 1: 2.2, which translates to a resolution of 2.2 μm per pixel.

(2) Multiple LEDs were powered with over-voltage to provide the minimum light source required for synchronizing the operation of the camera system with a shutter speed of 1/1000 s in order to freeze fast moving objects.

(3) Floc size distributions have been processed using MATLAB Image Processing Toolbox, through the process of background removal, thresholding, small object (noise) removal, dilation and erosion, on-broader particle removal, hole-filling, and pixel gradient checking. The selection of the threshold value and critical gradient depends on particle properties and ambient environments. Thus, the use of these values for other applications should be checked.

(4) Although the existence of salt promotes kaolinite flocculation, the effect will be saturated when the salinity is as low as 0.5 ppt.

(5) The effect of guar gum on kaolinite flocculation is highly dependent on its dosage. For kaolinite concentration $c = 0.52 \text{ g/L}$, the maximum equilibrium mean (56.6 μm) and median size (35.2 μm) appears when guar concentration $c_{\text{guar}} = 15 \text{ mg/L}$.

(6) The current flocculation model, which uses a constant aggregation and breakage fitting parameter C_1 and C_2 with 7 size classes, can reasonably simulate the floc size distribution as well as its representative size for pure kaolinite with or without salt. For

kaolinite with a high content of organic matters, however, it is sometimes difficult to match both the FSD and the mean size. This could be improved further by using more nodes when a high accurate compiler is available or when a better understanding of the aggregation and breakage processes is available.

Acknowledgments

The authors would like to acknowledge funding support from the Student Research Grant at the Virginia Institute of Marine Science (VIMS), a research grant (Contract number: 774080) from Korea Institute of Ocean Science and Technology (KIOST), China Scholarship Council (CSC) scholarship, the State Key Program of National Natural Science of China (Grant No. 41230640 & 51339005), and the National Natural Science Foundation of China (Grant No. 51409081). The authors also thank several apparatus and reagent assistances provided by Drs. J. D. Shields, G. M. Cartwright, and A. Miller.

References

- Agrawal, Y.C., Pottsmith, H.C., 2000. Instruments for particle size and settling velocity observations in sediment transport. *Marine Geology* 168, 89–114.
- Allen, T., 1997. Particle Size Measurement. In: Powder Sampling and Particle Size Measurement. Chapman and Hall, London.
- Ariathurai, R., MacArthur, R.C., Krone, R.B., 1977. Mathematical model of estuarial sediment transport, Technical Report D-77-12, U.S. Army Engineer Waterways Experiment Station, Vicksburg, MS.
- Avnimelech, Y., Ritvo, G., Meijer, L.E., Kochba, M., 2001. Water content, organic carbon and dry bulk density in flooded sediments. *Aquacultural Engineering* 25, 25–33.
- Bale, A.J., Morris, A.W., 1987. In situ measurement of particle size in estuarine waters. *Estuarine. Coastal and Shelf Science* 24, 253–263.
- BS3406 – British Standard Methods for Determination of Particle Size Distribution, 1963.
- Cartwright, G.M., Friedrichs, C.T., Sanford, L.P., 2011. In situ characterization of estuarine suspended sediment in the presence of muddy flocs and pellets. In: Wang, P., Rosati, J.D., Roberts, T.M., (eds.), *Coastal Sediments 2011*, World Scientific, pp. 642–655.
- Collins, T.J., 2007. ImageJ for microscopy. *BioTechniques* 43, 25–30.
- Curran, K.J., Hill, P.S., Milligan, T.G., 2003. Time variation of floc properties in a settling column. *Journal of Sea Research* 49, 1–9.
- de Boer, D.H., Stone, M., 1999. Fractal dimensions of suspended solids in streams: Comparison of sampling and analysis techniques. *Hydrological Processes* 13, 239–254.

- Ducoste, J. J., Clark, M.M., Weetman, R.J., 1997. Turbulence in flocculators: The effects of tank size and impeller type. *AIChE Journal* 43, 328–338.
- Ducoste, J.J., Clark, M.M., 1998. The influence of tank size and impeller geometry on turbulent flocculation: I. experimental. *Environmental Engineering Science* 15, 215–224.
- Ducoste, J.J., Clark, M.M., 1999. Turbulence in flocculators: Comparison of measurements and CFD simulations. *AIChE Journal* 45, 432 – 436.
- Dyer, K. R., 1985. Coastal and Estuarine Sediment Dynamics, John Wiley and Sons.
- Eisma, D., Schuhmacher, T., Boekel, H., Van Heerwaarden, J., Franken, H., Laan, M., Vaars, A., Eijgenraam, F., Kalf, J., 1990. A camera and image-analysis system for in situ observation of flocs in natural waters. *Netherlands Journal of Sea Research* 27, 43–56.
- Eisma, D., Bernard, P., Cadee G.C., Ittekkot, V., Kalf, J., Laane, R., Martin, J.M., Mook, W.G., Van Put, A., Schuhmacher, T., 1991. Suspended-matter particle size in some west-European estuaries; part I: Particle-size distribution. *Netherlands Journal of Sea Research* 28, 193–214.
- Eshel, G., Levy, G.J., Mingelgrin, U., Singer, M.J., 2004. Critical evaluation of the use of laser diffraction for particle-size distribution analysis. *Soil Science Society of America Journal* 68, 736–743.
- Fennessy, M.J., Dyer, K.R., Huntley, D.A., 1994. INSSEV: An instrument to measure the size and settling velocity of flocs in situ. *Marine Geology* 117, 107–117.
- Fettweis, M., 2008. Uncertainty of excess density and settling velocity of mud floc derived from in-situ measurements. *Estuarine, Coastal and Shelf Science* 78, 426–436.

- Flory, E.N., Hill, P.S., Milligan, T.G., Grant, J., 2004. The relationship between floc area and backscatter during a spring phytoplankton bloom. *Deep-Sea Research I* 51, 213–223.
- Furukawa, Y., Watkins, J.L., 2012. Effect of organic matter on the flocculation of colloidal montmorillonite: A modeling approach. *Journal of Coastal Research* 28, 726–737.
- Furukawa, Y., Reed, A.H., Zhang G., 2014. Effect of organic matter on estuarine flocculation: a laboratory study using montmorillonite, humic acid, xanthan gum, guar gum and natural estuarine flocs. *Geochemical Transactions* 15, 1–9.
- Gibbs, R.J., 1982. Floc stability during Coulter-Counter size analysis. *Journal of Sedimentary Research* 52, 657–660.
- Gonzalez, R.C., Woods, R.E., Eddins, S.L., 2009. Digital image processing using MATLAB (Second Edition). Gatesmark Publishing.
- Hopkins, D.C., Ducoste, J.J., 2003. Characterizing flocculation under heterogeneous turbulence. *Journal of Colloid and Interface Science* 264, 184–194.
- Jarvis, P., Jefferson, B., Parsons, S.A., 2005. Measuring floc structural characteristics. *Reviews in Environmental Science and Bio/Technology* 4, 1–18.
- Keyvani, A., Strom, K., 2013. A fully-automated image processing technique to improve measurement of suspended particles and flocs by removing out-of-focus objects. *Computers & Geosciences* 52, 189–198.
- Keyvani, A., Strom, K., 2014. Influence of cycles of high and low turbulent shear on the growth rate and equilibrium size of mud flocs. *Marine Geology* 354, 1–14.

- Krone, R.B., 1962. Flume studies of the transport of sediment in estuarial shoaling process, Final Report, Hydraulic Engineering Laboratory and Sanitary Engineering Research Laboratory, University of California, Berkeley.
- Kumar, R., Ruiz, A., Strom, K., 2009. A digital floc camera for nonintrusive measurement of floc parameters. *World Environmental and Water Resources Congress 2009*, 1–6.
- Kumar, R.G., Strom, K., Keyvani, A., 2010. Floc properties and settling velocity of San Jacinto estuary mud under variable shear and salinity conditions. *Continental Shelf Research* 30, 2067–2081.
- Kumar, M.N.V.R., 2000. A review of chitin and chitosan applications. *Reactive & Functional Polymers* 46, 1-27.
- Lintern, D.G., 2003. Influences of flocculation on bed properties for fine-grained cohesive sediment. (Ph.D. Dissertation) Oxford University, United Kingdom.
- Lintern, G., Sills, G., 2006. Techniques for automated measurement of floc properties. *Journal of Sedimentary Research* 76, 1183–1195.
- Liss, S.N., Droppo, I.G., Leppard, G.G., Milligan, T.G., 2005. Flocculation in natural and engineered environmental systems. CRC Press, Boca Raton, Florida.
- Maggi, F., Manning, A.J., Winterwerp, J.C., 2006. Image separation and geometric characterization of mud flocs. *Journal of Hydrology* 326, 325–348.
- Maggi, F., Mietta, F., Winterwerp, J.C., 2007. Effect of variable fractal dimension on the floc size distribution of suspended cohesive sediment. *Journal of Hydrology* 343, 43–55.
- Manning, A.J., Dyer, K.R., 2002. The use of optics for their situ determination of flocculated mud characteristics. *Journal of Optics A: Pure and Applied Optics* 4, S71–S81.

- Mazzoli, A., Moriconi, G., 2014. Particle size, size distribution and morphological evaluation of glass fiber reinforced plastic (GRP) industrial by-product. *Micron* 67, 169–178.
- McGraw, R., 1997. Description of aerosol dynamics by the quadrature method of moments. *Aerosol Science and Technology* 27, 255–265.
- Mehta, A.J., 2013. An introduction to hydraulics of fine sediment transport. World Scientific Publishing Company, pp. 1060.
- Mietta, F., Maggi, F., Winterwerp, J.C., 2008. Chapter 19: sensitivity to breakup functions of a population balance equation for cohesive sediments. INTERCOH 2005. *Sediment and Ecohydraulics* 9, pp. 275–286.
- Mietta, F., Chassagne, C., Winterwerp, J., 2009. Shear-induced flocculation of a suspension of kaolinite as function of pH and salt concentration. *Journal of Colloid and Interface Science* 336, 134–141.
- Mikes, D., Verney, R., Lafite, R., Belorgey, M., 2004. Controlling factors in estuarine flocculation processes: experimental results with material from the Seine estuary, Northwestern France. *Journal of Coastal Research* SI 41, 82–89.
- Mikkelsen, O.A., Pejrup, M., 2001. The use of a LISST-100 laser particle sizer for in-situ estimates of floc size, density and settling velocity. *Geo-marine Letter* 20, 187–195.
- Mikkelsen, O.A., Milligan, T.G., Hill, P.S., Moffatt, D., 2004. NSSECT—an instrumented platform for investigating floc properties close to the seabed. *Limnology and Oceanography: Methods* 2, 226–236.
- Mitchell, J.K., Soga, K., 2005. Fundamentals of soil behavior. (Third Edition). John Wiley & Sons, Inc., Hoboken, New Jersey.

- Monnier, O., Klein, J.P., Hoff, C., Ratsimba, B., 1996. Particle size determination by laser reflection: Methodology and problems. *Particle & Particle Systems Characterization* 13, 10–17.
- Nagata, S., 1975. Mixing: Principles and applications. John Wiley & Sons Inc., pp. 458.
- Otsu, N., 1979. A threshold selection method from gray-level histograms. *IEEE Transactions on Systems, Man and Cybernetics* 9, 62–66.
- Phillips, J.M., Walling, D.E., 1995. An assessment of the effects of sample collection, storage and resuspension on the representativeness of measurements of the effective particle size distribution of fluvial suspended sediment. *Water Research* 29, 2498–2508.
- Prat, O.P., Ducoste, J.J., 2006. Modeling spatial distribution of floc size in turbulent processes using the quadrature method of moment and computational fluid dynamics. *Chemical Engineering Science* 61, 75–86.
- Rasband, W., 1997. ImageJ. U.S. National Institutes of Health (<http://rsb.info.nih.gov/ij/>).
- Russ, J.C., 2011. The image processing handbook. Sixth ed., CRC Press, Boca Raton, Florida.
- Setayesh, M., Zhang, M., Johnston, M., 2013. A novel particle swarm optimisation approach to detecting continuous, thin and smooth edges in noisy images. *Information Sciences* 246, 28–51.
- Sezgin, M., Sankur, B., 2004. Survey over image thresholding techniques and quantitative performance evaluation. *Journal of Electronic Imaging* 13, 146–165.
- Shao, Y., Yan, Y., Maa, J. P.Y., 2011. In situ measurements of settling velocity near Baimao shoal in Changjiang estuary. *Journal of Hydraulic Engineering* 137, 372–380.

- Shen, X., Maa, J.P.Y., 2015. Modeling floc size distribution of suspended cohesive sediments using quadrature method of moments. *Marine Geology* 359, 106–119.
- Shen, X., 2016. Modeling flocculation and deflocculation processes of cohesive sediments. (Ph.D. Dissertation) Virginia Institute of Marine Science, The College of William and Mary, Gloucester Point, Virginia.
- Shih, F.Y., 2009. Image Processing and Mathematical Morphology. CRC Press, Boca Raton, Florida.
- Smerdon, A.M., Rees, J.M., Vincent, C.E., 1998. An acoustic backscatter instrument to measure near-bed sediment processes. Aquatec Electronic Ltd., Hampshire, United Kingdom.
- Smith, S.J., 2010. Fine sediment dynamics in dredge plumes. (Ph.D. Dissertation) The College of William and Mary, Gloucester Point, Virginia.
- Smith, S.J., Friedrichs, C.T., 2011. Size and settling velocities of cohesive flocs and suspended sediment aggregates in a trailing suction hopper dredge plume. *Continental Shelf Research* 31, 500–553.
- Smith, S.J., Friedrichs, C.T., 2015. Image processing methods for in situ estimation of cohesive sediment floc size, settling velocity, and density. *Limnology and Oceanography: Methods* 13, 250–264.
- Smoluchowski, M., 1917. Versuch einer Mathematischen Theorie der Koagulationskinetik Kolloider Lösungen. *Zeitschrift für Physikalische Chemie* 92, 129–168. (in German)
- Spicer, P.T., Keller, W., Pratsinis, S.E., 1996. The effect of impeller type on floc size and structure during shear-induced flocculation. *Journal of Colloid and Interface Science* 184, 112–122.

- Styles, R., 2006. Laboratory evaluation of the LISST in a stratified fluid. *Marine Geology* 227, 151-162.
- Su, J.W., Gu, Z.L., Li, Y., Feng, S.Y., Xu, X.Y., 2007. Solution of population balance equation using quadrature method of moments with an adjustable factor. *Chemical Engineering Science* 62, 5897–5911.
- Tajima, R., Kato, Y., 2011. Comparison of threshold algorithms for automatic image processing of rice roots using freeware ImageJ. *Field Crops Research* 121, 460–463.
- Tan, X., Zhang, G., Yin, H., Reed, A.H., Furukawa, Y., 2012. Characterization of particle size and settling velocity of cohesive sediments affected by a neutral exopolymer. *International Journal of Sediment Research* 27, 473–485.
- Tan, X., Hu, L., Reed, A.H., Furukawa, Y., Zhang, G., 2014. Flocculation and particle size analysis of expansive clay sediments affected by biological, chemical, and hydrodynamic factors. *Ocean Dynamics* 64, 143–157.
- Van Leussen, W., Cornelisse, J.M., 1993. The determination of the sizes and settling velocities of estuarine flocs by an underwater video system. *Netherlands Journal of Sea Research* 31, 231–241.
- Verney, R., Lafite, R., Brun-Cottan, J.C., 2009. Flocculation potential of estuarine particles: The importance of environmental factors and of the spatial and seasonal variability of suspended particulate matter. *Estuaries and Coasts* 32, 678-693.
- Winterwerp, J.C., 1998. A simple model for turbulence induced flocculation of cohesive sediment. *Journal of Hydraulic Research* 36, 309–326.

Yen, J.C., Chang, F.J., Chang, S., 1995. A new criterion for automatic multilevel thresholding.

IEEE Transactions on Image Processing 4, 370–378.

Zhang, G., Yin, H., Lei, Z., Reed, A.H., Furukawa, Y., 2013. Effects of exopolymers on

particle size distributions of suspended cohesive sediments. *Journal of Geophysical*

Research: Oceans 118, 3473–3489.

Zhu, Q., 1996. Efficient evaluations of edge connectivity and width uniformity. *Image and*

Vision Computing 14, 21–34.

Table 4.1 Summary of experimental conditions, camera measurement results and model simulation results.

Case	c (g/L)	G (s^{-1})	Salt	c_{guar} (mg/L)	T_f (hr)	d_{10M} (μm)	d_{10E} (μm)	D_{50M} (μm)	D_{50E} (μm)	C_1	C_2
1	0.28	55	No	0	48	25.5	24.7	18.5	20.9	0.85	3.2E-5
2	0.28	45	No	0	48	26.9	27.2	19.9	23.6	0.85	3.2E-5
3	0.52	55	No	0	48	34.7	32.9	25.8	25.8	0.85	3.2E-5
4	0.52	35	No	0	48	38.8	38.4	28.9	30.2	0.85	3.2E-5
5	0.28	55	Yes	0	24	37.1	37.9	27.9	30.0	0.95	1.7E-5
6	0.52	55	No	5	24	32.2	37.1	24.2	27.3	1.0	4.4E-5
7	0.52	55	No	10	24	-	45.4	-	28.8	-	-
8	0.52	55	No	15	24	-	56.6	-	35.2	-	-
9	0.52	55	No	20	24	-	47.7	-	29.9	-	-
10	0.52	55	No	30	24	-	40.0	-	22.3	-	-

Note: c – kaolinite weight concentration; G – shear rate; c_{guar} – guar gum concentration; T_f – measuring time which is representing equilibrium state; d_{10M} – model predicted mean size; d_{10E} – experimental measured mean size; D_{50M} – model predicted median size; D_{50E} – experimental measured median size.

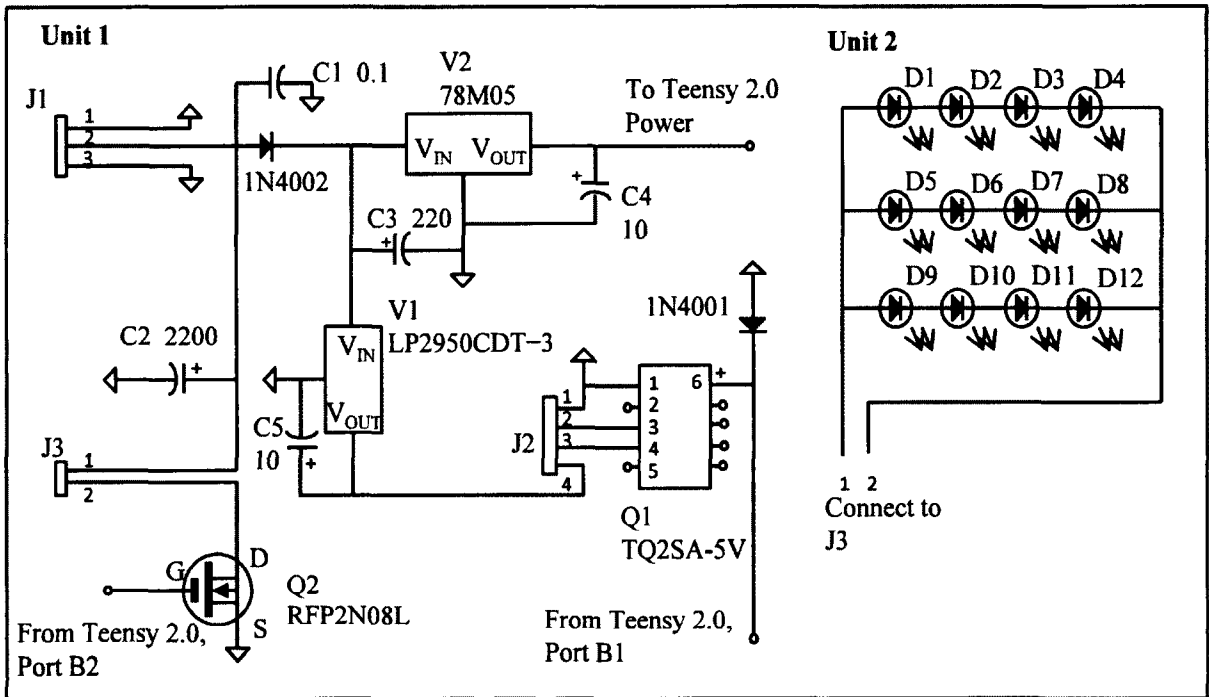


Fig. 4.1 Electric circuit for controlling camera for picture taking and LED light. D1 to D12 are the same surface mounted 1 watt white LED OVSPW1BCR4. C1 to C4 are capacitors with the number marked in unit of μF . Other electronic components are marked in the figure.

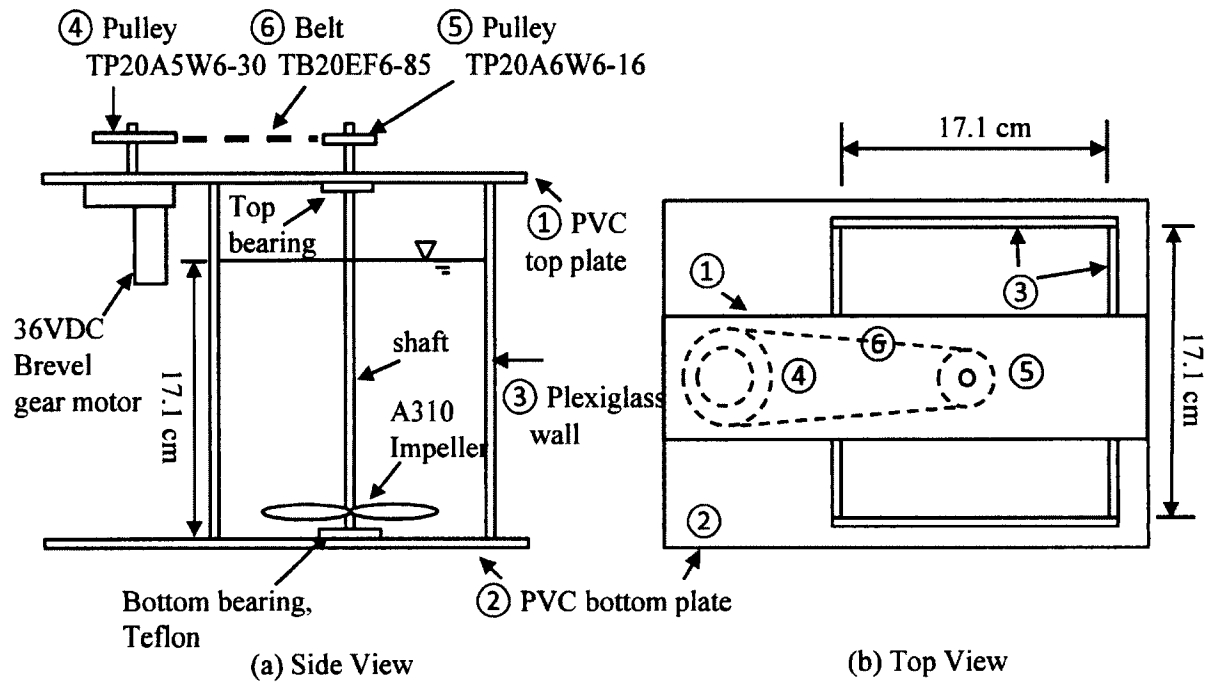


Fig. 4.2 The mixing chamber. The impeller is installed 4 cm above the bottom. The maximum chamber-averaged shear rate is 217 s^{-1} .

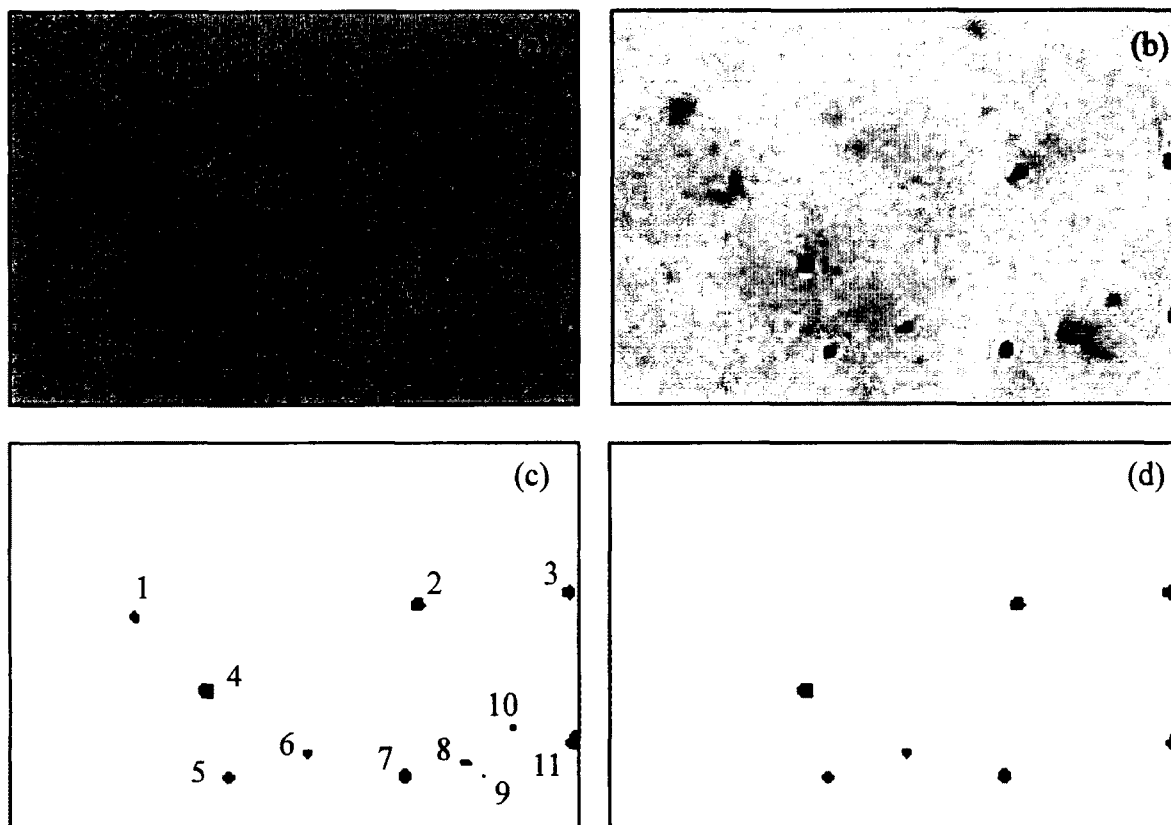


Fig. 4.3 Example of image analyzing procedure for silver coated hollow glass spheres with nominal size $10\ \mu\text{m}$. (a) Original greyscale figure, (b) after background removing, (c) after thresholding, and (d) after removing out-of-focus particles. Note that (a) and (b) are displayed as its negative with contrast adjustment. Since abundant particles are obtained in one image in this case, only the central $1/27 \times 1/27$ are represented in this diagram, so that the particle No. 11 in (c) is not on the border of the image.

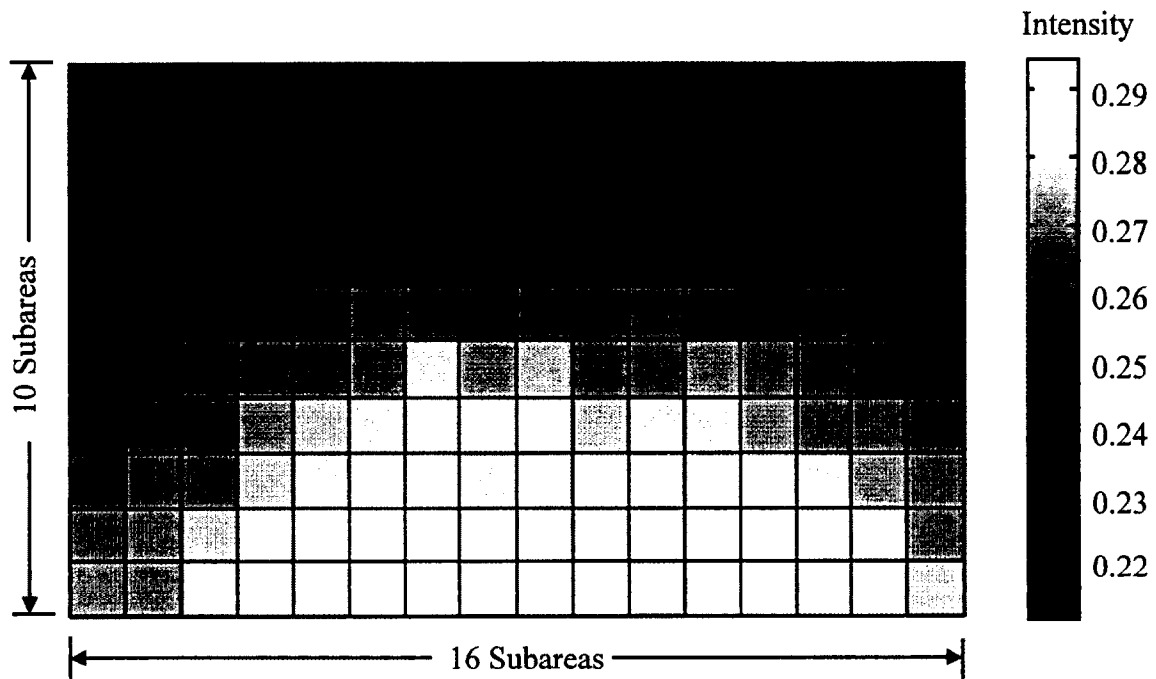


Fig. 4.4 Example to show the different background intensity in an image for polystyrene particles. 16×10 subareas are selected to cover the entire 4912×3264 pixels.

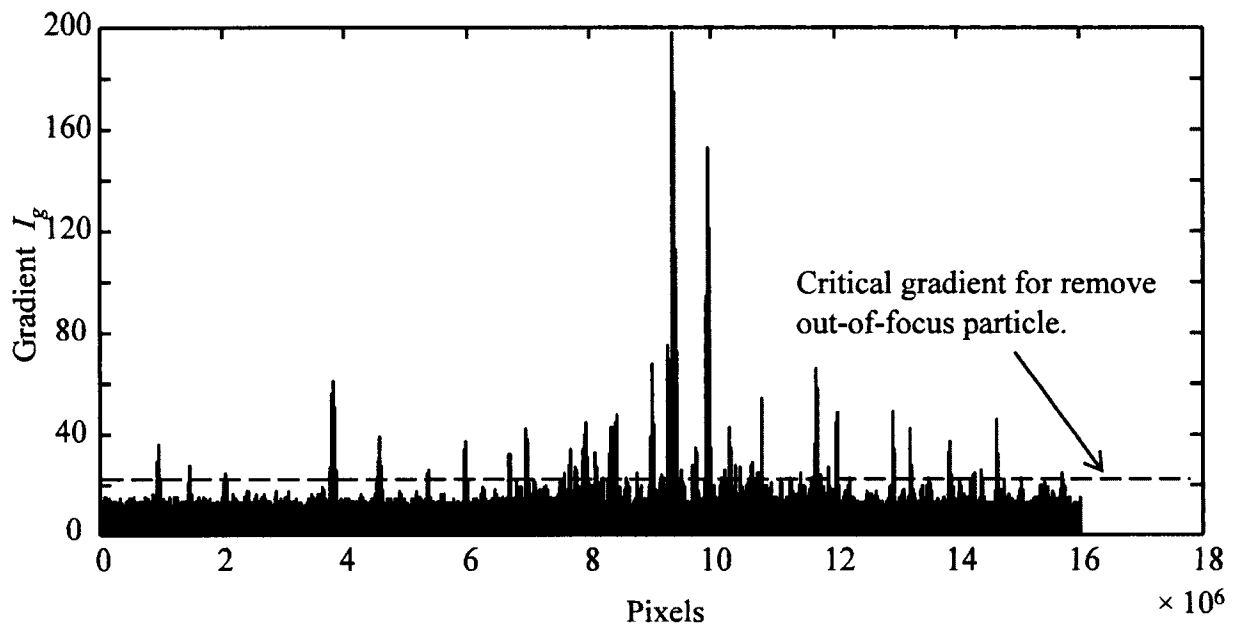


Fig. 4.5 Example of gradients for each pixel and the selection of the critical gradient for kaolinite suspensions.

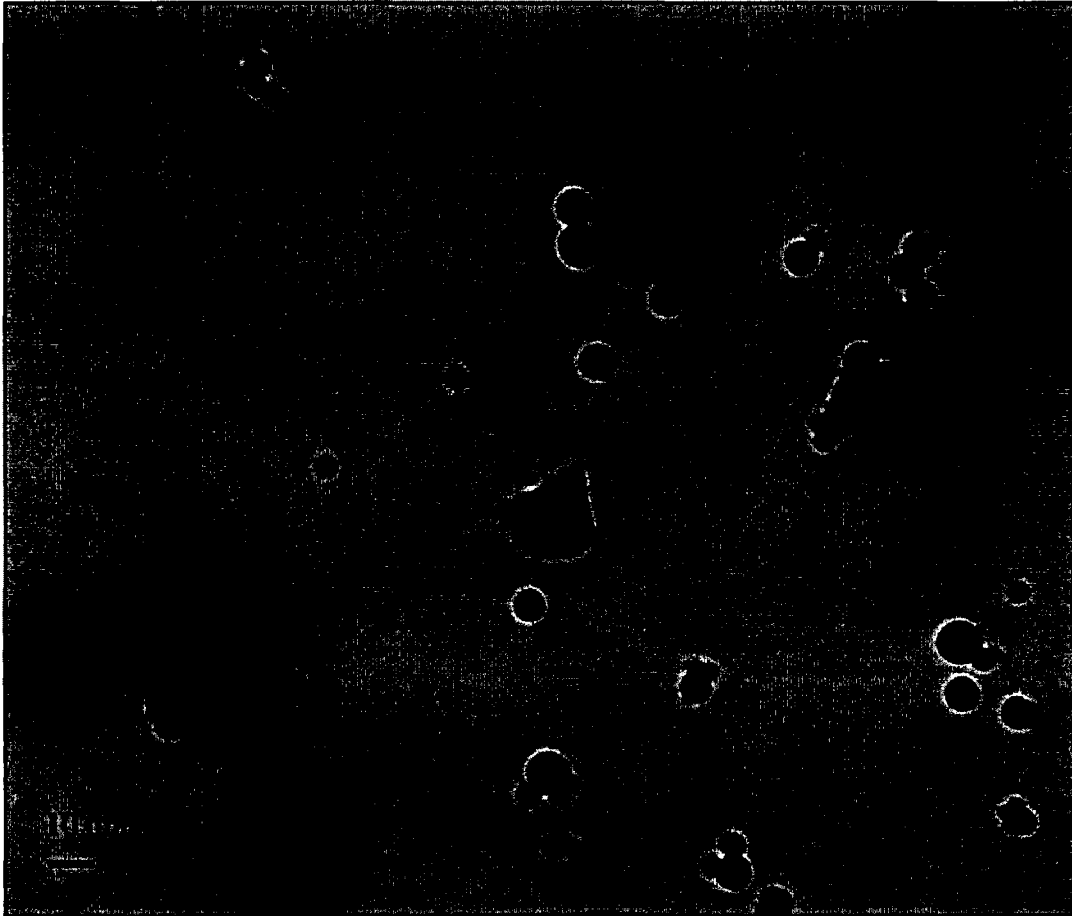


Fig. 4.6 Example of microscope image (magnified 400 times) of the silver coated hollow glass spheres. Even with 100 times magnification, the image is sharp enough to be used as a ground truth for validation purposes.

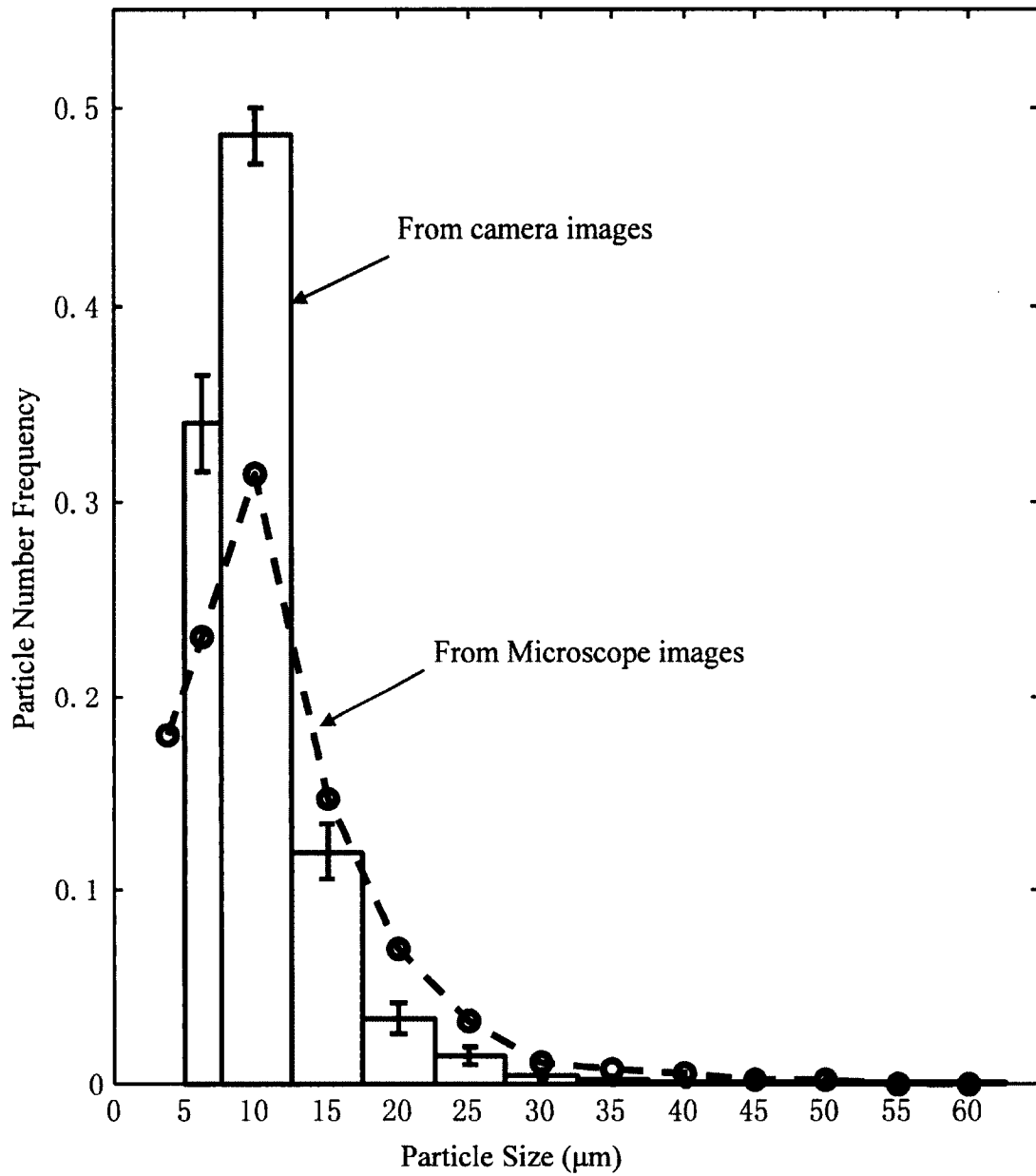


Fig. 4.7 Comparison of FSDs from images taken by using the microscope and the camera for the silver coated hollow glass spheres. Vertical line segments in the bar plot show the standard deviation of ten randomly selected images.

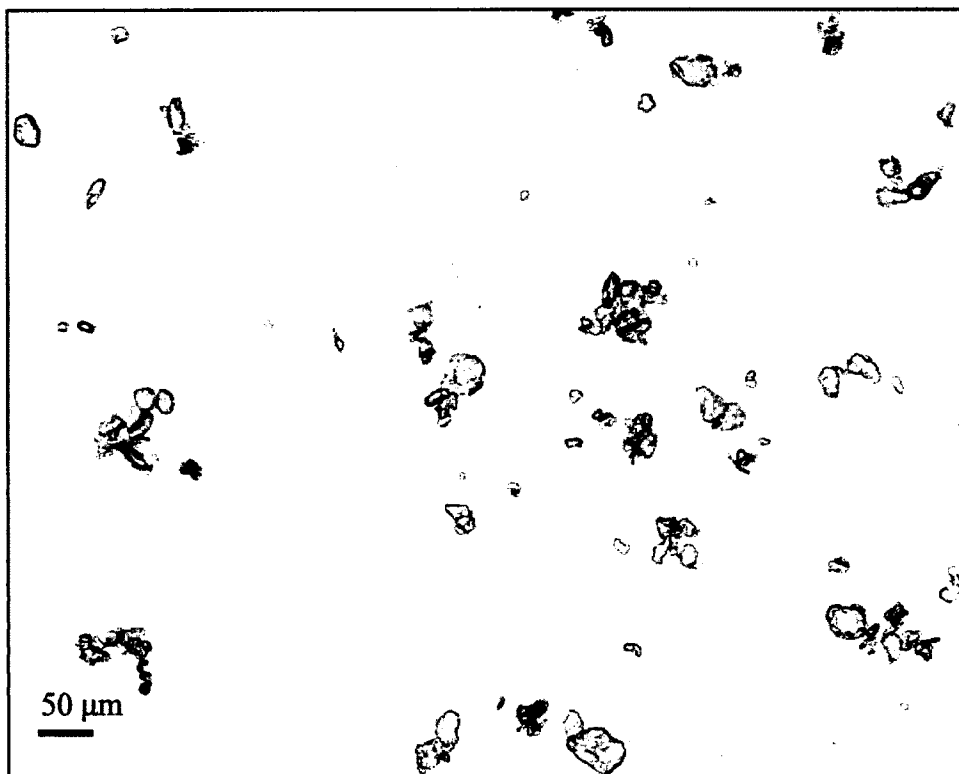


Fig. 4.8 Example of a microscope image (magnified 100 times) of the polystyrene particles.

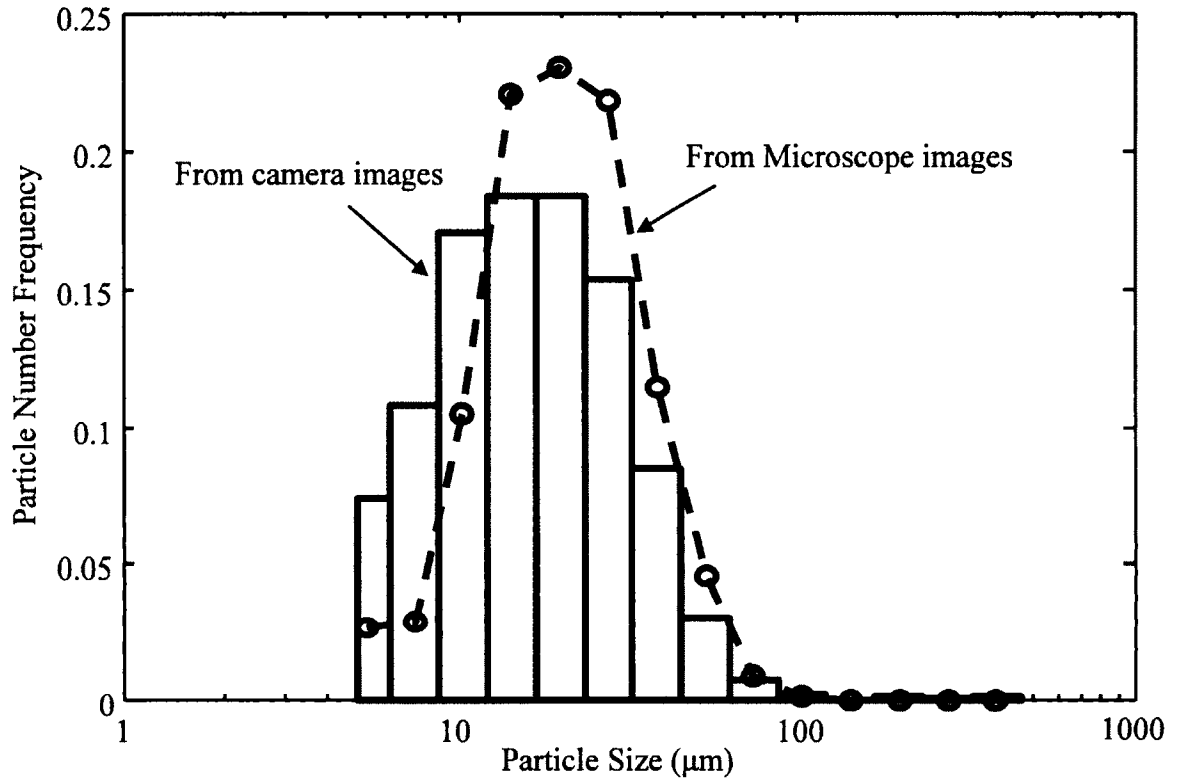


Fig. 4.9 Comparison of FSDs from images taken by using the microscope and the camera for the polystyrene particles.

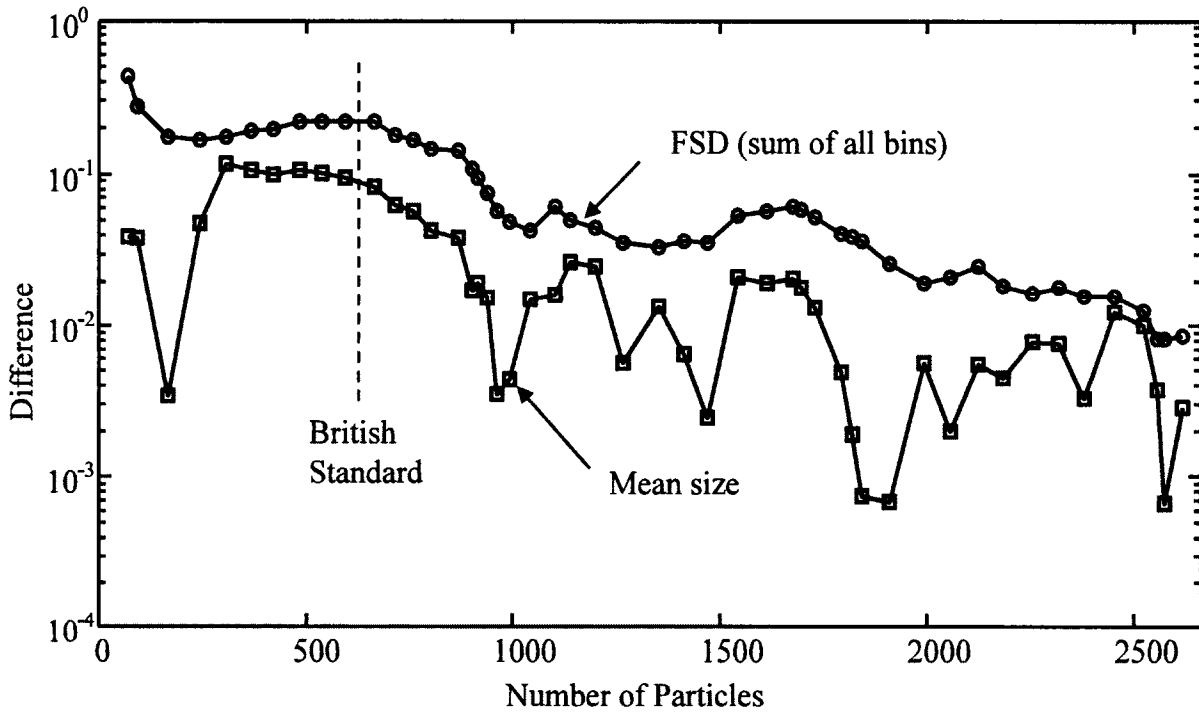


Fig. 4.10 The difference in calculated FSD and mean size with respect to the number of total polystyrene particles included in images used for processing FSD. Each symbol denotes one image, and the right most symbols represent using 49 images with a number of more than 2,500 particles. The dashed line represents that required by the British Standard, i.e., 625 particles, or 11 images.

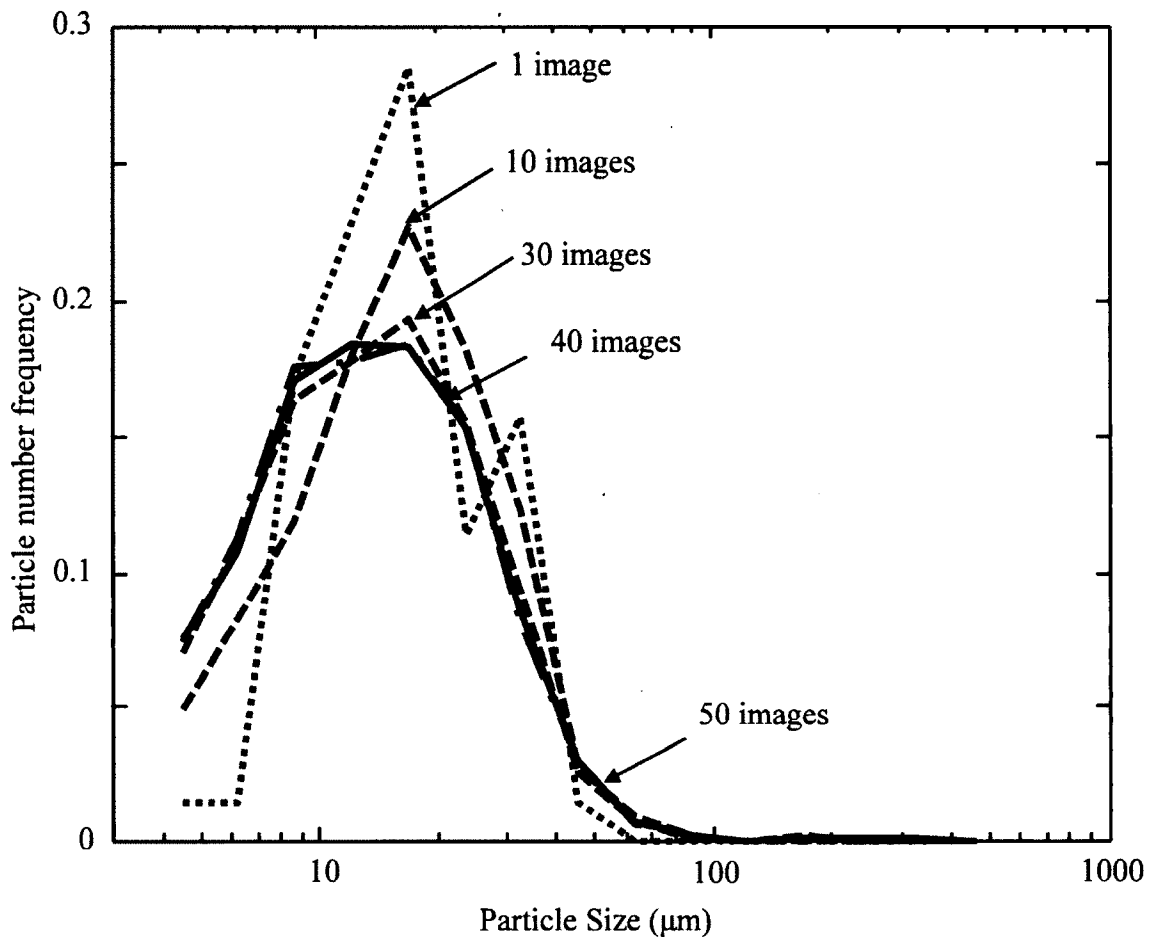


Fig. 4.11 The difference in each bin of the measured FSDs to show the convergence. The result of using 50 images is assumed as the ground truth.

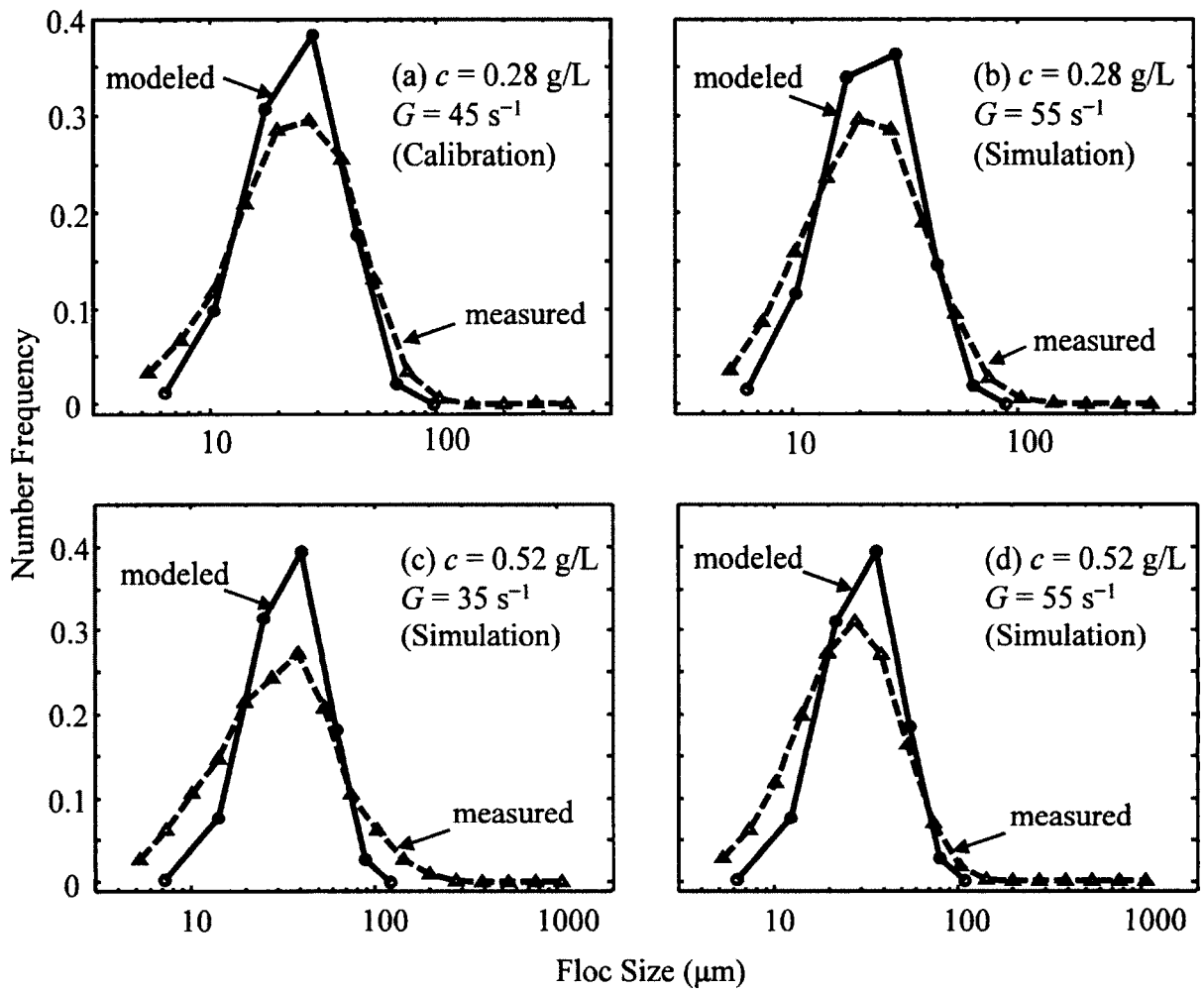


Fig. 4.12 Model calibration and simulation for pure kaolinite flocculation results for various shear rates and suspended sediment concentrations.

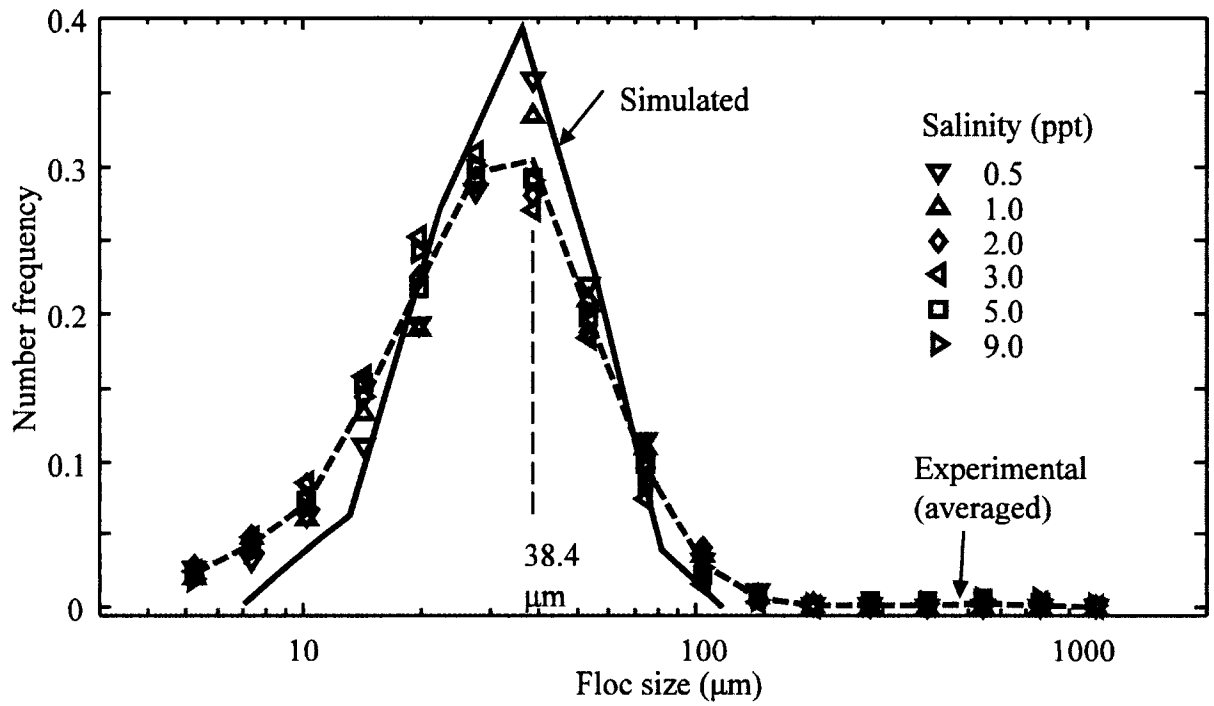


Fig. 4.13 Effects of salinity on equilibrium FSDs of suspended kaolinite with shear rate = 55 s^{-1} and suspended sediment concentration = 0.28 g/L .

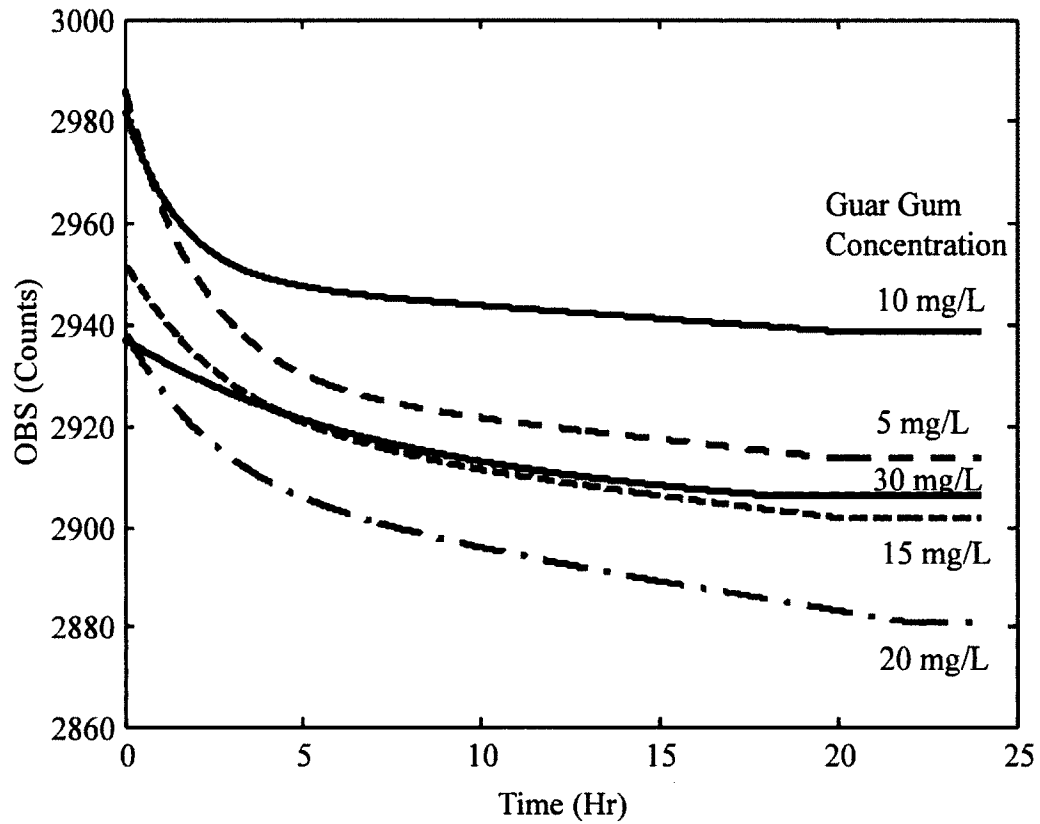


Fig. 4.14 Time evolution of OBS counts during flocculation tests for various guar gum dosages. Shear rate $G = 55 \text{ s}^{-1}$ and initial suspended kaolinite concentration $c = 0.52 \text{ g/L}$.

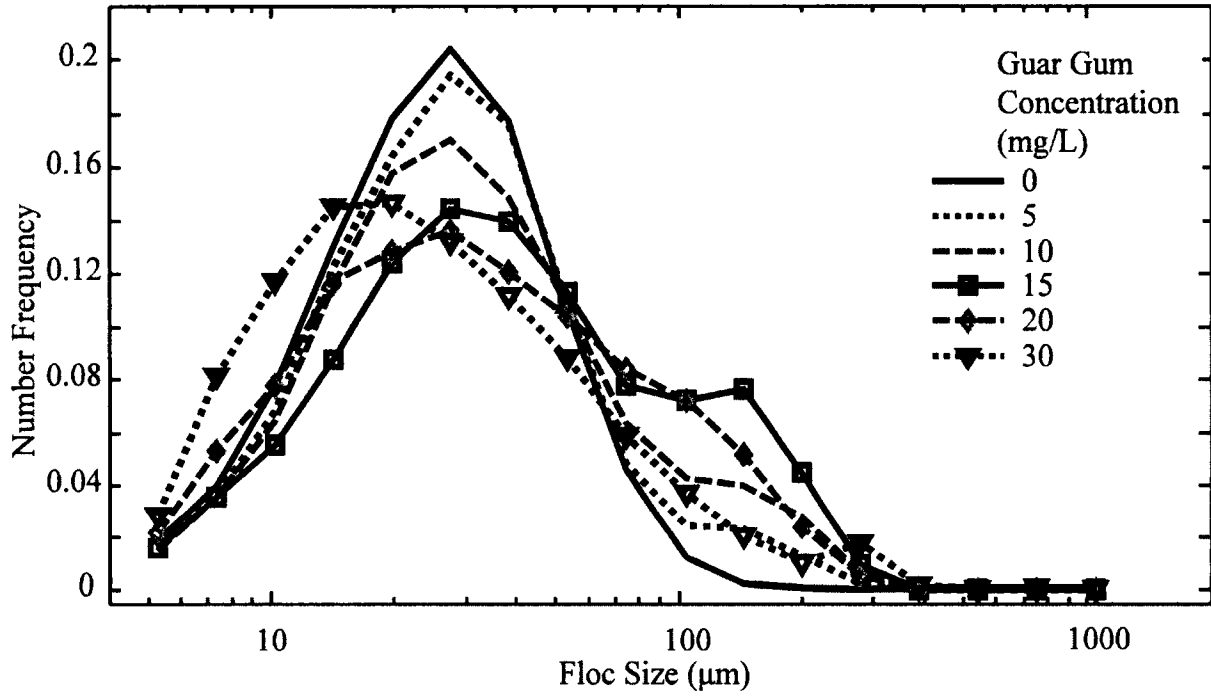


Fig. 4.15 Experimental results to show the effect of guar gum dosage on the equilibrium FSDs of kaolinite suspension in tap water. Shear rate $G = 55 \text{ s}^{-1}$ and initial suspended sediment concentration $c = 0.52 \text{ g/L}$.

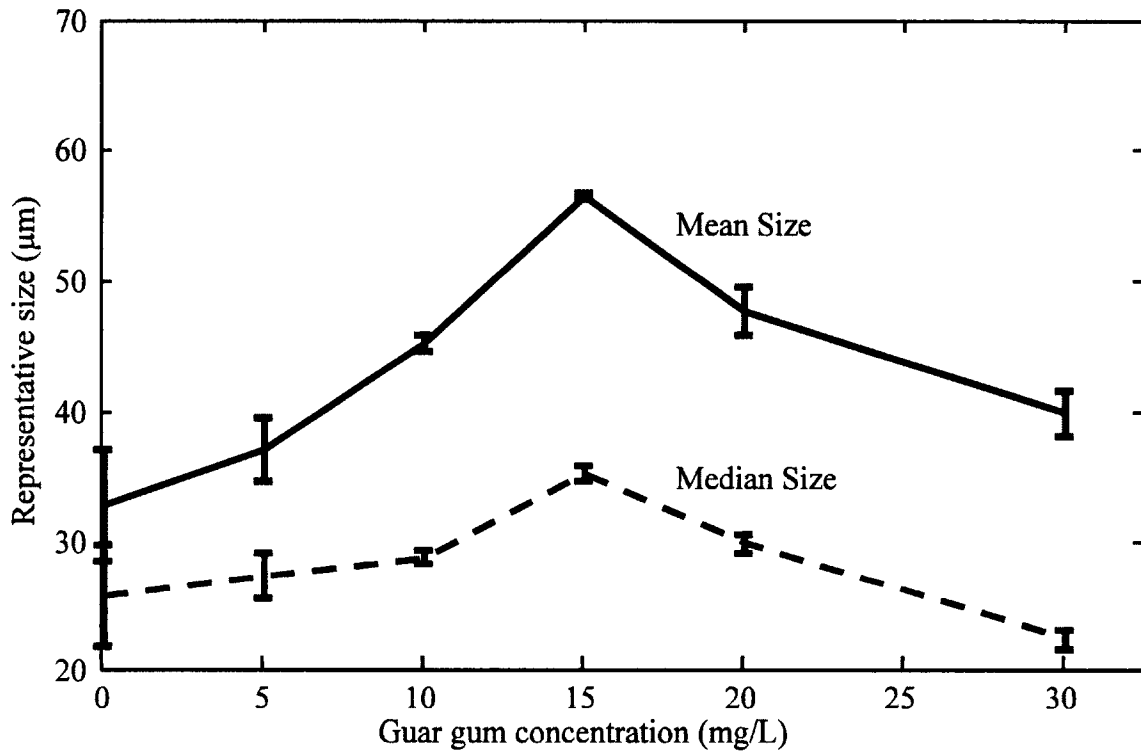


Fig. 4.16 The change of mean and median kaolinite floc sizes caused by different guar gum dosages. Vertical line segments represent the variation of measurements at 23.0 hr, 23.5 hr, and 24.0 hr. Shear rate $G = 55 \text{ s}^{-1}$ and initial suspended kaolinite concentration $c = 0.52 \text{ g/L}$.

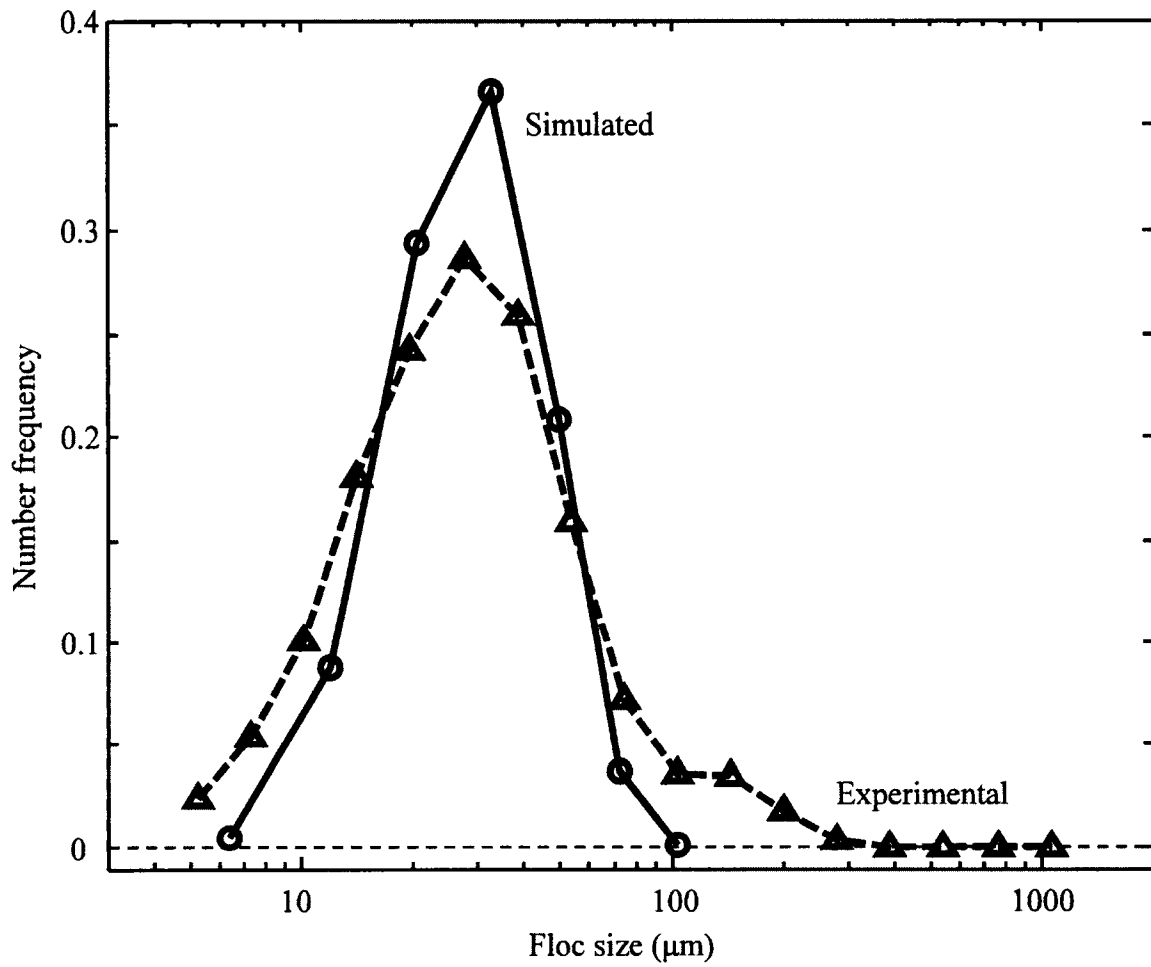


Fig. 4.17 Comparison of experimental and model-simulated equilibrium FSDs for kaolinite suspension with guar gum concentration $c_{\text{guar}} = 5 \text{ mg/L}$, shear rate $G = 55 \text{ s}^{-1}$, and initial suspended kaolinite concentration $c = 0.52 \text{ g/L}$.

CHAPTER V

FLOC SIZE DISTRIBUTIONS OF SUSPENDED KAOLINITE IN AN ADVECTION TRANSPORT DOMINATED TANK: MEASUREMENTS AND MODELING

Abstract

In estuaries and coastal waters, floc size and its statistical distributions of cohesive sediments are primarily important, due to their effects on the settling velocity and thus deposition rates of cohesive aggregates. The development of a robust flocculation model that includes the predictions of Floc Size Distributions (FSDs), however, is still in its infant stage. In this study, a one-dimensional (1-D) flocculation model along a conceptual streamtube is developed. This model is based on solving the population balance equation to find the FSDs by using the quadrature method of moments. To validate this model, a laboratory experiment is carried out to produce an advection transport dominant environment in a cylindrical tank. The flow field is generated by a marine pump mounted at the central bottom, with its outlet facing upward. This setup generates an axially symmetric flow which is measured by an acoustic Doppler velocimetry (ADV). The measurement results provide the input hydrodynamic data required for this 1-D model. The other measurement results, the FSDs, are acquired by using an automatic underwater camera system and the resulting images are analyzed to validate the predicted FSDs. This study shows that the FSDs as well as their representative sizes can be efficiently and reasonably simulated by this conceptual 1-D model.

Key words: kaolinite; flocculation; floc size distributions; streamtube model; laboratory experiment.

1. Introduction

Estuarine morphology is mainly influenced by mud deposition. Among all sedimentation processes, the settling of suspended particles is the most important process to determine mud deposition behaviors (e.g., Chisholm, 1999; McAnally, 2000; Mietta, 2010). Individual clay minerals have little chance to settle on the bed because of their small sizes, and thus, low settling velocities to resist upward transport. Clay sediments, however, are mostly presented as flocs or aggregates, which have higher settling velocities as the result of flocculation that significantly alters their structures (i.e., size, density, and population). In natural environments, flocs are formed after collision and attachment (because of cohesion) mainly due to the effect of turbulence shear, which practically limits the maximum floc size around the size of the Kolmogorov micro-scale if biological effects are excluded. Because of the effect of bio-factors such as extracellular polymeric substances, it is not uncommon to find that the sizes of bio-aggregates are much larger than the Kolmogorov micro-scale. These bio-flocs on one hand can provide food sources to promote the growth of aquatic animals, but on the other hand may also inhibit the growth of aquatic plants by light limitation, thereby preventing photosynthesis. These environmental issues are largely related to the flocculation processes of suspended particles, and their Floc Size Distributions (FSDs) are the most important indicator to quantitatively evaluate flocculation.

Flocculation is not a well-studied process because it can be affected by many factors such as sediment concentration, clay minerals, local shear rate, floc strength, ions in the water, and organic matter contents. Therefore, experiments that can isolate various affecting factors in order to understand the significance of each of the affected parameters in flocculation are

important. These experiments also provide valuable data to validate any numerical model.

Three types of devices, Couette reactors, oscillating grids, and chamber/tank mixers (either using a paddle/propeller/impeller or a pump), have been commonly used to examine the FSDs of suspended particles (Serra et al., 2008). In Couette flow experiments (e.g., Zhu et al., 2015; Vlieghe et al., 2014; Wyatt et al., 2013; Bubakova et al., 2013; Yuan and Farnood, 2010; Barbot et al., 2010; Frappier et al., 2010), the inner and outer cylinders can either both rotate (in the same or different directions), or only one rotates. The shear rate in this device is a constant and can be determined by the diameters and angular velocities of the cylinders. Serra et al. (2008) indicated that a Couette device produces larger flocs, compared with other flocculation devices that have the same average shear rate. This is because flocs in a Couette flow device are under a constant shear rate everywhere so that flocs have time to develop.

Oscillating grids are also widely used for studying flocculation processes and normally applied in settling columns/boxes (e.g., Pujol et al., 2010; Maggi et al., 2007). For small settling boxes, a micro-ADV (Acoustic Doppler Velocimetry) with a long “neck” can be inserted in the water column to measure turbulence directly (Pujol et al., 2010). Long settling columns can either provide zero-dimensional (0-D) conditions by only studying the floc conditions (e.g., size and density) at a selected location (Maggi et al., 2007) or provide one-dimensional (1-D) conditions by studying the floc conditions along the settling column (Van Leussen, 1994). In the above two cases, a homogenous turbulence field is generated in the entire column by using oscillating grids. Rectangular grids are often used for a best turbulent shear production, and the shear rates are controlled by the oscillation speed of the grids. For 0-D applications, equilibrium FSDs are measured at the lower part of the column

not far from the end of the grid to allow enough time to flocculate, while little change in turbulence along the falling trajectory. The existence of a homogenous shear rate in the entire vibration column, however, has not been verified yet. One can understand that turbulence at the vibration center of the grid should be larger than that at the edge of the grid.

Mixing chamber experiments are the other types of setups used to study flocculation (e.g., Mietta et al., 2009; Kumar et al., 2010). These experiments are primarily distinguished by the tank size, and thus, tank shape and turbulence generator. For small tanks, turbulence is usually generated by a rotating impeller. Tank averaged shear rate is determined by the impeller type (impeller diameter and power number), rotational speed, fluid volume, and fluid viscosity (Shen and Maa, *Submitted a*). By using the tank averaged shear rate and assuming a homogenous flow field, it provides a 0-D case for studying flocculation. The FSDs at the measuring location are assumed to represent the tank-averaged FSDs because of short trajectories for flocs to travel within the tank. For this reason, the tank cannot be big in order to limit the length of trajectory. Those using cubic tanks usually obtain floc images through the transparent wall (Keyvani and Strom, 2013; 2014; Shen and Maa, *Submitted a*), while those using cylindrical tanks (Mietta et al., 2009) often find FSDs through a laser diffraction device (e.g., Malvern Mastersizer) by assuming flocs are not broken during sampling, since taking images from a curvature wall to find floc size may produce bias on FSDs.

Note that even in these small mixing chambers, the flow field is not truly homogeneous. It is a complicated three-dimensional (3-D) flow that can be measured by using LDV (Laser Doppler Velocimeter, e.g., see Ducoste et al., 1997) or PIV (Particle Image Velocimetry

technology, e.g., see Ge et al., 2014). The spatial variability of FSDs within a small mixing chamber is limited because the time for a floc to travel among different shear zones is too short to reflect any significant change. Nevertheless, given enough time, the equilibrium FSD, which represents the balance of aggregation and breakup, can be used to display the results of the chamber-averaged shear rate (Ducoste et al., 1997).

In a relatively large tank as that used in this study with a volume about 0.5 m^3 , however, spatial variability of FSDs is measurable, although the differences are still limited. The shape of the tank is not important since the local FSDs are usually obtained by using an underwater camera system that takes pictures through a transparent cover of its waterproof house. The flow field can also be measured, e.g., by using an ADV device. The use of a LISST (Laser In-Situ Scattering and Transmissometer) instrument, however, is still difficult, if not impossible, because of the large size of the instrument itself.

Besides laboratory experiments, numerical modeling is another tool to study flocculation processes. A flocculation model usually simulates the change of number density n for particles with size L at any location x and at any time t . In this study, a Population Balance Model (PBM) (e.g., Shen and Maa, 2015) was used to simulate the FSDs by solving N differential equations for $dn_i(L_i, x, t) / dt$ ($i = 1, 2, \dots, N$) in which N is the number of size classes used to represent the FSD. PBMs have the advantage of considering various flocculation mechanisms (not limited to the effect of shear rate), and have the potential for further extension in order to include more floc properties (e.g., floc density) or include the biological and chemical effects (Shen, 2016). Previous PBMs for cohesive sediment flocculation are either based on discrete size classes that are only applicable for box (i.e., 0-D)

models (e.g., Maggi et al., 2007; Mietta et al., 2008, 2011), or use two-class PBMs (i.e., only two size classes) in order to be included in 1-D flow-mud applications (Lee et al., 2011; 2014). Therefore, none of those flocculation models can reasonably and efficiently simulate the FSDs of cohesive sediments without assuming a FSD shape *a priori*.

In this study, the FSDs of suspended kaolinite in an advection transport dominated tank are studied. This tank is large enough with a volume around 0.5 m^3 , so that it provides measurable changes of FSDs in the tank. It also provides the chance to check the development of a 1-D numerical model that simulates the FSDs along an idealized streamtube. The above are two objectives of this study. To achieve these two objectives, measurements of the flow field (e.g., mean velocity, turbulence kinetic energy, and energy dissipation rate) using an ADVOcean are carried out first. The measured flow field results are used as inputs for the 1-D model, which is an extension of a previously presented flocculation model for solving the FSDs (Shen and Maa, 2015). Through an updated camera system, the measurements of FSDs are gathered to validate the modeling results.

2. Experimental Setup

2.1 Flow field measurements

Tap water in a cylindrical tank (diameter = 0.75 m; water depth = 1.1 m) was agitated by using a RULE 3700 GPH (Gallon Per Hour) 12 Volt marine pump, mounted at the bottom of the tank (Fig. 5.1a). The pump outlet was modified by adding an adaptor, a 90 degree 1.5 inch PVC (polyvinyl chloride) elbow, an 8 cm long 1.5 inch PVC pipe, and a 1.5 inch PVC diffuser cap with hand drilled holes. The outlet was located at the center of the tank and 25

cm above the bottom of the tank. This setup generated an axially symmetric flow. The pump was powered with a fixed 12VDC power supply for at least half an hour until the flow field reached a steady condition. Velocity and turbulence were measured by using a 5MHz SonTek ADVOcean at selected points, and the measured values were used as inputs for the flocculation model.

ADV has been widely used as an excellent instrument for measuring 3-D fluid velocities based on the Doppler Effect (SonTek, 2001). A 5MHz SonTek ADVOcean, the ADV used in this study, measures the three velocity components of a sampling water parcel of about 2 cm^3 (a cylinder that has a 12 mm diameter and 18 mm height) which is located at 18 cm from the transmitter. The frequency of the instrument can be selected between 0.1 to 25 Hz, and velocity range settings can be selected between ± 5 and $\pm 500 \text{ cm/s}$.

The output of ADVOcean includes time series of instantaneous velocity components, amplitudes (signal strengths), and correlation parameters, for all three directions. At a few selected locations, where the signal strengths and correlations are high, data based on 10, 15, and 20 Hz measurement frequencies (with duration of 2, 4, and 6 minutes, respectively) are processed to check the differences of the mean velocities. Since there is no significance difference, velocity measurements in this study are collected at 10 Hz for 2 minutes (i.e., 1200 measurements) in these places, except for a few extremely high turbulence areas close to the pump outlet.

To obtain the time-averaged flow velocities from the measured time series of instantaneous velocity $u(t)$, $v(t)$, and $w(t)$, raw data were first filtered based on signal strength and its correlation. Signal strength is a measurement of the intensity of the reflected signal

and is recorded as a raw signal amplitude in units of counts, which is related to the signal-to-noise ratio (SNR) in dB by 1 count = 0.43 dB. SNR is used to demonstrate if there is sufficient particulate seeding. For a good measurement, SNR > 15 dB (or 35 counts) is required. This requirement is always satisfied in this study. Correlation coefficient is another filtering parameter, in which low correlation indicates the output velocity is dominated by noise. For median or low turbulent flow, such as most places in natural environments or those in the tank but far from the pump outlet, correlation is generally higher than 70%, with some places higher than 90% and even close to 100%. For high turbulent flow near the pump outlet, however, a correlation as low as 30% is considered suitable in this study (SonTek, 2001). Note that a sufficient amount of data (usually more than 70%) should be retained after filtering (Martin et al., 2002). For extremely high turbulence flow close to the pump outlet, little data may remain even after filtering with a 30% correlation. Increasing the velocity range is a practical way to increase the correlation coefficient (SonTek, 2001). Although the basic principle for selecting a velocity range is to use the lowest range that can cover the maximum expected velocities, it is worth it to increase the velocity range to reduce the noise and keep more data. If the problem of insufficient data still remains, these points might have to be excluded from the measurements (e.g., the points within 5 cm around the pump outlet in this study). After filtering data based on the signal strength and correlation, the mean flow velocities can be obtained by:

$$U = \frac{1}{T} \int_0^T u(t) dt, \quad V = \frac{1}{T} \int_0^T v(t) dt, \quad W = \frac{1}{T} \int_0^T w(t) dt \quad (5.1)$$

where T is time duration (2 min), and U , V , and W are time-averaged velocity components.

Because of the axially symmetrical flow, the ADVOcean is held in such a manner that

the marked direction on one of the three sensors is aligned with the radial direction (r), and thus, measures the radial velocity component, u . The other two measurements are the vertical velocity component, w , in the vertical direction, z , and the tangential velocity component, v , in the θ direction. In general, the tangential velocity component is miniscule ($v \approx 0$). Flow field in the z - r plane in the tank is displayed in Fig. 5.1b. Thus, a conceptual streamtube may be assigned which starts from a measurable point close to the outlet of the pump ($s = 0$). The streamtube goes straight up until it is close to the water's surface at the center ($s = 0$ to 80 cm), and then turns 90 degrees and goes horizontally to the side wall ($s = 80$ to 116 cm). From there, it turns another 90 degrees and moves downward along the side wall from surface to bottom ($s = 116$ to 226 cm). Finally, it goes back to the pump and then returns to the starting point. Notice that the tangential velocity component is generally low, except at the bottom of the tank. The flow field below $z = 80$ cm is measured by holding the ADV downward as shown in Fig. 5.1a, while the flow close to the surface is measured by holding the ADV upside down. Therefore, the vertical velocity measured within $s = 0$ to 80, and 116 to 226 cm, is set as U_s (velocity along the streamtube) with positive along the transport direction. For $s = 80$ to 116 cm, measured U velocity (which is parallel to the marked ADV receiver) is the main flow direction and thus it is set as U_s . The velocity at $X = 36$ cm ($s = 116$ to 226 cm) is assumed close to $X = 27$ cm, since it is the measured point closest to the side wall. Notice that U_s is always positive in this idealized streamtube.

Turbulent Kinetic Energy (TKE), K , is calculated as

$$K = \frac{1}{2} \left(\overline{(u')^2} + \overline{(v')^2} + \overline{(w')^2} \right) \quad (5.2)$$

where u' , v' and w' are velocity fluctuations with $u' = u - U$, $v' = v - V$, and $w' = w - W$,

respectively, and the over bar denotes the time average within the time duration T . Note that the velocity time series are usually contaminated by a few spikes. While the spikes have little influence on computing the mean velocities, they have a significant impact on computing TKE. Thus, de-spiking is required before calculating TKE. Various de-spiking methods have been reported. For example, Fugate (2002) suggests using a high pass filter in its energy spectrum with a cutoff frequency of 1.5 Hz to remove spikes. Islam and Zhu (2013) and Botev et al. (2010) suggest a kernel-density-based algorithm for de-spiking ADV data. However, none of these methods has shown good results in this study, and thus, by trial-and-error, any fluctuation that is larger than five times of the standard variation is considered a spike and is discarded from the statistics.

In a turbulent flow, instability of the main flow produces an eddy with similar wave length or scale as the main flow. This eddy is unstable and disintegrates into smaller and smaller eddies until all of their energy is dissipated by viscosity and converted to thermal energy (Kumar, 2010). It is understood that to directly measure the energy dissipation rate, ε , is difficult, because it is hard to capture precisely the smallest turbulent structures (Saarenrinne and Piirto, 2000). The method based on $\varepsilon = P / (\rho \cdot Vol)$ (e.g., Ducoste et al., 1997; Sanchez Perez et al., 2006; Shen and Maa, *Submitted a*), where P is the total power dissipated in mixing, ρ is the fluid density, and Vol is the system volume, is not for estimating the local ε (Zhou and Kresta, 1996; Ducoste and Clark, 1999).

Tennekes and Lumley (1972) suggest that in the inertial subrange in the region of fully turbulent flow, the wave-number-based energy spectral density E (m^3/s^2) can be expressed as

$$E(k) = A \cdot \varepsilon^{2/3} \cdot k^{-5/3} \quad (5.3)$$

where A is the 1-D Kolmogorov universal constant, ε is in units of m^2/s^3 , k (in units of m^{-1}) is the wave number, and the inverse of k is the size of the eddy. Since the ADV noise level is the lowest for the flow component that is parallel to the ADV instrument's source wave propagation direction, the vertical velocity spectrum is used in this study to estimate the energy dissipation rate (Feddersen, 2010; Thomson et al., 2012; Nimmo Smith et al., 2005).

Results of Fourier transform of $w(t)$ show energy at each frequency, f , thus it is necessary to transfer wave number k to wave frequency f . Based on the Taylor's frozen turbulence hypothesis, Lumley and Terray (1983) suggest

$$k = 2\pi / L = 2\pi f / W \quad (5.4)$$

in which L is the wave length, and W is the mean vertical velocity. Although Lien and D'Asaro (2006) suggest using instantaneous velocity instead of mean velocity, this study found that using instantaneous velocity merely introduces more spikes, and thus, was not used. Therefore, the energy spectrum based on wave frequency f can be obtained as (Fugate, 2002; Thomson et al., 2012)

$$E(f) = A \cdot \varepsilon^{2/3} \cdot f^{-5/3} \cdot \left(\frac{W}{2\pi} \right)^{2/3} \quad (5.5)$$

The selected spectrum domain is from about 1 Hz (same as that used by Feddersen, 2010) to about 5 Hz (Nyquist frequency, because of the 10 Hz sample frequency). In general, the inertial subrange is within this domain where the spectrum slope is $-5/3$, as shown in Fig. 5.2.

From Eq. 5.5, the energy dissipation rate ε can be estimated as (Fugate, 2002; Liu et al., 2011; Thomson et al., 2012)

$$\varepsilon = \frac{2\pi}{W} \cdot (C/A)^{3/2} \quad (5.6)$$

where $C = E(f=1)$ is the reading of energy at $f=1$ from the least square fitted line with a fixed slope of $-5/3$ in the log-log plot of $E(f)$ vs. f . Although A is a constant on the order of 1, it is selected as 0.7 because of the suggestions that $A = 0.71$ from Liu et al. (2011) and $A = 0.69$ from Thomson et al. (2012). MATLAB codes for finding energy dissipation rate based on spectrum method can be found in Shen (2016).

Because the created flow field is quite complex, it is difficult to use the typical formulation ($G = \partial u_i / \partial x_j + \partial u_j / \partial x_i$, where i and j are index notation) for estimating the shear rate. Camp and Stein (1943) suggest that the shear rate G can be expressed as Eq. 5.7 after knowing the energy dissipation rate ε

$$G = \sqrt{\frac{\varepsilon}{\nu}} \quad (5.7)$$

where ν is the kinematic viscosity of the fluid. In addition, Kolmogorov (1941) proposes that the Kolmogorov micro length scale λ , which is a length scale of eddy where viscosity is the major mechanism to dissipate energy (Thomas et al., 1999), can be estimated as

$$\lambda = \left(\frac{\nu^3}{\varepsilon} \right)^{1/4} \quad (5.8)$$

This length scale can be used to determine the possible maximum floc size. The eddy diffusivity D is assumed close to the eddy viscosity and can be estimated by

$$D = C_\mu \frac{K^2}{\varepsilon} \quad (5.9)$$

in which $C_\mu = 0.09$ is a constant that is widely used in turbulence models (e.g., Rodi, 1993).

2.2 FSD measurements

Kaolinite was soaked in de-ionized water for more than 30 days to reach a fully water-saturated condition (Ha, 2008). Then, a properly selected amount of high concentration sediment-water mixture was poured into the cylindrical tank and diluted with tap water until the same water depth (i.e., $z = 110$ cm) was reached as that of the previous flow field measuring experiment. As shown in Fig. 5.1b, from $s = 0$ to $s = 226$ cm, the main flow is along the streamtube. The transport time from $s = 0$ to $s = 226$ cm is around 33 s, according to the measured mean velocities along the streamtube. It is difficult to estimate when the flocculation process will reach the stable status, thus we wait for 48 hrs to give sufficient time for the system to become stable. An OBS (Optical Backscatter Sensor) is mounted at 50 cm above the bottom of the tank with the measuring point around 10 cm away from the wall. The measurements show the SSC is 0.38 g/L at the beginning and decreases to 0.36 g/L after 48 hrs (Fig. 5.3). This result is based on the calibration results of SSC and OBS counts for the same kaolinite suspension carried out earlier in the mixing chamber experiments (Shen and Maa, *Submitted a*). Several water samples were also collected from the port on the tank's wall at $t = 30$ min, and the results indicate that the average SSC is 0.40 g/L, which is close to the OBS monitoring results. If assuming the change of floc size distribution has no effect on the OBS calibration, an average SSC of 0.38 g/L may be used as one of the input parameters to model the FSDs along the entire streamtube.

An underwater camera system was developed to measure the FSDs of kaolinite suspensions. This camera system is improved based on that given by Shen and Maa (*Submitted a*). It includes a Sony Alpha NEX-5R camera body with 4912×3264 pixels for

images, a NEX E mount to Nikon F mount adaptor, three Kenko extension tubes (36 + 20 + 12 mm), a Nikon Macro Nikor 55 mm lens, and a +10 close-up lens that mounted sequentially (Fig. 5.4). These settings magnify the subject, from a subject size of 10.7×7.2 mm to an image size of 23.5×15.6 mm, i.e., a Subject-to-Image Ratio (SIR) of 1: 2.2, and thus, changes the resolution from $4.8 \mu\text{m}$ per pixel to $2.2 \mu\text{m}$ per pixel. Using at least 2×2 pixels to identify a floc, the minimum sphere equivalent floc size that can be identified by this camera system is around $5 \mu\text{m}$, which is roughly consistent with the primary particle median size of cohesive sediment minerals in the natural environment. The shutter speed is set to $1/1000$ s to catch the fast moving particles, the aperture is set at the maximum, $f/2.8$, to receive more lights and to limit the focus depth to about 2 mm. The ISO is set to 100 to minimize noise which may be considered as primary particles or small flocs. The trigger to take pictures is controlled by a commercially available remote control unit which is powered and controlled via a 4-pin connector, J2, on the control board. A 150 milliwatt (mW) green laser module with a concave lens to spread the laser light is mounted on the same side of the camera lens (i.e., front-illumination) and points to the center of the image window. This module is connected and controlled by the control board via a 3-pin connector, J1.

The above components are assembled and protected in a PVC tube with one cover made by PVC plate, and the other made by a 23 mm thick plexiglass plate to allow pictures to be taken. Through air dielectric, the Distance between the Subject and Lens (DSL) is slightly larger than 23 mm, but it increases to 29 mm when the plexiglass cover is placed between the lens and the subject. This gives around 5 mm distance between the cover and the front of the camera lens to take pictures for any subject that is within 1 mm of the other side of the

plexiglass cover. The power for this camera system is provided by a set of four 18650 Li rechargeable batteries (i.e., 16VDC) inside the PVC tube via the connector, J3. This power is converted to 3.7 V to provide power for the laser source, converted to 5 V for the microcontroller, and converted to 3 V for the camera remote control. A magnetic switch which is attached on the PVC cover can be turned on if a magnetic bar is placed on the other side of the PVC cover. Once the switch is closed, the microcontroller begins to work following the instruction of the control program. This program generates periodic pulses which are fed into the gate of two Field Effect Transistors (FETs), (i.e., 2N7000 and RFP2N08L, respectively) which behave as two electronic switches, K1 and K2. The timing of these two pulses matches so that when the camera is taking images, the laser light is on. The program is set to take pictures every 2 s until the battery for the camera is exhausted. Nevertheless, this system operates for 3 hours before the batteries need to be changed. This working duration is sufficient for the current application, and much longer than that which uses LED light source described in the earlier version of the camera system (Shen and Maa, *Submitted a*). Even for field measurements in a typical tidal estuary, it is tolerable because the batteries only need to be replaced once between a deployment for a flood, slack, and ebb period.

The acquired floc images are processed using the MATLAB Image Processing toolbox. Details of those processes have been reported in an earlier study (Shen and Maa, *Submitted a*), and thus, only a brief description is given next. These procedures include converting RGB images to grayscale images, removing background noise, contrast stretching and thresholding, removing small objects, dilation and erosion, filling the holes, removing on-border particles,

and checking pixel gradients. Since the laser source is in green, only the green part of the RGB figure is extracted and its intensity is used to generate the grayscale image. The histogram of the grayscale image shows intensities varying from 10 to 180, with the span three times wider compared with that from the image taken with LED light source (Fig. 5.5). This is one of the advantages to using laser light, since a quality image spans its pixels on a wider range (full range is from 0 to 255). The background light intensity is estimated by finding the minimum light intensity for a pixel within a block of each 30×30 pixels. The resulting 163×108 square blocks are bi-interpolated to all pixels to generate a continuous background light intensity. Notice that the selected block in this study is much smaller than that used in Shen and Maa (*Submitted a*). This is because the laser is better than the LED light in this application for generating the finer grid background. The range of the intensity of the background is from 0 to 0.6 in this study, compared with 0.2 to 0.3 for polystyrene particles used by Shen and Maa (*Submitted a*). Images are enhanced by a non-linear contrast stretching with input intensity $[0, 0.6]$ and mapping parameter 2 (mapping toward darker). Then, particles are separated and converted to a binary display using a constant threshold value 0.18 (a number determined by trial-and-error). Small objects with area less than 4 pixels or minor elliptic equivalent axis less than 2 pixels are removed as noise, dilation and erosion are applied to collect the morphology of flocs, and particles on the border are removed. The critical pixel gradient, which is estimated based on pixel gradient statistics, is set as 120. Any identified floc with a maximum pixel gradient below 120 is considered an out-of-focus particle or threshold noise, and thus, is removed. These values are used throughout this experiment. Circular equivalent diameter is thus calculated based on the

number of pixels to construct a floc, and converted to floc size in microns based on the SIR ratio of the camera system.

3. Floc size distribution model

A simplified FSD model along a selected streamtube is presented. A bundle of nearby streamlines may be used to constitute a streamtube. For a steady turbulent flow, the location of the selected streamtube may be considered as a fixed tube in space, except that this tube has no friction on the fluid flow. Since fluid only flows along the streamline, the transport of sediment also only moves along the tube. As shown in Fig. 5.1a, this idealized streamtube starts from $s = 0$ (close to the outlet of the pump where the velocity can be measured), goes along the measured streamline (with some degrees of idealization), and back to the starting point. The actual condition in our prediction is from $s = 0$ to $s = 226$ cm, and there is no measurement for $s > 262$ cm.

To find the governing equation for this 1-D floc distribution model, consider a control volume along a streamtube between two control surfaces, CS 1 and CS 2 (Fig. 5.6), in which we focus on size L particles. These particles enter the control volume at CS 1 with a number density (number of particles with size L per unit volume) n . At this location, the streamtube cross section is A , and the mean velocity along the streamtube is U_s . When leaving the control volume at CS 2, the corresponding properties become $n + dn$, $A + dA$, and $U_s + dU_s$. Since $U_s \gg w_s$ (settling velocity), the settling is ignored in the formulation.

At time t , the control volume contains particles with various sizes. Among these sizes, particles of size L have number density $n(L, s, t)$ at a location s and time t . At time $t + dt$, it is

assumed that the streamtube does not change, while the number density $n(L, s, t)$ might be altered. This is not only because particles flux in and out of the control volume, but also because particles flocculate within the control volume. During the flocculation processes in the control volume, total particle mass is conserved but particle number (number of particles either with all sizes and/or with a particular size L) may change because of aggregation and breakup processes.

The governing equation for the change of total particle number (N) for a particular size L is based on a balance of local change, advective transport, and flocculation sources and sinks:

$$\frac{\partial}{\partial t}(N)_{\text{Local}} + (N_{\text{out}} - N_{\text{in}}) = (\dot{N})_{\text{Floc}} \quad (5.10)$$

in which N_{in} and N_{out} are the total particle number transported in and out of the control volume through the control surfaces CS1 and CS2, respectively, and \dot{N}_{Floc} is the rate of particle number change due to flocculation processes within the control volume.

Since length of the control volume Δs and cross section A are selected as independent of time, the first term in Eq. 5.10 is given by

$$\frac{\partial}{\partial t}(N)_{\text{Local}} = \frac{\partial}{\partial t}(n \cdot A \cdot \Delta s) = \frac{\partial n}{\partial t} \cdot A \cdot \Delta s$$

The net difference of total number of size L particles entering and leaving the control volume (second term in Eq. 5.10) can be given as

$$\begin{aligned} (N_{\text{out}} - N_{\text{in}}) &= (n + \Delta n) \cdot (U_s + \Delta U_s) \cdot (A + \Delta A) - n \cdot U_s \cdot A \\ &\approx n \cdot U_s \cdot \Delta A + n \cdot A \cdot \Delta U_s + U_s \cdot A \cdot \Delta n \\ &= n \cdot U_s \cdot \frac{\partial A}{\partial s} \cdot \Delta s + n \cdot A \cdot \frac{\partial U_s}{\partial s} \cdot \Delta s + U_s \cdot A \cdot \frac{\partial n}{\partial s} \cdot \Delta s \end{aligned}$$

$$= \left(n \cdot U_s \cdot \frac{\partial A}{\partial s} + A \frac{\partial (n \cdot U_s)}{\partial s} \right) \cdot \Delta s$$

where higher order terms are ignored. The third term in Eq. 5.10 can be expressed as:

$$(\dot{N})_{\text{Floc}} = S \cdot A \cdot \Delta s$$

Here, S is the flocculation source and sink terms describing the rate of change of number of size L particles per unit volume due to aggregation and breakup. As a consequence, the instantaneous number density n for a particular size L at time t in a steady flow field along a streamtube can be written as:

$$\frac{\partial n}{\partial t} + \frac{\partial (n \cdot U_s)}{\partial s} + \frac{n \cdot U_s}{A} \cdot \frac{\partial A}{\partial s} = S \quad (5.11)$$

Applying the classical Reynolds averaging procedure to decompose the instantaneous properties into time-averaged and fluctuant sections gives:

$$n = \bar{n} + n' \quad (5.12)$$

$$U_s = \bar{U}_s + U'_s \quad (5.13)$$

The cross section A is assumed to be independent of time, so that it does not have a turbulent contribution. The flocculation source and sink terms S is more or less empirical and therefore the turbulent contribution is neglected as well (Winterwerp and van Kesteren, 2004). Substituting Eqs. 5.12 and 5.13 into Eq. 5.11 and averaging over the turbulent time scale gives

$$\frac{\partial \bar{n}}{\partial t} + \frac{\partial (\bar{n} \cdot \bar{U}_s)}{\partial s} + \frac{\partial (\overline{n' \cdot U'_s})}{\partial s} + \frac{\bar{n} \cdot \bar{U}_s}{A} \cdot \frac{\partial A}{\partial s} + \frac{\overline{n' \cdot U'_s}}{A} \cdot \frac{\partial A}{\partial s} = S \quad (5.14)$$

Applying Fick's law, i.e., assuming the $\overline{n' \cdot U'_s}$ term is proportional to the gradient of time average number density along the streamtube, gives

$$\overline{n' \cdot U'_s} = -D \cdot \frac{\partial \bar{n}}{\partial s} \quad (5.15)$$

in which D is the turbulent diffusivity coefficient, which can be evaluated by assuming it is close to the eddy viscosity of the fluid.

Substituting Eq. 5.15 into Eq. 5.14 yields

$$\frac{\partial \bar{n}}{\partial t} + \frac{\partial(\bar{n} \cdot \bar{U}_s)}{\partial s} - \frac{\partial}{\partial s} \left(D \frac{\partial \bar{n}}{\partial s} \right) + \frac{\bar{n} \cdot \bar{U}_s}{A} \cdot \frac{\partial A}{\partial s} - \frac{D}{A} \cdot \frac{\partial \bar{n}}{\partial s} \cdot \frac{\partial A}{\partial s} = S \quad (5.16)$$

After this point the symbol “bar” in \bar{n} and \bar{U}_s is omitted, thereby all variables are taken to be time-averaged. Therefore, the following governing equation for particles with a particular size L that specifies its time-averaged number density n at time t in a steady flow field along a streamtube is obtained:

$$\begin{aligned} & \frac{\partial n(L, s, t)}{\partial t} + \frac{\partial(n(L, s, t) \cdot U_s(s))}{\partial s} - \frac{\partial}{\partial s} \left(D(s) \cdot \frac{\partial n(L, s, t)}{\partial s} \right) \\ & + \frac{n(L, s, t) \cdot U_s(s)}{A(s)} \cdot \frac{\partial A(s)}{\partial s} - \frac{D(s)}{A(s)} \cdot \frac{\partial n(L, s, t)}{\partial s} \cdot \frac{\partial A(s)}{\partial s} = S \end{aligned} \quad (5.17)$$

In Eq. 5.17, the variables U_s , A , and D do not change with time, but do vary along the direction of the streamline s . The number density n is for a particular particle size L and can change with time t and space s . The flocculation source and sink term S can be expressed as (Shen and Maa, 2015).

$$\begin{aligned} S = & \frac{L^2}{2} \int_0^L \left[\frac{\beta((L^3 - \lambda^3)^{1/3}, \lambda) \cdot \alpha((L^3 - \lambda^3)^{1/3}, \lambda)}{(L^3 - \lambda^3)^{2/3}} \cdot n((L^3 - \lambda^3)^{1/3}, s, t) \cdot n(\lambda, s, t) \right] d\lambda \\ & - n(L, s, t) \int_0^\infty \beta(L, \lambda) \alpha(L, \lambda) n(\lambda, s, t) d\lambda + \int_L^\infty a(\lambda) \cdot b(L | \lambda) \cdot n(\lambda, s, t) d\lambda - a(L) \cdot n(L, s, t) \end{aligned} \quad (5.18)$$

in which λ is the integral variable with the same dimension of floc size L , $\beta(L, \lambda)$ is the Euclidean collision frequency function that describes the frequency of two spheres with size L and λ colliding to form a particle with size $(L^3 + \lambda^3)^{1/3}$, $\alpha(L, \lambda)$ is the collision efficiency that

includes the effects of particle geometry, contact efficiency, and sticking probability, $a(L)$ is a breakup frequency function that denotes the frequency of disruption for particles with size L , and $b(L|\lambda)$ is a fragmentation distribution function that represents particles with size L produced by the breakup of a particle with size λ . The four terms in Eq. 5.18 includes: the birth of flocs with size L due to aggregation of smaller particles, the death of flocs with size L due to aggregation with other particles, the birth of flocs with size L due to fragmentation of larger particles with size λ , and the death of flocs with size L due to themselves break up into smaller particles.

Eq. 5.17 with flocculation source and sink terms represented by Eq. 5.18 is the governing equation for the number density of size L particles. To further track the number, surface area, volume, etc. of particles of all sizes, the moment method is selected to solve the governing equation by applying Gaussian quadrature approximation with an adjustable factor, p . Details are given elsewhere (Shen and Maa, 2015).

$$m_{k/p}(s,t) = \int_0^{\infty} L^{k/p} n(L,s,t) dL = \sum_{i=1}^{N_d} \omega_i(s,t) \cdot L_i(s,t)^{k/p} \quad (k = 0, 1, \dots, 2N_d - 1) \quad (5.19)$$

in which n is integrated over the whole size range. $m_{k/p}$ is the (k/p) th order moments of FSD, with m_0 (i.e., $k = 0$), m_2 (i.e., $k = 2p$), and m_3 (i.e., $k = 3p$) proportional to the total number of all particles, total surface area, and total volume of all particles per unit fluid volume. The integral in Eq. 5.19 is numerically modeled using N_d - node Gaussian quadrature approximation (Press et al., 1992) using N_d Gaussian quadrature nodes L_i ($i = 1, 2, \dots, N_d$) and N_d corresponding weights ω_i ($i = 1, 2, \dots, N_d$) by tracking the first $(2N_d - 1)$ moments $k = 0, 1, \dots, 2N_d - 1$. The Gaussian quadrature nodes and corresponding weights are actually the characteristic sizes and number densities that can constitute the number-based FSD (Shen and

Maa, 2015). The variable p is an adjustable factor that controls the number of nodes (N_d) that can be tacked. For example, $p = 1, 2, 3, 4, 5$ for $N_d = 8$, and $p = 1, 2, 3, 4$ for $N_d = 7$. The optimum p is usually selected by trial-and-error.

Applying Eq. 5.19 to Eqs. 5.17 and 5.18, the governing equation becomes

$$\begin{aligned} \frac{\partial m_{k/p}(s,t)}{\partial t} + \frac{\partial(m_{k/p}(s,t) \cdot U_s(s))}{\partial s} - \frac{\partial}{\partial s} \left(D(s) \cdot \frac{\partial m_{k/p}(s,t)}{\partial s} \right) \\ + \frac{m_{k/p}(s,t) \cdot U_s(s)}{A(s)} \cdot \frac{\partial A(s)}{\partial s} - \frac{D(s)}{A(s)} \cdot \frac{\partial m_{k/p}(s,t)}{\partial s} \cdot \frac{\partial A(s)}{\partial s} = S_{k/p}(L_i, \omega_i) \end{aligned} \quad (5.20)$$

where

$$\begin{aligned} S_{k/p}(L_i, \omega_i) = \frac{1}{2} \sum_{i=1}^{N_d} \omega_i \sum_{j=1}^{N_d} \alpha(L_i, L_j) \cdot \beta(L_i, L_j) \cdot \omega_j \cdot (L_i^3 + L_j^3)^{\frac{k}{3p}} \\ - \sum_{i=1}^N L_i^{k/p} \omega_i \sum_{j=1}^N \alpha(L_i, L_j) \cdot \beta(L_i, L_j) \cdot \omega_j + \sum_{i=1}^N a_i \bar{b}_i^{(k/p)} \omega_i - \sum_{i=1}^N L_i^{k/p} a_i \omega_i \end{aligned} \quad (5.21)$$

$$\text{and} \quad \bar{b}_i^{(k/p)} = \int_0^\infty L^{k/p} b(L | \lambda) dL \quad (5.22)$$

The flocculation kinetic kernels given in the above equation (i.e., collision frequency β , collision efficiency α , breakup frequency a , and fragmentation distribution function b) for suspended kaolinite can be summarized as (Shen and Maa, 2015)

$$\beta(L_i, L_j) = \frac{G}{6} (L_i + L_j)^3 \quad (5.23)$$

$$\alpha(L_i, L_j) = C_1 \quad (5.24)$$

$$a(L_i) = C_2 \cdot \left(\frac{\mu}{F_y} \right)^{1/2} \cdot G^{3/2} \cdot L_i \cdot \left(\frac{L_i}{l_p} - 1 \right)^{3-n_f} \quad (5.25)$$

$$\bar{b}_i^{(k/p)} = 2^{(3-k/p)/3} L_i^{k/p} \quad (5.26)$$

in which G is the local shear rate, C_1 and C_2 are the aggregation and breakage parameters respectively, μ is the fluid dynamic viscosity, $l_p = 5 \mu\text{m}$ is the representative primary particle

size, F_y is the floc strength with a constant value of 10^{-10} N following the values given by Maggi et al. (2007) and Lee et al. (2011), and $\eta_f = 3 \cdot (L/l_p)^{-0.1}$ is the fractal dimension following the formulation given by Maggi et al. (2007) and Shen and Maa (2015) for suspended kaolinite. Eq. 5.26 assumes a floc splits into two equal sized spheres if it breaks up.

Note that Eq. 5.20 actually is a series of $(2N_d - 1)$ equations. At each time t , the left hand side of Eq. 5.20 is updated using a finite difference method, while the source and sink terms at time t (Eq. 5.21) is a constant if the value of L_i ($i = 1, 2, \dots, N_d$) and ω_i ($i = 1, 2, \dots, N_d$) are available. A total of $2N_d$ variables of L_i and ω_i at time t are calculated from a finite set of $2N_d$ moments ($m_0, m_{1/p}, \dots, m_{(2N_d-1)/p}$) at time $(t - \Delta t)$ using Eq. 5.19 based on the long quotient modified difference algorithm (Sack and Donovan, 1972; Wheeler, 1974; Press et al., 1992; Shen and Maa, 2015). Since advective transport dominates in this case, to avoid numerical instabilities, an explicit upwind scheme is used. Time step Δt is selected as $1.0E-4$ s for both transport and flocculation processes. Since the flow velocity is always positive along the streamtube, the upwind scheme actually becomes a backward difference scheme. The entire streamtube (292 cm) is divided into 58 grids with a resolution of 5 cm. The streamtube between $s = 0$ to $s = 226$ cm corresponds to grid cells 1 to 45.

The total mass of fluid and sediment (i.e., all particles) within the tube should be conserved. This is because the streamtube may be considered a rigid tube with no local storage (i.e., incompressible flow). This suggests that the cross section areas of the streamtube are altered according to its mean velocity. The conservation of total sediment volume, i.e., m_3 (indicator of volume) will remain unchanged, thus the source and sink term

$S_3 = 0$ when $k = 3p$ in Eq. 5.20.

A repetitive boundary condition is applied for m_3 between the last grid and the first grid. That is, m_3 in grid 59 (fictitious grid) is equal to m_3 in grid 1. This relation is also valid for the eddy diffusivity D , mean velocity u , and cross section A . For other moments m_{kp} ($k \neq 3p$), which are an indicator of FSD and other properties such as total particle number and total particle area, there is no need to specify the boundary condition because these moments at a downstream-most grid are only influenced by the one before.

4. Results and discussions

4.1 Model inputs

The measured flow properties along the streamtube are represented in Fig. 5.7, with $s = 0$ to $s = 80$ cm indicating a path near the center of the tank (center zone), $s = 80$ cm to $s = 116$ cm indicating close proximity to the water surface (surface zone), $s = 116$ cm to $s = 226$ cm indicating the side wall (side zone), and $s > 226$ cm indicating a return path for water to go back into the pump. Data from $s = 0$ to $s = 116$ cm are measured, while data from $s = 116$ to $s = 226$ cm at $X = 37$ cm (Fig. 5.1b) are assumed close to the vertical component for the measured data at $X = 27$ cm. The turbulence close to the pump outlet is high, with the main flow, U_s , more than 80 cm/s, the energy dissipation rate, ε , up to $1000 \text{ cm}^2/\text{s}^3$, the TKE, K , up to $1000 \text{ cm}^2/\text{s}^2$, and the eddy diffusivity, D , in the order of $100 \text{ cm}^2/\text{s}$. Between $s = 0$ to $s = 80$ cm, U_s , ε , and K all decrease more than one order of magnitude, while D shows a local minimum at $s = 25$ cm. At the water surface from $s = 80$ cm to $s = 116$ cm, U_s and K shows a gradual decrease, ε is relatively stable, and D continuously decreases to $1 \text{ cm}^2/\text{s}$. At the side

from $s = 116$ cm to $s = 226$ cm, which is a vertical downward flow, U_s and K are relatively stable. D shows a parabolic character with small values at the surface and bottom of the side, while their local maximum is located around 30 cm above the bottom. ε continues to decrease until $s = 190$ cm, and it must increase again between $226 \text{ cm} < s < 262 \text{ cm}$, since the velocity increases along the tank bottom and toward the pump. The local shear rate G and Kolmogorov micron scale λ are proportional to $1/2$ and $-1/4$ power of ε , respectively, such that they display similar or reverse shape as that of ε . From Fig. 5.7e, it is clearly seen that the shear rate close to the pump outlet could be as high as 300 s^{-1} , while at $s = 190$ cm it may be as low as 5 s^{-1} . With this level of shear rate, the Kolmogorov microscale shows that the maximum floc size without organic matter influences usually cannot exceed $60 - 500 \text{ }\mu\text{m}$ even with sufficient residence time for flocculation (Fig. 5.7f).

4.2 Model validation

The FSDs at $s = 130, 145, 160, 175, 190, 205,$ and 220 cm are processed using the MATLAB Image Processing toolbox based on the images taken by the underwater camera system. Particles from a consecutive 50 images are used (more than 1,000 particles) to have a stable FSD. In other words, all FSDs are the results of 2 minute measurements that were displayed with a $5 \text{ }\mu\text{m}$ bin size. These images were taken after running the pump for 48 hrs to assure it was steady. All FSDs (Fig. 5.8) show a decreasing trend with its peak at the smallest bin. At $s = 205$ cm (about 20 cm above bottom close to the side wall), it has the most abundant small particles with number fraction more than 60%, while at other measuring points the number fraction of flocs in the $5 - 10 \text{ }\mu\text{m}$ bin varies around 40 – 50%. The short

residence time (only ~ 33 s) is the reason that why small particles are abundant because flocs do not have enough time to flocculate. The FSD at $s = 205$ cm with the lowest shear rate ($G = 4 \text{ s}^{-1}$) is somewhat opposite to our expectation; thus, this may be an outlier.

The original selected timing for taking images (i.e., 48 hrs after starting the pump) does not reflect the residence time, since it only takes 33 s for the particles to go through the streamtube. Since this is an initial value problem (i.e., the FSD at any place along the streamtube is controlled by the strong pumping shear at the beginning), the 48 hour wait was proved to be unnecessary. As discussed in Shen and Maa (*Submitted b*), the selection of absolute values for the parameters C_1 & C_2 should be based on matching the measured and predicted mean floc sizes at $t = 33$ s. Meanwhile, the ratio C_1/C_2 should be the same as that given in Shen and Maa (*Submitted b*)'s box model, which simulates the FSDs in a mixing chamber experiment using the same sediment. This is because the ratio C_1/C_2 determines the FSD at the final equilibrium state while their absolute values determine the growth pathway to arrive at the final state in the box model (Shen and Maa, *Submitted b*). The fitted C_1 & C_2 based on both flocculation path and final FSD in the 0-D modeling results can be used in a 1-D model. However, it is important to notice that the simulated final FSDs in the 0-D and 1-D models may be different even for the same shear rate (i.e., chamber-averaged shear in the 0-D model and local shear rate in the 1-D model), due to the possible difference in residence time experienced by the flocs. By trial-and-error, $C_1 = 0.034$ and $C_2 = 1.28\text{E}-6$ are selected in this study for a reasonable match between the simulated and measured mean sizes at $t = 33$ s (Fig. 5.9). The ratio of C_1/C_2 is the same as that used in the Shen and Maa (*Submitted b*).

At $t = 33$ s, the normalized moments show the particle volume (m_3) along the tube is the

same as that specified for the initial condition, which illustrates the conservation of total particle volume in the tube (Fig. 5.10). If the initial m_3 is not uniform along the tube, it will arrive at uniform status quickly because of strong advective transport. m_0 , m_1 , and m_2 show that the total particle number, total particle length, and total particle surface area continuously decrease from $s = 0$ to $s = 150$ cm while relatively unchanged in the side zone (Fig. 5.10). On the other hand, m_4 and m_5 , which are proportional to the total surface area of sediment settling per unit time and the settling flux respectively (Mehta, 2013), continuously increase (Fig. 5.10). The same m_3 at $s = 0$ (starting point) and $s = 292$ cm (ending point) also illustrate the assigned repetitive boundary condition of sediment volume in the tube. Other moments, however, do not have this boundary condition.

At the beginning of the simulation, the total number of all particles (m_0) is the same everywhere. Between $s = 0$ and 50 cm, this number changes quickly to an equilibrium status, and does not change anymore because of strong shear. With enough residence time, m_0 should also approach an equilibrium status at $t = 60$ s (Fig. 5.11). The side zone is the last place to approach the equilibrium status, and only this zone has not reached the equilibrium status at $t = 33$ s. This is also an indication that the residence time is giving up its control to other parameters in the flocculation process after $t = 60$ s.

At $t = 33$ s, the predicted FSDs at $s = 176$ cm are compared with measured results, and show a reasonable agreement (Fig. 5.12). The initial condition at $t = 0$, and simulated FSDs at $t = 1$ s, 5 s are also shown in this figure. It appears that the model prediction at $t = 33$ s has more large flocs. This is different from the measurements, and may be caused by a more favorable aggregation condition specified in the modeling. Besides, as examples of a few

selected points, at $s = 58$ cm (at the center zone) and $s = 113$ cm (at the surface zone close to the starting point of the side zone), the time evolutions of the mean size show that it only takes 5 s and 10 s to reach the equilibrium state (Fig. 5.13), with their predicted FSDs (Fig. 5.14) illustrating that most of the particles are small flocs but large flocs are also present. At $s = 218$ cm (close to the end of the side zone), however, the residence time ($t = 33$ s) is less than that required to attend the equilibrium status (see Fig. 5.13), and thus, there are less large flocs (see the FSD at $t = 50$ s in Fig. 5.14).

5. Conclusions

A conceptual one-dimensional floc size distribution model along a conceptual streamtube is developed. The fluid and sediment are assumed to travel only along the streamtube. The governing equation shows the change of number density of a particular particle size based on a balance of local change, advection, diffusion, and flocculation. The settling term is omitted due to high advection and short residence time in this case.

A laboratory experiment was carried out to validate this model. A 3700 GPH marine pump was placed at the bottom center of a 0.5 m^3 cylindrical tank, with its outlet re-fitted to eject fluid upward at the center to create an axially symmetrical flow. The flow field was measured by using a 5MHz ADV-Ocean, and the measured data (mean flow, energy dissipation rate, turbulent kinetic energy, and the eddy viscosity, Kolmogorov micro length scale, and local shear rate) are put into the streamtube model for solving the change of Floc Size Distribution (FSD) along the streamtube. Both the measured and predicted FSDs show a small particle dominated distribution, with the peak at the smallest particle size. The ratio of

aggregation and breakage parameters C_1 / C_2 is consistent with that obtained in a five liter mixing chamber test for the same clay mineral (kaolinite). The absolute values of C_1 and C_2 depend on local environments, and they were determined by trial and error.

While this model is applied along a streamtube in a laboratory tank, minor modifications can be made so that it can be used in vertical 1-D applications for natural environments as long as the erosion and deposition rates can be reasonably estimated. For a vertical 1-D simulation, $G = \partial u / \partial z$ can be used instead. This will provide a better method to study flocculation density and settling velocity in the near future. The efficiency of this model makes coupling with hydrodynamic models relatively easy, and thus, make it possible for further improvements for modeling fine, cohesive sediment transport in estuaries.

Acknowledgements

This work and analysis was supported by the Virginia Institute of Marine Science (VIMS) Student Research Grant, a research grant (Contract number: 774080) from Korea Institute of Ocean Science and Technology (KIOST), China Scholarship Council (CSC) scholarship, the State Key Program of National Natural Science of China (Grant No. 41230640 & 51339005), and the National Natural Science Foundation of China (Grant No. 51409081).

References

- Barbot, E., Dussouillez, P., Bottero, J.Y., Moulin, P., 2010. Coagulation of bentonite suspension by polyelectrolytes or ferric chloride: Floc breakage and reformation. *Chemical Engineering Journal* 156, 83–91.
- Botev, Z.I., Grotowski, J.F., Kroese, D.P., 2010. Kernel density estimation via diffusion. *Annals of Statistics* 38, 2916–2957.
- Bubakova, P., Pivokonsky, M., Pivokonsky, R., Filip, P., 2013. The effect of shear rate on aggregate size distribution and structure at steady state: A comparison between a Taylor–Couette reactor and a mixing tank. *Journal of Water Supply: Research and Technology—AQUA* 62, 288–295.
- Camp, T.R., Stein, P.C., 1943. Velocity gradients and internal work in fluid motion. *Journal of the Boston Society of Civil Engineers* 30, 219–237.
- Chisholm, T.A., 1999. A two-component aggregation model. (Ph.D. Dissertation) Virginia Institute of Marine Science, College of William and Mary, Gloucester Point.
- Ducoste, J. J., Clark, M.M., Weetman, R.J., 1997. Turbulence in flocculators: The effects of tank size and impeller type. *AIChE Journal* 43, 328–338.
- Ducoste, J.J., Clark, M.M., 1999. Turbulence in flocculators: Comparison of measurements and CFD simulations. *AIChE Journal* 45, 432 – 436.
- Feddersen, F., 2010. Quality controlling surf zone acoustic Doppler velocimeter observations to estimate the turbulent dissipation rate. *Journal of Atmospheric and Oceanic Technology* 27, 2039–2055.

- Frappier, G., Lartiges, B. S., Skali-Lami, S., 2010. Floc cohesive force in reversible aggregation: A Couette laminar flow investigation. *Langmuir* 26, 10475–10488.
- Fugate, D.C., 2002. Estuarine suspended aggregate dynamics and characteristics. (Ph.D. Dissertation) Virginia Institute of Marine Science, College of William and Mary, Gloucester Point.
- Ge, C.Y., Wang, J.J., Gu, X.P., Feng, L.F., 2014. CFD simulation and PIV measurement of the flow field generated by modified pitched blade turbine impellers. *Chemical Engineering Research and Design* 92, 1027–1036.
- Ha, H.K., 2008. Acoustic measurements of cohesive sediment transport: Suspension to consolidation. (Ph.D. Dissertation) Virginia Institute of Marine Science, College of William and Mary, Gloucester Point.
- Islam, M. R., Zhu, D. Z., 2013. Kernel density-based algorithm to despiking ADV data, *Journal of Hydraulic Engineering* 139, 785–793.
- Keyvani, A., Strom, K., 2013. A fully-automated image processing technique to improve measurement of suspended particles and flocs by removing out-of-focus objects. *Computers & Geosciences* 52, 189–198.
- Keyvani, A., Strom, K., 2014. Influence of cycles of high and low turbulent shear on the growth rate and equilibrium size of mud flocs. *Marine Geology* 354, 1–14.
- Kolmogorov, A.N., 1941. The local structure of turbulence in incompressible viscous fluid for very large Reynolds numbers. *Proceedings of the USSR Academy of Sciences* 30, 9–13. (in Russian, reprinted in 1991 in English. *Proceedings of the Royal Society of London, Series A: Mathematical and Physical Sciences* 434, 9–13)

- Kumar, B., 2010. Energy dissipation and shear rate with geometry of baffled surface aerator. *Chemical Engineering Research Bulletin* 14, 92–96.
- Kumar, R.G, Strom, K.B., Keyvani, A., 2010. Floc properties and settling velocity of San Jacinto estuary mud under variable shear and salinity conditions. *Continental Shelf Research* 30, 2067–2081.
- Lee, B.J., Toorman, E., Molz, F.J., Wang, J., 2011. A two-class population balance equation yielding bimodal flocculation of marine or estuarine sediments. *Water Research* 45, 2131–2145.
- Lee, B.J., Toorman, E., Fettweis, M., 2014. Multimodal particle size distributions of fine-grained sediments: Mathematical modeling and field investigation. *Ocean Dynamics* 64, 429–441.
- Lien, R.C., D'Asaro, E.A., 2006. Measurement of turbulent kinetic energy dissipation rate with a Lagrangian float. *Journal of Atmospheric and Oceanic Technology* 23, 964–976.
- Liu, H., Wu, C., Ren, J., 2011. Estimation of turbulent kinetic energy dissipation rate in the bottom boundary layer of the Pearl River estuary. *China Ocean Engineering* 25, 669–678.
- Lumley, J.L., Terray, E.A., 1983. Kinematics of turbulence convected by a random wave field. *Journal of Physical Oceanography* 13, 2000–2007.
- Maggi, F., Mietta, F., Winterwerp, J.C., 2007. Effect of variable fractal dimension on the floc size distribution of suspended cohesive sediment. *Journal of Hydrology* 343, 43–55.
- Martin, V., Fisher, T.S.R., Millar, R.G, Quick, M.C., 2002. ADV data analysis for turbulent flows: Low correlation problem. *Hydraulic Measurements and Experimental Methods*, 1–10.

- McAnally, W.H., 2000. Aggregation and deposition of estuarial fine sediment. (Ph.D. Dissertation) University of Florida, Gainesville.
- Mehta, A.J., 2013. An introduction to hydraulics of fine sediment transport. World Scientific Publishing Company, pp. 1060.
- Mietta, F., Chassagne, C., Winterwerp, J.C., 2009. Shear-induced flocculation of a suspension of kaolinite as function of pH and salt concentration. *Journal of Colloid and Interface Science* 336, 134–141.
- Mietta, F., 2010. Evolution of the floc size distribution of cohesive sediments. (Ph.D. Dissertation) Delft University of Technology, Netherlands.
- Mietta, F., Maggi, F., Winterwerp, J.C., 2008. Chapter 19: sensitivity to breakup functions of a population balance equation for cohesive sediments. INTERCOH 2005. *Sediment and Ecohydraulics* 9, pp. 275–286.
- Mietta, F., Chassagne, C., Verney, R., Winterwerp, J.C., 2011. On the behavior of mud floc size distribution: model calibration and model behavior. *Ocean Dynamics* 61, 257–271.
- Nimmo Smith, W.A.M., Katz, J., Osborn, T.R., 2005. On the structure of turbulence in the bottom boundary layer of the coastal ocean. *Journal of Physical Oceanography* 35, 72–93.
- Press, W.H., Teukolsky, S.A., Vetterling, W.T., Flannery, B.P., 1992. Numerical Recipes in Fortran: The Art of Scientific Computing, 2nd ed. Cambridge University Press, Cambridge, United Kingdom.
- Pujol, D., Colomer, J., Serra, T., Casamitjana, X., 2010. Effect of submerged aquatic vegetation on turbulence induced by an oscillating grid. *Continental Shelf Research* 30, 1019–1029.

- Rodi, W. 1993. Turbulence models and their application in hydraulics. International Association for Hydraulic Research, 3rd edition, Delft, Balkema.
- Saarenrinne, P., Piirto, M., 2000. Turbulent kinetic energy dissipation rate estimation from PIV velocity vector fields. *Experiments in Fluids* 29, S300–S307.
- Sack, R.A., Donovan, A.F., 1972. An algorithm for Gaussian quadrature given modified moments. *Numerische Mathematik* 18, 465–478.
- Sanchez Perez, J.A., Rodriguez Porcel, E.M., Casas Lopez, J.L., Fernandez Sevilla, J.M., Chisti, Y., 2006. Shear rate in stirred tank and bubble column bioreactors. *Chemical Engineering Journal* 124, 1–5.
- Serra, T., Colomer, J., Logan, B.E., 2008. Efficiency of different shear devices on flocculation. *Water Research* 42, 1113–1121.
- Shen, X., 2016. Modeling flocculation and deflocculation processes of cohesive sediments. (Ph.D. Dissertation) Virginia Institute of Marine Science, College of William and Mary, Gloucester Point.
- Shen, X., Maa, J.P.Y., 2015. Modeling floc size distribution of suspended cohesive sediments using quadrature method of moments. *Marine Geology* 359, 106–119.
- Shen, X., Maa, J.P.Y., *Submitted a*. A camera and image processing system for floc size distributions of suspended particles. *Marine Geology*.
- Shen, X., Maa, J.P.Y., *Submitted b*. Numerical simulations of particle size distributions: Comparison with analytical solutions and kaolinite flocculation experiments. *Marine Geology*.
- SonTek, 2001, ADVField acoustic Doppler velocimeter: Technical documentation. SonTek/YSI Inc., California, 110 pp.

- Tennekes, H., Lumley, J.L., 1972. A first course in turbulence. M.I.T. Press, 300pp.
- Thomas, D.N., Judd, S.J., Fawcett, N., 1999. Flocculation modelling: A review, *Water Research* 33, 1579–1592.
- Thomson, J., Polagye, B., Durgesh, V., Richmond, M.C., 2012. Measurements of turbulence at two tidal energy sites in Puget Sound, WA. *IEEE Journal of Oceanic Engineering* 37, 363–374.
- Van Leussen, W., 1994. Estuarine macroflocs and their role in fine-grained sediment transport. (Ph.D. Dissertation) University of Utrecht, Netherlands.
- Vlieghe, M., Coufort-Saudejaud, C., Frances, C., Line, A., 2014. *In Situ* Characterization of Floc Morphology by Image Analysis in a Turbulent Taylor–Couette Reactor. *AIChE Journal* 60, 2389–2403.
- Wheeler, J.C., 1974. Modified moments and Gaussian quadratures. *Rocky Mountain Journal of Mathematics* 4, 287–296.
- Winterwerp, J.C., van Kesteren, W.G.M., 2004. Introduction to the physics of cohesive sediment in the marine environment. In: van Loon, T. (Ed.) *WL/ Delft Hydraulics & Delft University of Technology*, Delft, Netherlands.
- Wyatt, N.B., O'Hern, T.J., Shelden, B., Hughes, L.G., Mondy, L.A., 2013. Size and structure of *Chlorella zofingiensis*/FeCl₃ flocs in a shear flow. *Biotechnology and Bioengineering* 110, 3156–3163.
- Yuan, Y., Farnood, R.R., 2010. Strength and breakage of activated sludge flocs. *Powder Technology* 199, 111–119.

Zhou, G., Kresta, S.M., 1996. Impact of tank geometry on the maximum turbulence energy dissipation rate for impellers. *AIChE Journal* 42, 2476–2490.

Zhu, Z., Yu, J., Wang, H., Dou, J., Wang, C., 2015. Fractal dimension of cohesive sediment flocs at steady state under seven shear flow conditions. *Water* 7, 4385–4408.

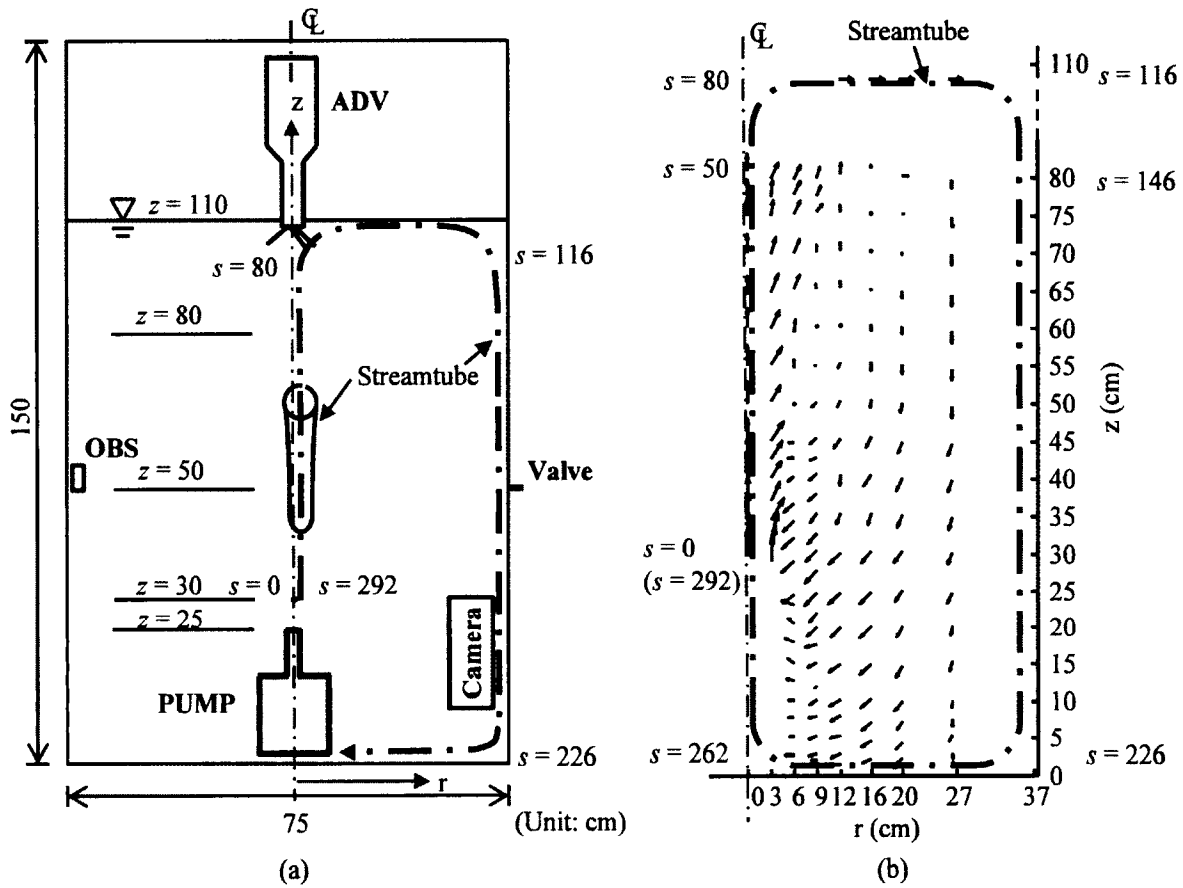


Fig. 5.1 Experimental Setup. The plot of the streamtube along the dashed line is not drawn to scale. It is small near the pump and becomes large when far away. The vertical coordinate, z , starts at the tank bottom and the stream tube coordinate, s , starts at $z = 30$ cm.

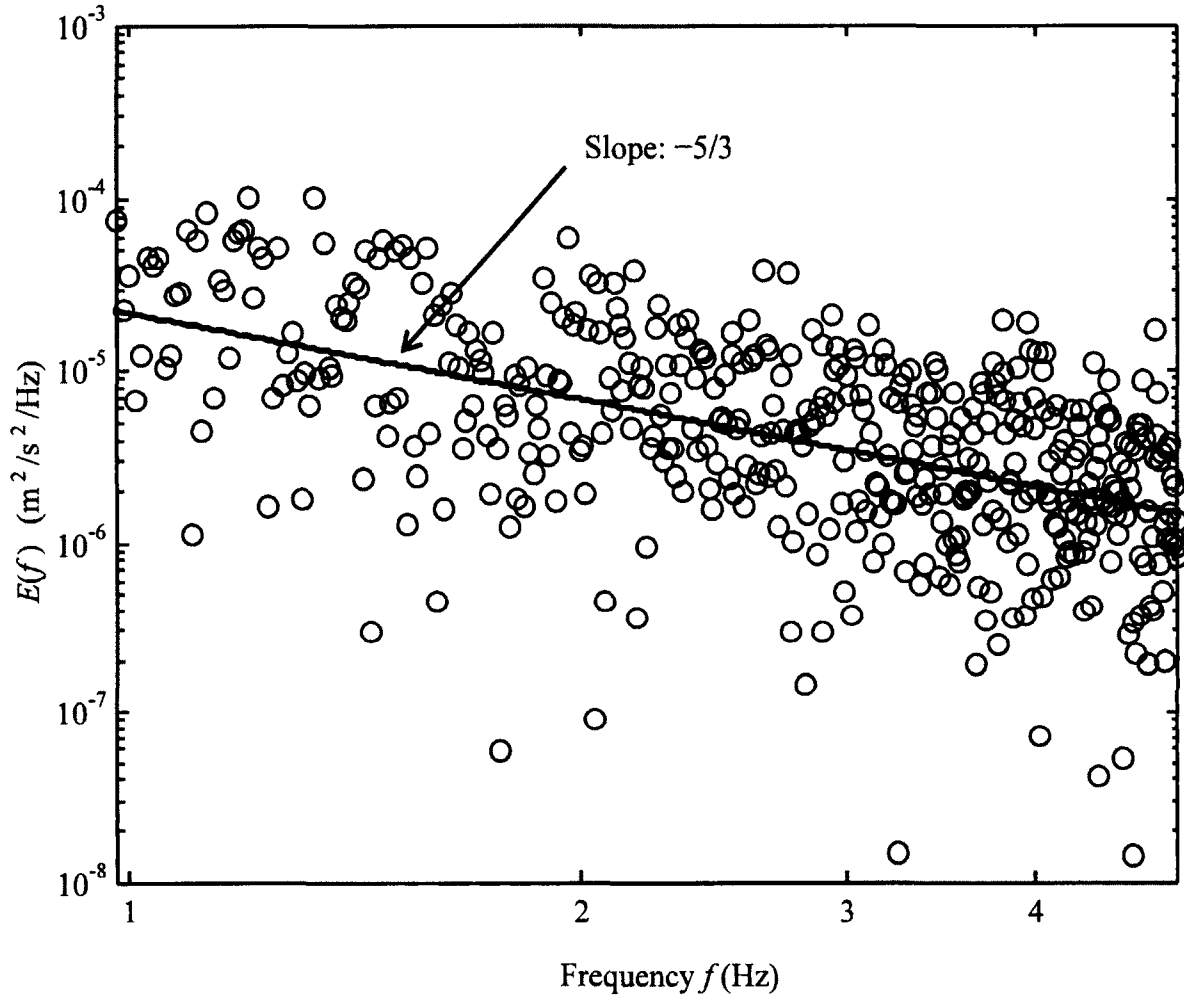


Fig. 5.2 Example of the energy dissipation rate calculated by using the vertical velocity component of the energy spectrum.

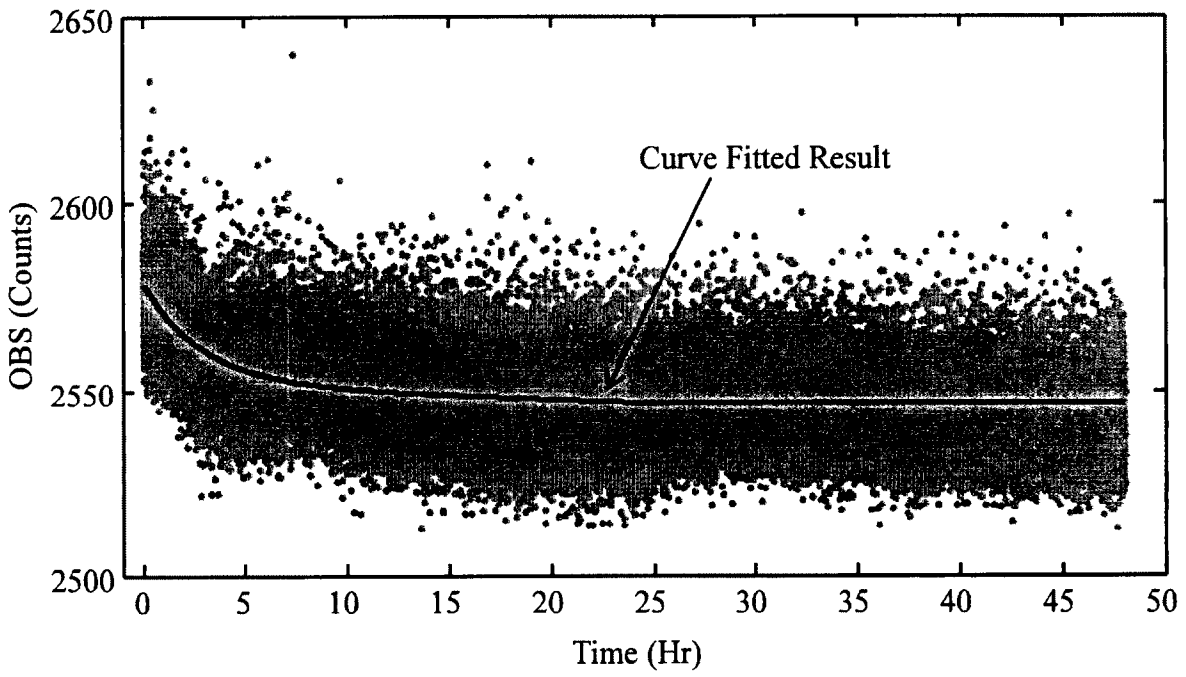


Fig. 5.3 Response of OBS counts during the experimental period.

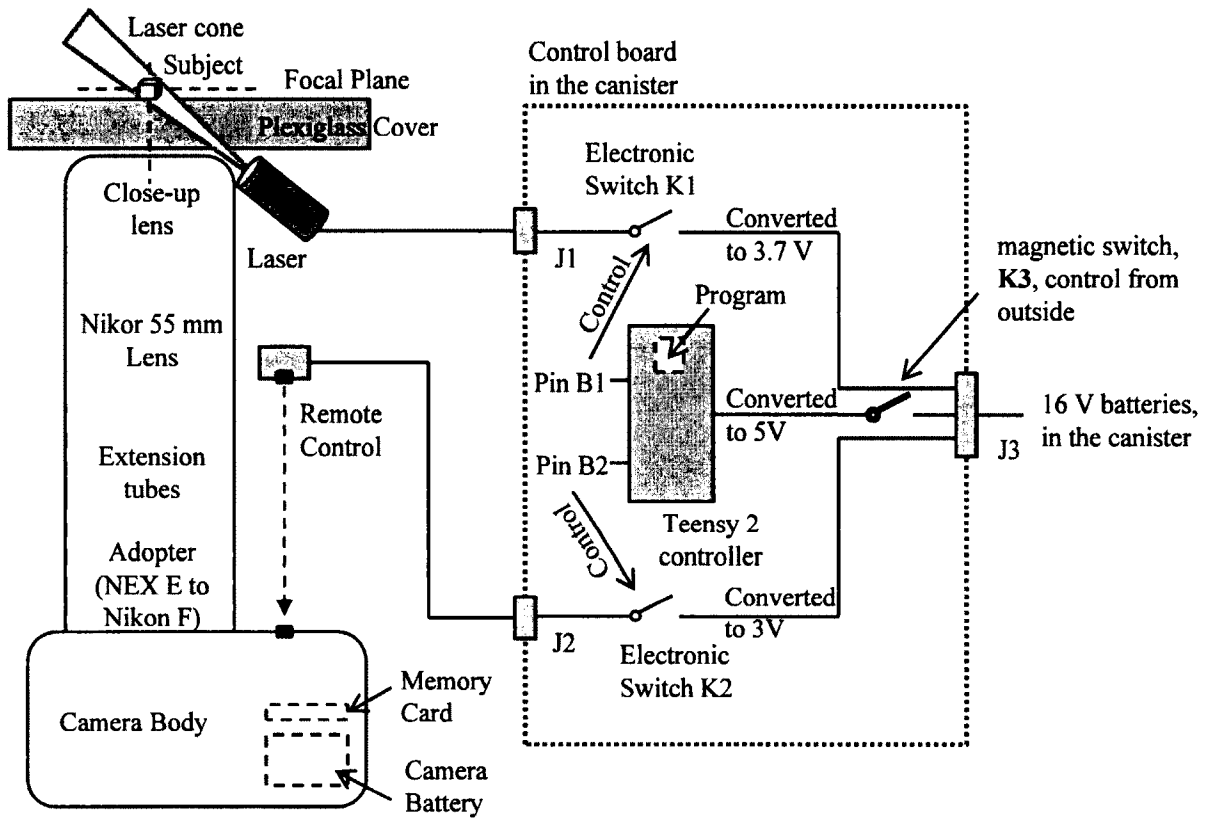


Fig. 5.4 Schematic diagram of the controlling system for acquiring images.

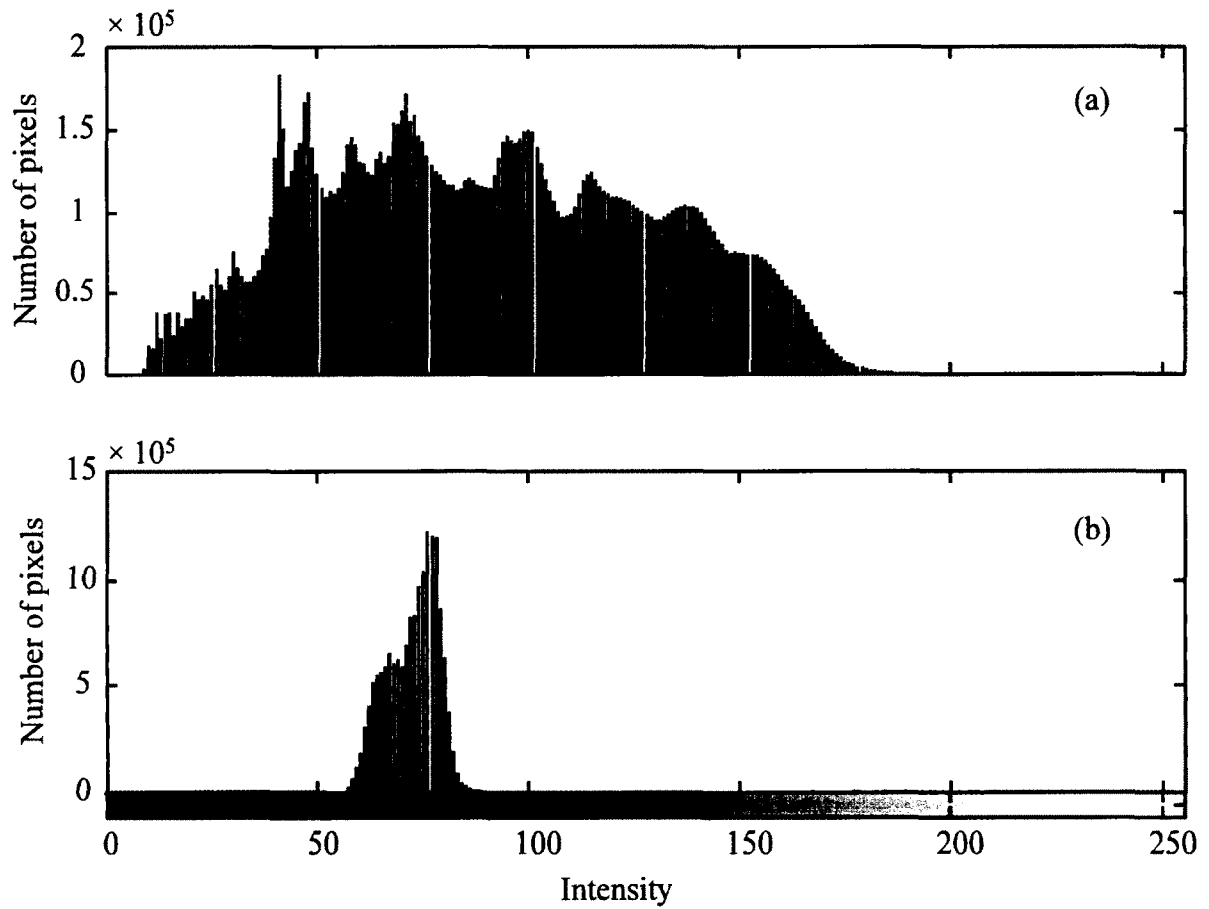


Fig. 5.5 Example of intensity diagram for the light source of (a) a green laser module and (b) twelve LEDs.

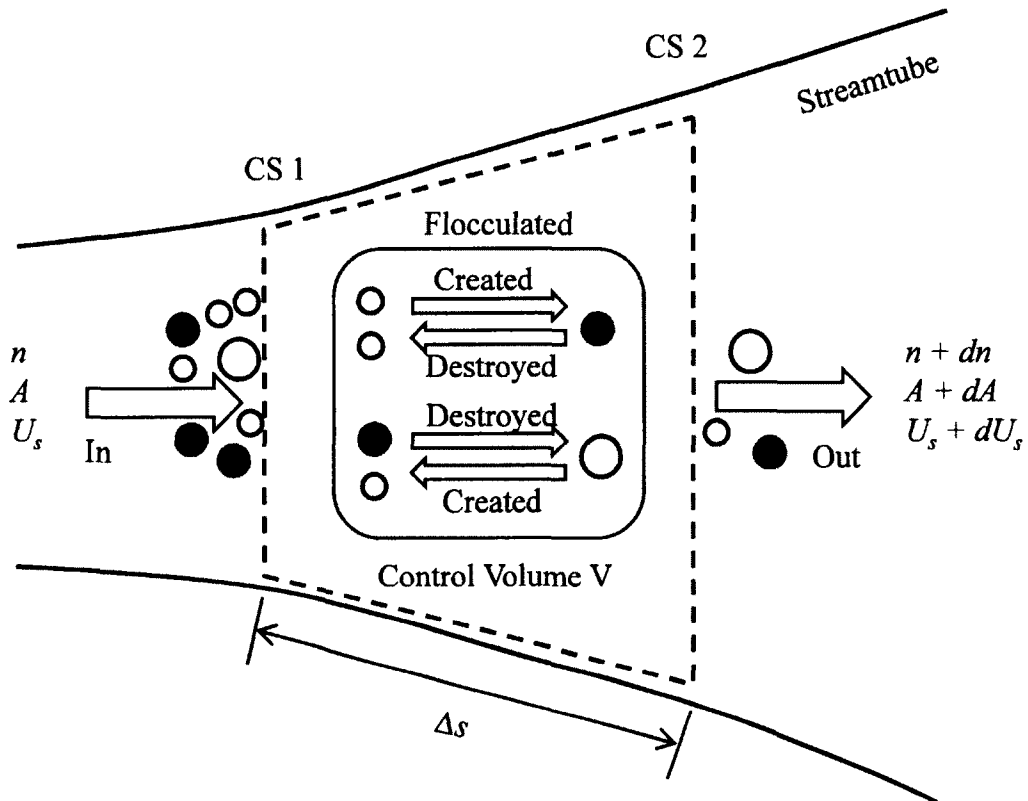


Fig. 5.6 Control volume to derive the governing equation of the conceptual 1-D FSD model along a streamtube. Filled circles represent floc with size L and the number density of this size floc is n .

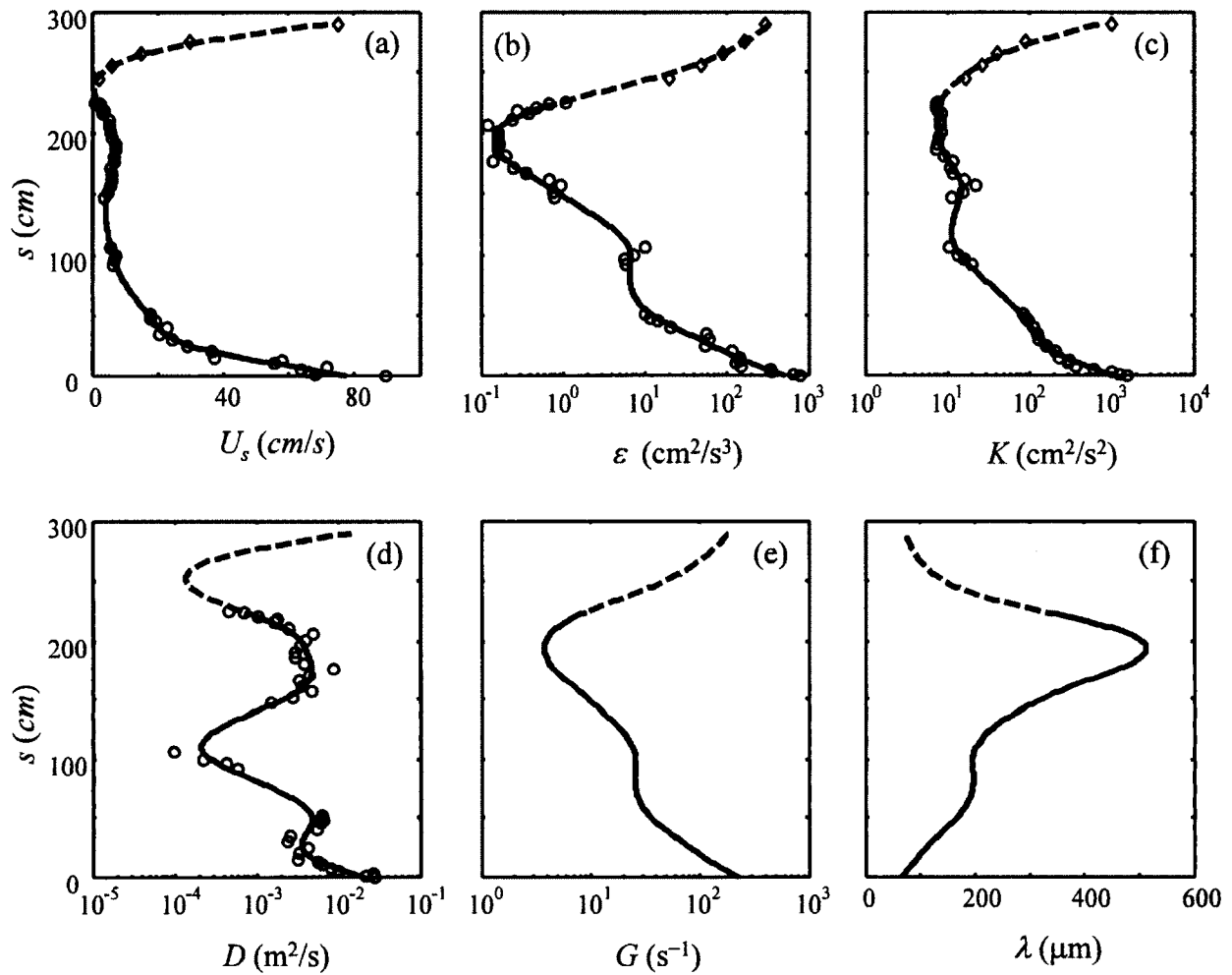


Fig. 5.7 Flow properties along the conceptual streamtube. Circles are measured results, and diamonds are estimated. Lines in (a) (b) and (c) are fitted results, while in (d) (e) and (f) are modeled results based on data shown in (b) and (c). (U_s – flow velocity along the streamtube; ε – energy dissipation rate; K – TKE; D – eddy diffusivity; G – local shear rate; λ – Kolmogorov scale.)

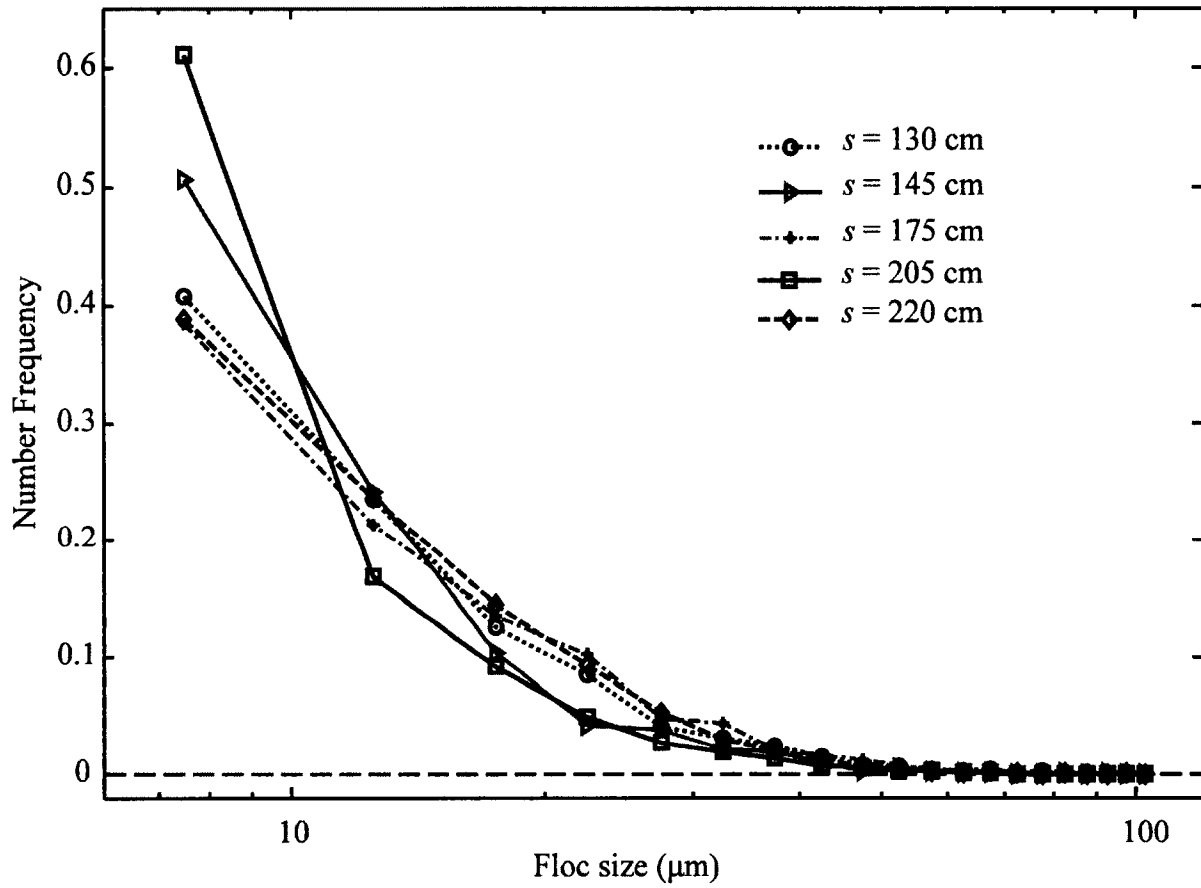


Fig. 5.8 Measured FSDs at varying elevation close to the side wall of the tank.

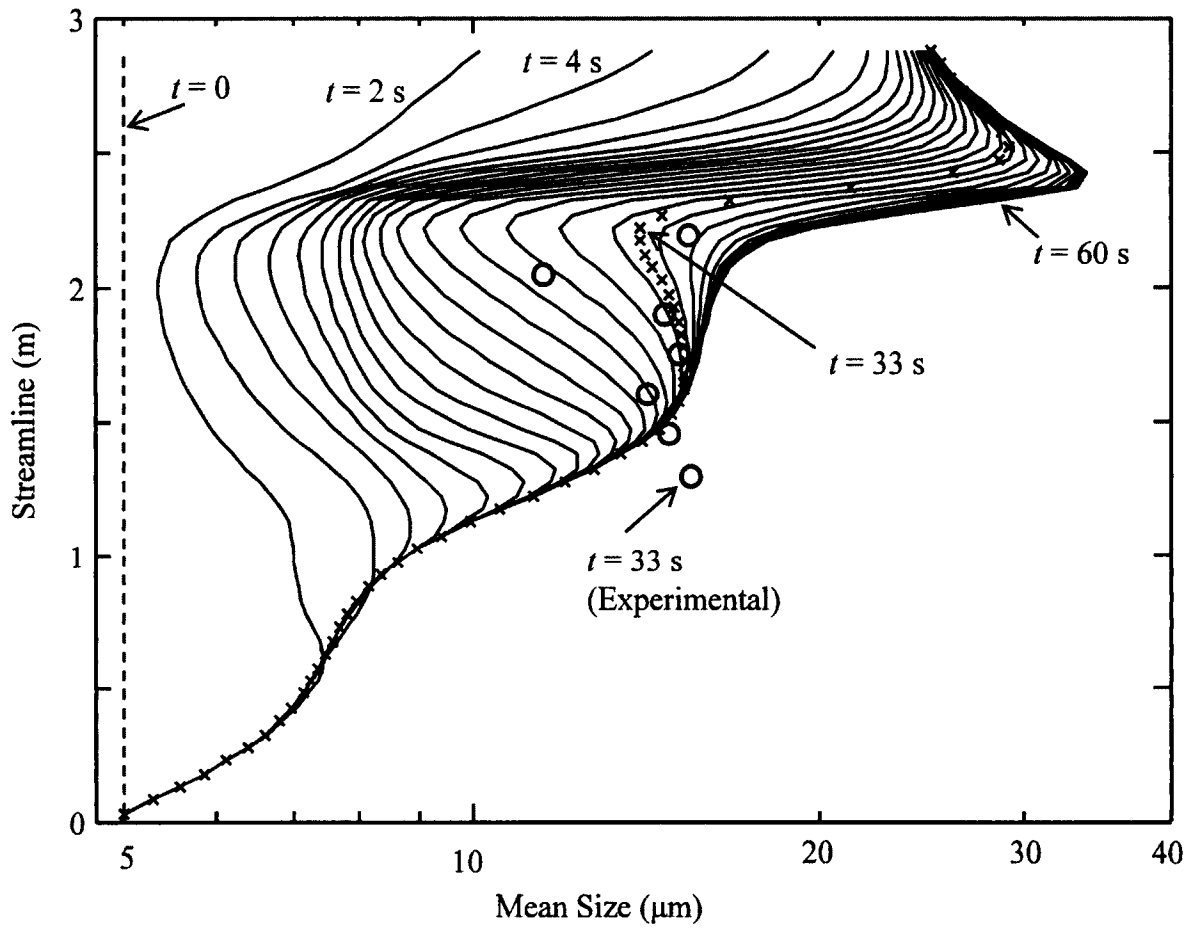


Fig. 5.9 Time evolution of mean size along the streamtube, with symbol “x” and “o” denoting predicted and measured results at residence time $t = 33$ s.

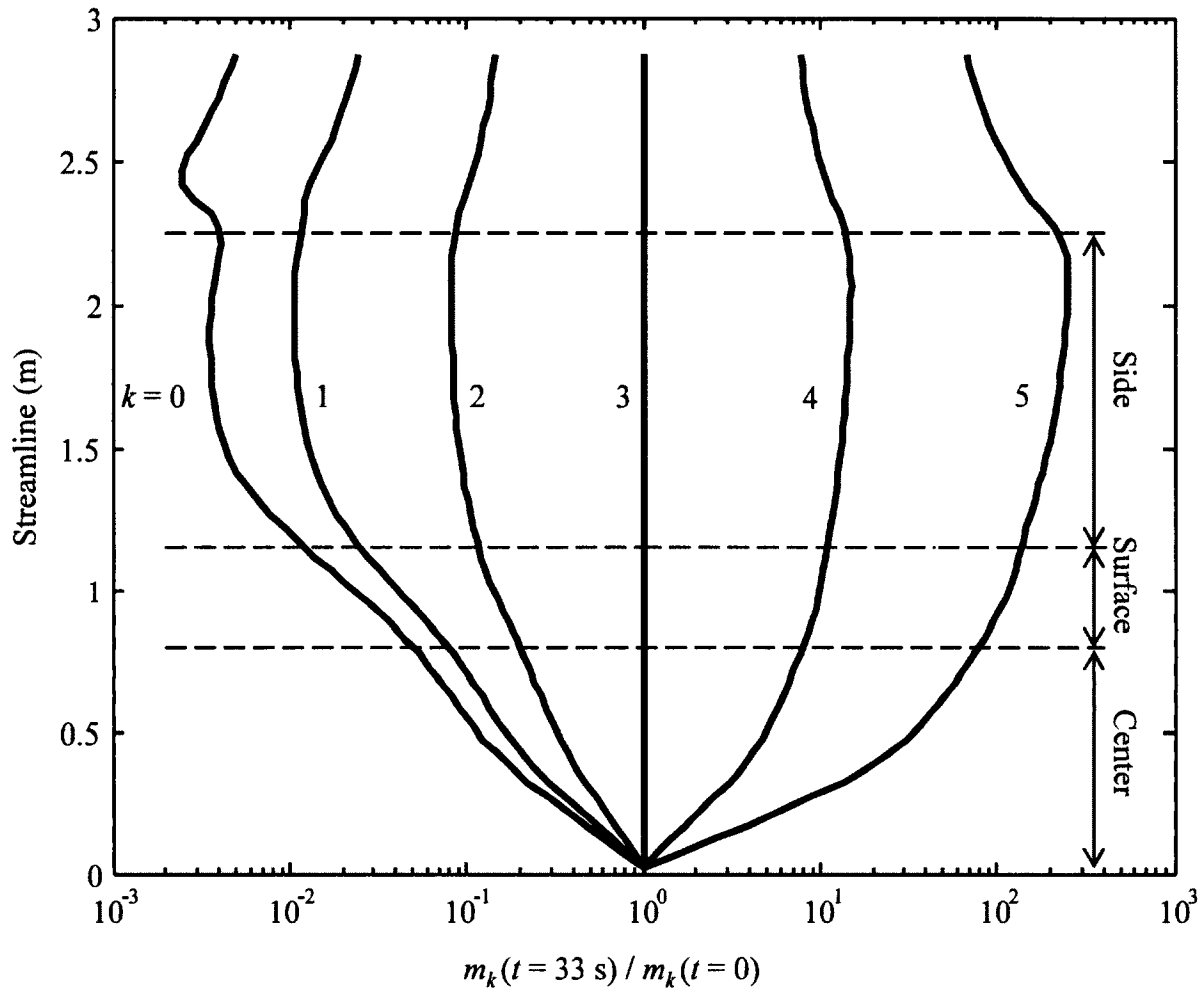


Fig. 5.10 Normalized moments $m_k(t = 33 \text{ s}) / m_k(t = 0)$ ($k = 0, 1, 2, 3, 4, 5$) at $t = 33 \text{ s}$ along the streamtube.

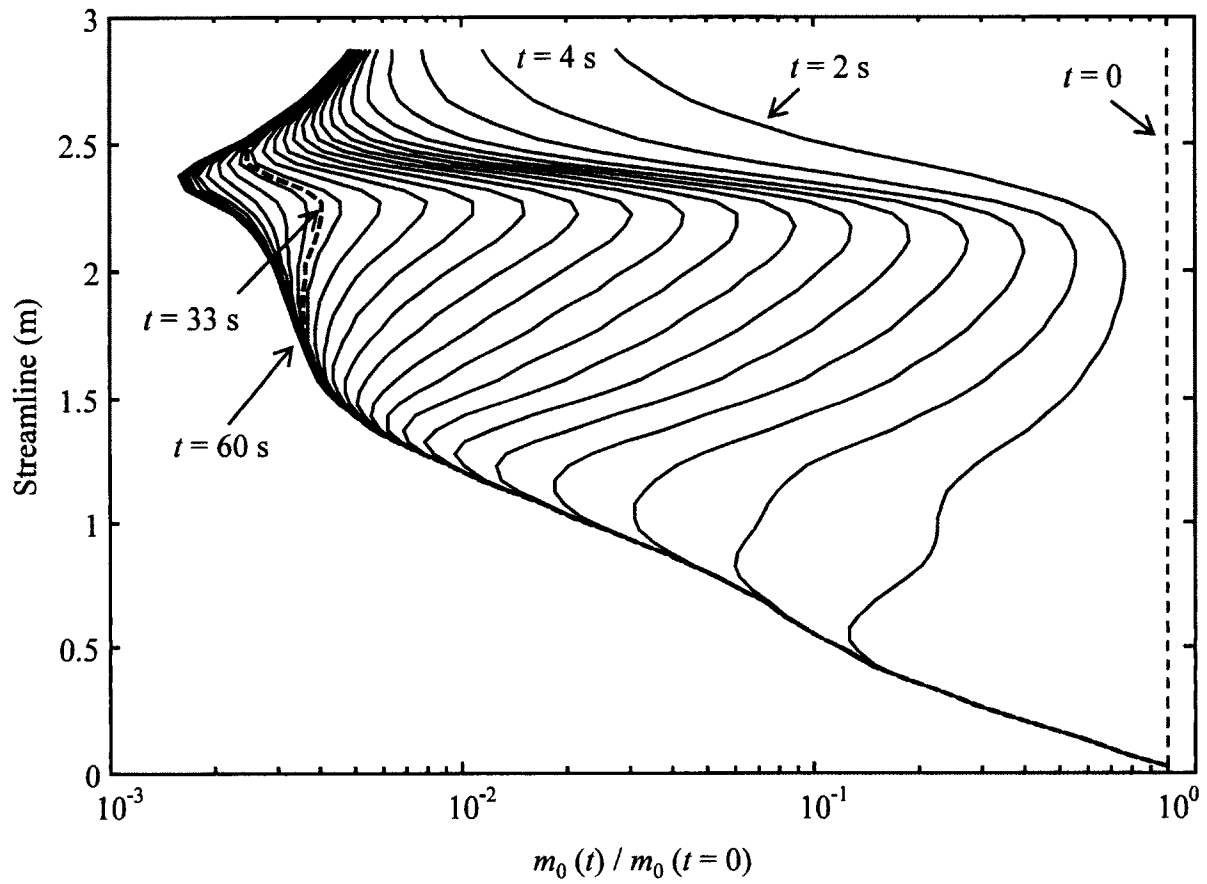


Fig. 5.11 Time evolution of normalized total particle number along the streamtube.

Lines are plotted every 2 s. The initial number is assumed the same along the streamtube.

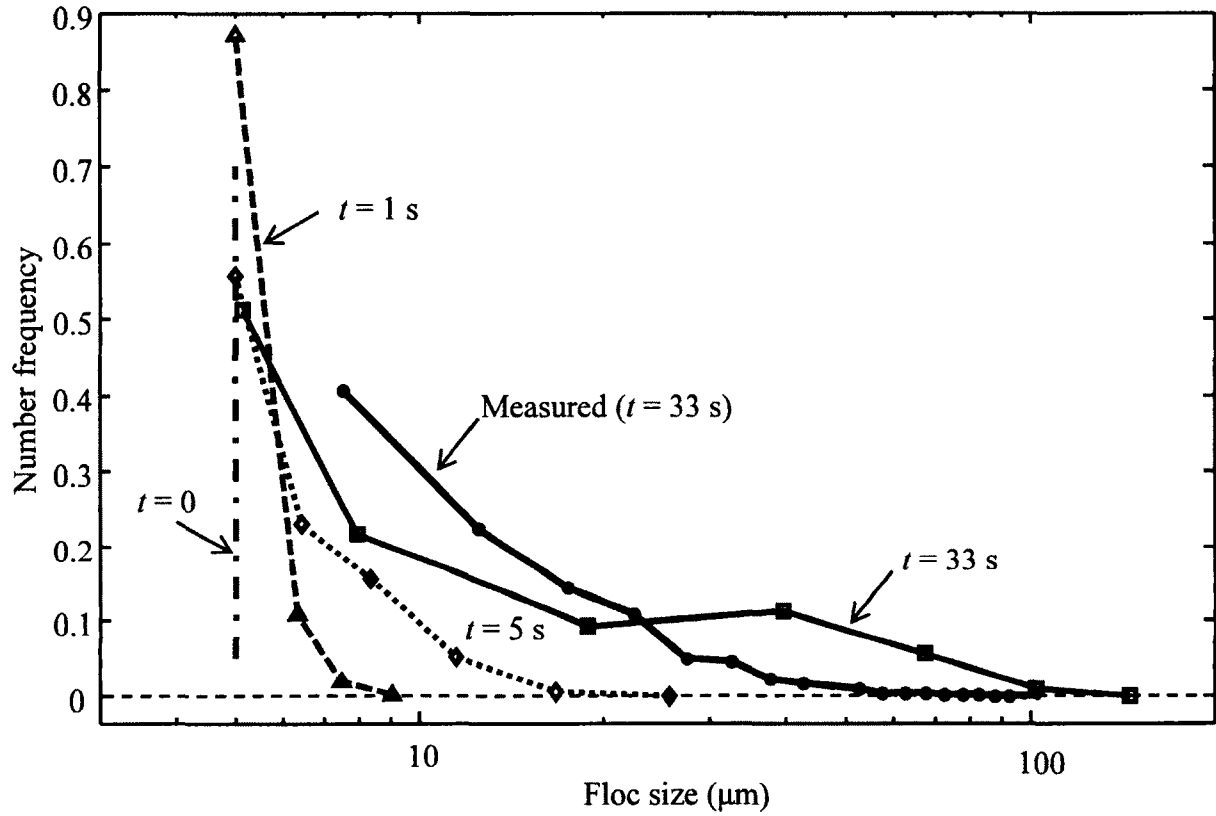


Fig. 5.12 Example of simulated time evolution of FSDs at 50 cm above the bottom of the tank close to the side wall ($s = 176\text{ cm}$). Measured FSD at $t = 33\text{ s}$ are also plotted as comparison.

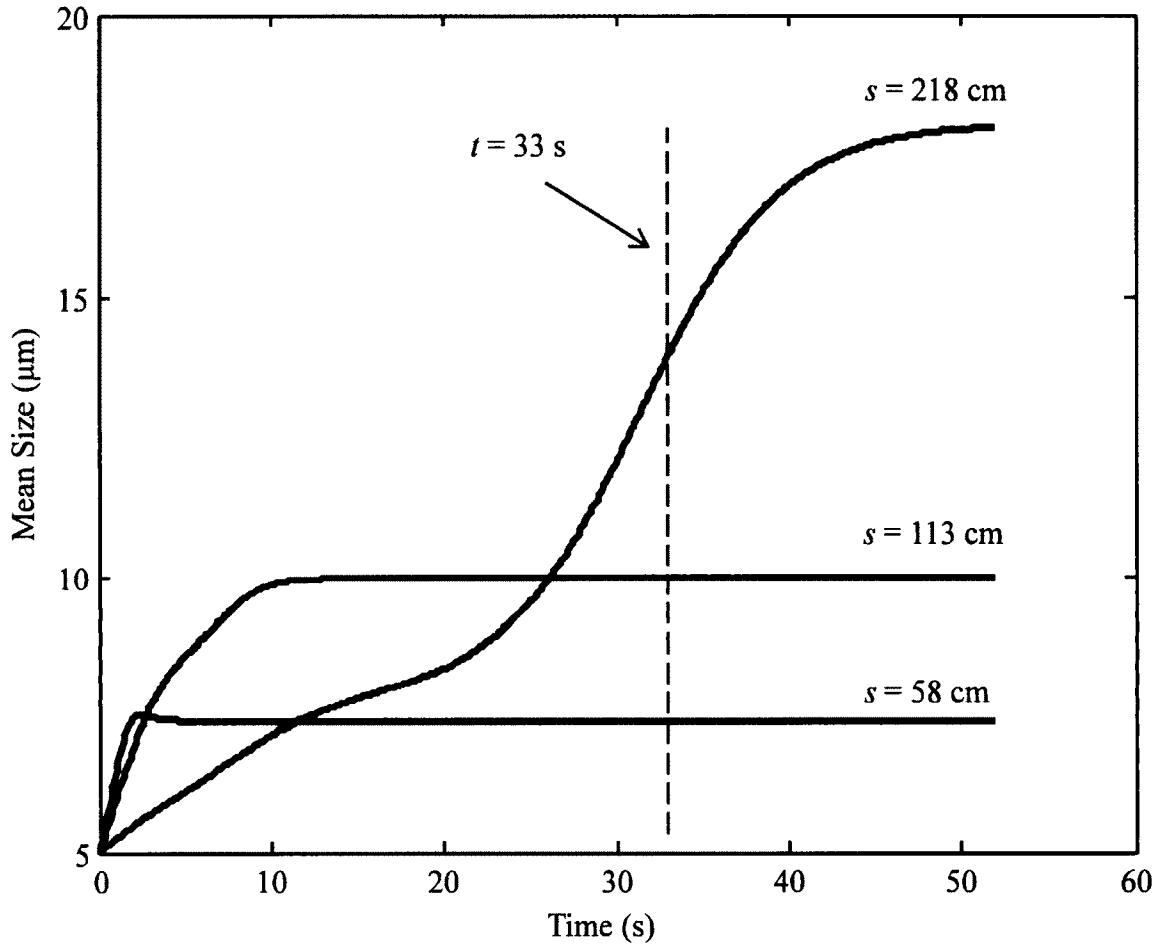


Fig. 5.13 Model predictions of time evolution of mean sizes at three selected locations.

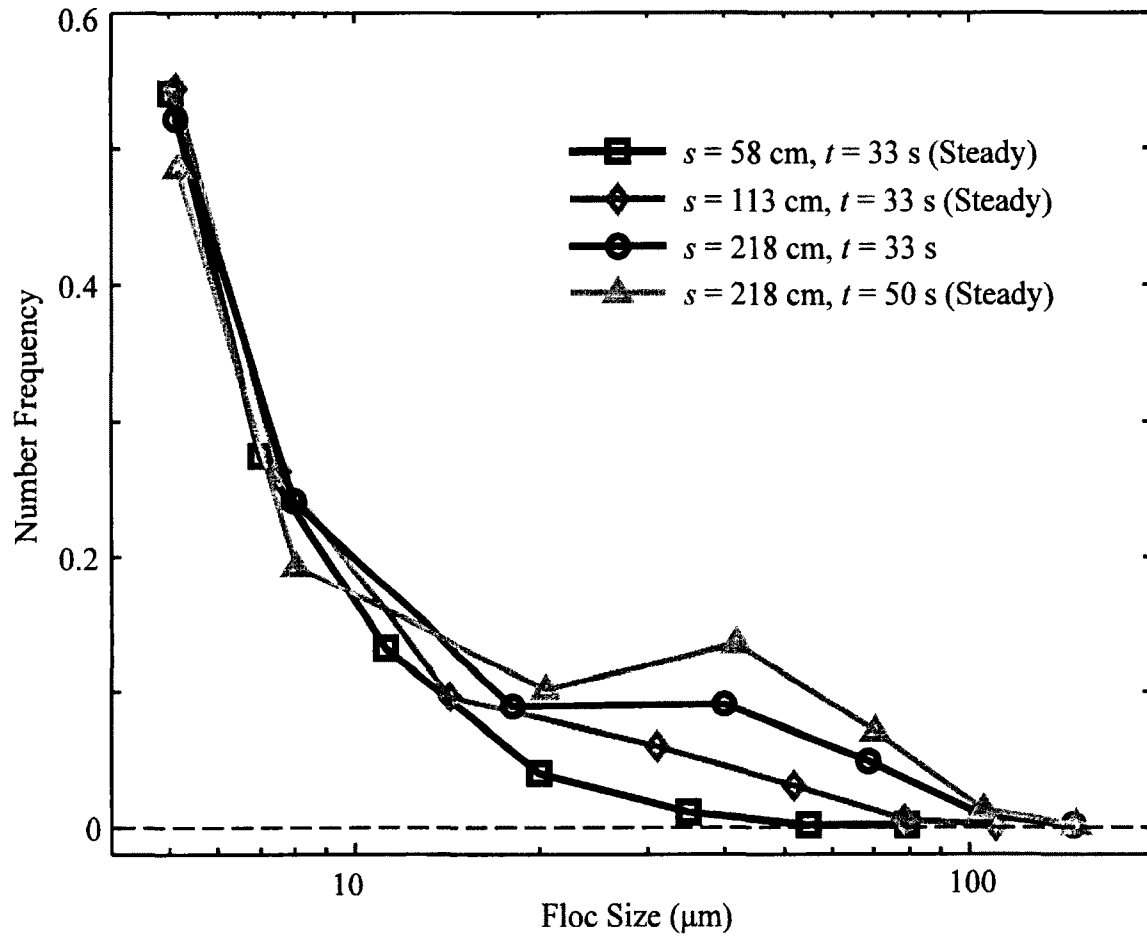


Fig. 5.14 Model predictions of FSDs at $t = 33\text{s}$ and at the equilibrium state for three selected locations.

CHAPTER VI

CONCLUSIONS AND PERSPECTIVES

1. Conclusions

This dissertation has contributed to the understanding of flocculation processes of cohesive sediments through numerical modeling and laboratory experiments. Essential findings of this study include:

(1) Generally, flocculation processes change the performance of suspended cohesive sediments as they enter natural water columns. Thus, floc characteristics (such as floc size, floc shape, floc density and their settling velocity) should be better simulated using a flocculation model to respond to various environmental parameters (such as flow and wind conditions, suspended sediment concentrations, and organic matters), rather than using empirical space and/or time independent values.

(2) Population Balance Model (PBM) solved by the Quadrature Method Of Moments (QMOM) can efficiently and reasonably simulate the evolution of Floc Size Distribution (FSD) of cohesive sediments for a relatively large domain.

(3) Better understanding the process will contribute to the further extension of the PBM. For example, more studies on the determination of flocculation parameters (e.g., the collision efficiency, the breakup frequency, and the fragmentation distribution function) will improve the model predictions by including various chemical and biological effects.

(4) Laboratory experiments such as those in mixing tanks or settling columns are critical to isolate environmental variables and provide data for model improvements based on its physical meanings. For example, settling columns can provide 0-D (zero-dimensional, without transport, e.g., Maggi, 2005; Maggi et al., 2007; Mietta et al., 2008) or 1-D (one-dimensional, e.g., Van Leussen, 1994) environments and mixing tanks/jars can provide

0-D (e.g., Mietta et al., 2009; Keyvani and Strom, 2014; Shen and Maa, *Submitted a*), 1-D (e.g., Shen and Maa, *Submitted b*) or 3-D (three dimensional, e.g., Prat and Ducoste, 2006) environments.

(5) Since flocs are too fragile to withstand collection, transportation, and storing, in-situ measurements (even in the laboratory) are required for reliable results. Thus, the image acquiring and processing system should be one of the necessary instruments to directly observe floc characteristics. Usually, a camera with faster shutter speed will better “freeze” particle movement to find the FSDs but requires a stronger light source. The cost and performance of a camera system should be considered for different applications.

2. Future Study

This section suggests the logical next steps in the line of investigation associated with this study. Future efforts to build upon this dissertation might address the following considerations:

(1) Flocculation models that can simulate FSDs of cohesive sediments include, for example, the PBM (Maggi et al., 2007; Shen and Maa, 2015) and the extended Boltzmann model (Zhang and Zhang, 2011; Zhang et al., 2013). Recent studies showed these two models might have the same origin (Ramkrishna, 2000; Solsvik and Jakobsen, 2015). In some cases, the Lattice Boltzmann Method (LBM), which is typically used to solve the Boltzmann equation, can also be employed to solve the PBM by including the source terms in PBM as force terms in LBM (Majumder et al., 2012a, 2012b). In other cases, the QMOM, which was one of the solution methods for PBM, can also be modified to solve the Boltzmann equation

(Yuan and Fox, 2011). However, a thorough description to relate these two models in terms of describing the fluid system with particulate suspensions is still not complete. If someone can clearly express the relationships and assumptions to bridge these two models, then it would be an improvement in flocculation modeling of cohesive sediments.

(2) It is difficult for the LBM and Class Method PBM (CM-PBM) to simulate the spatial and time variable FSDs for reasonably large domains, since they are limited by computational capabilities. Thus, FSD-capable QMOM-PBM is one of the most efficient models that can couple with computational fluid dynamics models. In this study, the monovariate (e.g., floc size) PBM is solved by the QMOM to give reasonable FSDs with a maximum of eight size classes using double precision. Besides floc size, floc shape, which is indicated by fractal dimension or floc density, is also critical to determine the floc settling velocity. Therefore, it would be a great improvement if someone could develop a bivariate (one property is floc size and the other can be floc density or fractal dimension) PBM to simulate the aggregation and breakage processes. Although various numerical schemes for solving bivariate (or multivariate) PBM have been reported (Wright et al., 2001; Buffo et al., 2013; John and Suciu, 2014), the difficulty in applying this model lies in modifying the fine sediment kinetic kernels (i.e., collision frequency, collision efficiency, breakup frequency, and fragmentation distribution function) to reasonably include both floc size and floc shape. Nevertheless, even the formulation of monovariate kinetic kernels (i.e., kinetic kernel only modeled as functions of floc size) needs further study (Maggi, 2007; Mietta et al., 2008). More variables (e.g., the concentration of different compositions for a floc) can be included in the PBM after bivariate PBMs are well-tested.

(3) Current flocculation models usually cannot explicitly include biological effects,

which nevertheless play an essential role in suspended particle flocculation dynamics. There will be a great improvement if someone can include the effect of organic matter in the model. The methods chosen to include the biological effects might depend on how the organic matter influences the total mass of the particle system. If the biological effects on total floc mass of the system can be neglected, then the flocculation model can be improved by extending the expression of fitting parameters C_1 & C_2 in the model (e.g., Furukawa and Watkins, 2012; Shen and Maa, 2015). If the organic matter fraction in a particle system is roughly fixed, a practical approach to include biological effects in the model is to use two independent PBMs to simulate the inorganic and organic fractions respectively, similar to the study by Maggi (2009). In most environments, however, the total mass may not be conserved when biological effects are included. At that condition, it might be necessary to add the processes of growth and/or nucleation in the source and sink terms of PBM (Kumar, 2006). The former term “growth” (distinguished with the term “aggregation” at this time) describes non-particulate organic matters that are added to the surface of a particle. This leads to an increased mass but unchanged number in a particle system. The latter term “nucleation” describes a new particle formed by non-particulate organic matters. The inclusion of these terms in the source terms of PBM will lead to a more comprehensive representation of flocculation in natural environments.

(4) Up until now, only the flocculation model itself is focused on, which needs flow condition, salinity profile, water depth, etc. as model inputs. A further objective is to couple this flocculation model with hydrodynamic models and turbulence models (e.g., $k-\varepsilon$ model) to simulate current, turbulence, and sediment transport simultaneously in estuaries. Such

performances can be initiated from vertical 1-D cases without wind and wave effects (Maa et al., *Submitted*), and then extended to vertical 2-D and 3-D cases. Surface wave and wind models can be further added as improvements when no-wind conditions are tested well. It is critical to notice that a robust flow-mud model also requires an understanding of the bottom boundary layer, the hindered settling process, and the erosion and deposition conditions of cohesive sediments. Some mathematical models give a nice start (e.g., Winterwerp, 2002; Lee et al., 2014) to include flocculation models in large scale flow-mud models, but more efforts should be emphasized besides the flocculation model, such as the determination of bottom roughness length, sediment gelling concentration, and critical shear stress for sediment erosion and deposition.

(5) Code speed accelerating based on parallel computing is another direction for future studies of model extensions. The majority of the scientific programs are written in sequence and only run on a single CPU (Central Processing Unit) core. The performance of a single CPU doubles approximately every 18 months, according to the widely accepted Moore's Law. Since 2003, however, clock frequency and the performance of products within a single CPU core are limited due to excessive power consumption and heat-dissipation issues. Since then, microprocessor vendors began to focus on increasing the number of cores rather than improving the performance of a single core. Traditional CPU-level parallel computing using MPI (Message Passage Interface, e.g., see Gropp et al., 1996) and OpenMP (Open Multi-Processing, e.g., see Dagum and Menon, 1998) can accomplish such parallel tasks through message passing and memory sharing. Nevertheless, these CPU parallels have to run on large-scale, expensive computers only affordable to a few institutes. With the advent of

NVIDIA's CUDA (Compute Unified Device Architecture) architecture in 2007 and PGI (the Portland Group Inc) CUDA Fortran compiler in 2009, it is possible to use a single PC with many Graphic Process Units (GPUs) to accelerate scientific codes (Kirk and Hwu, 2013; Ruetsch and Fatica, 2014). Recently, a few groups have been working to accelerate PBM codes (e.g., Santos et al., 2013) or finite difference (a typical solution method for transport equations) codes using GPUs (e.g., Ruetsch and Fatica, 2014). There will be a contribution if one can apply the GPU technique to any 1-D floc size distribution model, and then to a coupled flow-mud model.

(6) Model validation needs data from laboratory experiments and field measurements. Since the processes of cohesive sediments in natural environments are still poorly understood, laboratory experiments are initially favorable to simplify the environments, enhance the theory fundamental to the model, and understand the mechanisms and processes. The formulation of flocculation parameters, such as collision efficiency and breakup frequency, are most likely improved through laboratory experiments. Also, of course, the importance of collecting in-situ flow, wind, and sediment data from fields can never be underestimated. For example, salinity, temperature, and water depth data through CTD (Conductivity, Temperature and Depth sensor), flow profile through ADCP (Acoustic Doppler Current Profiler), point flow velocity and turbulence through ADV (Acoustic Doppler Velocimeter), sediment mass concentration through OBS (Optical Backscatter Sensor), FSDs through combinations of LISST (Laser *In Situ* Scattering Transmissometer) and a camera system etc., are critical to validate and improve the model predictions in natural waters.

References

- Buffo, A., Vanni, M., Marchisio, D.L., 2013. Multivariate quadrature-based moments methods for turbulent polydisperse gas-liquid systems. *International Journal of Multiphase Flow* 50, 41–57.
- Dagum, L., Menon, R., 1998. OpenMP: An industry standard API for shared-memory programming. *IEEE Computational Science & Engineering* 5, 46–55.
- Furukawa, Y., Watkins, J.L., 2012. Effect of organic matter on the flocculation of colloidal montmorillonite: a modeling approach. *Journal of Coastal Research* 28, 726–737.
- Gropp, W., Lusk, E., Doss, N., Skjellum, A., 1996. A high-performance, portable implementation of the MPI message passing interface standard. *Parallel Computing* 22, 789–828.
- John, V., Suciu, C., 2014. Direct discretizations of bi-variate population balance systems with finite difference schemes of different order. *Chemical Engineering Science* 106, 39–52.
- Keyvani, A., Strom, K., 2014. Influence of cycles of high and low turbulent shear on the growth rate and equilibrium size of mud flocs. *Marine Geology* 354, 1–14.
- Kirk, D.B., Hwu, W.W., 2013. Programming massively parallel processors: A hands-on approach. Second ed. Morgan Kaufmann, Waltham, MA.
- Kumar, J., Numerical approximations of population balance equations in particulate systems. (Ph.D. Dissertation) Otto-von-Guericke University Magdeburg, Germany.
- Lee, B.J., Toorman, E., Michael, F., 2014. Multimodal particle size distributions of fine-grained sediments: mathematical modeling and field investigation. *Ocean Dynamics* 64, 429–441.

- Maa, J.P.Y., Shao, Y., Shen, X., Shen, J., *Submitted*. Simulating extremely high ebb current velocities in the Changjiang deep-water navigation channel.
- Maggi, F., 2005. Flocculation dynamics of cohesive sediment. (Ph.D. Dissertation) Delft University of Technology, Netherlands.
- Maggi, F., 2007. Variable fractal dimension: a major control for floc structure and flocculation kinematics of suspended cohesive sediment. *Journal of Geophysical Research* 112, C07012.
- Maggi, F., 2009. Biological flocculation of suspended particles in nutrient-rich aqueous ecosystems. *Journal of Hydrology* 376, 116–125.
- Maggi, F., Mietta, F., Winterwerp, J.C., 2007. Effect of variable fractal dimension on the floc size distribution of suspended cohesive sediment. *Journal of Hydrology* 343, 43–55.
- Majumder, A., Kariwala, V., Ansumali, S., Rajendran., A., 2012a. Lattice Boltzmann method for population balance equations with simultaneous growth, nucleation, aggregation and breakage. *Chemical Engineering Science* 69, 316–328.
- Majumder, A., Kariwala, V., Ansumali, S., Rajendran., A., 2012b. Lattice Boltzmann method for multi-dimensional population balance models in crystallization. *Chemical Engineering Science* 70, 121–134.
- Mietta, F., Maggi, F., Winterwerp, J.C., 2008. Chapter 19: sensitivity to breakup functions of a population balance equation for cohesive sediments. INTERCOH 2005. Sediment and Ecohydraulics 9, pp. 275–286.

- Mietta, F., Chassagne, C., Manning, A.J., Winterwerp, J.C., 2009. Influence of shear rate, organic matter content, pH and salinity on mud flocculation. *Ocean Dynamics* 59, 751–763.
- Prat, O.P., Ducoste, J.J., 2006. Modeling spatial distribution of floc size in turbulent processes using the quadrature method of moment and computational fluid dynamics. *Chemical Engineering Science* 61, 75–86.
- Ramkrishna, D., 2000. Population balances: Theory and applications to particulate systems in engineering. Academic Press, San Diego.
- Ruetsch, G., Fatica, M., 2014. CUDA Fortran for scientists and engineers: Best practices for efficient CUDA Fortran programming. Morgan Kaufmann, Amsterdam.
- Santos, F.P., Senocak, I., Favero, J.L., Lage, P.L.C., 2013. Solution of the population balance equation using parallel adaptive cubature on GPUs. *Computers and Chemical Engineering* 55, 61–70.
- Shen, X., Maa, J.P.Y., 2015. Modeling floc size distribution of suspended cohesive sediments using quadrature method of moments. *Marine Geology* 359, 106–119.
- Shen, X., Maa, J.P.Y., *Submitted a*. A camera and image processing system for floc size distributions of suspended particles.
- Shen, X., Maa, J.P.Y., *Submitted b*. Floc size distributions of suspended kaolinite in an advection transport dominated tank: Measurements and modeling.
- Solsvik, J., Jakobsen, H.A., 2015. The foundation of the population balance equation: A review. *Journal of Dispersion Science and Technology* 36, 510–520.

- van Leussen, W., 1994. Estuarine macroflocs and their role in fine-grained sediment transport. (Ph.D. Dissertation) University of Utrecht, Netherlands.
- Winterwerp, J.C., 2002. On the flocculation and settling velocity of estuarine mud. *Continental Shelf Research* 22, 1339–1360.
- Wright, D.L., McGraw, R., Rosner, D.E., 2001. Bivariate extension of the quadrature method of moments for modeling simultaneous coagulation and sintering of particle populations. *Journal of Colloid and Interface Science* 236, 242–251.
- Yuan, C., Fox, R.O., 2011. Conditional quadrature method of moments for kinetic equations. *Journal of Computational Physics* 230, 8216–8246.
- Zhang, J.F., Zhang, Q.H., 2011. Lattice Boltzmann simulation of the flocculation process of cohesive sediment due to differential settling. *Continental Shelf Research* 31, S94–S105.
- Zhang, J.F., Zhang, Q.H., Maa, J.P.Y., Qiao, G.Q., 2013. Lattice Boltzmann simulation of turbulence-induced flocculation of cohesive sediment. *Ocean Dynamics* 63, 1123–1135.

APPENDIX A:

FLOC SIZE DISTRIBUTION BOX MODEL

(CODE IN FORTRAN)

File name: 'Floc0D.f90'.

! This is a 0-D Floc Size Distribution (FSD) model for flocculation processes
of cohesive sediments.

! Written by Xiaoteng Shen

! (Virginia Institute of Marine Science, xiaoteng@vims.edu).

! Short-term Purpose: Solve FSDs.

! Long-term Purpose: Couple with hydrodynamic models, turbulence models,
and sediment transport models.

! Governing Equation: Population Balance Equation (PBE).

! Solution Method: Quadrature Method Of Moments (QMOM).

! Input file: (*.log)

! File 1: Selected quadrature points.log (For future extensions)

! --- Only used when fixed pivot QMOM approach is selected.

! File 2: Floc1D.log

! --- Basic input parameters.

! File 3: Initial moments.log (Optional)

! --- Only used when primary particle size distribution is available.

! Output file: (*.lis)

! File 92: Time record.lis --- Records time for results saving.

! File 93: SSTERM_death_bre.lis --- Death of flocs due to breakage.

! File 94: SSTERM_birth_bre.lis --- Birth of flocs due to breakage.

! File 95: SSTERM_death_agg.lis --- Death of flocs due to aggregation.

! File 96: SSTERM_birth_agg.lis --- Birth of flocs due to aggregation.

! File 97: Abscissas and Weights.lis --- Records the characteristic
class sizes and corresponding characteristic number frequencies.

! File 98: Adjustable moments evolution.lis --- Records the time evolution
of the adjustable moments of FSDs.


```

! File 99: Warning File.lis (Optional)      --- Warning.

! Global constant
module global
  integer, parameter:: NP = selected_real_kind(8) ! Double precision
  real(kind=NP), parameter:: pi = 3.141592653589793d0
  real(kind=NP), parameter:: mvis = 1.0d-6 ! Molecular viscosity, m2/s
  real(kind=NP), parameter:: rho_w = 1.0d3 ! Density of water, kg/m3
  ! real(kind=NP), parameter:: haymaker = 3.5d-21 ! Hamaker constant, J
  real(kind=NP), parameter:: rho_s = 2.65d3 ! Density of sediment, kg/m3
end module

! Main program
PROGRAM FLOC0D
  use global
  implicit none
  integer i, il, j, n, Nd, nt, ncheck, Ninital, N_m1, N_m2, N_m3, &
    nout, break_flag
  integer option_solv, option_Gauss, option_initial, &
    option_beta, option_alpha, option_break, option_fragdis
  real(kind=NP) G, dt, adjust, C1, C2, lp, N0, time, lpmax, Cm
  real(kind=NP), allocatable:: birth_agg(:), birth_bre(:), &
    death_agg(:), death_bre(:), anu(:), ssterm(:), x(:), w(:), &
    agg(:), bre(:)
  character*100 mark

  write(*,*) 'This program is solving the population-balance-based'
  write(*,*) 'flocculation model using quadrature method of moments.'
  write(*,*) '(Xiaoteng Shen, Virginia Institute of Marine Science,'
  write(*,*) ' xiaoteng@vims.edu, 2014.'
  write(*,*) '-----'
  write(*,1020)

1020  format('      time(s)      Number      ssterm(1)      Volume
Mean d10(um)')

! Read the input file of this flocculation model

```

```

open(2, file = 'Floc0D.log', form = 'formatted', status = 'old')
do i=1,17
    read(2,'(a100)') mark
end do
read(2,*) Nd, n, adjust, dt, nt, ncheck, option_solv, option_Gauss, &
    lp, G, Cm
allocate(x(Nd), w(Nd), anu(n), ssterm(n), birth_agg(n), &
    birth_bre(n), death_agg(n), death_bre(n), agg(n), bre(n))

do i=1,4
    read(2,'(a100)') mark
end do
read(2,*) option_initial

do i=1,9
    read(2,'(a100)') mark
end do
read(2,*) option_beta, option_alpha, option_break, option_fragdis, &
    C1, C2

close(2)

time=0.0d0
N_m3 = Int(adjust*3.0d0+0.40d0)+1
N_m2 = Int(adjust*2.0d0+0.40d0)+1
N_m1 = Int(adjust*1.0d0+0.40d0)+1

if (option_initial == 1) then
    ! "Cm" in g/L; "rho_s" in kg/m3; "lp" in micron; "N0" in #/m3
    N0 = Cm/rho_s/lp**3.0d0*1.0d18
    do i = 1,n
        anu(i) = N0*lp**((i-1)/adjust)
    end do
else
    ! Read the initial ADJUSTABLE moments
    open(3, file = 'Initial moments.log', form = 'formatted', status = 'old')

```

```

        do i = 1,32      ! 32 is possible maximum number of size class
            read(3,*, end = 1006) anu(i)
        end do
1006      Ninital=i-1 ! # of initial moments in "Initial moments.log"
        close(3)
        N0 = anu(1)*Cm/rho_s/anu(N_m3)*1.0d18
        do i = 1,n
            anu(i)=N0*anu(i)
        end do
    end if

    open(98,file = "Adjustable Moments Evolution.lis")
        write(98, *)      "% Evolution of Moments (Row - Time Evolution; &
                           Column 1 to 2Nd - Adjustable Moments)"
        write(98, *)      "% Number of tracked moments:",n,";&
                           Number of abscissas:",Nd
        write(98, *)      "%-----"
        write(98, '(64D19.10)') (anu(i)/N0,i = 1,n)
    close(98)

    ! Compute and record the initial abscissas and nodes
    if (option_solv == 1) then
        call wheeler(Nd, anu, x, w, option_Gauss, lp, nout)
    elseif (option_solv == 2) then
        open(99,file="Warning File.lis")
            write(99,*) "Warning: Please give subroutine for &
                        fixed pivot quadrature!"
        close(99)
        stop
    end if

    do i=1,Nd
        x(i)=x(i)**adjust
    end do

    lpmax=x(nout)

```

```

do i = 1,Nd
  if (x(i) < 0.0d0) then
    x(i) = 0.0d0
    w(i) = 0.0d0
    nout = nout-1
  end if
end do

end do

open(97,file="Abscissas and Weights.lis")
write(97, *)   "% Evolution of Abscissas and Weights"
write(97, *)   "% Number of tracked moments:",n,"; &
               Number of abscissas:",Nd
write(97, *)   "% Note: Row - Time Evolution; Column 1 to Nd - Abscissas;
Column Nd+1 to 2Nd - Weights."
write(97, *)   "%-----"
write(97, '(64D19.10)') (x(i),i = 1,Nd), (w(i)/anu(1),i = 1,Nd)
close(97)

! Compute and record initial source and sink terms
break_flag = 1
call flocssterm (option_beta, option_alpha, option_break, &
                 option_fragdis, nout, n, G, adjust, C1, C2, lp, &
                 x, w, N0, anu(1), lpmax, nout, break_flag, N_m2, &
                 N_m3, anu, birth_agg, death_agg, &
                 birth_bre, death_bre, agg, bre, ssterm)

open(96,file = "SSTERM_birth_agg.lis")
write(96, *)   "% Source and Sink Terms &
               Part 1. Floc birth due to aggregation. "
write(96, *)   "% Number of tracked moments:",n,"; &
               Number of abscissas:",Nd
write(96, *)   "%-----"
write(96, '(64D19.10)') (birth_agg(i),i=1,n)
close(96)

open(95,file = "SSTERM_death_agg.lis")
write(95, *)   "% Source and Sink Terms &

```

```

                Part 2. Floc death due to aggregation"
write(95, *)    "% Number of tracked moments:",n,";"&
                Number of abscissas:",Nd
write(95, *)    "%-----"
write(95, '(64D19.10)') (death_agg(i),i = 1,n)
close(95)

open(94,file = "SSTERM_birth_bre.lis")
write(94, *)    "% Source and Sink Terms &
                Part 3. Floc birth due to breakup"
write(94, *)    "% Number of tracked moments:",n,";"&
                Number of abscissas:",Nd
write(94, *)    "%-----"
write(94, '(64D19.10)') (birth_bre(i),i = 1,n)
close(94)

open(93,file = "SSTERM_death_bre.lis")
write(93, *)    "% Source and Sink Terms &
                Part 4. Floc death due to breakup"
write(93, *)    "% Number of tracked moments:",n,";"&
                Number of abscissas:",Nd
write(93, *)    "%-----"
write(93, '(64D19.10)') (death_bre(i),i = 1,n)
close(93)

open(92,file = "Time record.lis")
write(92, *)    "% Time (in second)"
write(92, *)    "%-----"
write(92, '(f12.3)') time
close(92)

write(*,1021) time, anu(1)/N0 , ssterm(1)/N0, &
                anu(N_m3)/N0, anu(N_m1)/anu(1)
1021  format (f13.2, f18.10, f18.10, f18.6, f10.3)

! Next time step
do j = 1,nt

```

```

1030  time=time+dt

! Update the moment
! Can be extended to 1-D for adding a subroutine
do i = 1,n
    anu(i) = anu(i)+dt*ssterm(i)
end do

! Find the abscissas and weights, depending on different solving method
if (option_solv == 1) then
    call wheeler(Nd, anu, x, w, option_Gauss, lp, nout)
elseif (option_solv == 2) then ! Leave for further extension
    open(99,file="Warning File.lis")
        write(99,*) "Warning: Please give subroutine &
                    for fixed pivot quadrature!"
    close(99)
    stop
end if

do i = 1,Nd
    x(i) = x(i)**adjust
end do

do i=1,Nd
    if (x(i) < 0.0d0) then
        x(i) = 0.0d0
        w(i) = 0.0d0
        nout = nout-1
    end if
end do

break_flag=2
call flocssterm (option_beta, option_alpha, option_break, &
                option_fragdis, nout, n, G, adjust, C1, C2, lp, &
                x, w, N0, anu(1), lpmax, nout, break_flag, N_m2, &
                N_m3, anu, birth_agg, death_agg, &
                birth_bre, death_bre, agg, bre, ssterm)

```

```

if (j == 600*int(j/600) .OR. j == nt) then
    write(*,1021) time, anu(1)/N0 , ssterm(1)/N0, &
        anu(N_m3)/N0, anu(N_m1)/anu(1)
end if

! Record every "ncheck" time step and the last time step
if (j == ncheck*int(j/ncheck) .OR. j == nt) then
    open(98,file = "Adjustable Moments Evolution.lis", &
        position = "append")
    write(98, '(64D19.10)') (anu(i)/N0,i = 1,n)
    close(98)

    open(97,file = "Abscissas and Weights.lis", position = "append")
    write(97, '(64D19.10)') (x(i),i = 1,Nd), (w(i)/anu(1),i = 1,Nd)
    close(97)

    open(96,file = "SSTERM_birth_agg.lis", position = "append")
    write(96, '(64D19.10)') (birth_agg(i),i = 1,n)
    close(96)

    open(95,file = "SSTERM_death_agg.lis", position = "append")
    write(95, '(64D19.10)') (death_agg(i),i = 1,n)
    close(95)

    open(94,file = "SSTERM_birth_bre.lis", position = "append")
    write(94, '(64D19.10)') (birth_bre(i),i = 1,n)
    close(94)

    open(93,file = "SSTERM_death_bre.lis", position = "append")
    write(93, '(64D19.10)') (death_bre(i),i = 1,n)
    close(93)

    open(92,file = "Time record.lis", position = "append")
    write(92, '(f12.3)') time
    close(92)
end if

```

```

        if (j == nt) pause
    end do

END PROGRAM FLOC0D

!+++++

SUBROUTINE FLOCSSTERM (option_beta, option_alpha, option_break, &
                      option_fragdis, Ndd, n, G, adjust, C1, C2,lp,&
                      x, w, N0, amu0, lpmax, nout,break_flag, &
                      N_m2, N_m3, anu, birth_agg, death_agg, birth_bre, &
                      death_bre, agg, bre, ssterm)

    use global
    implicit none

    integer          option_beta, option_alpha, option_break, option_fragdis
    integer          n, Ndd, break_flag, N_m2, N_m3, nout
    real(kind=NP)    eps, adjust, C1, C2, lp, lpmax
    real(kind=NP)    ssterm(n), x(Ndd), w(Ndd)
    real(kind=NP)    birth_agg(n), birth_bre(n), death_agg(n), death_bre(n)
    real(kind=NP)    agg(n), bre(n), birth(n), death(n), anu(n)

! Purpose: For each time step, computing flocculation source and sink term,
!           as well as the abscissas and weights.

! Input:
! option_beta   Indicator of function of collision frequency.
! option_alpha  Indicator of function of collision efficiency.
! option_break  Indicator of function of breakup frequency.
! option_fragdis Indicator of breakup distribution function.
! Ndd           Number of nodes.
! n            Number of tracked moments.
! G            Shear rate.
! adjust       Adjustable factor.
! C1           Empirical factor for collision efficiency.
! C2           Empirical factor for breakup frequency.
! lp           Size of primary particle, in micrometer.

```



```

! x(Ndd)          Abscissas.
! w(Ndd)          Weights.
!
! Output:
! ssterm(n)       Total source and sink terms for n moment equations.
! birth_agg(n)    Birth of flocs due to aggregation.
! birth_bre(n)    Birth of flocs due to breakup.
! death_agg(n)    Death of flocs due to aggregation.
! death_bre(n)    Death of flocs due to breakup.
!
! Others:
! beta(Ndd,Ndd)   Collision frequency
! alpha(Ndd,Ndd)  Collision efficiency
! breakup(Ndd)    Break frequency of particle with size xi(i=1,...Nd)
! fragdis(Ndd,n)  Breakup distribution of particle with size xi(i=1,...Nd) for
n moment equations.

```

```

integer          i, j, k
real(kind=NP)    G, lambda, N0, amu0
real(kind=NP)    beta(Ndd,Ndd), alpha(Ndd,Ndd), breakup(Ndd), fragdis(Ndd,n)
real(kind=NP),external:: ws, nf, strength

```

```

! Initialize source and sink term for each time step

```

```

do k = 1,n
  birth_agg(k) = 0.0d0
  death_agg(k) = 0.0d0
  birth_bre(k) = 0.0d0
  death_bre(k) = 0.0d0
end do

```

```

! Collision frequency

```

```

if (option_beta == 1) then

```

```

  do j = 1,Ndd

```

```

    do I = 1,Ndd

```

```

      ! Effect of shear only

```

```

      beta(i,j) = 1.0d0/6.18d0*G*(x(i)+x(j))**3.0d0*1.0d-18

```

```

    end do
  end do

```

```

        end do
    else
        open(99,file = "Warning File.lis")
        write(99,*) "Warning: Please give other used defined &
                    collision frequency function!"

        close(99)

        stop
    end if

! Collision efficiency
if (option_alpha == 1) then
    do j = 1,Ndd
        do i = 1,Ndd
            alpha(i,j)=C1    ! Constant
            !if (alpha(i,j) > 1.0d0 )    alpha(i,j) = 1.0d0
        end do
    end do
else
    open(99,file = "Warning File.lis")
    write(99,*) "Warning: Please give other used defined &
                collision efficiency function!"

    close(99)

    stop
end if

! Aggregation source and sink term
do k = 1,n
    do j = 1,Ndd
        do i = 1,Ndd
            birth_agg(k)= birth_agg(k)+ 0.5d0*beta(i,j) &
                        *alpha(i,j)*w(i)*w(j)*(x(i)**3.0d0+ &
                        x(j)**3.0d0)**((k-1.0d0)/3.0d0/adjust)
            death_agg(k)= death_agg(k)+beta(i,j)*alpha(i,j) &
                        *w(i)*w(j)*x(i)**((k-1.0d0)/adjust)
        end do
    end do
end do

```

```

! Breakup frequency
if (option_break == 1) then
  do i = 1,Ndd
    if (x(i) < lp*2.0d0**(1.0d0/3.0d0)) then
      breakup(i) = 0.0d0
    else
      breakup(i) = C2*(mvis*rho_w/strength(x(i),lp)) &
        **0.5d0*G**1.5d0*x(i)*(x(i)/lp-1.0d0)** &
        (3.0d0-nf(x(i),lp))*1.0d-6 ! Winterwerp, 1998
    end if

    ! if breakup frequency>1, let it equal to 1
    if (breakup(i)>1.0d0) breakup(i)=1.0d0
  end do
else
  open(99,file="Warning File.lis")
  write(99,*) "Warning: Please give other used defined &
    breakup frequency function!"
  close(99)
  stop
end if

! Fragmentation distribution function
if (option_fragdis == 1) then
  do k = 1, n
    do i = 1,Ndd
      if (x(i) >= lp*2.0d0**(1.0d0/3.0d0)) then
        ! Binary Breakup
        fragdis(i,k)= x(i)**((k-1.0d0)/adjust)* &
          (2.0d0**((3.0d0*adjust-(k-1.0d0))/3.0d0/adjust))
      else
        fragdis(i,k) = 0.0d0
      end if
    end do
  end do
else

```

```

open(99,file = "Warning File.lis")
  write(99,*) "Warning: Please give other used defined &
              Fragmentation distribution function!"
close(99)
stop
end if

! Breakup source and sink term
do k = 1,n
  do i = 1,Ndd
    birth_bre(k) = birth_bre(k)+fragdis(i,k)*breakup(i)*w(i)
    death_bre(k) = death_bre(k)+x(i)**((k-1.0d0)/adjust)&
                  *breakup(i)*w(i)
  end do
end do

! Total source and sink term
do k = 1,n
  ssterm(k) = birth_agg(k)-death_agg(k)+birth_bre(k)-death_bre(k)
  agg(k)    = birth_agg(k)-death_agg(k)
  bre(k)    = birth_bre(k)-death_bre(k)
  birth(k)  = birth_agg(k)+birth_bre(k)
  death(k)  = death_agg(k)+death_bre(k)
end do

RETURN
END SUBROUTINE FLOCSSTERM

!+++++

SUBROUTINE WHEELER (n, mom, x, w, option_Gauss, lp, nout)
  implicit none
  integer,parameter:: NP = selected_real_kind(8)
  integer          n, option_Gauss, nout
  real(kind=NP) mom(2*n), x(n), w(n)
  real(kind=NP) lp

```

! This program is to extract the abscissas and weights from the given moments.

! Reference:

! [1] Press, W.H., Teukolsky, S.A., Vetterling, W.T., and Flannery, B.P., 1992. Numerical Recipes in Fortran 77: The Art of Scientific Computing, Cambridge University Press, Cambridge.

! [2] Yuan., C., and Fox, R.O., 2011. Conditional quadrature method of moments for kinetic equations. Journal of computational physics 230, 8216-8246.

! INPUT:

! n Maximum # of nodes

! mom(2*n) Moments from 0 to 2*n-1 [mom(1), ..., mom(2*n)]

! OUTPUT:

! x(n) Abscissas in descending order. Actual # of nodes is "nout", the rest is set to null.

! w(n) Corresponding weights.

! nout Actual # of nodes (with positive weight) (0 < nout <= n)

! Others:

! werror This algorithm fails when werror > 0

! eabs Minimum distance between distinct abscissas

! rmin Minimum ratio w(min)/w(max). rmin(1) is for 'vacuum' state, i.e., density is null;

! rmin(nl) is minimum ratio for nl nodes, nl = 2, 3, ..., n

integer i, j, k, l, werror, nl, m

real(kind=NP) eabs, cutoff, bmin, dab, mindab, maxdab, minw, maxw, amu0

real(kind=NP) rmin(n), nu(n), a(n), b(n), d_sig(2*n+1), al(n)

real(kind=NP), allocatable:: z(:, :)

amu0 = mom(1)

do i = 1, 2*n

mom(i) = mom(i)/amu0

end do

! Control parameter

```
! eabs: Minimum distance between distinct abscissas.
```

```
eabs = 1.0d-5
```

```
! rmin: Depend on how accurately the moments are reproduced, with less  
accurate moments requiring larger values. A larger value would reduce the number  
of nodes.
```

```
! rmin(1) can be set very small
```

```
! rmin(2) controls the switch from one-to two-node quadrature, can be  
relatively small since lower-order moments are typically more accurate.
```

```
rmin(1) = 1.0d-26
```

```
do i = 2,n
```

```
    rmin(i) = 1.0d-20
```

```
end do
```

```
! Set initial value of abscissas, weights
```

```
do i = 1,n
```

```
    x(i) = 0.0d0
```

```
    w(i)=0.0d0
```

```
end do
```

```
cutoff = 0.0d0
```

```
werror = 0
```

```
if (mom(1) < 0) then
```

```
    print*, 'Negative number density!'
```

```
    werror = 1
```

```
    pause
```

```
    goto 1007
```

```
elseif (mom(1) == 0) then
```

```
    nout=1
```

```
    goto 1007
```

```
end if
```

```
if (n == 1 .OR. mom(1) < rmin(1)) then
```

```
    w(1) = mom(1)
```

```
    x(1) = mom(2)/mom(1)
```

```
    nout = 1
```

```

        goto 1007
end if

! Compute modified moments equal to moments
do i=1,n
    nu(i)=mom(i)
end do

! Construct recurrence matrix
do i = 1,n
    a(i) = 0.0d0
    b(i) = 0.0d0
end do

call whorthog(n, mom, a, b, option_Gauss, lp, d_sig)

! Determine maximum n using diag elements of sig
m = n
do k = (n+1),3,-1
    if (d_sig(k) <= cutoff) then
        m = k-2
        if (m == 1) then
            w(1) = mom(1)
            x(1) = mom(2)/mom(1)
            nout = 1
            goto 1007
        end if
    end if
end do

! Compute quadrature using maximum n
do i = 1,n
    a(i) = 0.0d0
    b(i) = 0.0d0
end do

call whorthog(m, mom, a, b, option_Gauss, lp, d_sig)

```

```

! Check if moments are not realizable (should never happen)
! Find bmin
bmin = b(1)
do i = 1,m
    if (bmin > b(i)) bmin = b(i)
end do

if (bmin < 0) then
    print*, 'Negative number density!'
    pause
    werror = 1
    goto 1007
end if

! Setup Jacobi matrix
do nl = m,1,-1
    if (nl == 1) then
        w(1) = mom(1)
        x(1) = mom(2)/mom(1)
        nout = 1
        goto 1007
    end if

    allocate(z(nl,nl))

    do j = 1,nl
        do i = 1,nl
            z(i,j) = 0.0d0
        end do
    end do

    do i = 1,(nl-1)
        b(i) = b(i)**0.5d0
    end do
    b(nl) = 0.0d0

```



```

! Compute weights and abscissas
call imtql2(nl, a, b, al, z)
call eigsrt(al, z, nl)

do i = 1,n
    w(i) = 0.0d0
    x(i) = 0.0d0
end do

do i = 1,nl
    w(i) = mom(1)*(z(1,i)**2.0d0)
    x(i) = al(i)
end do

mindab = abs(x(1)-x(2)); maxdab = mindab
do i = nl,2,-1
    do j = 1,i-1
        dab = abs(x(i)-x(j))
        if (mindab > dab) mindab = dab
        if (maxdab < dab) maxdab = dab
    end do
end do

if (nl == 2) then
    maxdab = 1
end if

! Check conditions that weights and abscissas must both satisfy
minw = w(1); maxw = w(1)
do i = 1,nl
    if (minw > w(i)) minw = w(i)
    if (maxw < w(i)) maxw = w(i)
end do

if ( minw/maxw > rmin(nl) .AND. mindab/maxdab > eabs) then
    nout = nl
    goto 1007

```

```

        else
            deallocate(z(n1,n1))
        end if
    end do

1007 do i = 1,n
        w(i) = w(i) * amu0
    end do

    do i = 1,2*n
        mom(i) = mom(i) * amu0
    end do

    RETURN
END SUBROUTINE WHEELER

!+++++

SUBROUTINE WHORTHOG(n, anu, a, b, option_Gauss, lp, d_sig)
    implicit none
    integer,parameter:: NP = selected_real_kind(8)
    integer n, option_Gauss
    real(kind=NP) a(n), anu(2*n), b(n), d_sig(2*n+1), lp

! This program is modified from that given by program "orthog" in Press et
al.(1992), Numerical Recipes in Fortran 90.

! Purpose: Calculate the coefficients a(i) & b(i) of the real symmetric
! tridiagonal Jacobi matrix using Wheeler's algorithm (Press et al.,1992).
! In other words, construct the following matrix:
! [a(1)  b(1)                ]
! [b(1)  a(2)  b(2)         ]
! [      b(2)  a(3)  b(3)   ]
! [      ...   ...   ...   ]
! [      ...   ...   ...   ]
! [      b(n-2)  a(n-1)  b(n-1) ]
! [      b(n-1)  a(n)    ] (n x n)

```

```

! Input:
! n      # of quadrature points
! anu(2*n) Moments m(0), m(1), ..., m(2*n-1);
!      with anu(1)=m(0); anu(2)=m(1), ..., anu(2*n)=m(2*n-1)
!
! Output:
! a(n)   Coefficients of the main diagonal of the Jacobi matrix
!      a(1), a(2), ..., a(n)
!
! b(n)   Coefficients of the subdiagonal/superdiagonal of the Jacobi
!      matrix b(2), ..., b(n). Note: b(n) could be arbitrary.

integer      k, l, i, j
real (kind=NP) sig(2*n+1, 2*n+1)

do j = 1, (2*n+1)
  do i = 1, (2*n+1)
    sig(i, j) = 0.0d0
  end do
end do

do l = 2, 2*n+1
  sig(2, l) = anu(l-1)
end do

a(1) = anu(2)/anu(1)
b(1) = 0.0d0      ! Here, b(1) is arbitrary!

do k = 3, n+1
  do l = k, 2*n-k+3
    sig(k, l) = sig(k-1, l+1) - a(k-2)*sig(k-1, l) - b(k-2)*sig(k-2, l)
  end do
  a(k-1) = sig(k, k+1)/sig(k, k) - sig(k-1, k)/sig(k-1, k-1)
  b(k-1) = sig(k, k)/sig(k-1, k-1)
end do

```

```

do i = 1,2*n+1
  d_sig(i) = sig(i,i)
end do

if (option_Gauss == 2) then
  open(99,file = "Warning File.lis")
  write(99,*) "Warning: Please give subroutine for Gauss Radau
quadrature!"
  close(99)
  stop

elseif (option_Gauss == 3) then
  open(99,file = "Warning File.lis")
  write(99,*) "Warning: Please give subroutine for Gauss Lobatto
quadrature!"
  close(99)
  stop
end if

do i = 1,n-1
  b(i) = b(i+1)      ! Change to b(n) is arbitrary!
end do

b(n) = 0.0d0

RETURN
END SUBROUTINE WHORTHOG

```

!+++++

```

SUBROUTINE IMTQL2(n,d,e,d1,z)
  implicit none
  integer,parameter:: NP = selected_real_kind(8)
  integer          i, j, k, l, m, n, ii, nm, mml, ierr
  real(kind=8)     d(n), e(n), z(n,n), d1(n), e1(n)
  real(kind=8)     b, c, f, g, p, r, s, tst1, tst2, pythag, t

```

! This subroutine is a translation of the algol procedure imtql2, num. math.

12, 377-383(1968) by martin and wilkinson,
! as modified in num. math. 15, 450(1970) by dubrulle. Handbook for auto. comp.,
vol.ii-linear algebra, 241-248(1971).
! www.netlib.org/eispack/imtql2.f (EISPACK)

! This subroutine finds the eigenvalues and eigenvectors of a symmetric
tridiagonal matrix by the implicit QL method.

! Use pythag for dsqrt(a*a + b*b) .

! Input:

! n The order of the matrix.
! d(n) The diagonal elements of the input matrix.
! e(n) The subdiagonal elements of the input matrix
! in its last n-1 positions. e(n) is arbitrary.

! Output:

! dl(n) The eigenvalues in ascending order. If an error exit is made, the
eigenvalues are correct but unordered for indices 1,2,...,ierr-1.
! e(n) Output of $e(n)=[\text{Input of } e(n)]^{**2}$.
! z Orthonormal eigenvectors of the symmetric tridiagonal matrix.
! If an error exit is made, z contains the eigenvectors associated with
the stored eigenvalues.

! Others

! ierr ierr=0 for normal return; ierr=j if the j-th eigenvalue has not been
! determined after 30 iterations.

! Questions and comments should be directed to burton s. garbow, mathematics
and computer science div, argonne national laboratory. This version dated august
1983.

! Store the value of d(n) and e(n) in dl(n) and el(n) , respectively

do i = 1,n

 dl(i) = d(i)

 el(i) = e(i)

end do

```

! Initialize
ierr = 0
nm = n
do j = 1,n
  do i = 1,nm
    z(i,j) = 0.0d0
  end do
end do

do i = 1,n
  z(i,i) = 1
end do

do 1015 l = 1, n
  j = 0
  ! Look for small sub-diagonal element
1012  do m = 1, n
    if (m .eq. n) go to 1013
    tst1 = dabs(d(m)) + dabs(d(m+1))
    tst2 = tst1 + dabs(e(m))
    if (tst2 .eq. tst1) go to 1013
  end do

1013  p = d(l)
    if (m .eq. 1) go to 1015
    if (j .eq. 30) go to 1010
    j = j + 1

    ! Form shift
    g = (d(l+1) - p) / (2.0d0 * e(l))
    r = pythag(g,1.0d0)
    g = d(m) - p + e(l) / (g + dsign(r,g))
    s = 1.0d0
    c = 1.0d0
    p = 0.0d0
    mml = m - 1

```

```

! For i=m-1 step -1 until 1 do
do ii = 1, mml
  i = m - ii
  f = s * e(i)
  b = c * e(i)
  r = pythag(f,g)
  e(i+1) = r
  if (r .eq. 0.0d0) go to 1014
  s = f / r
  c = g / r
  g = d(i+1) - p
  r = (d(i) - g) * s + 2.0d0 * c * b
  p = s * r
  d(i+1) = g + p
  g = c * r - b

! Form vector
do k = 1, n
  f = z(k,i+1)
  z(k,i+1) = s * z(k,i) + c * f
  z(k,i) = c * z(k,i) - s * f
end do
end do

d(1) = d(1) - p
e(1) = g
e(m) = 0.0d0
go to 1012

! Recover from underflow
1014 d(i+1) = d(i+1) - p
     e(m) = 0.0d0
     go to 1012
1015 continue

! Order eigenvalues and eigenvectors .

```

```

do 1017 ii = 2, n
  i = ii - 1
  k = i
  p = d(i)

do 1016 j = ii, n
  if (d(j) .ge. p) go to 1016
  k = j
  p = d(j)
1016 continue

if (k .eq. i) go to 1017
d(k) = d(i)
d(i) = p

do j = 1, n
  p = z(j,i)
  z(j,i) = z(j,k)
  z(j,k) = p
end do

1017 continue

go to 1011

! Set error -- no convergence to an eigenvalue after 30 iterations.
1010 ierr = 1

! Exchange d(1) and d1(1), e(1) and e1(1)
1011 do i = 1,n
  t = d1(i)
  d1(i) = d(i)
  d(i) = t
end do

do i = 1,n
  t = e1(i)

```



```

        e1(i) = e(i)
        e(i) = t
    end do

    do i = 1,n
        e(i) = e(i)**2.0d0
    end do

    RETURN
END SUBROUTINE IMTQL2

!+++++

SUBROUTINE EIGSRT(d, v, n)
    implicit none
    integer, parameter :: NP = selected_real_kind(8)
    integer n
    real(kind=NP) d(n), v(n,n)

! This program is originally presented in Press et al., 1992.
!
! Purpose: Given the eigenvalue matrix d(n) and eigenvector matrix v(n,n),
! this routine sorts the eigenvalues into descending order,
! and rearranges the columns of v correspondingly.
! The method is straight insertion.
!
! Input:
!     n      Integer. The order of the input matrix.
!     d(n)   Real. Eigenvalue.
!     v(n,n) Real. Eigenvectors. The i-th colume of matrix V is the
!             eigenvector correspond to eigenvalue d(i) .
! Output:
!     d(n)   Real. Eigenvalue in descending order.
!     v(n,n) Real. Corresponding eigenvectors of d(n).

    integer    i, j, k
    real(kind=NP) p

```

```

do i = 1,n-1
  k = i
  p = d(i)
  do j = i+1,n
    if(d(j).ge.p)then
      k = j
      p = d(j)
    end if
  end do
  if(k.ne.i)then
    d(k) = d(i)
    d(i) = p
    do j = 1,n
      p = v(j,i)
      v(j,i) = v(j,k)
      v(j,k) = p
    end do
  end if
end do

RETURN
END SUBROUTINE EIGSRT

!+++++

DOUBLE PRECISION FUNCTION PYTHAG(a,b)
  implicit none
  double precision a,b

! Finds dsqrt(a**2+b**2) without overflow or destructive underflow
! www.netlib.org/eispack/3090vf/double/pythag.f (EISPACK)

  double precision p,r,s,t,u

  p = dmax1(dabs(a),dabs(b))
  if (p .eq. 0.0d0) go to 1019

```

```

    r = (dmin1(dabs(a),dabs(b))/p)**2
1018  continue
    t = 4.0d0 + r
    if (t .eq. 4.0d0) go to 1019
    s = r/t
    u = 1.0d0 + 2.0d0*s
    p = u*p
    r = (s/u)**2 * r
    go to 1018
1019  pythag = p

    RETURN
END FUNCTION PYTHAG

!+++++

FUNCTION NF(L,lp)
  use global
  implicit none
  real(kind=NP) L, lp
  real(kind=NP) nf

! This function is used to compute the fractal dimension nf based on the floc
size.

  real(kind=NP) xi_nf, delta_nf

! Maggi et al., 2007, can also be expressed based on other relationships
xi_nf      = -0.1d0
delta_nf   = 3.0d0

  if (L <= lp) then
    nf = 3.0d0
  else
    nf = delta_nf*(L/lp)**xi_nf
    ! Can be
  end if

```

```

    RETURN
END FUNCTION NF

!+++++

FUNCTION STRENGTH(L,lp)
  use global
  implicit none

  real(kind=NP) L,lp
  real(kind=NP) strength

! This function is used to compute the floc strength based on the floc size.
! Uses function NF

  !real(kind=NP) C1
  !real(kind=NP),external:: nf

  Strength = 1.0d-10 ! Constant
                   ! Can be extended to variable floc strength

  RETURN
END FUNCTION STRENGTH

```

APPENDIX B:

EXAMPLE OF INPUT FILE OF FLOC SIZE DISTRIBUTION BOX MODEL

File name: 'Floc0D.log'.

Input File of Flocculation Box Model.

(Xiaoteng Shen, Virginia Institute of Marine Science, College of William & Mary,
xiaoteng@vims.edu, Jan 2014.)

=====

1. Basic parameters.

Note: (1) Maximum number of nodes, Nd.

(2) Number of tracked moments, n.

(3) Adjustable factor, p.

(4) Size of time increment, dt, in second.

(5) Number of time step, nt.

(6) To skip this number of time steps before saving, ncheck.

(7) Solution method. 1 for unfixed pivot approach; 2 for fixed pivot approach.

(Note: If one chooses fixed pivot approach, specify the quadrature nodes in the file 'Selected quadrature points.log');

(8) Quadrature type. For unfixed pivot approach, 1 - Standard Gaussian quadrature, 2 - Gaussian-Radau quadrature, 3 - Gaussian-Lobatto quadrature. For fixed pivot approach, set to 0.

(9) Size of primary particle lp, in micron;

(10) Shear rate (/s);

(11) Suspended sediment concentration (g/L).

8 16 5.0d0 0.1d0 180000 1000 1 1 5.0d0 45.0d0 0.28

2. Initial condition.

Note: 1 - Initially one class with size of primary particles;

2 - Refer to the file 'Initial moments.log' to read the initial normalized moments.

1

3. Kernel structures.

(1) Collision frequency, beta: 1 for default, others for user defined;

(2) Collision efficiency, alpha: 1 for default, others for user defined;
(3) Breakup frequency, a: 1 for default, others for user defined;
(4) Fragment distribution function, b: 1 for default, others for user defined.
Note: C1 is the fitting parameter for collision efficiency, set to 0 if no aggregation;

C2 is the fitting parameter for breakup frequency, set to 0 if no breakup.

(1)	(2)	(3)	(4)	C1	C2
1	1	1	1	0.85d0	3.2d-5

APPENDIX C:

MICRO-CONTROLLER OPERATING PROGRAM

(CODE IN ASSEMBLER LANGUAGE)

File name: 'FlocCameraSony.asm'.

```
; Assembler codes for Teensy 2.0 (with Atmel microcontroller Mega32U4, 16 MHz)
; For control a remote control for Sony NEX-5R and the external flush light.
;
; Port-address
.equ   DDRB   = 0x04
.equ   PORTB  = 0x05
.equ   CLKPR  = 0x61
.equ   PORTD  = 0x0A
.equ   DDRD   = 0x0B

; The following two statements are directives
.cseg           ; Code segment
.org   0        ; Set program origin

; Use clock prescaler to reduce power. If someone leaves this
; plugged into their laptop, which continues providing USB power
; in sleep mode, it's nice to conserve their battery.
;
; One can easily try different speeds by just uncommenting a
; different line, instead of having to edit the delay code below.
;
ldi r16, 0x80 ; CPU Clock   LED Off   LED On

; ldi r17, 0x00 ; 16 MHz   11.07 mA  13.97 mA
; ldi r17, 0x01 ; 8 MHz    6.71 mA   9.65 mA
; ldi r17, 0x02 ; 4 MHz    4.67 mA   7.61 mA
; ldi r17, 0x03 ; 2 MHz    2.98 mA   5.93 mA
; ldi r17, 0x04 ; 1 MHz    2.18 mA   5.14 mA
ldi r17, 0x05 ; 500 kHz   1.70 mA   4.66 mA
```

```

; ldi r17, 0x06 ; 250 kHz 1.46 mA 4.43 mA
; ldi r17, 0x07 ; 125 kHz 1.34 mA 4.30 mA
; ldi r17, 0x08 ; 62.5 kHz 1.28 mA 4.25 mA

sts CLKPR, r16
sts CLKPR, r17

sbi DDRB,0 ; Set Port B.0 for output
cbi PORTB,0 ; Clear Port B.0 (For flush light)

sbi DDRB,1 ; Set Port B.1 for output
cbi PORTB,1 ; Clear Port B. 1 (For camera)

sbi DDRD,6 ; Set Port D.6 for output
cbi PORTD,6

; Blinking on-board LED 5 times
sbi PORTD,6 ; Set PORTD.6 high
rcall delay_100ms ; Delay about 100 ms
cbi PORTD,6 ; Set PORTD.6 low
rcall delay_100ms
sbi PORTD,6
rcall delay_100ms
cbi PORTD,6
rcall delay_100ms
sbi PORTD,6
rcall delay_100ms
cbi PORTD,6
rcall delay_100ms
sbi PORTD,6
rcall delay_100ms
cbi PORTD,6
rcall delay_100ms
sbi PORTD,6
rcall delay_100ms
cbi PORTD,6
rcall delay_100ms

```



```

loop:
    sbi PORTB,1          ; Set Port B.1 high to trigger camera.

    rcall delay_100ms
    rcall delay_100ms

    sbi PORTB,0          ; Set Port B.0 high to turn on flush light.
    rcall delay_100ms
    rcall delay_100ms

    cbi PORTB,1          ; Set Port B.1 low to stop camera.
    rcall delay_100ms

    cbi PORTB,0          ; Set Port B.0 low to turn off flush light.

    rcall delay_100ms
    rcall delay_100ms
    rcall delay_100ms
    rcall delay_100ms
    rcall delay_100ms
    rcall delay_100ms
    rcall delay_100ms
    rcall delay_100ms
    rcall delay_100ms
    rcall delay_100ms
    rcall delay_100ms
    rcall delay_100ms
    rcall delay_100ms
    rcall delay_100ms

; Blink on-board LED once
    sbi PORTD,6          ; Set PORTD.6 high
    rcall delay_100ms
    cbi PORTD,6          ; Set PORTD.6 low
    rcall delay_100ms
    rjmp loop           ; Endless loop

```

```
; Simple Delay Function (Approximately 100 ms, not exactly) used in Teensy 2.0  
(Atmel mega32U4, 16 MHz)
```

```
delay_100ms:
```

```
    ldi  R19,50      ; R19 = 50
```

```
delay0: ldi  R20,255 ; R20 = 255
```

```
delay1: nop
```

```
    dec  R20        ; Decrease R20 value
```

```
    brne delay1    ; if (R20 != 0) goto delay1 label
```

```
    dec  R19        ; Decrease R19 value
```

```
    brne delay0    ; if (R19 != 0) goto delay0 label
```

```
    ret           ; Return to the caller
```

APPENDIX D:

EMPIRICAL IMAGE PROCESSING SOFTWARE

(CODE IN MATLAB)

```
% This program is an image processing tool to find the Floc Size
% Distributions (FSDs) of suspended particles for a SINGLE image.

% One can easily modify it as a subroutine to process a large number of
% images.

% Written by Xiaoteng Shen (xiaoteng@vims.edu, May 2015)
% Virginia Institute of Marine Science, Gloucester Point, VA 23062, USA

% Camera: Sony Alpha NEX-5R
% Original Sensor resolution: 4912 x 3264 (23.5 mm x 15.6 mm),
%                               4.8 micron/pixel
% Subject to image ratio: 1: 2.2, thus, 2.2 micron/pixel for 10.7 x 7.1 mm
% Light Source: Laser

clc; clear all; close all; imtool close all;

f = imread ('DSC02161.jpg'); % RGB figure, matrix [3264 x 4912 x 3]
Resolution = 2.2; % micron/pixel
figure, imshow (f);

F = f(:,:,2); % Converts RGB images to grayscale (0 -- black, 255 -- white)
% Note: This laser source is Green.
figure, imshow(F);

sigma = 2.0; % Standard deviation of the Gaussian distribution
[Igx,Igy]= gaussgradient(F,sigma);
Ig = abs(Igx)+ abs(Igy);
Igg = reshape(Ig,1,[]);

% Statistical distribution of pixel gradients
```

```

figure, plot(Igg); xlabel('Pixels'); ylabel('Gradient');

% Background illumination correction

% Light may strong in some place but weaker in other. This may cause
% problem with the thresholding to detect the objects. The
% image is divided into small parts and computes the minimum value (the
% blackest pixel) in each part. Then it creates an image with the size of
% the original one with these values. Finally, this background
% representation image is subtracted from the original image.

backApprox = blkproc (F, [30 30], 'min(x(:))');
[XbApp,YbApp]=size(backApprox);
backApprox(XbApp,:)=backApprox(XbApp-1,:);
backApprox(:,YbApp)=backApprox(:,YbApp-1);

backApprox = double(backApprox)/255;
figure,surf(backApprox);
set(gca,'ydir','reverse');axis equal;
% colormap('gray');
set (gca,'FontSize',16);

BBB=imresize(backApprox,size(F),'bilinear');
f1=im2double(F)-BBB;
f1=max(min(f1,1),0); % Clip the pixel vales to the valid range [0 1].

% Image Enhancement (Contrast stretching / correction)
% It is necessary to adjust the contrast. It rescales the image
% intensity redistributing the pixel intensity values between the
% minimum and the maximum intensity values.

f2 = imadjust (f1, [0 0.60], [], 2); % Empirical
imtool(f2)

% Thresholding
% Highly empirical, other threshold methods may use for different
% applications.

```

```

level = 0.18;
% level = graythresh(f2) % Otsu's method: Otsu (1979)

% Convert to a binary image
f3 = im2bw(f2,level);
imtool(f3)

% Manipulate the binary image

% Remove background noise
% Remove small objects with area < 4 pixels or minor axis < 2 pixels
f4 = bwareaopen(f3, 4, 8);
Conn = bwlabel(f4,8);
MinAx = regionprops(Conn, 'MinorAxisLength');
f4 = ismember(f4, find([MinAx.MinorAxisLength]>=2));
clear Conn MinAx;

% Morphological operations
% Connect pixels separated by single-pixel gaps
f4 = bwmorph (f4, 'bridge');

% Dilation and Erosion.
% Pixels are added and then removed from the outside of each floc.
B = [1 1 1; 1 1 1; 1 1 1];
f4 = imdilate(f4, B);
f4 = imerode (f4, B);

% Fill the holes
f4 = imfill(f4,'holes');

% Remove incomplete objects on the border
f4 = imclearborder (f4);

% Remove small objects again.
f4 = bwareaopen(f4, 4, 8);
Conn = bwlabel(f4,8);
MinAx = regionprops(Conn, 'MinorAxisLength');

```

```

f4 = ismember(f4, find([MinAx.MinorAxisLength]>=2));
clear Conn MinAx;

% Find processed objects
f5 = f4;
[L, N] = bwlabel (f5, 4);
N

% Removing out-of-focus objects
alpha_cr = 100; % Critical clarity value

f6 = f5; % "f6" is original "f5", will not change; "f5" will be updated.
for ii=1: N;
    %ii
    [RR, CC]=find(bwlabel(f6)==ii);
    ROIx1 = min(RR)-1; ROIx2 = max(RR)+1; % Boundary Removed
    ROIy1 = min(CC)-1; ROIy2 = max(CC)+1;
    alpha = max(max(Ig(ROIx1:ROIx2, ROIy1:ROIy2)));

    if alpha < alpha_cr; % If the object is out-of-focus
        for jj=1:length(RR);
            f5(RR(jj),CC(jj))= 0; % Remove the object, set it to background
        end
    end
end

% Find objects after removal of out-of-focus objects
[L1, N1] = bwlabel (f5, 4);
N1

RemainInFoucs = N1/N % The ratio of particle remain in focus.

% Particle properties
graindata = regionprops (L1, 'area', 'EquivDiameter','MajorAxisLength',
'MinorAxisLength','Perimeter','Solidity'); % N x 1 struct, i.e., N objects

% Plot FSDs

```

```

% Compute equivalent diameter based statistics
De = [graindata.EquivDiameter]; % in pixel
De = De * Resolution; % in micron
Dmin_micron = min(De)
Dmax_micron = max(De)
Dmean_micron = mean(De)
Dmedian_micron = median(De)

% In this program, only FSDs based on one image is plotted.
% However, one can record the size of particles, for example, in 100 images,
% and find a converged FSD.

% May use other edges for different applications.
edges= [Dmin_micron 7.5:5:62.5];
[bincounts] = histc(De, edges)
figure, bar(edges, bincounts, 'histc');
title('Histogram of Floc Size Distribution');
xlabel('Size (Micron)');ylabel('Number');
set(gca,'xtick',[5 10 15 20 25 30 35 40 45 50 55 60]);

% ++++++

% The following subroutine are freely available online and contributed by
% anyone else.

function [gx,gy]=gaussgradient(IM,sigma)
% GAUSSGRADIENT Gradient using first order derivative of Gaussian.
% [gx,gy] = gaussgradient(IM,sigma) outputs the gradient image gx and gy of
% image IM using a 2-D Gaussian kernel. Sigma is the standard deviation of
% this kernel along both directions.
%
% Contributed by Guanglei Xiong (xgl99@mails.tsinghua.edu.cn)
% at Tsinghua University, Beijing, China.

% Determine the appropriate size of kernel. The smaller epsilon, the larger
% size.
epsilon=1e-2;

```

```

halfsize=ceil(sigma*sqrt(-2*log(sqrt(2*pi)*sigma*epsilon)));
size=2*halfsize+1;

% Generate a 2-D Gaussian kernel along x direction
for i=1:size
    for j=1:size
        u=[i-halfsize-1 j-halfsize-1];
        hx(i,j)=gauss(u(1),sigma)*dgauss(u(2),sigma);
    end
end
hx=hx/sqrt(sum(sum(abs(hx).*abs(hx))));

% Generate a 2-D Gaussian kernel along y direction
hy=hx';

%2-D filtering
gx=imfilter(IM,hx,'replicate','conv');
gy=imfilter(IM,hy,'replicate','conv');

function y = gauss(x,sigma)
%Gaussian
y = exp(-x^2/(2*sigma^2)) / (sigma*sqrt(2*pi));

function y = dgauss(x,sigma)
%first order derivative of Gaussian
y = -x * gauss(x,sigma) / sigma^2;

```


APPENDIX E:

TURBULENCE CHARACTERISTICS COMPUTING SOFTWARE

(CODE IN MATLAB)

```
% This program is used to analysis ADV data to find the mean flow and
% turbulence AT ONE POINT (one file).
% One can easily modify it as a subroutine to process large number of files.

% Write by Xiaoteng Shen (Virginia Institute of Marine Science,
% xiaoteng@vims.edu, Sep 2014, Version 2.0)

% Instrument: 5MHz ADVOcean.
% Data is collected by the software: SonTek SonUtils.

clc; clear all; close all; format short g;

Hz = 10;          % Frequency of ADV, Hz
T = 2;           % Time average, min

Npm = Hz*60;     % # of recorded data per min
Ntot = Npm*T;    % Total # of data used for analysis
time = 1/Hz:1/Hz: T*60;

% Read the ADV raw data.

A = load('Aug2014_#100.log');
    % Totally 15 columns
    % Column 1: Sample number.
    % Column 2-4: Three instantaneous velocity components.(Units: 0.1 mm/s)
    % Column 5-7: Amplitude. Signal strength for the 3 acoustic receivers.
    %             (Unit: counts, 1 count = 0.43db) If in units of db, it
    %             becomes SNR.
    % Column 8 -10: Correlation (0-100).
    % Column 11-13: Heading (0-3600, step 0.1 degree),Pitch, Roll.
    % Column 14 : Temperature. (Unit: 0.01 C)
```

```

    % Column 15 : Pressure. (Unit: counts, can converted to dBar).

RawData = A (1:Ntot,:); % For T min average, find the first Ntot data.
clear A;

% Velocity time series (Raw data)
figure(1);clf;
subplot(311);
plot(time,RawData(:,2)/100,'b-');
ylabel('u ( cm/s )'); xlabel ('Time (s)');
title('Velocity Time Series (Raw Data)');

subplot(312);
plot(time,RawData(:,3)/100,'r-');
ylabel('v ( cm/s )'); xlabel ('Time (s)');

subplot(313);
plot(time, RawData(:,4)/100,'k-');
ylabel('w ( cm/s )'); xlabel ('Time (s)');

% SNR & Correlation filtering to find mean flow.

% Filter the data based on SNR. SNR is to verify there are sufficient
% particulate matter. For good operating conditions: SNR > 15 db (35
% counts).

str1 = 'Raw data filtering based on SNR and correlation.'
jj=1;
for ii = 1: Ntot;
    if RawData(ii,5)>= 35 && RawData(ii,6)>= 35 && RawData(ii,7) >= 35;
        FilterData1(jj,:)=RawData(ii,:);
        jj=jj+1;
    end
end
N_flt1 = jj-1;
clear ii jj;

```

```

% Filter the data based on correlation coefficient. Ideally, correlation
% values should >= 70%. Conditions in high turbulent flows,
% correlation >= 30 - 40%. After filtering, sufficient # of data should be
% retained.
jj=1;
for ii = 1: N_flt1;
    if FilterData1(ii,8)>= 30 && FilterData1(ii,9)>= 30 ...
        && FilterData1(ii,10)>= 30;
        FilterData2(jj,:)= FilterData1(ii,:);
        jj=jj+1;
    end
end
N_flt2 = jj-1;
RatioDataRemain=N_flt2/Ntot
clear ii jj;

figure(2);clf;
subplot(311);
plot(FilterData2(:,2)/100,'b-');
ylabel('u ( cm/s )'); xlabel ('# of Data');
title('Velocity Time Series (After SNR and Correlation Filtering)');

subplot(312);
plot(FilterData2(:,3)/100,'r-');
ylabel('v ( cm/s )'); xlabel ('# of Data');

subplot(313);
plot(FilterData2(:,4)/100,'k-');
ylabel('w ( cm/s )'); xlabel ('# of Data');

% Note: After SNR and Correlation Filtering, it may still have spikes,
%     but have little influence on mean velocity.
u = FilterData2(:,2)/100; % Instaneous u velocity, in cm/s
v = FilterData2(:,3)/100; % Instaneous v velocity, in cm/s
w = FilterData2(:,4)/100; % Instaneous w velocity, in cm/s
U = mean(u) % in cm/s
V = mean(v) % in cm/s

```

```

W = mean(w) % in cm/s

% Despiking (based on standard variation) to find reasonable
% Turbulent Kinetic Energy (TKE)
str2 = 'Despiking based on mean standard variation.'
std_u = mean((u-U).^2);
std_v = mean((v-V).^2);
std_w = mean((w-W).^2);

jj=1;
for ii = 1: N_flt2;
    if (u(ii)-U)^2 <= 5* std_u && (v(ii)-V)^2 <= 5* std_v ...
        && (w(ii)-W)^2 <= 5* std_w
        FilterData3(jj,:)= FilterData2(ii,:);
        jj=jj+1;
    end
end
N_flt3 = jj-1;
RatioDataRemain=N_flt3/Ntot
clear ii jj;

figure(3);clf;
subplot(311);
plot(FilterData3(:,2)/100,'b-');
ylabel('u ( cm/s )'); xlabel ('# of Data');
title('Velocity Time Series (After SNR, Correlation Filtering & Despiking)');

subplot(312);
plot(FilterData3(:,3)/100,'r-');
ylabel('v ( cm/s )'); xlabel ('# of Data');

subplot(313);
plot(FilterData3(:,4)/100,'k-');
ylabel('w ( cm/s )'); xlabel ('# of Data');

% clear u v w;
u1 = FilterData3(:,2)/100; % Instaneous u velocity, in cm/s

```

```

v1 = FilterData3(:,3)/100; % Instaneous v velocity, in cm/s
w1 = FilterData3(:,4)/100; % Instaneous w velocity, in cm/s
U1 = mean(u1); % in cm/s
V1 = mean(v1); % in cm/s
W1 = mean(w1); % in cm/s

TKE = 0.5*(mean((u1-U1).^2)+ mean((v1-V1).^2)+ mean((w1-W1).^2)) % cm2/s2

% Spectrum Analysis to find reasonable Energy Dissipation Rate (EPS)

uu = FilterData3(:,2)/10000; % Instaneous u velocity, in m/s
vv = FilterData3(:,3)/10000; % Instaneous v velocity, in m/s
ww = FilterData3(:,4)/10000; % Instaneous w velocity, in m/s

dt = 1/Hz; % Time interval for two continuous data, s
N = length(uu); % # of data for spectrum analysis
Time = (0:N-1)*dt; Time = Time'; % in second, assuming first data at t=0

UU = mean(uu); % Mean velocity, in m/s
VV = mean(vv);
WW = mean(ww);
Vel = sqrt(UU.^2+VV.^2+WW.^2);

% Frequency spectrum
% Do FFT for time series
delt_freq = 1/(dt*N);
freq = 0 : delt_freq : ((N-1))*delt_freq;

uul = uu - UU; vvl = vv - VV; wwl = ww - WW; % Remove the mean
fu = fft(uul); fv = fft(vvl); fw = fft(wwl);

% Energy
Eu = [fu.*conj(fu)]/(N/dt);
Ev = [fv.*conj(fv)]/(N/dt);
Ew = [fw.*conj(fw)]/(N/dt);

% Because of symmetrical, fold it and multiple by 2 when plot it.

```

```

Eu = Eu * 2;
Ev = Ev * 2;
Ew = Ew * 2;
Ek = Eu + Ev + Ew;

figure(4); clf;
set(gcf,'position',[220 200 900 600]);
y00=1.0E-4*freq.^(-5/3); % Show -5/3 slope in the figure
% y01=1.0E-4*freq.^(-4/3);
% y02=1.0E-4*freq.^(-6/3);

subplot(221);
loglog (freq, Eu,'r-','linewidth',1); hold on;
%loglog (freq,y00,'k--',freq,y01,'k--',freq,y02,'k--', 'linewidth',2);
loglog (freq,y00,'k-', 'linewidth',2);
xlabel('Frequency (Hz)');ylabel('E_u (m^2/s^2/Hz)');
set(gca,'xlim',[0 freq(end)/2]);

subplot(222);
loglog (freq, Ev,'b-','linewidth',1); hold on;
loglog (freq,y00,'k-', 'linewidth',2);
xlabel('Frequency (Hz)');ylabel('E_v (m^2/s^2/Hz)');
set(gca,'xlim',[0 freq(end)/2]);

subplot(223);
loglog (freq, Ew,'m-','linewidth',1); hold on;
loglog (freq,y00,'k-', 'linewidth',2);
xlabel('Frequency (Hz)');ylabel('E_w (m^2/s^2/Hz)');
set(gca,'xlim',[0 freq(end)/2]);

subplot(224);
loglog (freq, Ek,'-','color',[0.5 0.5 0.5],'linewidth',1); hold on;
loglog (freq,y00,'k-', 'linewidth',2);
xlabel('Frequency (Hz)');ylabel('E (m^2/s^2/Hz)');
set(gca,'xlim',[0 freq(end)/2]);

% Taylor's frozen turbulence hypothesis

```

```

% f --> k : k = 2*pi/L = 2 * pi * f / u

alpha = 0.7; % 0.71 (Liu et al., 2011), or 0.69 (Thomson et al., 2012)

IdFreUp = fix(length(freq)/2); % About 5 Hz
IdFreLow = fix(length(freq)/10); % About 1 Hz

Freq = freq(IdFreLow:IdFreUp)';
EW = Ew(IdFreLow:IdFreUp);

% Least Squares with fixed slope
Yi = log10(EW); Xi = log10(Freq);
Intercept = (sum(Yi)+5/3*sum(Xi))/length(Yi); Intercept = 10^Intercept;
eps = (Intercept/alpha)^1.5/(abs(W/100)/2/pi)

figure(5);clf;
Energy = alpha* eps ^ (2/3).*Freq.^(-5/3)*(abs(W/100)/2/pi)^(2/3);
loglog (Freq, EW,'ko','linewidth',1); hold on;
loglog (Freq,Energy, 'k-', 'linewidth',2.5);
xlabel('Frequency (Hz)'); ylabel('E_w (m^2/s^2/Hz)');
set(gca,'xtick',[1 2 3 4]);

% Other flow parameters
ShearRate = sqrt(eps/1.0e-6) % Shear Rate, s-1
KolmoScale = (1.0e-6^3/eps).^0.25*1.0e6 % Kolmogorov microscale, micron
Az = 0.09*(TKE*1.0e-4)^2/eps % Eddy viscosity, m2/s

```

VITA

Shen, Xiaoteng

Shen, Xiaoteng (simplified Chinese: 沈骁腾; traditional Chinese: 沈驍騰; pinyin: *Shěn Xiāoténg*) was born in Wuxi, Jiangsu Province, People's Republic of China on December 22, 1987. He earned Bachelor of Science degree in Harbor, Waterway and Coastal Engineering from Hohai University (Nanjing, Jiangsu Province, China) in June 2009. He then worked as a Research Assistant at Hohai University from August 2009 to July 2011. He entered Master's program in College of William and Mary, School of Marine Science / Virginia Institute of Marine Science in August 2011. By-passed the Master's degree, he entered the doctoral program in September 2013. Shen defended his Ph.D. dissertation in November 2015. He will officially graduate in January 2016 with a Ph.D. in Marine Science, concentrating in physical oceanography.